

Gyrokinetic simulations of turbulence in magnetic fusion plasmas using a delta-f PIC scheme with evolving background

Présentée le 25 avril 2024

Faculté des sciences de base
SPC - Théorie
Programme doctoral en physique

pour l'obtention du grade de Docteur ès Sciences

par

Moahan MURUGAPPAN

Acceptée sur proposition du jury

Prof. V. Savona, président du jury
Prof. L. Villard, Dr S. Brunner, directeurs de thèse
Dr S. Ethier, rapporteur
Dr A. Mishchenko, rapporteur
Dr J. Decker, rapporteur

“They will marvel at how vulnerable the repository of all our potential once was, how perilous our infancy, how humble our beginnings, how many rivers we had to cross, before we found our way.”

Carl Sagan, *Pale Blue Dot*

To the *MUSMAN* team

Abstract

This thesis has been carried out in the context of a worldwide effort to develop nuclear fusion as a viable energy source of the future. As of today, the most promising state-of-the-art test reactors are tokamaks, where plasmas of 10 to 100 million degree Kelvin are confined in a toroidal magnetic cage for a few seconds. The success of future fusion power plants relies on the complete understanding of various physical aspects of the reactor-plasma configuration, one of which is turbulent transport. In order to achieve ignition, particle and heat transport need to be kept low. It turns out that neoclassical theory, which models transport via Coulomb collisions, severely underestimates experimentally found transport coefficients. This enhanced *anomalous* transport has been found to be caused by microturbulence, driven by free energy associated to profile gradients. Amongst the zoo of various microinstabilities, the electrostatic Ion-Temperature-Gradient (ITG) modes and Trapped-Electron modes (TEM) play a significant role in enhancing particle and heat transport. The study of these modes is conveniently based on the gyrokinetic model, involving an averaging over the fast gyromotion of the particles. As a result, the distribution functions describing plasma species represented in a reduced 5-dimensional phase space and evolved according to the gyrokinetic Vlasov equation, coupled with Maxwell's equations for the self-consistent fields. The Particle-In-Cell (PIC) scheme is known to be one of the standard methods with which the aforementioned system of nonlinear partial differential equations is solved numerically. To address the issue of numerical sampling error inherent in this Monte Carlo approach, which would tend to drown in noise the relatively small physical fluctuations in the core of fusion reactors, the PIC scheme can be further refined using the so-called δf approach, which relies on the assumption that the full distribution function $f = f_0 + \delta f$ does not deviate significantly from a known background f_0 .

Verifying this condition becomes however challenging when modelling the plasma edge where fluctuation amplitudes are high, or determining quasi-steady state profiles corresponding to given sources (flux-driven simulations) over long time scales, where plasma profiles can evolve significantly, in which case the smallness condition on δf would be violated if f_0 remained stationary. This thesis addresses this sampling noise problem by considering f_0 as a time-evolving Maxwellian background distribution, which in terms of configuration variables is assumed to be a magnetic flux function. The evolution of the density and temperature of this Maxwellian is achieved by absorbing via relaxation equations corresponding flux-surface-averaged velocity moments growing in δf

The advantage of the adaptive scheme via a time-dependent ion temperature is first studied using the global gyrokinetic code called GKengine with simplified physics and geometry. Simulations involving ITG modes triggered by steep temperature gradients in sheared-slab geometry are conducted. Sources/sinks are in-

troduced to prevent profiles from relaxing below critical gradients. The adaptive scheme, accounting in this case for the evolution of just the ion temperature profile, is shown to be able to prevent an otherwise indefinite noise accumulation in the zonal component, which ultimately would lead to the unphysical suppression of turbulence. In most cases, similar or even better quality results can be obtained under the adaptive scheme with marker numbers as low as 1/4 of that of the corresponding non-adaptive simulation.

The adaptive scheme is subsequently developed in the framework of the global gyrokinetic PIC code ORB5, where the time-dependent control variate is generalised to adapt both density and temperature profiles in toroidal geometry. Two different physical studies are done using TCV-like profiles and equilibrium magnetic fields. The first involves flux-driven toroidal-ITG simulations with adiabatic electrons. In this case, large heat sources are introduced, generating a strong ion temperature profile deviation from initial values. Considering a local Maxwellian background with time-dependent density and temperature, all simulations under the adaptive scheme have noise kept at a low level, with the potential of reaching quasi-steady state from a single marker-loading.

The second physical study involves a mixed ITG-TEM regime using an upgraded hybrid electron model. Simulations of this study are conducted both in temperature-gradient- and flux-driven modes. Here, the adaptive background involves time-dependent density and temperature profiles for the ions and electrons separately. Diagnostics of weight variance and phase-space sampling are further analysed for these simulations, which all exhibit large profile deviations. Numerical sampling problems near the magnetic axis for high-energy electrons as well as low-energy ions are revealed and investigated. Despite these issues, for all studies conducted in this work, results show that the adaptive scheme always performs better than those of the corresponding non-adaptive ones, in the sense that numerical sampling noise is significantly better controlled at long times, and physical quantities are found to be closer to numerical convergence.

Despite its relative simplicity, the time-dependent f.s.a. Maxwellian control variate coupled with a set of relaxation equations, is shown to be a reliable adaptive background scheme for collision-less electrostatic turbulence simulations. The capability of simulating situations with strong deviations from the initial background has been demonstrated, including for long, up to $c_s t/a \sim 1300$, flux-driven simulations. Therefore, this work should therefore prove useful to the PIC community as a first step towards extending it to global electromagnetic simulations, or developing more sophisticated adaptive control variates to also handle simulations of edge and Scrap-Off-Layer (SOL) conditions.

Keywords: gyrokinetic, PIC, control variate, background Maxwellian, noise control, turbulence, magnetic confinement

Résumé

Cette thèse a été réalisée dans le cadre d'un effort mondial visant à développer la fusion nucléaire en tant que source d'énergie viable pour l'avenir. À l'heure actuelle, les réacteurs d'essai de pointe les plus prometteurs sont les tokamaks, où des plasmas de 10 à 100 millions de degrés Kelvin sont confinés dans une cage magnétique toroïdale pendant quelques secondes. Le succès des futures centrales de fusion repose sur la compréhension complète de divers aspects physiques de la configuration du réacteur de plasma, dont le transport turbulent. Pour obtenir l'allumage, le transport des particules et de la chaleur doit être maintenu à un niveau faible. Il s'avère que la théorie néoclassique, qui modélise le transport par des collisions de Coulomb, sous-estime fortement les coefficients de transport trouvés expérimentalement. Il s'est avéré que ce transport augmenté, dit anormal, est dû à la microturbulence, entraînée par l'énergie libre associée aux gradients de profil. Parmi diverses micro-instabilités, les modes électrostatiques de gradient de température ionique (Ion-Temperature-Gradient, ITG) et les modes d'électrons piégés (Trapped Electron Modes, TEM) jouent un rôle important dans l'augmentation du transport des particules et de la chaleur. L'étude de ces modes est basée sur le modèle gyrocinétique, impliquant une moyenne sur le mouvement de gyration rapide des particules. En conséquence, les fonctions de distribution décrivant les espèces du plasma sont représentées dans un espace de phase réduit à 5 dimensions et évoluent selon l'équation gyrocinétique de Vlasov, couplée aux équations de Maxwell pour les champs auto-cohérents.

Le schéma PIC (Particle-In-Cell) est connu pour être l'une des méthodes standard avec laquelle le système susmentionné d'équations différentielles partielles non linéaires est résolu numériquement. Pour résoudre le problème de l'erreur d'échantillonnage numérique inhérente à cette approche, qui tendrait à noyer dans le bruit les petites fluctuations physiques relatives dans le cœur des réacteurs de fusion, le schéma PIC peut être affiné en utilisant l'approche dite δf , qui repose sur l'hypothèse que la fonction de distribution complète $f = f_0 + \delta f$ ne s'écarte pas de manière significative d'un arrière-plan connu f_0 .

La vérification de cette condition devient cependant difficile lorsqu'on effectue des simulations dites forcées par les flux sur de longues échelles de temps, où les profils du plasma peuvent évoluer de manière significative, auquel cas l'hypothèse de petitesse de δf est violée si f_0 reste stationnaire. Cette thèse aborde ce problème de bruit d'échantillonnage en considérant f_0 comme une distribution de fond maxwellienne évoluant dans le temps, qui en termes de variables de configuration est supposée être une fonction de flux magnétique. L'évolution de la densité et de la température de cette maxwellienne est réalisée en absorbant, via des équations de relaxation, les moments de vitesse correspondants moyennés sur les surfaces de flux de δf .

Comme le schéma utilise essentiellement l'intégration de Monte Carlo pour calculer les sources des équations de Maxwell, les résultats sont noyés dans le bruit

si cette hypothèse n'est pas respectée. Ceci est particulièrement vrai lors de la modélisation du plasma de bord, où les amplitudes de fluctuation sont élevées, ou lors de la détermination des profils d'état quasi-stationnaire correspondant à des sources données (simulations forcées par le flux). Cette thèse aborde le problème du bruit d'échantillonnage du schéma PIC en introduisant une variable de contrôle adaptative. Grâce à un ensemble d'équations de relaxation, la distribution de fond maxwellienne est rendue dépendante du temps via les profils de densité et de température moyennés sur les surfaces de flux lors de la simulation de la turbulence électrostatique sans collision.

L'avantage du schéma adaptatif via une température ionique dépendante du temps est d'abord étudié en utilisant un code gyrocinétique global appelé GKengine avec une physique et une géométrie simplifiées. Des simulations impliquant des modes ITG déclenchés par de forts gradients de température dans une géométrie plane cisailée sont effectuées. Des sources et des puits sont introduits pour empêcher la relaxation du profil. Le schéma adaptatif, qui tient compte dans ce cas de l'évolution du seul profil de température des ions, permet d'éviter une accumulation indéfinie de bruit dans la composante zonale, qui conduirait finalement à la suppression non physique de la turbulence. Dans la plupart des cas, des résultats similaires, ou même de meilleure qualité, peuvent être obtenus avec le schéma adaptatif avec des nombres de marqueurs aussi bas que 1/4 de ceux du schéma non adaptatif correspondant.

Le schéma adaptatif est ensuite développé dans le cadre du code PIC gyrocinétique global ORB5, où les variables de contrôle dépendant du temps sont généralisées pour adapter les profils de densité et de température dans une géométrie toroïdale. Deux études physiques différentes sont réalisées en utilisant des profils et des champs magnétiques d'équilibre de type TCV. La première implique des simulations de modes ITG toroïdaux forcés par le flux, avec des électrons adiabatiques. Dans ce cas, de puissantes sources de chaleur sont introduites, générant une forte déviation du profil de température des ions par rapport aux valeurs initiales. En considérant un arrière-plan Maxwellien local avec une densité et une température dépendant du temps, toutes les simulations avec le schéma adaptatif ont un bruit maintenu à un faible niveau, avec le potentiel d'atteindre un état quasi-stationnaire à partir d'une seule initialisation des marqueurs.

La deuxième étude physique concerne un régime mixte ITG-TEM utilisant un modèle d'électrons hybrides amélioré. Les simulations de cette étude sont menées à la fois en mode gradient de température et en mode de forçage de flux. Ici, l'arrière-plan adaptatif implique des profils de densité et de température dépendant du temps pour les ions et les électrons séparément. Les diagnostics de variance de poids et d'échantillonnage de l'espace de phase sont analysés plus en détail pour ces simulations, qui présentent toutes de grandes déviations de profil. Les problèmes d'échantillonnage numérique près de l'axe magnétique pour les électrons à haute énergie et les ions à basse énergie sont révélés et étudiés. Malgré ces problèmes, pour toutes les études menées dans ce travail, les résultats obtenus avec le schéma adaptatif sont toujours meilleurs que ceux des schémas non adaptatifs correspondants, en ce sens que le bruit d'échantillonnage numérique est nettement mieux contrôlé à long terme et que les quantités physiques sont plus proches de la convergence numérique.

Malgré sa relative simplicité, la méthode des variables de contrôle maxwelliennes

moyennées sur les surfaces de flux et dépendantes du temps, couplées à un ensemble d'équations de relaxation, s'avère être un schéma d'arrière-plan adaptatif fiable pour les simulations de turbulence électrostatique. La capacité de simuler des situations avec de fortes déviations de l'arrière-plan initial a été démontrée, y compris pour de longues simulations focées par le flux. Ce travail devrait donc s'avérer utile à la communauté PIC en tant que première étape vers son extension aux simulations électromagnétiques globales, ou vers le développement de méthodes de variables de contrôle adaptatif plus sophistiquées pour gérer également les simulations du bord et de la couche périphérique du plasma.

Mots-clés: gyrocinétique, PIC, variables de contrôle, maxwellienne, contrôle du bruit, turbulence, confinement magnétique.

List of Acronyms

| | |
|--------|-------------------------------|
| ETG | electron-temperature-gradient |
| FEM | finite element method |
| FLR | finite Larmor radius |
| f.s.a. | flux-surface-averaged |
| ITG | ion-temperature-gradient |
| LCFS | last-closed-flux-surface |
| l.h.s. | left-hand-side |
| MRS | mode rational surface |
| PIC | particle-in-cell |
| QNE | quasi-neutrality equation |
| r.h.s. | right-hand-side |
| SOL | scrape-off layer |
| TEM | trapped-electron-mode |

List of Figures

| | | |
|-----|---|----|
| 1.1 | Fusion cross section of three nominations for fusion reactions. The constituents D, T, and ^3He represents deuterium, tritium and Helium-3 respectively. c.o.m. represents ‘centre of mass’. Figure is taken from Ref. [66]. | 2 |
| 1.2 | Schematics illustrating how plasma is magnetically confined in a tokamak (a), and a cut-out of ITER (b). Figures (a) and (b) are taken from Refs. [29] and [66] respectively. | 3 |
| 1.3 | Schematics of the three numerical approaches commonly used in fusion plasma simulations. Figures are taken from Ref. [28]. | 5 |
| 2.1 | Cylindrical geometry (R, φ, Z) and tokamak geometry (r, φ, θ^*) . Figure is taken from Ref. [25]. | 9 |
| 2.2 | Poloidal cross-section showing the most dominant ITG mode $n \approx 28$ at $c_s t/a = 32$ for the ITG case of Ch. 5. The balloon structure is represented by the non-zonal perturbed potential $(\phi - \langle \phi \rangle)/T_{0e}(s_0)$. Contour curves represent constant $s = [0.1, 0.2, \dots, 1.0]$ flux surfaces (see Eq. (2.7)) of the magnetic field geometry of the TCV shot #43516 used in this work. | 14 |
| 2.3 | Passing (top) and trapped (bottom) guiding centre orbits. Drift motion causes guiding centres to deviate from a constant magnetic surface as they travel along a field line. Besides parallel velocity reversal, trapped particles further exhibit toroidal precession over bounce motion. Right sub-figures show the poloidal cross-section. Figure is taken from Ref. [28]. | 16 |
| 2.4 | In the circle on the right, ‘energy return’ indicates the process of energy return to drift waves. Figures are taken from Ref. [18]. | 17 |
| 3.1 | Fourier-filters for a fixed radial position s applied to the B-spline coefficients of the r.h.s. of the QNE. These are defined on a discrete grid of integer poloidal m and toroidal n Fourier modes. The band $\mathcal{F}_1 = m + nq(s) \leq \Delta m$ (green) of half-width Δm , indicates modes that are nearly field-aligned. Red dots represent the mode numbers chosen to be resolved, which are found in the overlap region of \mathcal{F}_1 and the box $(m, n) \in [m_{min}, m_{max}] \times [n_{min}, n_{max}]$. The pink side bands \mathcal{F}_2 are used for SNR diagnostics. They are of the same width, and are at a distance of $3\Delta m$ from centre to centre w.r.t. \mathcal{F}_1 , i.e. $\mathcal{F}_2 : m \pm 3\Delta m + nq(s) \leq \Delta m$ | 36 |

| | | |
|-----|---|----|
| 3.2 | Overview of the ORB5 algorithm for 1 sub-step of a 4 th order explicit Runge-Kutta (RK4) scheme. \times and $+$ represent marker data structure (gyro-centre and Larmor points respectively), and cubes represent fields on grid structure. Figure taken from Ref. [64]. | 41 |
| 3.3 | Flux-surface-averaged of $\hat{b} \cdot \nabla \times \hat{b} / \Omega_c$ for the singly charged ion, for the magnetic equilibrium geometry used in this thesis, i.e. TCV shot #43516. | 45 |
| 3.4 | Amplitude of the f.s.a. heating operator $\hat{S}_H(\psi, \mathcal{E})$ of Eq. (3.82), at a fixed radial position ψ | 60 |
| 4.1 | The sheared-slab magnetic geometry (see Eq. (4.1)) used for simulations of this chapter. | 66 |
| 4.2 | Symmetrised profiles used for this chapter. Blue: Initial (solid) and typical final (dashed) T_i . Red: Heat γ_h (solid) and noise control γ_n (dashed). | 68 |
| 4.3 | Maximum growth rate of linear modes as a function of each toroidal mode number n , for normalised ion temperature logarithmic gradient $a d \log T_i / dx = 4.0$ and $(d \log T_i / dx) / (d \log n / dx) = 10$. The poloidal mode number m is radially dependent and is determined by the Fourier filter. | 70 |
| 4.4 | Time traces for various marker numbers, considering the non-adaptive and adaptive cases. The adaptive rate is set to $\alpha_E = 1.92\gamma_{\max}$ where applicable. A moving time-averaging window of half-width $c_s t / L_x = 10$, which is equivalent to $\gamma_{\max} t = 1.6$, has been implemented. | 70 |
| 4.5 | Radial averaged absolute value of the zonal flow shearing rate $\omega_{E \times B}$ at (a) initial time $c_s t / L_x = 0$ and (b) end-time $c_s t / L_x = 753$, as a function of the inverse square root of marker number N_p . The adaptive case (orange) adapts at a rate $\alpha_E = 1.92\gamma_{\max}$. All simulations are initialised with perturbations with toroidal mode $n \neq 0$ | 72 |
| 4.6 | Signal-to-noise ratio (SNR) time traces for signal (a) including (see Eqs. (3.27)) and (b) excluding (see Eq. (3.28)), the $(m, n) = (0, 0)$ mode, for increasing marker number N_p , and considering both the non-adaptive (solid line) and adaptive (dashed line) cases. | 72 |
| 4.7 | F.s.a. profiles at quasi-steady state averaged over a time interval of $c_s t / L_x \in [1030, 1130]$ for various marker numbers N_p under the non-adaptive scheme for the ion temperature (a) relative deviation with respect to background $[\langle T_i \rangle(s) - T_{0i}(s)] / T_{0i}(s)$ and its (b) logarithmic gradient $-\partial \log T_i(s) / \partial s$, and the (c) zonal flow shearing rate $\omega_{E \times B}$ | 73 |
| 4.8 | F.s.a. profiles at quasi-steady state averaged over a time interval of $c_s t / L_x \in [1030, 1130]$ for various marker numbers N_p under the adaptive scheme with adaptive rate $\alpha_E = 1.92\gamma_{\max}$ for the ion temperature (a) relative deviation with respect to adapted background, (b) relative deviation with respect to background at initial time $t = 0$, its (c) logarithmic gradient, and the (d) zonal flow shearing rate. | 74 |

| | | |
|------|---|----|
| 4.9 | Diagnostics under four different adaptive scenarios (see description in text) for the radially averaged absolute (a) heat diffusivity χ_H and (b) zonal flow shearing rate $\omega_{E \times B}$, and the signal-to-noise (SNR) ratio with signal (c) including and (d) excluding, the $(m, n) = (0, 0)$ mode. Marker number set to $N_p = 256M$, and adaptive rate to $\alpha_E = 1.92\gamma_{\max}$ where applicable. A moving time-averaging window of half-width $c_s t/L_x = 10$ has been implemented. | 76 |
| 4.10 | Local f.s.a. weight standard deviation σ_w through time under four different adaptive scenarios (see description in text), illustrated with the cases of (a) (no,no), (b) (no,yes) with $\alpha_E = 1.92\gamma_{\max}$, (c) (yes,no) with $\alpha_E = 1.92\gamma_{\max}$, (d) (yes,no) with $\alpha_E = 0.12\gamma_{\max}$, and (e) (yes,yes) with $\alpha_E = 1.92\gamma_{\max}$. σ_w is defined by $\sqrt{\sum_{p \in i} w_p^2/N_i - (\sum_{p \in i} w_p/N_i)^2}$, with $N_i = N_p/N_x$ the average number of markers of the i^{th} radial bin, taken to be uniform for all bins. Marker number set to $N_p = 256M$. All figures share the same colour scale. | 77 |
| 4.11 | Diagnostics for various noise control strength γ_n considering both the non-adaptive and adaptive cases. Marker number set to $N_p = 256M$. The sum of f.s.a. weight standard deviation is calculated by summing the standard deviations of f.s.a. weights from each radial bin, and multiplying by the sum by L_x/N_x | 78 |
| 4.12 | Time evolution of f.s.a. ion temperature relative deviation from its time-evolved adapted $T_{0i}(t)$, $(\langle T_i \rangle(x, t) - T_{0i}(x, t))/T_{0i}(t)$ under various adaptive rates α_E . Marker number set to $N_p = 256M$ | 79 |
| 4.13 | Time traces with varying adaptation rates α_E . Marker number set to $N_p = 256M$ | 79 |
| 4.14 | Time traces under various tuning parameter λ (see Eq. (4.7)). The adaptive rate is set to $\alpha_E = 1.92\gamma_{\max}$. A moving time-averaging window of half-width $c_s t/L_x = 10$ has been implemented. Total number of markers is set to $N_p = 256M$ | 80 |
| 4.15 | Time traces for various marker numbers N_p . The tuning parameter is set to $\lambda = 0.95$, and the adaptive rate is set to $\alpha_E = 1.92\gamma_{\max}$ where applicable. A moving time-averaging window of half-width $c_s t/L_x = 10$ has been implemented. | 81 |
| 4.16 | Global SNR time traces with signal excluding the $(m, n) = (0, 0)$ mode, under various tuning parameter λ (see Eq. (4.7)) considering the non-adaptive and the adaptive cases. Marker number set to $N_p = 256M$, and adaptive rate to $\alpha_E = 1.92\gamma_{\max}$ where applicable. | 82 |
| 4.17 | Time snapshot at $c_s t/L_x = 2259$ with tuning parameter λ of the ion temperature T_i relative non-zonal deviation on each magnetic surface, expressed by $(\delta T_i - \langle \delta T_i \rangle)/\langle T_i \rangle$, where $T_i = T_{0i} + \delta T_i$, integrated over the toroidal z direction. s_y is the normalised poloidal y axis. Both quasi-steady state cases have adaptive rate and marker number set to $\alpha_E = 1.92\gamma_{\max}$ and $N_p = 256M$, respectively. | 82 |
| 4.18 | Relative fluctuation averaged over $c_s t/L_x \in [1807, 2259]$ of ion temperature T_i and its f.s.a. profile $\langle T_i \rangle$, as measured by its standard deviation over mean, see Eq. (4.8), for the cases of $\lambda = 1.00, 0.95$ with adaptive rate $\alpha_E = 1.92\gamma_{\max}$ and marker number $N_p = 256M$ | 84 |

| | | |
|------|---|-----|
| 5.1 | Safety factor profile for the TCV shot #43516 used in this work. . . . | 88 |
| 5.2 | Initial gyrocentre density and temperature profiles and its logarithmic gradient for the ion and electrons used in Chs. 5 and 6. | 89 |
| 5.3 | Maximum linear growth rate for each toroidal mode number n . The maximum linear growth rate over all n is found to be $\gamma_{\max}/\Omega_{ci} = 0.00084$ ($\gamma_{\max}a/c_s = 0.2$) for $n = 28$ | 90 |
| 5.4 | Fixed heat source profile (see Eq. (3.82)) $G_H(\psi)$ (dotted line) fitted to the effective flux-surface- and time- averaged heat source of the temperature-gradient-driven run (black solid line) using the standard case with $N_p = 256M$. The orange line shows the source profile with twice the power, which is used for this chapter. Buffer edge is taken to be $s_b = 0.745$ (see Eq. (3.83)). | 91 |
| 5.5 | Radially averaged $s \in [0.7, 0.9]$ ion heat diffusivity for various marker numbers N_p under the standard and adaptive schemes. Grey shaded areas represent two time windows for profile analysis, considered in Sec. 5.5. | 92 |
| 5.6 | Time dependence of absolute value of the radially averaged $s \in [0.7, 0.9]$ zonal flow shearing rate $\omega_{E \times B}$. Grey shaded areas represent two time windows for profile analysis, considered in Sec. 5.5. | 93 |
| 5.7 | Time evolution up to $c_s t/a = 2451$ of the radial profile of the zonal flow shearing rate, $\omega_{E \times B}(s, t)$, for various marker numbers N_p under the standard and adaptive schemes. Grey area indicates the first profile time-averaging window $c_s t/a \in [1225, 1430]$. All plots share the same colour scale. | 94 |
| 5.8 | Time dependence of global Signal-to-Noise Ratio (SNR) values, for various marker numbers N_p under the standard and adaptive schemes. The signal excludes the zonal component $(m, n) = (0, 0)$. Horizontal dashed line indicates the empirically set minimum value of 10 for quality simulations. Grey shaded areas represent two time windows for profile analysis, considered in Sec. 5.5. | 95 |
| 5.9 | Time evolution of the ion f.s.a. weight standard deviation profiles $\sigma_w = \sqrt{\langle w^2 \rangle - \langle w \rangle^2}$. All plots share the same colour scale. | 96 |
| 5.10 | F.s.a. weight standard deviation profiles $\sigma_w(s) = \sqrt{\langle w^2 \rangle(s) - \langle w \rangle^2(s)}$ at $s = 0.6$, for various marker numbers under the standard and adaptive schemes. | 97 |
| 5.11 | Time averaged $c_s t/a \in [1225, 1430]$ of f.s.a. ion gyrocentre profiles, for various marker numbers N_p under the standard and adaptive schemes. The dotted lines indicate the initial profiles. | 98 |
| 5.12 | Radial profile of the time-averaged $c_s t/a \in [2246, 2451]$ zonal flow shearing rate $\omega_{E \times B}$, for various marker numbers under the standard and adaptive schemes. | 99 |
| 5.13 | Time averaged $c_s t/a \in [4697, 4902]$ of f.s.a. ion gyrocentre temperature profile and its logarithmic gradient, for marker numbers $N_p = 128M$ and $N_p = 64M$ under the adaptive scheme. Dashed lines show profiles at initial time. | 100 |

| | | |
|------|--|-----|
| 5.14 | Time averaged $c_s t/a \in [4697, 4902]$ of f.s.a. ion gyrocentre density profiles and its logarithmic gradient, for marker numbers $N_p = 128M$ and $N_p = 64M$ under the adaptive scheme. Time-evolved background quantities contributed by f_0 are not shown, as they coincide with the full measure contributed by $f_0 + \delta f$ | 101 |
| 5.15 | Time evolution up to $c_s t/a = 4902$ of the radial profile of the zonal flow shearing rate, $\omega_{E \times B}(s, t)$, for marker numbers $N_p = 128M$ under the adaptive scheme. | 101 |
| 5.16 | Ion marker count fractional difference $\Delta N v_{th}^2(s)/V_s(s)N_{max}(t = 0)$ at time $c_s t/a = 4902$, with $N_p = 128M$ under the adaptive scheme. $N_{max}(t = 0)$ indicates the global maximum marker number per bin at initial time $t = 0$. s_{push} is the flux surface which pseudo-cartesian coordinates are used. | 103 |
| 6.2 | Maximum linear growth rate for each toroidal mode number. Maximum linear growth rate is found to be $\gamma_{max}/\Omega_{ci} = 0.0038$ ($\gamma_{max}a/c_s = 0.931$). | 106 |
| 6.1 | Initial density and temperature profiles of both ions and electrons as well as corresponding logarithmic gradients. | 107 |
| 6.3 | Radially averaged $s \in [0.7, 0.9]$ heat diffusivities χ and heat diffusivity ratio χ_i/χ_e , for various marker numbers N_p under the standard and the adaptive schemes. Subscripts P and T for the electron heat diffusivity χ_e represent passing and trapped contributions respectively. The grey time window is used to plot time-averaged profiles of Figs. 6.9 and 6.10. | 109 |
| 6.4 | Time traces of radially averaged $s \in [0.7, 0.9]$ ion gyrocentre flux as well as ion-electron gyrocentre flux difference $\Gamma_i - \Gamma_e$, for various marker numbers N_p under both the standard and the adaptive schemes. 'trapped' and 'passing+trapped' curves use χ_e contributed by trapped only and passing and trapped electrons, respectively. | 110 |
| 6.5 | Time-averaged volume integrated heat source $\int_0^s ds' \left\langle \int d^3v \frac{mv^2}{2} S \right\rangle$ and heat flux through flux surface $\left\langle \vec{q}_H \cdot \frac{\nabla\psi}{ \nabla\psi } \right\rangle$, for various marker numbers N_p under the standard and the adaptive schemes. The electron heat flux includes both passing and trapped contributions. The time averaging window is taken to be $c_s t/a \in [273, 286]$ | 111 |
| 6.6 | Time dependence of global Signal-to-Noise ratio (SNR) values, for various marker numbers N_p under the standard and the adaptive schemes. The signal includes the zonal component $(m, n) = (0, 0)$ | 112 |
| 6.7 | Time evolution of ion f.s.a weight standard deviation profiles $\sqrt{\langle w^2 \rangle - \langle w \rangle^2}$. All plots share the same colour scale. Corresponding results for electrons give similar trends. | 113 |
| 6.8 | s -cuts of ion f.s.a. weight standard deviation profiles $\sigma_w = \sqrt{\langle w^2 \rangle - \langle w \rangle^2}$. Electrons give similar trends. | 114 |

- 6.9 End-time time-averaged $c_s t/a = [273, 286]$ gyrocentre density profiles, for various marker numbers N_p under the standard and adaptive schemes. ‘background’ and ‘background + deviation’ represent the profile contributed by f_0 and $f_0 + \delta f$, respectively. (c) shows gyrocentre density difference contributed by $f_0 + \delta f$ 115
- 6.10 Time-averaged $c_s t/a \in [273, 286]$ logarithmic gradient profiles of gyrocentre temperature, for various marker numbers N_p under the standard and adaptive schemes. ‘background’ and ‘background + deviation’ represent the profile contributed by f_0 and $f_0 + \delta f$, respectively. 116
- 6.11 $E \times B$ zonal flow shearing rate $\omega_{E \times B}$, for various marker numbers N_p under the standard and the adaptive schemes. ‘correction’ refers to the r.h.s. of the QNE. The time-averaging window for (a) is $c_s t/a \in [274, 286]$ and the radial averaging window for (b) is $s \in [0.1, 0.9]$. . . 117
- 6.12 Time evolution of zonal flow shearing rate profile $\omega_{E \times B}(s, t)$, for various marker numbers N_p under the standard and the adaptive schemes. All plots share the same colour scale. 118
- 6.13 Phase-space volume diagnostic applied to Cartesian bins in (s, v^2) space for the standard case with $N_p = 128\text{M}$ at $c_s t_{\text{end}}/a = 286$. Shown is the ratio $\Omega(t_{\text{end}})/\Omega^{(a)}$, of which values near 1 reflect good sampling, while ratios deviating significantly from 1 reflect poor/deficient sampling. The red dashed line on the contour plots indicate the energy upper-bound during initial marker loading, given by $m\kappa^2 v_{\text{th}}^2(s)$. As $\Omega^{(a)}$ appears in the denominator, it is taken without the v^2 -cut-off to avoid singularities (see Eq. (3.17)). The dashed lines in (c) and (d) are taken at $t = 0$ 119
- 6.14 Normalised marker count $\bar{N} = N/N_{\text{max}}(t = 0)$ for the standard case with $N_p = 128\text{M}$ at time $c_s t/a = 286$. Here, $N_{\text{max}}(t = 0)$ is the global maximum marker count per (s, v^2) -bin at initial time $t = 0$. (a) and (b) show marker count differences $\Delta\bar{N} = \bar{N}(t_{\text{end}}) - \bar{N}(t = 0)$. Subplots (c) and (d) show different s -cuts at time $t = 0$ (dashed lines) and at t (full lines). 121
- 6.15 Phase-space volume diagnostic applied to Cartesian bins in (s, v^2) space for the adaptive case with $N_p = 128\text{M}$ at $c_s t_{\text{end}}/a = 286$. Shown is the ratio $\Omega(t_{\text{end}})/\Omega^{(a)}$, of which values near 1 reflect good sampling, while ratios deviating significantly from 1 reflect poor/deficient sampling. The red dashed line on the contour plots indicate the energy upper-bound during initial marker loading, given by $m\kappa^2 v_{\text{th}}^2(s)$. As $\Omega^{(a)}$ appears in the denominator, it is taken without the v^2 -cut-off to avoid singularities (see Eq. (3.17)). The dashed lines in (c) and (d) are taken at $t = 0$ 122
- 6.16 Normalised marker count $\bar{N} = N/N_{\text{max}}(t = 0)$ for the adaptive case with $N_p = 128\text{M}$ at time $c_s t_{\text{end}}/a = 286$. Here, $N_{\text{max}}(t = 0)$ is the global maximum marker count per (s, v^2) -bin at initial time $t = 0$. (a) and (b) show marker count differences $\Delta\bar{N} = \bar{N}(t_{\text{end}}) - \bar{N}(t = 0)$. Subplots (c) and (d) show different s -cuts at time $t = 0$ (dashed lines) and $t = t_{\text{end}}$ (full lines). 123

| | | |
|------|--|-----|
| 6.17 | Fixed heat source profiles $G_H(\psi)$ (orange) for the flux-driven simulations fitted to the effective flux surface and time-averaged heat source of the temperature-gradient-driven run using the standard case with $N_p = 256M$. Buffer edges for the ions and electrons are taken to be $s_B = 0.75$ and $s_B = 0.80$, respectively (see Eq. (3.83)). | 124 |
| 6.18 | Radially averaged $s \in [0.7, 0.9]$ ion and electron heat diffusivities as well as ion-electron heat diffusivity ratio χ_i/χ_e , for various marker numbers N_p under the standard and the adaptive schemes. 'trapped' and 'all' curves use χ_e contributed by trapped only and passing and trapped electrons, respectively. Grey shaded areas represent two time windows for profile analysis, given in Sec. 6.3.4 and 6.3.7 respectively. | 126 |
| 6.19 | Radially averaged $s \in [0.7, 0.9]$ absolute value of the $E \times B$ zonal flow shearing rate $\omega_{E \times B}$, for various marker numbers N_p under the standard and the adaptive schemes. Grey shaded areas represent two time windows for profile analysis, given in Secs. 6.3.4 and 6.3.7 respectively. | 127 |
| 6.20 | Radially averaged $s \in [0.7, 0.9]$ ion gyrocentre flux and ion-electron particle flux difference, for various marker numbers N_p under the standard and the adaptive schemes. 'trapped' and 'passing+trapped' curves use χ_e contributed by trapped only and passing and trapped electrons, respectively. | 128 |
| 6.21 | F.s.a. weight standard deviation profiles $\sigma_w(s) = \sqrt{\langle w^2 \rangle(s) - \langle w \rangle^2(s)}$ for marker number $N_p = 128M$, under both the standard and adaptive schemes. | 129 |
| 6.22 | F.s.a. weight standard deviation profiles $\sigma_w(s) = \sqrt{\langle w^2 \rangle(s) - \langle w \rangle^2(s)}$ at $s = 0.534$ for marker number $N_p = 128M$, under both the standard and adaptive schemes. | 130 |
| 6.23 | Time dependence of global Signal-to-Noise Ratio (SNR) values, for various marker numbers N_p under the standard and the adaptive schemes. The signal includes the zonal component $(m, n) = (0, 0)$. Horizontal dashed line indicates the empirically set minimum value of 10 for quality simulations. Grey shaded areas represent two time windows for profile analysis, considered in Secs. 6.3.4 and 6.3.7 respectively. | 130 |
| 6.24 | Time-averaged $c_s t/a \in [592, 613]$ gyrocentre density profiles, for various marker numbers N_p under the standard and adaptive schemes. 'background' and 'background + deviation' represent the profile contributed by f_0 and $f_0 + \delta f$, respectively. (c) shows gyrocentre density difference contributed by $f_0 + \delta f$. All profiles are the result of binning markers with the appropriate weights, $f_0 \Omega$ and w for f_0 and δf contributions respectively. | 132 |
| 6.25 | Time-averaged $c_s t/a \in [592, 613]$ f.s.a. gyrocentre temperature profile and its logarithmic gradient, for various marker numbers N_p under the standard and adaptive schemes. 'background' and 'background + deviation' represent contributions from f_0 (dashed curves) and $f_0 + \delta f$ (solid curves) to the profile, respectively. All profiles are the result of binning markers with the appropriate weights, $f_0 \Omega$ and w for f_0 and δf contributions respectively. | 133 |

- 6.26 Time-averaged volume integrated heat source $\int_0^s ds' \left\langle \int d^3v \frac{mv^2}{2} S \right\rangle$ and heat flux through flux surface $\left\langle \vec{q}_H \cdot \frac{\nabla\psi}{|\nabla\psi|} \right\rangle$, for various marker numbers N_p under the standard and the adaptive schemes. The electron heat flux includes both passing and trapped contributions. The time averaging window is taken to be $c_s t/a \in [592, 613]$ 134
- 6.27 Ion phase-space volume diagnostic applied to Cartesian bins in (s, v^2) -space for the standard and adaptive cases for various marker numbers N_p at $c_s t/a = 612$. Shown is the ratio $\Omega(t_{\text{end}})/\Omega^{(a)}$, of which values near 1 reflect good sampling, while ratios deviating significantly from 1 reflect poor/deficient sampling. The red dashed line on the contour plots indicate the energy upper-bound during initial marker loading, given by $m\kappa_v^2 v_{\text{th}}^2(s)$, i.e. $v^2 = \kappa_v^2 v_{\text{th}}^2(s, t = 0)$. As $\Omega^{(a)}$ appears in the denominator, it is taken without the v^2 -cut-off to avoid singularities (see Eq. (3.17)). All plots share the same colour scale. 136
- 6.28 Ion phase-space volume diagnostic s -cuts, for various marker numbers N_p under the standard and adaptive schemes at $c_s t/a = 612$. Shown is the ratio $\Omega/\Omega^{(a)}$. Ratio values near 1 reflect good sampling, while ratios deviating significantly from 1 reflect poor/deficient sampling. As $\Omega^{(a)}$ appears in the denominator, it is taken without the v^2 -cut-off to avoid singularities (see Eq. (3.17)). The dashed lines are taken at $t = 0$ 137
- 6.29 Normalised ion marker count $\bar{N} = N(t)/N_{\text{max}}(t = 0)$ for the standard and adaptive cases with $N_p = 128\text{M}$ at $c_s t/a = 612$. Here, $N_{\text{max}}(t = 0)$ is the global maximum marker count per (s, v^2) -bin at initial time $t = 0$. (a) and (b) show marker count differences $\Delta\bar{N} = \bar{N}(t) - \bar{N}(t = 0)$. Subplots (c) and (d) show different s -cuts at time $t = 0$ (dashed lines) and at t (full lines). 138
- 6.30 Normalised electron marker count $\bar{N} = N(t)/N_{\text{max}}(t = 0)$ distribution using $N_p = 128\text{M}$ markers, normalised to V_s/v_{th}^2 , where N_{max} is the global maximum marker count per bin at marker loading, under the standard and adaptive schemes. The normalisation factor $V_s(s)/v_{\text{th}}^2(s)$ (see Eq. (3.13)) is used to display a uniform distribution at marker loading. Marker difference is given by $\Delta\bar{N} = \bar{N}(t) - \bar{N}(t = 0) \leq -1$. The black dashed curve of (a) and (b) represents the marker loading cut-off in velocity v^2 -space, i.e. $v^2 = \kappa_v^2 v_{\text{th}}^2(s)$. Both (a) and (b) share the same colour scale. The dashed and solid curves of (c) and (d) represent N at $t = 0$ and at $c_s t/a = 612$, respectively. 139
- 6.31 Electron marker count fractional difference $\Delta N v_{\text{th}}^2(s)/V_s(s)N_{\text{max}}(t = 0)$ at time $c_s t/a = 75$, with $N_p = 64\text{M}$ under the adaptive scheme, for three different sets of marker push boundaries s_{push} and RK4 step-size Δt . $N_{\text{max}}(t = 0)$ indicates the global maximum marker number per bin at initial time $t = 0$. All figures share the same colour (saturated) scale. 140

- 6.32 s -cuts of the normalised electron marker count $\bar{N} = N(t)/N_{\max}(t = 0)$ for adaptive case with $N_p = 64\text{M}$, for different radial positions, corresponding to the 2D plots of Fig. 6.32. Here, $N_{\max}(t = 0)$ is the global maximum marker count per (s, v^2) -bin at initial time $t=0$. Dashed and full lines correspond to results for $c_s t/a = 0$ and $c_s t/a = 75$ respectively. 141
- 6.33 Radial profile of the time averaged $c_s t/a \in [102, 123]$ zonal flow $E \times B$ shearing rate $\omega_{E \times B a}/c_s$ with marker number $N_p = 128\text{M}$ for various QNE r.h.s. correction models: **exact**: using an exact f_0 (Sec. 3.2.10.1), **expansion**: using an expansion in $(\hat{\psi}_0, \hat{\mathcal{E}})$ for f_0 with $(N_\psi, N_{\mathcal{E}}, N_{\text{eval}}) = (64, 32, 600)$ (Sec. 3.2.10.2), **f.s.a.**: equates the electron background density to the f.s.a. ion background gyrodensity (Sec. 3.2.10.3), **no corr.**: no r.h.s. correction. These adaptive cases are compared against the standard: **std.** 142
- 6.34 Evolution up to time $c_s t/a = 123$ of the radial profile of the zonal flow $E \times B$ shearing rate $\omega_{E \times B}$, with marker number $N_p = 128\text{M}$ under various methods of QNE r.h.s. correction calculation under the adaptive scheme (a)-(d). An identical run under the standard scheme is shown in (e) for reference. All results are run with marker number $N_p = 128\text{M}$. All plots share the same colour scale. 144
- 6.35 Time- and flux-surface- averaged gyrocentre density over the time window $c_s t/a \in [1246, 1266]$, for various marker numbers N_p under the adaptive scheme. Profiles are contributions from both the f_0 and δf . Profiles contributed by f_0 only are indistinguishable to the respective $f_0 + \delta f$ ones. All profiles are the result of binning of markers with $f_0 \Omega + w$ weights. 145
- 6.36 Time- and flux-surface averaged logarithmic gradient profiles of gyrocentre density over the time window $c_s t/a \in [1246, 1266]$, for various marker numbers N_p under the adaptive scheme. Profiles are contributions from both the f_0 and δf . Profiles contributed by f_0 only are indistinguishable to the respective $f_0 + \delta f$ ones. All profiles are the result of binning of markers with $f_0 \Omega + w$ weights. 145
- 6.37 Time- and flux-surface- averaged gyrocentre temperature and its logarithmic gradient over the time window $c_s t/a \in [1246, 1266]$, for various marker numbers N_p under the adaptive scheme. Profiles are contributions from both the f_0 and δf . Profiles contributed by f_0 only are indistinguishable to the respective $f_0 + \delta f$ ones. All profiles are the result of binning of markers with $f_0 \Omega + w$ weights. 147
- 6.38 Ion and electron phase-space volume diagnostic s -cuts, for marker numbers $N_p = 128\text{M}$ and $N_p = 64\text{M}$ under the adaptive scheme at $c_s t/a = 1266$. Shown is the ratio $\Omega/\Omega^{(a)}$. Ratio values near 1 reflect good sampling, while ratios deviating significantly from 1 reflect poor/deficient sampling. As $\Omega^{(a)}$ appears in the denominator, it is taken without the v^2 -cut-off to avoid singularities (see Eq. (3.17)). The dashed lines are taken at $t = 0$ 148

| | | |
|-----|--|-----|
| B.1 | Convergence analysis with quadrature points of the $f_0(\vec{R}, v_{\parallel}, \mu, t) - f_0(\vec{R}, v_{\parallel}, \mu, 0)$ term of the r.h.s. of Eq. (4.5). (N_q, N_c, N_l) quadrature points are used for the integration of the dimensions x, α and μ respectively. For each of the above cases, the quadrature point number for a dimension is set to vary, while the other two are fixed at either 32 or 64. | 159 |
| C.1 | Radial profile of the time-averaged $c_s t/a \in [531, 612]$ zonal flow shearing rate $\omega_{E \times B}$, for marker number $N_p = 128M$ under the standard (black) and adaptive schemes. The adaptive scheme uses a canonical control variate (see Eq. (3.53)), adapting only the temperature (see Eq. (3.54)). N_{ψ} refers to the adaptive background profile radial grid resolution (see Eq. (3.48)). | 161 |
| C.2 | Time evolution up to $c_s t/a = 612$ of the radial profile of the zonal flow shearing rate, $\omega_{E \times B}(s, t)$, for marker numbers $N_p = 128M$ under the standard and adaptive schemes, with and without r.h.s correction to the QNE (see Eq. (3.63)). The adaptive scheme uses a canonical control variate (see Eq. (3.53)) with $N_{\psi} = 128$ (see Eq. (3.48)), and for case (b), has correction to the r.h.s. of the QNE calculated exactly (see Sec. 3.2.10.1). All plots share the same colour scale. | 162 |
| C.3 | Radial profile of the time-averaged $c_s t/a \in [1103, 1225]$ zonal flow shearing rate $\omega_{E \times B}$, for marker number $N_p = 128M$ under the standard (black) and adaptive schemes. The adaptive scheme uses a canonical control variate (see Eq. (3.53)) with $N_{\psi} = 128$ (see Eq. (3.48)), and three different adaptive algorithms: adapt T only (red), adapt both n and T with interleave (blue) and the simultaneous (green) methods, see Sec. 3.2.4. | 163 |
| C.4 | Time evolution up to $c_s t/a = 1225$ of the radial profile of the zonal flow shearing rate, $\omega_{E \times B}(s, t)$, for various marker numbers N_p under the standard and adaptive schemes. The adaptive scheme uses a canonical control variate (see Eq. (3.53)) with $N_{\psi} = 128$ (see Eq. (3.48)). The adaptive scheme of: (b) adapts the background temperature only; (c) adapts the density and temperature via the interleaved algorithm (see Sec. 3.2.3); and (d) adapts the density and temperature via the simultaneous algorithm. | 164 |
| C.5 | Shearing rate $\omega_{E \times B}$ | 165 |
| C.6 | Radial profile of the time-averaged $c_s t/a \in [1103, 1225]$ zonal flow shearing rate $\omega_{E \times B}$, for various marker numbers N_p under the standard (black) and adaptive (green and purple) schemes. The adaptive scheme uses a local control variate (see Eq. (3.53)) and adapts via the simultaneous algorithm (see Sec. 3.2.4). N_{ψ} is the adaptive background radial grid resolution (see Eq. (3.48)). The 2^{nd} (purple) and 3^{rd} (green) order spline refers to the order of B-spline of the basis functions $\{\Lambda(s)\}$ of Eq. (3.48). | 165 |

C.7 Time evolution up to $c_s t/a = 1225$ of the radial profile of the zonal flow shearing rate, $\omega_{E \times B}(s, t)$, for various marker numbers N_p under the standard (a) and adaptive (b) schemes. The adaptive scheme uses a local control variate (see Eq. (3.42)) with $N_\psi = 128$ with 3rd-order spline basis functions $\{\Lambda(s)\}$ (see Eq. (3.48)). 165

List of Tables

| | | |
|-----|---|-----|
| 3.1 | Possible moments M to simultaneously conserve on every flux surface ψ via the correction term S^c . The operator $\langle \cdot \rangle_{\text{b.a.}}$ represents the bounce average. | 62 |
| 3.2 | Reference units of ORB5. $s = s_0$ is a user-specified reference flux surface label, $s_0 \in [0, 1]$ | 62 |
| 3.3 | Common derived quantities of ORB5. The ion species is the reference (first) ion species of Tab. 3.2. | 62 |
| 3.4 | Diagnostic quantities in ORB5 and physical units | 63 |
| 4.1 | Equilibrium and heating profile parameters. Ions and electrons share identical equilibrium density and temperature profiles. The maximum linear growth rate $\gamma_{\text{max}} = 1.169 \times 10^{-3} \Omega_{ci} = 0.155 c_s / L_x$ is assumed, based on Fig. 4.3. | 69 |
| 5.1 | Profile parameters of Eq. (5.1) for density and temperature profiles for both background ions and electrons. | 89 |
| 5.2 | Parameters of the adaptive scheme used in this chapter. Adaptive rate α is common for both gyrocentre density α_n and energy (temperature) α_E | 90 |
| 5.3 | Parameters relating to sources of Eqs. (3.80) and (3.83) used in this chapter. | 92 |
| 6.1 | Profile Eq. (5.1) parameters for initial density and temperature for both background ions and electrons. | 106 |
| 6.2 | Parameters of the adaptive scheme for both ions and electrons used in this chapter. Adaptive rate α is common for both gyrocentre density α_n and energy (temperature) α_E . Temperature adaptation is only done for Sec. 6.3. | 107 |

Contents

| | | |
|----------|---|-----------|
| 1 | Introduction | 1 |
| 1.1 | Thermonuclear fusion as an energy source | 1 |
| 1.2 | Magnetically confined plasma | 2 |
| 1.3 | Anomalous transport | 3 |
| 1.4 | Simulations of fusion plasmas | 4 |
| 1.5 | Contribution of this thesis | 5 |
| 1.6 | Thesis outline | 7 |
| 2 | Physical model | 9 |
| 2.1 | Magnetic field geometry | 9 |
| 2.2 | Electrostatic microinstabilities | 12 |
| 2.2.1 | Ion-Temperature-Gradient driven instabilities | 12 |
| 2.2.2 | Trapped-Electron-Mode driven instabilities and its coupling to ITG modes | 15 |
| 2.2.3 | Zonal flows, GAMs and turbulence regulation | 16 |
| 2.3 | Gyrokinetic theory | 17 |
| 2.3.1 | Fully kinetic model | 17 |
| 2.3.2 | Phase space reduction by averaging out gyration phase | 18 |
| 2.4 | Equilibrium and background distributions | 20 |
| 2.5 | Quasi-neutrality equation | 22 |
| 2.5.1 | Cancellation of the initial ion and electron densities | 22 |
| 2.5.2 | Electron models used in this work | 24 |
| 3 | Numerical methods | 27 |
| 3.1 | Particle-In-Cell scheme | 27 |
| 3.1.1 | Discretisation: a Monte Carlo interpretation | 28 |
| 3.1.2 | Initial loading and marker probability distribution | 30 |
| 3.1.3 | Discretising δf | 32 |
| 3.1.4 | Relation between weight variance and field equation | 36 |
| 3.1.5 | Solving the field equation with a B-spline finite element method | 38 |
| 3.1.6 | Overview of ORB5 | 41 |
| 3.2 | Adaptive background scheme | 42 |
| 3.2.1 | Motivation and idea | 42 |
| 3.2.2 | Starting equations | 43 |
| 3.2.3 | Interleaved scheme | 45 |
| 3.2.4 | Simultaneous scheme | 46 |
| 3.2.5 | Application to a canonical Maxwellian as control variate | 48 |
| 3.2.6 | No parallel flow adaptation | 49 |

| | | |
|----------|---|------------|
| 3.2.7 | Implementation of the adaptive scheme | 49 |
| 3.2.8 | Weight redefinition | 52 |
| 3.2.9 | Control variate and background | 52 |
| 3.2.10 | Correction to the r.h.s. of the QNE | 52 |
| 3.2.11 | Update on the l.h.s. of the QNE | 58 |
| 3.3 | Heat sources and noise control | 59 |
| 3.3.1 | Krook operator as noise control and heat source | 59 |
| 3.3.2 | Fixed heat source and edge buffer sink | 60 |
| 3.3.3 | Source correction term | 61 |
| 3.4 | Normalisations and transport measures | 62 |
| 4 | GKengine ITG adiabatic electrons | 65 |
| 4.1 | Simplified physical model | 65 |
| 4.2 | Time-dependent control variate | 67 |
| 4.3 | Profiles and simulation parameters | 68 |
| 4.4 | Results | 70 |
| 4.4.1 | Marker convergence | 70 |
| 4.4.2 | Adaptive control variate and noise control | 74 |
| 4.4.3 | Noise control strength and adaptive rate variations | 78 |
| 4.4.4 | Adjusting the f.s.a. potential term | 80 |
| 4.5 | Conclusion | 83 |
| 5 | ITG turbulence with adiabatic electrons | 87 |
| 5.1 | Parameters and profiles | 88 |
| 5.2 | Heat source radial profile | 91 |
| 5.3 | Heat transport | 92 |
| 5.4 | Weight variance measure | 95 |
| 5.5 | Profile evolution | 97 |
| 5.5.1 | Time window #1 | 98 |
| 5.5.2 | Time window #2 | 100 |
| 5.6 | Limitations of long time simulations | 101 |
| 6 | Mixed TEM/ITG regime in TCV | 105 |
| 6.1 | Parameters and profile | 105 |
| 6.2 | Temperature-gradient-driven simulation | 107 |
| 6.2.1 | Heat and particle transport | 108 |
| 6.2.2 | Signal-to-noise and weight variance | 112 |
| 6.2.3 | Profile evolution | 115 |
| 6.2.4 | Zonal flow shearing rate | 117 |
| 6.2.5 | Phase-space volume diagnostic | 119 |
| 6.3 | Flux-driven simulations | 123 |
| 6.3.1 | Heat source radial profile | 123 |
| 6.3.2 | Transport time traces | 124 |
| 6.3.3 | Weight variance | 128 |
| 6.3.4 | Transient results: first time window | 131 |
| 6.3.5 | Electron marker count at high energies | 140 |
| 6.3.6 | QNE r.h.s. correction comparison | 142 |
| 6.3.7 | Quasi-steady state results: second time window | 145 |
| 6.4 | Results overview | 149 |

| | | |
|----------|---|------------|
| 7 | Conclusion and outlook | 151 |
| A | Alternative simultaneous adaptive scheme | 155 |
| B | Quadrature point convergence for r.h.s. of QNE | 157 |
| C | Canonical control variate with adiabatic electrons | 161 |
| C.1 | Canonical control variate | 161 |
| C.2 | Local control variate | 164 |
| C.3 | Further notes | 166 |
| D | Curriculum Vitae | 174 |

Chapter 1

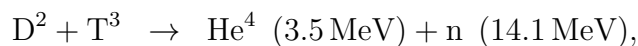
Introduction

1.1 Thermonuclear fusion as an energy source

The energy stored within atomic nuclei has served humankind as a valuable source of energy for the century. This is because the energy release from nuclear reactions is on the order of MeV per nuclei, where eV is the electron-volt, whereas those from chemical reactions, for example by burning fossil fuels, is on the order of keV per atom. Current existing nuclear power plants harness nuclear energy by the means of nuclear fission. That is, by splitting a heavy elements, e.g. ^{235}U and releasing energy in the form of kinetic energy of its lighter constituents.

In cold war era, in tandem with the development of the hydrogen bomb, military facilities in the United States and former Soviet Union were secretly advancing research on the use of nuclear fusion as an energy source. In 1956, Soviet scientist I. V. Kurchatov disclosed to the Western scientists the feasibility of controlled fusion via the tokamak concept (see Sec. 1.2). Then in 1958, after the *2nd Atoms for Peace Conference*, scientists around the world shared research results and thus the harnessing of nuclear fusion for energy as a global effort began [23]. Besides its greater energy yield compared to that from nuclear fission, fusion does not result in radioactive isotopes as waste.

As an example of a naturally occurring ‘fusion reactor’, Bethe and von Weizsäcker independently proposed, in 1938, that our Sun is powered by fusion. Under intense gravitational pressure in its core, hydrogen fuses via the proton-proton cycle, releasing energy. The proton-proton reaction, however, has such a small cross-section that it could not even be measured in a laboratory. Scientists agreed that the D-T reaction,



unlike that which occurs in the Sun’s core, is the reaction to lead fusion in laboratories due to its high fusion cross-section (see Fig. 1.1). Here, D and T represents the hydrogen isotopes deuterium and tritium respectively, and the reactions products He and n represent the alpha particle and neutron, respectively. The number in brackets represents their respective energies. The D-T reaction is chosen as it exhibits the highest fusion cross-section at temperatures T around 10 keV to 100 keV, with $1 \text{ eV} \sim 10^7 \text{ K}$. The figure of merit for fusion experiments is given by the Lawson criterion [55]

$$n\tau_E \gtrsim 1.5 \times 10^{20} \text{m}^{-3}\text{s},$$

at $T \simeq 30$ keV, for breakeven. The latter happens when the total amount of power losses balance the total fusion power. Here, n is the number density, and τ_E is the energy confinement time. There are currently two main approaches to fusion. The first is via magnetic confinement, and the second is inertial fusion. This work concerns with simulations of magnetically confined plasmas, and thus it is this method which will be further elaborated.

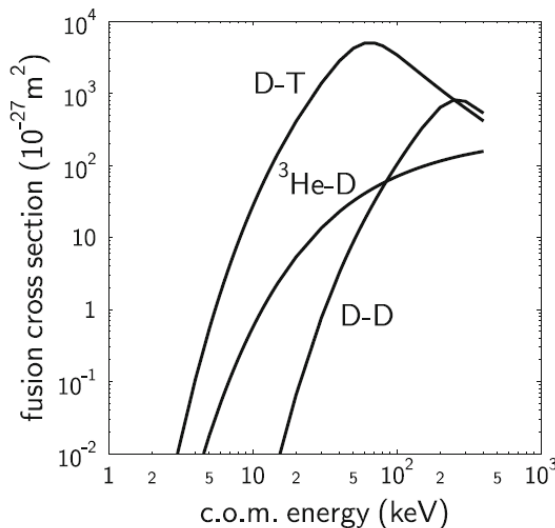


Figure 1.1: Fusion cross section of three nominations for fusion reactions. The constituents D, T, and ${}^3\text{He}$ represents deuterium, tritium and Helium-3 respectively. c.o.m. represents ‘centre of mass’. Figure is taken from Ref. [66].

1.2 Magnetically confined plasma

In order to initiate D-T reactions, at temperatures as high as $T \sim 10^8$ K, the reactants, namely deuterium and tritium¹, are in the plasma state. Also due to its high T , the plasma is confined via magnetic fields in a vacuum chamber. Magnetic confinement is possible as charged particles gyrate around magnetic field lines, thus confined in the perpendicular direction. As these particles are also free to flow along field lines, most field lines should not terminate at reactor wall. The simplest magnetic field geometry that exhibits closed field lines is the torus, and thus magnetically confined fusion reactors are toroidally symmetric vacuum chambers, called the ‘tokamak’. Further analysis shows that particles drift across field lines due to field-line curvature and perpendicular field strength gradient. Therefore, the confining field has to have both toroidal and poloidal components. The toroidal fields are generated by external poloidal superconducting solenoid coils, and the poloidal field by running a current through the plasma. This current is induced by treating the plasma volume as the secondary winding of a transformer (see Fig. 1.2a). This entails that the tokamak concept can only operate in pulses. At the time of writing, the largest tokamak reactor called ITER (see Fig. 1.2b), is being built in Cadarache. Though it will still not be a nuclear power plant, this multi-national funded test reactor is designed to deliver at steady operations lasting $\sim 10^2$ s, a fusion power of

¹Due to its short half-life, there is little naturally occurring tritium. The latter is bred when neutrons hit a lithium blanket at the reactor wall.

500 MW at

$$Q = \frac{\text{fusion power}}{\text{heating power}} = 10.$$

Note that given enough fuel, a burning plasma self-sustained by the resultant hot alpha particles would lead to $Q \rightarrow \infty$. The experiments that will be conducted, along with the physical knowledge and engineering know-how that ITER will encourage, will benefit future fusion power plant designs.

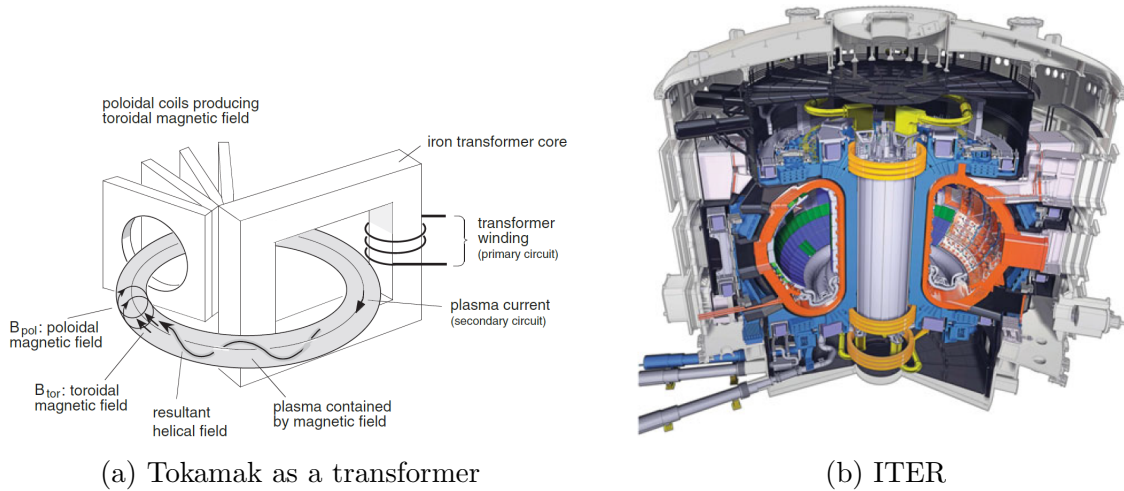


Figure 1.2: Schematics illustrating how plasma is magnetically confined in a tokamak (a), and a cut-out of ITER (b). Figures (a) and (b) are taken from Refs. [29] and [66] respectively.

1.3 Anomalous transport

One of the main challenges of magnetically confined plasma is how to keep charged particles and energy confined as long as possible. As described, charged particles gyrate around, and flow freely along, magnetic field lines. This creates great anisotropy in terms of particle, momentum and energy transport, with higher transport along the field lines. As field lines are toroidal by construction, what concerns us is radial (perpendicular to the magnetic surfaces) transport. Neoclassical transport describes radial transport via collisions in inhomogeneous and curved magnetic background configurations. However, experimentally measured transport coefficients show that these coefficients are one or two orders of magnitude higher than the neoclassical prediction. This ‘anomalous transport’ is due to drift-waves instabilities driven by a temperature and/or density gradients. As turbulence caused by these instabilities have wavelengths of the order of the Larmor radius, they are also termed ‘microinstabilities’².

A wide variety of microinstabilities exists, and their properties are deduced from reduced models characterised by their physical assumptions of the gyrokinetic equation [32]. Microinstabilities can be generally categorised by whether electromagnetic perturbations are involved, namely, either electromagnetic or electrostatic. The

²To be distinguished from magnetohydrodynamic (MHD) instabilities caused by certain configuration of magnetic field geometry and macroscopic plasma profiles.

presence of collisions adds to the categorisation. Further categorisation included the value of β , which is the ratio of plasma over magnetic field pressure. As this work concerns only with collisionless low- β electrostatic microinstabilities, only the ones common to toroidally confined fusion plasmas will be mentioned here. The first is the toroidal ITG mode [37, 67], which is responsible for anomalous ion heat transport. This instability is induced by the interaction of toroidal drifts and $E \times B$ convection due to an ion temperature gradient. Its linear eigenmodes exhibit ballooning structures on the low-field-side of the torus. A good illustration of this mechanism is given for example in Ref. [8]. Next, when trapped electrons are allowed to complete several bounce periods in the presence of low collisionality, their toroidal precession can be in phase with the toroidal phase velocity of perturbations, which can lead to an instability in the presence of an electron temperature gradient, leading to turbulence driven by the Trapped-Electron-Modes (TEMs). These modes have wavenumbers in a similar range as those of the ITG modes, have similar ballooning structures, but have different instability gradient thresholds. TEM and toroidal ITG modes usually occur in tandem, both having perpendicular spatial scales of the order of the ion Larmor radius. The final instability that will be mentioned here is the Electron-Temperature-Gradient (ETG) mode. These modes have perpendicular wavelengths of the order of the electron Larmor radius and are isomorphic to ITG modes, with ions having an adiabatic response [12]. Both TEM and ETG modes are thought to contribute to electron heat transport, though the significance of the latter contribution is still up for debate [57].

The simulations of this work concerns only the toroidal ITG modes and TEM. Therefore, their characteristics will be further elaborated in Ch. 2. Nonetheless, a good overview of drift wave instabilities can found for example in Ref. [36].

1.4 Simulations of fusion plasmas

The task of simulating magnetically confined fusion plasmas involves obtaining the solution of the Vlasov-Boltzmann equation for the species distribution functions. This equation is closed with Maxwell's equations for the self-consistent fields, along with appropriate boundary conditions. On the outset, there exists multi-scale physics, both in space and time, along with strong anisotropy due to the strong magnetic field. To simplify the problem, one introduces reduced physical models, depending on the regime one is interested in. Therefore, the common framework when describing the plasma species is either fully kinetic, gyrokinetic, or (gyro-)fluid. Kinetic descriptions lead to equations of motion for the particle trajectories. They are useful when one wishes to study processes relating to velocity space dependence of the distribution, e.g. wave-particle interactions. This description is generally more computationally expensive than the fluid description. The latter lead to coupled partial differential equations of various moments of the distribution. This thesis works within the gyrokinetic framework, where the fast gyration motion of the particles is averaged out. This does not only reduce the phase space dimension from six to five, but also allows for a larger time step in integration.

There are three main numerical approaches for gyrokinetic simulations of fusion plasmas. The first is the Particle-In-Cell (PIC) scheme. This scheme relies on representing particles as Lagrangian 'markers', whose characteristics are dictated by the equations of motion. This approach solves for the fields via Monte Carlo in-

tegration, thus giving the distribution a statistical interpretation. This also means that it inherits the main problems of Monte Carlo sampling, notably the statistical sampling error problem called ‘noise’ in the following. Unless appropriate noise control measures are implemented, this problem severely limits simulation time. This is especially true for cases that exhibit significant deviation from initial profiles and/or large fluctuation amplitudes. Nonetheless, PIC schemes are easily parallelised and extended to problems with higher dimensions. Gyrokinetic codes which use the Lagrangian-PIC scheme include XGC [49, 50], GTC [58], GT3D [38], GEM [15], EUTERPE [46] (for stellarators), and ORB5 [54]. The latter is the code used in this work. The next approach is the Eulerian scheme. This approach defines the distribution function on a grid, and solves the Boltzmann-Maxwell equation via a finite difference scheme. Though this approach does not suffer from statistical noise, it is severely limited in time integration by the CFL condition unless an implicit time-stepping scheme is used. A compromise between numerical dissipation and overshoot needs also to be made when choosing the finite-difference scheme. Gyrokinetic codes which use the Eulerian approach include GENE [42, 30], GYRO[14], GS2 [47, 21] and GT5D [40, 39]. The third approach is the semi-Lagrangian method [71], which aims to combine the benefits of the Lagrangian and Eulerian approaches. It advances the distribution by back-projecting along characteristics to a point on a mesh of the distribution at the previous time step. This circumvents the CFL restriction. Nonetheless, this scheme still faces the problem of the use of appropriate interpolation methods to evaluate distribution values between grid points, and problems of particle conservation. An example of a gyrokinetic semi-Lagrangian code is GYSELA [31]. An overview of the use of these approaches to simulate turbulent transport can be found in Ref. [28].

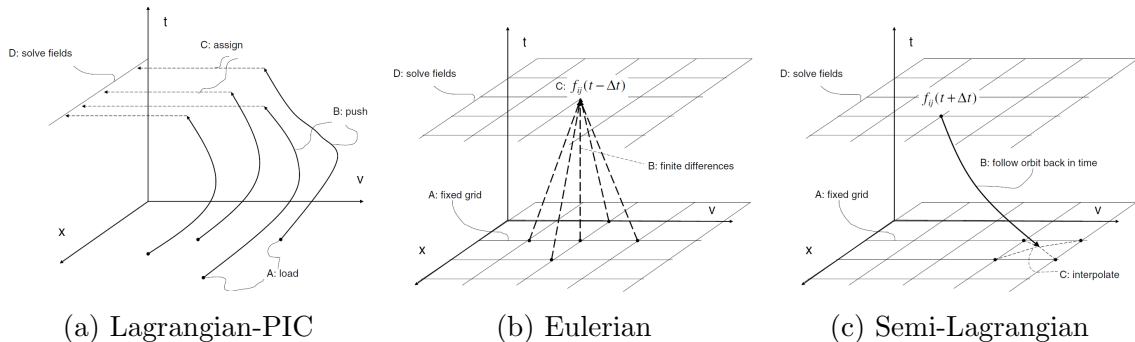


Figure 1.3: Schematics of the three numerical approaches commonly used in fusion plasma simulations. Figures are taken from Ref. [28].

1.5 Contribution of this thesis

The aim of this work is to improve the statistical sampling noise problem of the PIC scheme in order to apply it to long simulations, targeting cases with strong gradients and/or large deviations from initial profiles. For plasma simulations where the distribution function f does not deviate more than a few percent from its initial state f_{init} over characteristic time scales of microinstabilities and turbulent processes, one usually adopts the delta- f splitting. The approach splits f into a stationary (and often analytic) distribution f_0 , and a time-dependent perturbation part δf , which

is represented by numerical markers. This delta-f PIC method is to be contrasted with the full-f PIC scheme, which represents the whole f in terms of markers. The gain in noise reduction of the delta-f scheme relies on the reduced variance of the marker weights, provided that the assumption $\|\delta f\|/\|f\| \ll 1$ for some definition of the norm $\|\cdot\|$ is met. However, for plasma simulations exhibiting a large perturbed component δf , one usually falls back to the full-f scheme, which entails using high marker numbers to achieve low noise levels. This is the case, for example, when simulating the plasma edge with steep profile gradients and low-density levels, which often leads to conditions with fluctuation levels as large as the background. As marker numbers typically need to be at least at the order of 10 – 100 per grid cell, an adequate simulation of the core of a medium-sized tokamak plasma, like that of the Tokamak à Configuration Variable (TCV) at EPFL [76] is feasible, but larger marker numbers may approach the computational limits of most computers, even more so for particularly large plasma volumes like that of ITER. In order to still possibly retain some advantage of the delta-f scheme, one could also evolve f_0 , albeit at a longer timescale than that of the fluctuating δf . This approach has for example been suggested in Refs. [13, 2, 50]. This work explores the implications of a specific implementation of this approach. Namely, to have a time-evolving background by constraining f_0 to be a flux-surface-dependent Maxwellian which is furthermore time-dependent via its evolving density and temperature profiles. Another source of statistical sampling noise is due to ‘weight-spreading’ [13, 16] as a result of the implementation of collision operators using a Langevin approach. However, this problem will be not addressed in this work as collisions are not considered. The study on the advantages of the evolving background is done in three stages.

As a first step and a proof-of-principle, the adaptive scheme is implemented in the gyrokinetic GKengine code [65] which simulates a single kinetic ion species in sheared-slab geometry with simplified physics. That is, the configuration space is Cartesian, with periodic boundaries for the ‘poloidal’ and ‘toroidal’ directions. The equilibrium magnetic field is only a function of the radial coordinate. No curvature drift is considered, and adiabatic electrons are assumed. As this assumption results in no particle transport, the adaptive scheme implemented here only exhibits time dependence through the flux-surface-averaged (f.s.a.) ion gyrocentre temperature profile. All simulations performed with this code involves setting up a steep temperature gradient to induce a slab-ITG instability. These profiles are chosen motivated by the potential use of the adaptive scheme at the plasma edge, which is characterised by steep gradients. As there are no sources, the profiles are clamped at the high and low ends of the temperature profile to prevent relaxation below critical gradient. The resulting large temperature deviation from the initial profile indeed increased the statistical sampling noise of the non-adaptive scheme. However, under the adaptive scheme, noise is shown to be kept at low values. Implications on the behaviour of zonal flows, which play a crucial role in turbulent regulation, will be studied in detail.

In the next stage, the adaptive scheme is implemented in toroidal geometry via the global gyrokinetic ORB5 code [54]. Here, realistic physics for simulating from the plasma core to the last closed flux surface (LCFS) is afforded. In an attempt to still work with an adaptive temperature profile, simulations are done with a kinetic ion species with adiabatic electrons. Also, a generalisation of the adaptive scheme from Cartesian to toroidal geometry is made. The simulations run are flux-driven,

with input fluxes having twice the integrated source power of a previously done temperature-gradient run. This results in large temperature profile deviations from initial state, turbulence driven by toroidal-ITG modes. Like cases with sheared-slab geometry, the adaptive scheme is shown to be able to maintain low statistical noise for long times. However, it turns out that one needs to also adapt the gyrocentre density, and correct for the parallel flow coming from the perturbed distribution, in order to keep the adaptive scheme stable. This may be due to the limitations of the Maxwellian control variate assumption. Nonetheless, using a coarse grid for the adapting background profiles solves the instability issue.

In the final stage of this work, the adiabatic assumption for the electrons is relaxed. A hybrid electron response allows particle transport, thus resulting in gyrocentre density profile deviations as well as those of temperature. This allows for the merits of an adaptive scheme for both density and temperature, for both ions and electrons separately, to be demonstrated. Both temperature-gradient- and flux-driven simulations are conducted, with instabilities now driven by both electrons and ions, in a mixed ITG-TEM regime. Unlike the case with adiabatic electrons, the adaptive scheme under such conditions is stable, thus allowing for the study of the implementation of various corrections terms, along with the importance of various components that make up the adaptive scheme. When compared to non-adaptive cases, results of the adaptive scheme are shown to once again exhibit low errors resulting from statistical sampling noise. Evolved profiles under the adaptive scheme with much lower marker numbers are shown to match those of the non-adaptive cases.

1.6 Thesis outline

This thesis manuscript is organised as follows. Ch. 2 introduces the magnetic geometry of the ORB5 code used in this work, which is followed by a description of the two main instabilities involved in this work, namely the toroidal ITG and TEM. A brief recapitulation of the gyrokinetic model is also given. This leads to the description of the equations of motion for the gyrocentre. As this work deals with electrostatic turbulence, a discussion of the quasi-neutrality equation (QNE), along with the various electron response models, conclude the chapter. Ch. 3 begins the discussion of the numerical models by explaining the PIC method (Sec. 3.1). It explains how a control variate leads to better integral evaluation in the Monte Carlo sense. The discussion continues with marker loading in phase space, followed by the discretisation of the δf , namely to represent it as a Klimontovich distribution. The concept of marker weights introduced leads to the discussion of the main diagnostic that measures its variance, which is the Signal-to-Noise ratio. An overview of ORB5 then follows. Sec. 3.2 then details the adaptive scheme, which is the focus of this work. It begins by motivating the starting relaxation equations, and enumerating all assumptions made. This is followed by the scheme's implementation in the ORB5 code. This also involves various correction calculations to the right-hand-side (r.h.s.) to the QNE. A short discussion on the possibility of partly 'de-linearising' the ion polarisation density afforded by the adapting background follows. The chapter concludes with a description on the noise control and all sources used in this work in Sec. 3.3 and normalisations used in Sec. 3.4. The remaining chapters deal with results pertaining to the implementation of the adaptive scheme.

Chapter 4 describes the work done leading to Ref. [63]. It begins by describing the simplified physics of GKengine in Sec. 4.1, and the basic formalism of the adaptive scheme with evolving f.s.a. background temperature in Sec. 4.2. This is followed by the description on the periodic radial profile and parameters used in Sec. 4.3. Results comparing the standard (non-adaptive) to the adaptive approach then begins in Sec. 4.4. Marker convergence analysis is first conducted. A discussion on the significance of an adaptive control variate, as opposed to an ‘adaptive’ noise control operator is investigated, which is followed by a study on the effects of noise control strengths and adaptive rates on simulation results. This is followed by an analysis of how modifications to the electron adiabatic response can lead to non-decreasing heat flux driven by slab-ITG modes.

Chapter 5 explores the use of the temperature adaptation scheme in toroidal geometry using the global gyrokinetic ORB5 code [54]. Sec. 5.2 introduces the heat flux radial profiles used to induce large temperature profile deviation from initial state. Sec. 5.3 then compares transport time traces of the non-adaptive and adaptive cases. Next, Sec. 5.4 shows how the adaptive reduces weight variance with time. Sec. 5.5 considers the time evolved profiles time-averaged over two time windows and compares the results from the non-adaptive and adaptive cases. This is followed by Sec. 5.6 which exposes the limitations of the simulations settings on long time simulations.

Chapter 6 explores the implications of a control variate with both time-dependent density and temperature profiles. It is split into two parts: temperature-gradient-, and flux- driven results analysis. Sec. 6.2.3 describes the profiles, along with sources/sinks which are used for all simulations of this chapter. Sec. 6.2 analysis the results from gradient-driven-runs with the use of a time-dependent density background profile. Comparisons between the non-adaptive and adaptive cases are made for the heat and particle transport time-traces, along with weight variance diagnostics. Time-evolved profiles of both cases are compared, along with their respective zonal flow shearing rate. The final part of this section introduces the phase-space volume diagnostic. Sec. 6.3 discusses the results of flux-driven runs. Similar analysis procedure is done here as those for Sec. 6.2. Due to large profile deviations from initial state, time evolved profiles are studied in two distinct time windows. The problem of energetic electron accumulation near magnetic axis is discussed, and comparison of various methods of calculating the correction term on the r.h.s. of the QNE is conducted.

Chapter 7 concludes this work by recounting the main achievements, and suggests possible extensions of the current adaptation scheme.

Chapter 2

Physical model

Here, we give an overview of the physical concepts and models used in this work. As the plasma turbulence simulated is highly anisotropic, we begin by describing the toroidal magnetic field geometry in Sec. 2.1. This is followed by a discussion on the main microinstabilities involved in the simulations in Sec. 2.2, namely, the ITG and TEM modes, along with the role of zonal flows. Sec. 2.3 then gives a brief overview of gyrokinetic theory and its equations of motion. Then, the important ideas of equilibrium and background distributions are introduced in Sec. 2.4. Finally, Sec. 2.5 discusses the quasi-neutrality-equation (QNE), along with the various electron models used in this thesis.

2.1 Magnetic field geometry

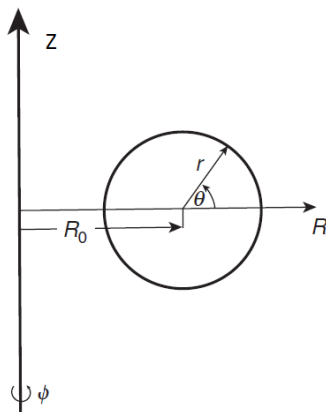


Figure 2.1: Cylindrical geometry (R, φ, Z) and tokamak geometry (r, φ, θ^*) . Figure is taken from Ref. [25].

Let (R, φ, Z) be a right-handed cylindrical coordinate system, as shown in Fig. 2.1. Here, R is the radial coordinate, φ the azimuthal (toroidal) angle, and Z the vertical. Then, a toroidally symmetric magnetic field \vec{B} that is also divergent-free, $\nabla \cdot \vec{B} = 0$, may be written in the form

$$\vec{B}(R, Z) = F(\psi)\nabla\varphi + \nabla\psi \times \nabla\varphi. \quad (2.1)$$

Here, F is the poloidal current function indexed by ψ . The latter is the poloidal flux function, defined by

$$\psi(R, Z) = \frac{1}{2\pi} \int_{\Sigma} d^2r \hat{n} \cdot \vec{B}(R, Z) \quad (2.2)$$

where $\Sigma(R, Z)$ is a toroidal ribbon emanating from the magnetic axis with surface unit normal \hat{n} . From Eq. (2.1), we see that $\vec{B} \cdot \nabla\psi = 0$. This means that each field line described by \vec{B} lies on a particular magnetic surface, which is labelled by ψ . As field lines cannot overlap, flux functions labelled by $\psi(R, Z) = \text{const}$ can be used as a radial coordinate with origin at the magnetic axis. The magnetic field \vec{B} is further described by Ampère's law, and the condition for ideal magnetohydrodynamic (MHD) equilibrium, given respectively by

$$\nabla \times \vec{B} = \mu_0 \vec{J} \quad (2.3)$$

and

$$\vec{J} \times \vec{B} = \nabla p. \quad (2.4)$$

μ_0 here is the magnetic permeability of free space, \vec{J} the current density, and p the isotropic pressure. We have employed Ampère's law neglecting the displacement current as we only consider phase velocities of field perturbation very small w.r.t. the speed of light. Furthermore, it can be shown [25] that $p = p(\psi)$, and therefore both field lines of \vec{J} and \vec{B} lie on flux surfaces $\psi = \text{const}$, on which p is constant. Eliminating \vec{J} by inserting Eq. (2.3) into (2.4), and replacing \vec{B} from Eq. (2.1) into the resulting equation, leads to the Grad-Shafranov equation:

$$\nabla \cdot \left(\frac{1}{R^2} \nabla \psi \right) = -\mu_0 p'(\psi) - \frac{(F^2)'}{2R^2}. \quad (2.5)$$

Equation (2.5) is used to solve for $\psi = \psi(R, Z)$ given the pressure p and poloidal current profile F , with appropriate boundary conditions. The poloidal cross-section of $\psi = \text{const}$ contours are generally not circular (e.g. the contour lines of Fig. 2.2). In order to define a radial coordinate more closely related to the geometrical minor radius, we consider the following. An example of an analytic solution to Eq. (2.5) with $F' = 0$ and $p' = \text{const}$, is the Solovév equilibrium [41]

$$\psi(R, Z) = \frac{\psi_{\text{edge}}}{(R_0 a)^2} \left[(RZ)^2 + \frac{1}{4}(R^2 - R_0^2) \right], \quad (2.6)$$

with a the minor radius, R_0 the major radius (see Fig. 2.1) and ψ_{edge} the value of ψ on the boundary. In the large aspect ratio $R_0/a \gg 1$ limit, Eq. (2.6) becomes $\psi = \psi_{\text{edge}} r^2/a^2$, implying circular $\psi = \text{const}$ surfaces with radius r from the magnetic axis. This suggests a new radial label

$$s = \sqrt{\frac{\psi}{\psi_{\text{edge}}}}, \quad (2.7)$$

which will be used extensively through this work. However, equilibrium \vec{B} field geometries usually do not have circular cross-sections, e.g. exhibit finite triangularity,

nor have finite Shafranov shift [29]. This leads to s^2 not being proportional to the enclosed volume V . Thus an alternative radial label commonly used in the literature is defined by

$$\rho_V = \sqrt{\frac{V(\psi)}{V(\psi_{\text{edge}})}}.$$

Nonetheless, only radial labels s and ψ/ψ_{edge} will be used throughout this work, depending on the profile under study.

Coming back to the geometry of \vec{B} , we first define the geometrical poloidal angle θ with reference at the magnetic axis (see Fig. 2.1). It turns out [25] that \vec{B} cannot be perfectly toroidal. Let us for the moment consider only toroidal field lines. As the guiding centres travel along these field lines toroidally, they will experience a radially-outward centrifugal force. The latter will cause guiding centres to drift vertically. Furthermore, the direction of this drift is charge sign dependent, thus resulting in a vertical charge separation. This charge separation in turn creates a vertical electric field, which leads to an $E \times B$ force on all particles. As this force is charge sign independent, the bulk plasma is ejected radially outwards, leading to lost of confinement. Therefore, the remedy of this is to have the \vec{B} field lines ‘twist’ poloidally as it goes around toroidally, thus short-circuiting the charge separation. This field-line twist on each $\psi = \text{const}$ surface is described by the safety factor $q(\psi)$, defined by

$$q(\psi) = \frac{1}{2\pi} \int_0^{2\pi} d\theta \frac{\vec{B} \cdot \nabla \varphi}{\vec{B} \cdot \nabla \theta}. \quad (2.8)$$

It is useful to define a ‘straight-field-line’ poloidal angle θ^* on each ψ surface, which relates to θ by

$$\theta^* = \frac{1}{q(\psi)} \int_0^\theta d\theta' \frac{\vec{B} \cdot \nabla \varphi}{\vec{B} \cdot \nabla \theta'}. \quad (2.9)$$

The term ‘straight-field-line’ derives from the fact that \vec{B} field lines are straight when projected on the (θ^*, φ) plane at $\psi = \text{const}$. This is shown simply by

$$\frac{\vec{B} \cdot \nabla \theta^*}{\vec{B} \cdot \nabla \varphi} = \frac{\vec{B} \cdot \nabla \theta}{\vec{B} \cdot \nabla \varphi} \frac{d\theta^*}{d\theta} = \frac{1}{q(\psi)},$$

where use has been made of Eq. (2.9). The configuration space coordinate system (s, θ^*, φ) is termed the ‘straight-field-line’ coordinate system, and is used thoroughly in this work. The motivation for the use of θ^* instead of θ is that micro-instabilities tend to be field-aligned. The configuration space under study allows us to express any perturbed field quantity as

$$\phi(s, \theta^*, \varphi, t) = \sum_{mn} \phi_{mn}(s, t) e^{im\theta^* + in\varphi}, \quad (2.10)$$

with poloidal and toroidal mode numbers m and n respectively. Then, the pertur-

bation that aligns with \vec{B} is proportional to

$$\begin{aligned}
 \vec{B} \cdot \nabla \phi &= (F \nabla \varphi + \nabla \psi \times \nabla \varphi) \cdot \left(\nabla_s \frac{\partial}{\partial s} + \nabla \theta^* \frac{\partial}{\partial \theta^*} + \nabla \varphi \frac{\partial}{\partial \varphi} \right) \phi \\
 &= \sum_{mn} (F \nabla \varphi + \nabla \psi \times \nabla \varphi) \cdot \left(\nabla_s \frac{1}{\phi_{mn}} \frac{\partial \phi_{mn}}{\partial s} + im \nabla \theta^* + in \nabla \varphi \right) \phi_{mn} e^{im\theta^* + in\varphi} \\
 &= \sum_{mn} (nF |\nabla \varphi|^2 + m \nabla \psi \times \nabla \varphi \cdot \nabla \theta^*) i \phi_{mn} e^{im\theta^* + in\varphi} \\
 &= \sum_{mn} [nq(s) - m] \frac{i}{J_s} \phi_{mn} e^{im\theta^* + in\varphi},
 \end{aligned}$$

where use has been made of Eqs. (2.1), (2.9) and (2.11) for the Jacobian (see below). Using (s, θ^*, φ) , the expression in the bracket, $nq - m$ depends only on ψ , and is amenable to a Fourier filter on each ψ -surface to enforce $k_{\parallel}/k_{\perp} \sim$ small (see Sec. 3.1.4.1).

Finally, using Eqs. (2.1) and (2.9), with $|\nabla \varphi|^2 = 1/R^2$, the Jacobian [17] of the configuration space in straight-field-line coordinate system is given explicitly by

$$\begin{aligned}
 J_s(s, \theta^*) &= \frac{1}{|\nabla_s \times \nabla \theta^* \cdot \nabla \varphi|} \\
 &= \frac{1}{|\nabla \psi \times \nabla \theta^* \cdot \nabla \varphi|} \left| \frac{d\psi}{ds} \right| \\
 &= \frac{1}{|\vec{B} \cdot \nabla \theta^*|} \frac{d\psi}{ds} \\
 &= \frac{q(s) R^2(s, \theta^*)}{F[\psi(s)]} \frac{d\psi(s)}{ds}.
 \end{aligned} \tag{2.11}$$

An operator that is used throughout this work, especially in diagnostics, is the flux-surface-averaged operator $\langle \cdot \rangle$, defined for a g in configuration space by

$$\langle g \rangle(s) = \frac{\int d\theta^* d\varphi g(s, \theta^*, \varphi) J_s(s, \theta^*)}{\int d\theta^* d\varphi J_s(s, \theta^*)}. \tag{2.12}$$

2.2 Electrostatic microinstabilities

This section summarises the properties of the two examples of electrostatic microinstabilities that will be encountered in this work. Turbulence driven by these modes generate fluxes of particle, momentum and heat, which can result in significant profile deviation from the initial state. Handling such strong profile evolution is a challenge for gyrokinetic simulations. Our intent is to prove the merit of an evolving background scheme. Nonetheless, the reader interested in a more thorough discussion on this topic may consult references like Refs. [12], [8], [43], and [19], from which this summary is made.

2.2.1 Ion-Temperature-Gradient driven instabilities

We consider a collisionless plasma, consisting of a single ion species of unit charge e and electron species in slab geometry. We use Cartesian coordinates in configuration

space $\vec{r} = [x, y, z]$, with respective unit vectors $\{\mathbf{e}_x, \mathbf{e}_y, \mathbf{e}_z\}$. We designate z as the direction of the magnetic field everywhere, i.e. $\vec{B} = B(x)\mathbf{e}_z$. We allow for perpendicular x -variation of the ion density $N = N(x)$ and temperature $T_i = T_i(x)$ respectively. On the other hand, the electrons are assumed to be adiabatic with density N and temperature T_e respectively. Finally, we consider a constant force

$$\vec{F} = F\mathbf{e}_x = -m \left(\frac{v_{\parallel}^2}{2} + v_{\perp}^2 \right) \frac{\partial}{\partial x} \log B \mathbf{e}_z,$$

with m the ion mass, and $v_{\parallel} = v_z$ and $v_{\perp} = \sqrt{v_x^2 + v_y^2}$ the parallel and perpendicular velocities respectively. This force mimicks the effects of the ∇B drift force. This also implies a constraint on $B(x)$ to be linear in x . The Vlasov equation

$$\left[\frac{\partial}{\partial t} + \vec{v} \cdot \nabla_r + \frac{1}{m} (-\nabla \phi + \vec{v} \times \vec{B} + \vec{F}) \cdot \nabla_v \right] f = 0 \quad (2.13)$$

is then solved by decomposing the ion distribution function f into $f = f_0 + \delta f$, i.e. an equilibrium distribution f_0 , and a perturbed distribution δf . f_0 is assumed to be a Maxwellian function of the constants of motion, and δf assumes the form

$$\delta f = \delta \hat{f}(x) \exp[i(k_y y + k_z z - \omega t)].$$

Here, the perturbed wave has wave vector $\vec{k} = k_y \mathbf{e}_y + k_z \mathbf{e}_z$ and angular frequency ω . The potential ϕ also assumes the form akin to δf with identical \vec{k} and ω . After some algebra, by solving for the dielectric function via the quasi-neutrality equation, leads one to the dispersion relation

$$0 = \frac{T_i}{T_e} + 1 + (\omega - \omega_{Ni}) \int d^3v \frac{f_0}{N} \frac{J_0^2(\xi)}{\omega_{Fi} - \omega + k_z v_{\parallel}} - \omega_{Ti} \int d^3v \frac{f_0}{N} \left(\frac{E}{T_i} - \frac{3}{2} \right) \frac{J_0^2(\xi)}{\omega_{Fi} - \omega + k_z v_{\parallel}}. \quad (2.14)$$

Here, the ion drift frequencies are $\omega_{Ni} = T_i k_y / (eB) / d \log N / dx$ due to a density gradient, $\omega_{Ti} = T_i k_y / (eB) dT_i / dx$ due to a temperature gradient, and $\omega_{Fi} = -k_y F(\vec{v}) / (eB)$ due to a constant perpendicular force, respectively. $E = mv^2/2 - Fx$ is the ion kinetic energy. J_0 is the zero-th order Bessel function of the first kind, with argument $\xi = k_y v_{\perp} / \Omega$, where Ω is the ion cyclotron frequency. To arrive at Eq. (2.14) we have considered only the zero-th order cyclotron harmonic. The J_0^2 term represents the lowest order Finite-Larmor-Radius (FLR) effects. The denominator with frequency shifted by ω_{Fi} constitutes Landau-damping.

By considering the fluid limit, i.e. $|\omega / (k_z v_{\text{th}i})| \ll 1$, with $v_{\text{th}i} = \sqrt{T_i / m_i}$ the ion thermal velocity, and $|\omega / \omega_{Fi}| \gg 1$, and neglecting FLR effects, Eq. (2.14) simplifies to¹

$$0 = 1 - \left(1 - \frac{\omega_{Ti}}{\omega} \right) \left[\left(\frac{k_z c_s}{\omega} \right)^2 + \frac{T_e \bar{\omega}_{Fi}}{T_i \omega} \right],$$

¹The absence of a force \vec{F} , and therefore $\omega_{Fi} = 0$, leads to the dispersion relation for the slab-ITG mode.

where $c_s = \sqrt{T_e/m}$ is the ion sound speed and $\bar{\omega}_{Fi} = 2T_i k_y / (eBR)$ is the velocity averaged ω_{Fi} , with R the gradient length of B , i.e. $R = -(\text{d log } B / \text{d}x)^{-1}$. Considering only the effect of large ion temperature gradient i.e. $|\omega_{Ti}/\omega| \gg 1$, and letting $k_z \rightarrow 0$, leads to the well-known relation

$$\omega = \pm \sqrt{-2 \frac{T_e}{T_i} \left(\frac{k_y T_i}{eB} \right)^2 \frac{\partial \log T_i}{\partial x} \frac{\partial \log B}{\partial x}} \quad (2.15)$$

for the growth rate of the toroidal ITG mode. Eq. (2.15) states that (in the absence of a density gradient) toroidal ITG modes will only be unstable where $\nabla \log T_i \cdot \nabla \log B > 0$, giving rise to ‘ballooning’ structures, as shown in Fig. 2.2. This region is also known as the bad curvature region.

When Eq. (2.14) is solved numerically for typical values like $T_e = T_i$, $|\nabla \log T_i| / |\nabla \log N| > 1$, and $k_z \rightarrow 0$, the maximum growth rate for the toroidal ITG mode is located at $k_y v_{thi} / \Omega \approx 0.5$. The growth rate also increases with increasing T_i logarithmic gradient for a fixed N logarithmic gradient. At short wavelengths $k_y v_{thi} / \Omega \approx 1$, FLR effects stabilise the toroidal ITG mode. ITG modes are known to be the main drive in ion heat transport.

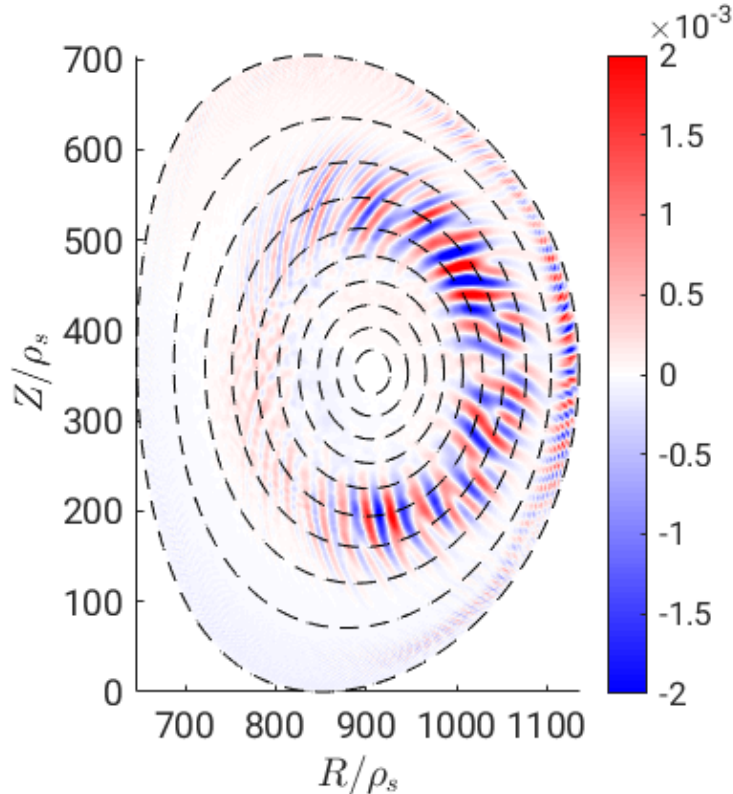


Figure 2.2: Poloidal cross-section showing the most dominant ITG mode $n \approx 28$ at $c_s t / a = 32$ for the ITG case of Ch. 5. The balloon structure is represented by the non-zonal perturbed potential $(\phi - \langle \phi \rangle) / T_{0e}(s_0)$. Contour curves represent constant $s = [0.1, 0.2, \dots, 1.0]$ flux surfaces (see Eq. (2.7)) of the magnetic field geometry of the TCV shot #43516 used in this work.

2.2.2 Trapped-Electron-Mode driven instabilities and its coupling to ITG modes

This work considers plasma magnetically confined by a toroidal magnetic field (see Sec. 2.1). This \vec{B} field is generated by a combination of a central solenoid and an induced current in the plasma (see Fig. 1.2a). The resulting field thus exhibit strong $1/R$ inhomogeneity in the radial direction, and curvature in field lines. For a guiding centre travelling along a field line toroidally, it experiences varying B strength as the field line has a poloidal component. This leads to a ‘magnetic mirror’ force, which reverses the direction of parallel flow at the strong B region, i.e. the High-Field-Side (HFS), and thus ‘trapping’ particles to the region of low B , i.e. the Low-Field-Side (LFS). These particles are thus termed ‘trapped’. When projected on the poloidal plane, these closed ‘banana’ orbits lie on the LFS, leading once again to ballooning structures at the bad curvature region. The distance from the toroidal axis of the reflection point depends on the magnitude of the parallel flow, and has its shortest value at the in-board mid-plane. Therefore, if a guiding centre has a large enough parallel velocity component, it will only suffer a parallel deceleration there, but not a reversal, as it travels toroidally along a field line. Particles of this category are termed ‘passing’ (see Fig. 2.3), and the ratio of their parallel to perpendicular velocities satisfy

$$\left| \frac{v_{\parallel}}{v_{\perp}} \right| > \sqrt{\frac{B_{\max}(\psi)}{B(s, \theta^*)} - 1},$$

with B_{\max} the maximum magnetic field strength on the ψ -surface on which each particle lie.

Trapped electrons executing oscillatory motion along a magnetic field-line do not undergo Landau damping. Furthermore, these electrons do not return to the same poloidal plane after one bounce period, but execute a toroidal precession. This precession drift can interact with a perturbation which results in the Trapped-Electron-Mode (TEM) microinstability, which propagates in the electron diamagnetic direction. The TEM can be destabilised with wavenumber in the same range of that of the toroidal ITG mode, though with a lower stability threshold [67]. As these modes are not sensitive to FLR effects due to the small electron Larmor radius, these modes can also exist at much shorter wavelength.

As it stands, the ‘1’ term in the dispersion relation Eq. (2.14) for the toroidal ITG mode represents the electrons’ fully adiabatic response. This can be modified to include passive drift-kinetic trapped electrons, and passing electrons with an adiabatic response. The fraction of trapped electron population is introduced into Eq. (2.14) via the trapped electron fraction α_T . The result is that trapped electrons reduces the total electron population’s adiabatic response, thus destabilising ITG modes at a lower threshold. These ITG modes have a larger linear growth rate and are also destabilised at longer wavelengths. Though dominant ITG turbulence does lead to electron heat transport, TEM still remains to be the dominant drive. On the other hand, particle transport occurs for both ITG-dominant and TEM-dominant regimes [5].

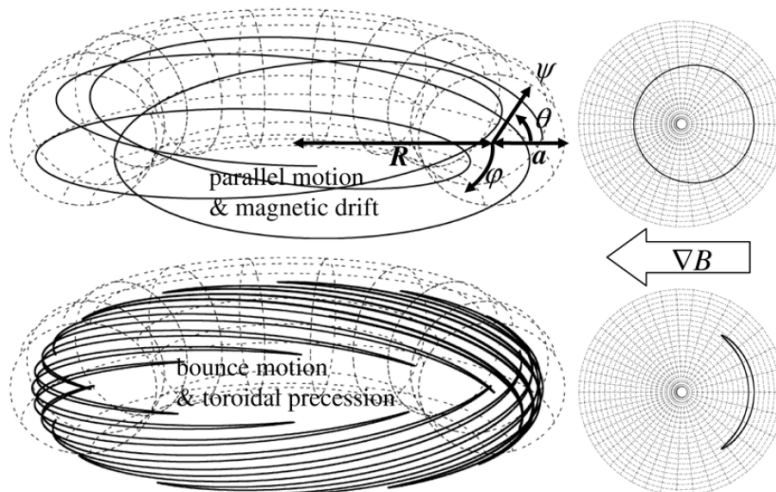


Figure 2.3: Passing (top) and trapped (bottom) guiding centre orbits. Drift motion causes guiding centres to deviate from a constant magnetic surface as they travel along a field line. Besides parallel velocity reversal, trapped particles further exhibit toroidal precession over bounce motion. Right sub-figures show the poloidal cross-section. Figure is taken from Ref. [28].

2.2.3 Zonal flows, GAMs and turbulence regulation

Zonal flows are sheared $E \times B$ plasma flow with $(m, n) = (0, 0)$, which are generated through Reynolds stress in the drift wave turbulence. In toroidal geometry, the $(m, n) = (0, 0)$ mode can couple with the $n = 0$ and $m \neq 0$ which results in the generation of Geodesic-Acoustic-Modes [80] (GAMs). Both of these modes can be understood via the zonal flow linear response function [69]. It was shown that in the presence of a source, the response function can be separated into short-time GAMs and long-time residual zonal flow. In the absence of collisions, residual zonal flows are undamped. GAMs on the other hand are oscillatory, with a characteristic frequency given [26] by $\omega_{GAM} \simeq \sqrt{7/2 + 2(T_e/T_i)}v_{thi}/R$. Unlike residual zonal flow, they are Landau-damped. This damping is however weaker at higher safety factor q , leading to their presence predominantly at the plasma edge.

Zonal flows play an important role in ITG turbulence regulation. Visually, they can be thought of as sheared flows that destroy turbulent eddies or the ballooning structures of the ITG modes (see Fig. 2.4a). The result is the reduction in ion heat transport. On the other hand, the role of zonal flows in the saturation of TEMs has been the subject of debate and appears to be case-dependent [51]. Zonal flows themselves are damped by either collisions, or via nonlinear damping, though these topics are beyond the scope of this thesis. This interactive system is summarised in Fig. 2.4b. The interested reader may consult Ref. [18] for a thorough overview on zonal flows.

In this work, the effect of zonal flows in turbulence regulation is determined via the zonal flow $E \times B$ shearing rate $\omega_{E \times B}$ (see Eq. (3.87)), which is derived from the f.s.a. electrostatic potential $\langle \phi \rangle$. As a rule of thumb, $\omega_{E \times B}$ has to be at least as large as the instability linear growth rate for turbulence suppression [78]. Simulations of zonal-flow-turbulence interactions using particle codes can be delicate: numerical sampling noise can accumulate in the undamped component of the zonal flows,

creating in the long run high amplitudes of $\omega_{E \times B}$ and consequently suppressing turbulence in an unphysical way. This phenomenon is shown and analysed in Ch. 4.

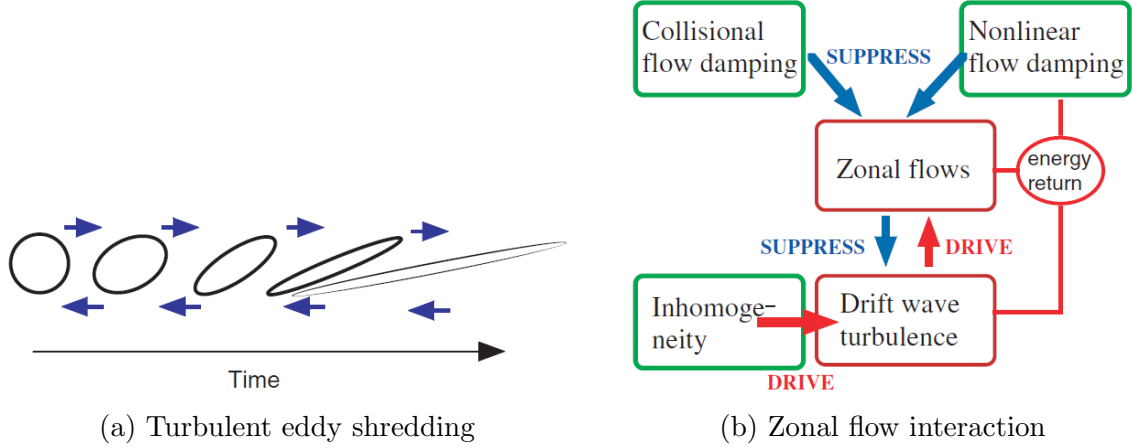


Figure 2.4: In the circle on the right, ‘energy return’ indicates the process of energy return to drift waves. Figures are taken from Ref. [18].

2.3 Gyrokinetic theory

2.3.1 Fully kinetic model

The most vigorous method to solve for the motion of charge particles in a magnetic field is the fully kinetic theory. Let each particle be described by a point $\vec{Z} = \vec{R}, \vec{V}$ in a six-dimensional phase space, with position $\vec{R} = [X, Y, Z]$ and velocity $\vec{V} = [V_x, V_y, V_z]$. The equations are simply given by Newton’s second law:

$$\frac{d\vec{R}}{dt} = \frac{\vec{V}}{m_j}, \quad \frac{d\vec{V}}{dt} = \frac{\sigma_j}{m_j} \vec{V} \times \vec{B}.$$

with m_j and σ_j the mass and charge of the j^{th} species respectively. We have also omitted the force by an electric field $\sigma_j \vec{E}$ to account for the fact that a plasma is quasi-neutral. The distribution function for each j^{th} species is then described by the Vlasov equation

$$\frac{\partial f_j}{\partial t} + \frac{d\vec{R}}{dt} \cdot \nabla_R f_j + \frac{d\vec{V}}{dt} \cdot \nabla_V f_j = 0, \quad \forall j,$$

with $\nabla_R = [\partial_X, \partial_Y, \partial_Z]$ and $\nabla_V = [\partial_{V_x}, \partial_{V_y}, \partial_{V_z}]$, where we have assumed no sources or collisions for this discussion. These equations are closed via the Maxwell equations with

$$\rho = \sum_j \sigma_j \int d^3v f_j, \quad \vec{J} = \sum_j \sigma_j \int d^3v \vec{v} f_j$$

which are the charge and current densities, respectively. Here, $\int d^3v = \int dV_x dV_y dV_z$ represents the integration over velocity space. Before discussing further simplifications, let us identify two constants of motion. The first is the particle energy per mass $\mathcal{E} = v^2/2$, with

$$\frac{d\mathcal{E}}{dt} = \sigma_j \vec{v} \cdot \vec{v} \times \vec{B} = 0.$$

For the second constant of motion, let us consider the j^{th} species particle Lagrangian in cylindrical coordinates (see Fig. 2.1),

$$\mathcal{L}_j = \frac{m_j}{2}(\dot{R}^2 + R^2\dot{\varphi}^2 + \dot{Z}^2) + \sigma_j(A_R\dot{R} + A_\varphi R\dot{\varphi} + A_Z\dot{Z}).$$

Here, $\vec{A} = [A_R, A_\varphi, A_Z]$ is the vector potential $\vec{B} = \nabla \times \vec{A}$, and $\dot{}$ represents the total time derivative. The conjugate momentum to the cyclic variable φ in axisymmetric geometry is called the ‘toroidal canonical momentum’

$$\psi_{0j} = \frac{1}{\sigma_j} \frac{\partial \mathcal{L}_j}{\partial \dot{\varphi}} = \psi + \frac{v_{\parallel}}{\Omega_j} F(\psi), \quad (2.16)$$

which is a constant of motion, where v_{\parallel} is the particle velocity parallel to the local \vec{B} field, and $\Omega_j = \sigma_j B/m_j$ is the cyclotron frequency. Despite having each \vec{B} field line lying on a particular $\psi = \text{const.}$ surface, the particles do not strictly gyrate around that field line, but drift perpendicularly due to ∇B and curvature drifts. The ψ deviation resulting from orbit drifts is represented by the second term of Eq. (2.16).

2.3.2 Phase space reduction by averaging out gyration phase

Now, modelling magnetically confined fusion plasma using the six-dimensional kinetic model is a numerically expensive task. This is because the plasma exhibits multi-scale behavior, both in space and in time. Turbulent eddies induced by MHD instabilities are typically on the order of 1m (the size of the tokamak minor radius), whereas those induced by micro-instabilities studies in this work are on the order of 10^{-3}m (the size of the ion Larmor radius). On the other hand, drift frequencies of these micro-instabilities are on the order of 10^6s^{-1} , whereas the ion cyclotron frequency is on the order of 10^8s^{-1} . In view of this large time-scale separation, gyrokinetic theory allows one to average out the fast ion cyclotron motion, and only solve for the particle guiding centre trajectories. This reduces the dimension of phase space from six to five, and also allows for longer time step-size for particle orbit integration. Various formalisms of averaging out cyclotron motion and their respective orderings of small parameters exist. In this work, we shall employ the gyrokinetic equations as derived by Hahm [32]. These equations of motion are derived from a Hamiltonian formalism that preserves energy and canonical toroidal momentum conservation. Furthermore, to preserve the magnetic moment μ as an adiabatic invariant under field perturbations, a coordinate transformation from particle guiding centres to gyrocentres has been derived by the use of Lie perturbation theory. Visually, particle gyrocentre is the shifted guiding-centre to account for circular Larmor orbit distortion due to perturbations. A complete tutorial on the derivation of the gyrokinetic model used in this work can be found in references like Refs. [72],[73] and [27]. An overview of the use of gyrokinetics for modelling plasma turbulence can be found in Ref. [28].

Hahm’s nonlinear gyrokinetic theory employs the parameters ϵ_g and ϵ_B for smallness ordering:

$$\epsilon_g \sim \frac{\omega}{\Omega_i} \sim \frac{e\phi}{T_e} \sim \frac{k_{\parallel}}{k_{\perp}} \sim \frac{\rho_L}{L_n} \sim \frac{\rho_L}{L_T}, \quad \epsilon_B \sim \frac{\rho_L}{L_B},$$

where ω is the typical frequency of the instability under study and Ω_i the ion cyclotron frequency. $e\phi/T_e$ is the ratio of the perturbed field energy and the electron

temperature, which implies small drift velocities v_{drift} w.r.t. the electron thermal velocity v_{the} . k_{\parallel}/k_{\perp} is the ratio of the parallel and perpendicular component of the wave vector w.r.t. the local magnetic field \vec{B} , respectively. It implies turbulence eddies are mostly field aligned. ρ_L is the reference ion Larmor radius, and L_g is the average global gradient length scale of the profile g , which are the density n , temperature T , and magnetic field B . Measure of ρ_L/L_g implies that gradient length scales should be at least a few Larmor radius in length. For tokamak plasmas, the difference between ϵ_B and ϵ_g is the inverse of the aspect ratio $\epsilon_a = a/R_0$, i.e. $\epsilon_B/\epsilon_g \sim \epsilon_a$.

Under the gyrokinetic theory, magnetically confined plasma is modeled by describing the time evolution of species' distribution function f in a five-dimensional phase space Ω . Each point in Ω is described by $\vec{Z} = [\vec{R}, v_{\parallel}, \mu]$, which represents the particle gyrocentre position, parallel velocity, and magnetic moment per mass, respectively. μ relates to the perpendicular velocity via $\mu = v_{\perp}^2/2B$. The gyrokinetic Boltzmann-Maxwell equation for the distribution function f_j of the j^{th} species (subscript omitted), is given by

$$\frac{df}{dt} = \left(\frac{\partial}{\partial t} + \frac{d\vec{R}}{dt} \cdot \nabla_{\vec{R}} + \frac{dv_{\parallel}}{dt} \frac{\partial}{\partial v_{\parallel}} + \frac{d\mu}{dt} \frac{\partial}{\partial \mu} \right) f = S. \quad (2.17)$$

Here, S is the a general source term. We have dropped the collision operator C as all simulations of this work are collision-less. The equations of motion of the gyrocentre position in phase space when studying electrostatic turbulence are given by

$$\begin{aligned} \frac{d\vec{R}}{dt} &= v_{\parallel} \hat{b} + \frac{1}{B_{\parallel}^*} \left[\frac{\mu B + v_{\parallel}^2}{\Omega_c} \hat{b} \times \nabla B - \frac{v_{\parallel}^2}{\Omega_c} \hat{b} \times (\hat{b} \times \nabla \times \vec{B}) - \nabla \tilde{\phi} \times \hat{b} \right] \\ \frac{dv_{\parallel}}{dt} &= -\mu \nabla B \cdot \left[\hat{b} - \frac{v_{\parallel}}{B_{\parallel}^* \Omega_c} \hat{b} \times (\hat{b} \times \nabla \times \vec{B}) \right] - \\ &\quad \frac{\nabla \tilde{\phi}}{\Omega_c} \cdot \left\{ \vec{B} + \frac{B v_{\parallel}}{B_{\parallel}^* \Omega_c} [\hat{b} \times \nabla B - \hat{b} \times (\hat{b} \times \nabla \times \vec{B})] \right\} \end{aligned} \quad (2.18)$$

$$\frac{d\mu}{dt} = 0. \quad (2.20)$$

All fields like the magnetic field $\vec{B} = B \hat{b}$ and the potential ϕ are functions of the gyrocentre coordinate \vec{Z} , on which the spatial gradient ∇ operator also act. $\Omega_c = \sigma B(\vec{R})/m$ is the species local cyclotron frequency. The term $\tilde{\phi}$ is ϕ under the gyroaveraging operator $\tilde{\cdot}$, given by

$$\tilde{\phi}(\vec{R}, \mu, t) = \frac{1}{2\pi} \int_0^{2\pi} d\alpha \phi(\vec{R} + \vec{\rho}_L(\mu, \alpha), t), \quad (2.21)$$

where α is the gyroangle, and $\vec{\rho}_L$ is the local Larmor radius with magnitude $\rho_L = \sqrt{2\mu B}$. The term B_{\parallel}^* is the component parallel to \vec{B} of the vector

$$\vec{B}^* = \vec{B} + \frac{B v_{\parallel}}{\Omega_c} \nabla \times \hat{b}, \quad (2.22)$$

i.e. $B_{\parallel}^* = \vec{B}^* \cdot \hat{b} = B(1 + v_{\parallel} \hat{b} \cdot \nabla \times \hat{b} / \Omega_c)$. Looking at Eqs. (2.18) and (2.19), the terms involving $\hat{b} \times (\hat{b} \times \nabla \times \vec{B})$ represents the diamagnetic drift induced by a pressure p gradient, i.e.

$$\hat{b} \times (\hat{b} \times \nabla \times \vec{B}) = \frac{1}{B^2} \vec{B} \times (\vec{B} \times \vec{J}) = \frac{\nabla p \times \vec{B}}{B^2}.$$

Based on Eq. (2.18), the velocity of \vec{R} is determined, by successive terms, the parallel component, the ∇B and curvature drifts, the diamagnetic drift, and the $E \times B$ drift. As for Eq. (2.19), the parallel acceleration is determined by the magnetic mirror term, the interaction of the magnetic field gradient with the diamagnetic drift, the parallel acceleration by electric field, and the interaction between the electric field and the curvature and diamagnetic drifts. Finally, Eq. (2.20) is the statement of μ being an adiabatic invariant. Eqs. (2.18), (2.19) and (2.20) are derived up to order $\mathcal{O}(\epsilon_g \epsilon_B)$, i.e. drift terms on the order of $\mathcal{O}(\epsilon_B^2)$ are neglected. These equations are closed by the self-consistent electrostatic potential ϕ by solving Poisson's equation, which will be discussed in Sec. 2.5. Thus, terms in Eqs. (2.18) and (2.19) that involve the perturbed field ϕ make them nonlinear.

Finally, B_{\parallel}^* appears in the Jacobian determinant for the velocity transformation, as in

$$\int d^3v = \int dV_x dV_y dV_z = \int dv_{\parallel} d\mu d\alpha B_{\parallel}^* \equiv \int dv_{\parallel} d\mu, 2\pi B_{\parallel}^* = \int dv_{\parallel} d\mu J_v \quad (2.23)$$

where α is the gyroangle, $J_v = 2\pi B_{\parallel}^*$ is the velocity Jacobian for the gyrocentre velocity variables.

2.4 Equilibrium and background distributions

Let us for the moment consider the homogeneous form of Eq. (2.17), termed the gyrokinetic Vlasov-Maxwell equation. It is useful to separate the un-perturbed and perturbed trajectories, i.e.

$$\frac{df}{dt} = \left. \frac{df}{dt} \right|_0 + \left. \frac{df}{dt} \right|_1 = 0. \quad (2.24)$$

The operator $\left. \frac{d}{dt} \right|_1$ ($\left. \frac{d}{dt} \right|_0$) that describes the perturbed (unperturbed) trajectories contains only terms with (without) ϕ in Eqs. (2.18), (2.19) and (2.20). Furthermore, the distribution $f = f_{\text{eq}}$ that describes a system in gyrokinetic equilibrium is defined by

$$\left. \frac{df_{\text{eq}}}{dt} \right|_0 = 0. \quad (2.25)$$

In order for Eq. (2.25) to be satisfied, f_{eq} must be function of the constants of motion of the unperturbed system only. Namely, the canonical toroidal momentum $\hat{\psi}_0$ (Eq. (2.16)), the energy per mass

$$\mathcal{E} = \frac{v^2}{2} = \frac{v_{\parallel}^2}{2} + \mu B(\vec{R}), \quad (2.26)$$

and the magnetic moment μ . That is $f_{\text{eq}} = f_{\text{eq}}(\hat{\psi}_0, \mathcal{E}, \mu)$. If we could postulate that throughout the simulation, the distribution f will not deviate too much from an initially known distribution f_{init} , we could in all generality introduce the ‘delta-f’ splitting

$$f = f_{\text{init}} + \delta f, \quad (2.27)$$

where δf represents the deviation f from f_{init} . Note that this splitting does not require f_{init} to describe a gyrokinetic equilibrium f_{eq} . To solve for δf , we then insert Eq. (2.27) into Eq. (2.24) leading to

$$\frac{d\delta f}{dt} = - \left. \frac{df_{\text{init}}}{dt} \right|_0 - \left. \frac{df_{\text{init}}}{dt} \right|_1. \quad (2.28)$$

Thus, if $f_{\text{init}} = f_{\text{eq}}$, the first term of the r.h.s. of Eq. (2.28), the ‘neo-classical’ term, vanishes.

A common choice for the functional form of f_{init} is the Maxwellian function f_M , with density and temperature profiles constant on magnetic surfaces, i.e. functions of the radial coordinate ψ ,

$$f_M(\psi, \mathcal{E}) = \frac{n_0(\psi)}{[2\pi T_0(\psi)/m]^{3/2}} \exp \left[-\frac{\mathcal{E}}{T_0(\psi)/m} \right], \quad (2.29)$$

where n_0 and T_0 are the f.s.a. gyrocentre number density and temperature of the species respectively². Here, an isotropic temperature profile is assumed. This choice of the ‘local’ Maxwellian is motivated by the fact that given high enough collisionality, plasma distributions tend to be close to f_M . However, Eq. (2.29) does not describe a gyrokinetic equilibrium and thus the neoclassical term of Eq. (2.28) has to be included. Unfortunately, when Eq. (2.29) is used for f_{init} , this leads to spurious zonal flow drive [38] at the beginning of the simulation. Nonetheless, it is common practice in the PIC community to drop the neoclassical term. An alternative is to have $f_{\text{init}} = f_M$, and using ψ_0 (see Eq. (2.16)) instead of ψ as the radial coordinate,

$$f_M(\psi_0, \mathcal{E}) = \frac{n_0(\psi_0)}{[2\pi T_0(\psi_0)/m]^{3/2}} \exp \left[-\frac{\mathcal{E}}{T_0(\psi_0)/m} \right]. \quad (2.30)$$

We shall call this a ‘canonical Maxwellian’³. Using Eq. (2.30) as f_{init} , the neo-classical term can now be dropped. Note that, the distinction between Eq. (2.29) and Eq. (2.30) for f_{init} is only important for the ion species, as the term accounting for particle drift away from magnetic surface ψ is small for the electrons in Eq. (2.16). Therefore, f_{init} for electrons in this work will always assume Eq. (2.29) and also dropping the electron neo-classical term.

The idea of delta-f splitting can be generalised to

$$f = f_0 + \delta f \quad (2.31)$$

with f_0 representing the ‘background’ distribution, i.e. the distribution appropriately time-averaged over turbulent fluctuation time-scales, and δf representing the

²Here, we assumed zero parallel flow.

³Strictly speaking, this is no longer a Maxwellian function as ψ_0 depends also on the velocity variables.

fast fluctuating part. In this approach, which is at the core of the adaptive scheme presented in more detail in Sec. 3.2, f_0 is a slowly evolving time-dependent distribution, and is thus in principle distinct from f_{init} and is furthermore not necessarily an equilibrium distribution f_{eq} . Especially for a Particle-In-Cell scheme (see Sec.3.1) used in this work, f_0 is taken to be a smooth analytic function with only few, non-zero, low-order velocity moments, and thus δf accounts for all the fine details of f in phase space, e.g. higher order moments of velocity, represented by numerical particles or ‘markers’ (see Sec. 3.1.3). In this context, f_0 plays the role of the control variate (see Sec. 3.1.1).

2.5 Quasi-neutrality equation

The work of this thesis deals with a single ion species of single charge $\sigma_i = e$, and electrons. Functions of these species will be denoted by subscripts i and e respectively.

2.5.1 Cancellation of the initial ion and electron densities

The general statement of the quasi-neutrality equation is that $n_i - n_e = 0$. Namely, that the ion and electron number density cancel each other at all times. Before discussing in detail the various forms of this equation, we first concern ourselves with the initial distributions for the ions f_{initi} and electrons f_{inite} . For this work, we take f_{inite} to be Eq. (2.29). We now wish to use f_{inite} to describe a gyrokinetic equilibrium, Eq. (2.30). The problem is that, even when the n_{0i} and n_{0e} share the same functional form, the densities obtained after integrating Eq. (2.29) and (2.30) do not match⁴. A better radial coordinate for ions, which is also a constant of motion [3], is

$$\hat{\psi}_0 = \psi + \frac{v_{\parallel} F(\psi)}{\Omega_c} - \text{sign}[v_{\parallel}] \frac{m_i R_0}{e} \sqrt{2[\mathcal{E} - \mu B_{\text{max}}(\psi_0)]} \mathcal{H}[\mathcal{E} - \mu B_{\text{max}}(\psi_0)], \quad (2.32)$$

where $B_{\text{max}}(\psi)$ is the maximum magnitude of \vec{B} on the flux surface ψ , and \mathcal{H} is the Heaviside function. Here, we have used ψ_0 as the radial coordinate for B_{max} , and it is taken specifically to be $B_{\text{max}} = B(s = \sqrt{\psi_0}, \theta = \pi)$. Thus, f_{initi} now adopts

$$f_M(\hat{\psi}_0, \mathcal{E}) = \frac{n_0(\hat{\psi}_0)}{[2\pi T_0(\hat{\psi}_0)/m]^{3/2}} \exp \left[-\frac{\mathcal{E}}{T_0(\hat{\psi}_0)/m} \right]. \quad (2.33)$$

The specific form of the quasi-neutrality equation (QNE) used to solved for the self-consistent electrostatic potential as a function of straight-field-line coordinates (see Eq. (2.9)) $\phi = \phi(\vec{r}, t)$ with $\vec{r} = [s, \theta^*, \varphi]$, of Eqs. (2.17), (2.18), (2.19), and (2.20)

⁴Precisely, in the presence of negligible perturbed fields at initial time, it is the ion gyrodensity and electron density that have to match.

is [54]

$$\begin{aligned}
 -\nabla_{\perp} \cdot \left(\frac{m_i n_{0i}(\psi)}{eB^2} \nabla_{\perp} \phi \right) &= \int \frac{d\alpha}{2\pi} \int d\Omega f_i(\vec{R}, v_{\parallel}, \mu, t) \delta[\vec{R} + \vec{\rho}_L(\mu, \alpha) - \vec{r}] - \\
 &\quad \int d\Omega f_e(\vec{R}, v_{\parallel}, \mu, t) \delta[\vec{R} - \vec{r}] \\
 &= \int d^3v \tilde{f}_i - \int d^3v f_e. \tag{2.34}
 \end{aligned}$$

The term on the left is the ion polarisation density in the long-wavelength limit $k_{\perp} \rho_{\text{th}i} \ll 1$, with $\rho_{\text{th}i}$ the thermal ion Larmor radius. In the present of the ion polarisation density, the $\nabla^2 \phi$ term from the Poisson equation from which Eq. (2.34) is derived is $(\lambda_D / \rho_{\text{th}i})^2$ -smaller, where λ_D is the Debye length. Therefore, under fusion parameters, the $\nabla^2 \phi$ term is dropped. The ion polarisation density is linearised by replacing the ion density n_i with that of the initial density n_{0i} . Specifically, it is the function n_0 in Eq. (2.29) or (2.33) indexed by the radial coordinate ψ . Eq. (2.34) can be solved as a linear system with finite elements (see Sec. 3.1.5). ∇_{\perp} is the gradient perpendicular to the local \vec{B} field, and is approximated to be the gradient in the poloidal plane [43], i.e.

$$\begin{aligned}
 \nabla_{\perp} &= \nabla_s \frac{\partial}{\partial s} + \nabla \theta^* \frac{\partial}{\partial \theta^*} + \nabla \varphi \frac{\partial}{\partial \varphi} - \hat{b} \frac{F(\psi)}{R^2 B} \left[\frac{\partial}{\partial \varphi} + \frac{1}{q(\psi)} \frac{\partial}{\partial \theta^*} \right] \\
 &\approx \nabla_s \frac{\partial}{\partial s} + \nabla \theta^* \frac{\partial}{\partial \theta^*}.
 \end{aligned}$$

The terms on the r.h.s. of Eq. (2.34) constitute the difference between the ion gyrodensity and the electron density. Owing to the relatively small electron Larmor radius $\rho_{Le} / \rho_{Li} = m_e / m_i \ll 1$, the electron gyrodensity is approximated as the electron total density. $d\Omega$ is the gyrocentre phase-space differential,

$$\int d\Omega = \int d^3R d^3v = \int 2\pi B_{\parallel}^*(s, \theta^*, v_{\parallel}) J_s(s, \theta^*) ds d\theta^* d\varphi dv_{\parallel} d\mu, \tag{2.35}$$

with J_s given by Eq. (2.11).

Replacing Eq. (2.31) into Eq. (2.34) leads to

$$-\nabla_{\perp} \cdot \left(\frac{m_i n_{0i}(\psi)}{eB^2} \nabla_{\perp} \phi \right) = \tilde{n}_{0i} + \delta \tilde{n}_i - n_{0e} - \delta n_e. \tag{2.36}$$

In order to further simplify the r.h.s. of Eq. (2.36), the reader is reminded that we take Eq. (2.33) and Eq. (2.29) as the initial distributions for the ions f_{0i} and electrons f_{0e} respectively. In this work, n_{0i} and n_{0e} is also chosen such that they have the same functional form, denoted by n_0 . Since f_{0i} and f_{0e} describe gyrokinetic equilibria, the ion polarisation density vanishes at initial time $\phi(t=0) = 0$. However, \tilde{n}_{0i} is not constant on ψ -surfaces as a consequence of using Eq. (2.33) and thus cannot cancel n_{0e} everywhere. We now make the assumption that

$$n_{0i}(t=0) = n_{0e}(t=0) + \mathcal{O}(\rho_{\star}^2) \approx n_{0e}(t=0).$$

Under these circumstances, Eq. (2.36) becomes

$$-\nabla_{\perp} \cdot \left(\frac{m_i n_{0i}(\psi)}{eB^2} \nabla_{\perp} \phi \right) = \delta \tilde{n}_i - \delta n_e. \tag{2.37}$$

2.5.2 Electron models used in this work

Depending on the type of electrostatic instability under study, the electron response can be further classified. Eq. (2.37) as it stands, describes electrons as fully drift-kinetic. The problem when using the fully drift kinetic electron response to study TEM turbulence is that the ω_H mode, which is the electrostatic limit of the kinetic Alfvén wave is present in the spectrum [56]. It has frequency $\omega_H = (k_{\parallel}/k_{\perp})\sqrt{m_i/m_e}\Omega_{ci}$, where Ω_{ci} is the ion cyclotron frequency, and becomes large for long perpendicular wavelengths. Resolving the small time-scales of the ω_H mode severely limits the time integration step size. To circumvent this problem, a so-called ‘upgraded hybrid electron model’ has been devised in Ref. [39]. This model features:

1. All electron orbits are followed according to the drift-kinetic assumption.
2. Trapped electrons contribute fully to the r.h.s. of the QNE.
3. Passing electrons contribute only to the zonal (i.e. flux-surface-average) component of the r.h.s. of the QNE
4. For the non-zonal modes, the passing electrons contribution to the QNE is assumed adiabatic.

Property (2) allows for the description of TEMs. Property (3), together with (1), allow for the model to satisfy the ambipolarity condition. Indeed, it was shown in Ref. [39] that neglecting the zonal response of passing electrons results in a violation of the ambipolarity condition. Property (3) also ensures to correctly capture [53, 52] the frequency of the GAM [80]. Property (4) implies that, on the other hand, ETG modes cannot be described by this model. Thus, the QNE Eq. (2.37), is modified to

$$\begin{aligned}
 & \alpha_P(\psi, \theta^*) \frac{en_{0e}(\psi)}{T_{0e}(\psi)} (\phi - \langle \phi \rangle) - \nabla_{\perp} \cdot \left(\frac{m_i n_{0i}(\psi)}{eB^2} \nabla_{\perp} \phi \right) \\
 &= \delta \tilde{n}_i - \delta n_{e,T} - \delta n_{e,P} |_{(m,n)=(0,0)} \\
 &= \int d\Omega \int \frac{d\alpha}{2\pi} \delta[\vec{R} + \vec{\rho}_L - \vec{r}] \delta f_i - \int d\Omega \delta[\vec{R} - \vec{r}] \delta f_{e,T} - \int d\Omega \delta[\vec{R} - \vec{r}] \delta f_{e,P} \Big|_{(m,n)=(0,0)}
 \end{aligned} \tag{2.38}$$

Here, the subscripts P and T represent the passing and trapped populations of electrons, respectively. m and n are the poloidal and toroidal mode numbers of the electrostatic potential ϕ , Eq. (2.10) respectively. α_P is the electron passing fraction, which is given by

$$\alpha_P(\psi, \theta^*) = 1 - \sqrt{1 - \frac{B(\psi, \theta^*)}{B_{\max}(\psi)}},$$

where $B_{\max}(\psi)$ is the maximum of \vec{B} on the ψ -surface. The term $en_{0e}(\phi - \langle \phi \rangle)/T_{0e}$ is the Boltzmann response with reference to initial electron f.s.a. density and temperature. The zonal passing electrons are given a kinetic response to correctly capture [53, 52] the frequency of the GAM [80].

Finally, Eq. (2.38) can be simplified even further when studying instabilities driven by ITG modes. It consists in considering all electrons as adiabatic. Note that with this assumption, no particle transport is expected because the perturbed potential is in phase with the perturbed density. Another practical consequence is that electron orbits do not need to be computed, which allows for using larger time steps. Eq. (2.38) then reduces to

$$\frac{en_{0e}(\psi)}{T_{0e}(\psi)}(\phi - \langle \phi \rangle) - \nabla_{\perp} \cdot \left(\frac{m_i n_{0i}(\psi)}{eB^2} \nabla_{\perp} \phi \right) = \int d\Omega \int \frac{d\alpha}{2\pi} \delta[\vec{R} + \vec{\rho}_L - \vec{r}] \delta f_i. \quad (2.39)$$

Chapter 3

Numerical methods

This chapter develops the central focus of this thesis, namely the implementation of an adaptive background scheme using a flux-surface-averaged Maxwellian as control variate. Sec. 3.1 begins by introducing the PIC approach as a method to solve for the distribution function of plasma species. Sec. 3.1.1 introduces the basic ideas of Monte Carlo integration, along with the use of control variates to reduce variance. Sec. 3.1.2 describes how phase space is sampled in ORB5. This is followed by the discretisation of distribution functions, representing them as markers in Sec. 3.1.3. Sec. 3.1.4 then introduces the two main diagnostics particularly useful to a PIC scheme. Sec. 3.1.5 briefly describes how the QNE is solved in ORB5, which is then followed by an overview of the ORB5 algorithm in Sec. 3.1.6. Sec. 3.2 introduces the adaptive scheme by first presenting its central ideas in Sec. 3.2.1. Sec. 3.2.2 then delves into the relaxation equations that governs the time-dependence of adaptive background profiles along with two proposed algorithms. Sec. 3.2.7 then illustrates the implementation of the said algorithms via the example of the adaptation of the kinetic energy. Sec. 3.2.10 then details calculation of the necessary correction to the r.h.s. of the QNE due to a time-dependent background. Discussion around the QNE continues with Sec. 3.2.11 mentioning ideas on delinearising the polarisation density and updates to the l.h.s. of the QNE in light of time-dependent background profiles. The chapter concludes with Sec. 3.3 mentioning the sources/sinks used in this work, and Sec. 3.4 giving an overview of normalisations used.

3.1 Particle-In-Cell scheme

The Particle-In-Cell (PIC) scheme solves for the distribution function f_j of each species j via a collection of ‘computational particles’ called markers or tracers [7, 35], moving in the phase space that f_j occupies. For gyrokinetic simulations, the phase space is 5-dimensional, describing the gyrocentre coordinates $\vec{Z} = [\vec{R}, v_{\parallel}, \mu]$, and the motion of each marker is defined by the gyrokinetic equations of motion Eqs. (2.18)-(2.20). In the so-called standard ‘full-f’ PIC scheme, the full distribution f is sampled with markers. In the so-called ‘delta-f’ PIC scheme, the full distribution is split into a known function f_0 and a δf part, $f = f_0 + \delta f$. In this case, only δf is sampled with markers. We shall see that an adequate choice for f_0 can reduce the sampling error, hence the name ‘control variate’ PIC scheme. The rest of this section analyses the PIC scheme under the Monte Carlo framework, following very closely the interpretation of Ref. [6].

3.1.1 Discretisation: a Monte Carlo interpretation

The two main sources of error¹ for a PIC scheme are the numerical integration of the marker trajectories according to the equations of motion Eqs. (2.18)-(2.20), and the numerical integration of the various moments of the distribution function on the r.h.s. of the field equations. The former results from the truncation error made at each time-step of the numerical integration scheme used, which for this work is the 4th order explicit Runge-Kutta method (RK4), whereas the latter results from the error of using a finite number of samples from a distribution to evaluate integrals. This work focuses on minimising the error resulting from the latter and therefore a discussion on evaluation of integrals using the Monte Carlo method follows.

3.1.1.1 Solution to integrals via random samples

Let \vec{Z} be an n -dimensional random variable in phase space Ω , sampled according to the probability distribution $P_\Omega(\vec{Z})$, normalised to

$$\int d\Omega P_\Omega(\vec{Z}) = \int d^n Z J_Z(\vec{Z}) P_\Omega(\vec{Z}) := \int d^n Z P_Z(\vec{Z}) = 1,$$

with $d\Omega = J_Z(\vec{Z}) d^n Z$ the differential phase-space volume element, with the Jacobian $J_Z(\vec{Z})$ resulting from the transformation to the variables \vec{Z} from Cartesian ones. We have also made the assignment for the effective probability distribution in \vec{Z} , $P_Z(\vec{Z}) = P_\Omega(\vec{Z}) J_Z(\vec{Z})$. The expectation value of a function G of the variable \vec{Z} is given by

$$\mathbf{E}[G] = \int d\Omega G(\vec{Z}) P_\Omega(\vec{Z}). \quad (3.1)$$

Also, the variance of G is thus given by

$$\begin{aligned} \mathbf{Var}[G] &= \int d\Omega (G(\vec{Z}) - \mathbf{E}[G])^2 P_\Omega(\vec{Z}) \\ &= \mathbf{E}[G^2] - \mathbf{E}[G]^2. \end{aligned} \quad (3.2)$$

Now, we can approximate the integral on the r.h.s. of Eq. (3.1) using the sample mean

$$\bar{G} = \frac{1}{N_p} \sum_{p=1}^{N_p} G(\vec{Z}_p), \quad (3.3)$$

with N_p identical independent (idd) random variables \vec{Z}_p labeled by p , all with the same $P_Z(\vec{Z})$. Eq. (3.3) is an example of an unbiased estimator ($\mathbf{E}[\bar{G}] = \mathbf{E}[G]$), that

¹The discretisation of the self-consistent fields, e.g. via an FEM representation, constitutes another source of error.

leads to

$$\begin{aligned}
 \mathbf{Var}[\bar{G}] &= \frac{1}{N_p^2} \mathbf{Var} \left[\sum_{p=1}^{N_p} G(\vec{Z}_p) \right] \\
 &= \frac{1}{N_p} \mathbf{Var}[G], \quad (\text{this is true when } \vec{Z} \text{ are iid random variables}) \\
 \implies \sigma[\bar{G}] &= \sqrt{\mathbf{Var}[\bar{G}]} \\
 &= \frac{\sigma[G]}{\sqrt{N_p}}.
 \end{aligned} \tag{3.4}$$

which reveals the famous $1/\sqrt{N_p}$ law for the Monte Carlo sampling error. From Eq. (3.4), there are two ways to reduce the error to Eq. (3.1). The first is to increase the number of markers N_p , which requires more computational memory and operations. The second is to reduce the variance $\mathbf{Var}[G]$. This work focuses on the latter.

3.1.1.2 Variance reduction via a control variate

Integrals involving the distribution f occur in the PIC approach when evaluating field quantities, e.g. on the r.h.s. of the QNE. The general form of such an integral can be expressed as

$$\begin{aligned}
 I_f(\vec{r}, t) &= \int d\Omega f(\vec{Z}, t) A(\vec{Z}) \\
 &= \int d\Omega P_\Omega(\vec{Z}) \frac{f(\vec{Z}, t) A(\vec{Z})}{P_\Omega(\vec{Z})},
 \end{aligned} \tag{3.5}$$

for some distribution $A(\vec{Z})$. Eq. (3.5) can be calculated based on the expectation value of the following estimator:

$$\begin{aligned}
 \bar{I}_f &= \frac{1}{N_p} \sum_{p=1}^{N_p} \frac{f(\vec{Z}_p, t) A(\vec{Z}_p)}{P_\Omega(\vec{Z}_p)}, \\
 \implies \mathbf{Var}[\bar{I}_f] &= \frac{1}{N_p} \mathbf{Var} \left[\frac{f A}{P_\Omega} \right] \simeq \frac{f A}{N_p},
 \end{aligned} \tag{3.6}$$

where every p^{th} realisation of the random variable \vec{Z}_p is termed a ‘marker’. However, Eq. (3.6) will potentially have large variance resulting from the large variations of amplitudes of fA/P_Ω throughout the phase-space volume Ω . We now introduce the control variate f_0 so that $f = f_0 + \delta f$ (c.f. Eq. (2.27)) We assume that the functional form of f_0 is simple so that I_{f_0} can be evaluated analytically (or by means of grid-based numerical quadratures). Then, consider the following new estimator [68] for Eq. (3.5):

$$\bar{I}'_f = \frac{1}{N} \sum_{p=1}^N \frac{\delta f(\vec{Z}_p, t) A(\vec{Z}_p)}{P_\Omega(\vec{Z}_p)} + I_{f_0} \tag{3.7}$$

which has identical expectation value, i.e. $\mathbf{E}[\bar{I}_f] = \mathbf{E}[\bar{I}'_f] = I_f$. However, the variance is now given by

$$\mathbf{Var}[\bar{I}'_f] = \frac{1}{N_p} \mathbf{Var} \left[\frac{\delta f A}{P_\Omega} \right] \simeq \frac{\delta f A}{N_p}$$

following same derivation as for obtaining Eq. (3.4). Therefore, if the delta-f assumption

$$\frac{\|\delta f\|}{\|f\|} \ll 1, \quad (3.8)$$

is met at all times, the new estimator Eq. (3.7) for a given sample size N will lead to more accurate evaluation of Eq. (3.5). The function f_0 used in this context of variance reduction, is termed the ‘control variate’.

3.1.1.3 Variance reduction via importance sampling

An alternative method to reduce the variance is importance sampling. Returning to Eq. (3.6), if $P_\Omega(\vec{Z})$ can be suitably chosen so that the variance of Eq. (3.6)

$$\mathbf{Var}[\bar{I}_f] = \frac{1}{N_p} \mathbf{Var} \left[\frac{f(\vec{Z}, t) A(\vec{Z})}{P_\Omega(\vec{Z})} \right]$$

is small for all times, \bar{I}_f will serve as an estimator with small errors. For example, the choice of $P_\Omega(\vec{Z}) = f(\vec{Z}, 0)$ can be made, if sampling from $f(\vec{Z}, 0)$ is achievable. A potential problem arises if $f(\vec{Z}, t)$ deviates significantly from $f(\vec{Z}, 0)$ with simulation time. Then, in order keep the variance of \bar{I}_f low, resampling has to be periodically done according to new P_Ω 's.

In this work, resampling is not done, i.e. $P_\Omega(\vec{Z})$ is not modified mid-simulation, and an improvement on the control variate method for variance deduction is pursued. Attempts at applying importance sampling can be found in Ref. [34].

3.1.2 Initial loading and marker probability distribution

3.1.2.1 Configuration space loading

Let $P_R(\vec{R})$ be the initial probability distribution of markers in configuration space, with position given by \vec{R} and spanning the volume enclosed by the last closed flux surface. In practice it is chosen to be uniform over this whole domain:

$$1 = \int d^3R P_R(\vec{R})$$

$$P_R(\vec{R}) = \frac{1}{V},$$

with $V = \int d^3R$ the total volume of configuration space. In this work, configuration space is represented using the curvilinear magnetic coordinates (s, θ^*, φ) with Jacobian $J_s(s, \theta^*) = \nabla S \times \nabla \theta^* \cdot \nabla \varphi$. Here, the radial coordinate S is defined as in Eq. (2.7) and θ^* is the straight-field-line poloidal angle as in Eq. (2.9). Therefore, the expression for the configuration space volume is

$$V = 2\pi \int_0^1 ds \int_0^{2\pi} d\theta^* J_s(s, \theta^*).$$

3.1.2.2 Velocity space loading

Let $P'_v(\vec{R}, v_{\parallel}, v_{\perp})$ and $P_v(\vec{R}, v_{\parallel}, \mu)$ be the marker probability distributions in the $[\vec{R}, v_{\parallel}, v_{\perp}]$ - and $[\vec{R}, v_{\parallel}, \mu]$ -space respectively, such that

$$dv_{\parallel} dv_{\perp} P'_v(\vec{R}, v_{\parallel}, v_{\perp}) = d^3v P_v(\vec{R}, v_{\parallel}, \mu) \quad (3.9)$$

with $d^3v = dv_{\parallel} d\mu J_v$, where $J_v = 2\pi B_{\parallel}^*(\vec{R}, v_{\parallel})$ is the velocity Jacobian (Eq. (2.23)). For each configuration space point \vec{R} , P'_v is chosen to be uniform in the semi-circle of radius $\kappa_v v_{\text{th}}$ in the $[v_{\parallel}, v_{\perp}]$ -plane, where $v_{\text{th}} = \sqrt{T_0/m}$ is the local background thermal velocity, function of the radial coordinate s , and $\kappa_v = 5$ in this work. This implies

$$\begin{aligned} 1 &= \int dv_{\parallel} dv_{\perp} P'_v(\vec{R}, v_{\parallel}, v_{\perp}) \\ &= P'_v(\vec{R}, v_{\parallel}, v_{\perp}) \int dv_{\parallel} dv_{\perp} \\ P'_v(\vec{R}, v_{\parallel}, v_{\perp}) &= \frac{1}{\frac{\pi}{2} [\kappa_v v_{\text{th}}]^2}. \end{aligned}$$

Given that $\mu = v_{\perp}^2/(2B)$, one has $d\mu/dv_{\perp} = v_{\perp}/B$, so that from Eq. (3.9) one obtains

$$P_v(\vec{R}, v_{\parallel}, \mu) = \frac{B(\vec{R}) P'_v(\vec{R}, v_{\parallel}, \mu)}{2\pi B_{\parallel}^*(\vec{R}, v_{\parallel}) v_{\perp}(\vec{R}, \mu)} = \frac{B}{B_{\parallel}^* v_{\perp} [\pi \kappa_v v_{\text{th}}]^2}. \quad (3.10)$$

Therefore, the total marker probability distribution function of Eq. (3.1) with $\vec{Z} = [s, \theta^*, \varphi, v_{\parallel}, \mu]$ is

$$P_{\Omega}(s, \theta^*, \varphi, v_{\parallel}, \mu) = P_R P_v = \frac{B}{V B_{\parallel}^* v_{\perp} [\pi \kappa_v v_{\text{th}}]^2}. \quad (3.11)$$

We now demonstrate that P_{Ω} is constant along marker trajectories. Let the number of markers in an infinitesimal volume in phase space be $P_{\Omega} d\Omega = P_{\Omega} J_Z d^5Z$ with Jacobian $J_Z = J_s J_v$, with J_s and J_v given respectively by Eqs. (2.11) and (2.23). Then, by the conservation of markers,

$$\begin{aligned} 0 &= \frac{\partial}{\partial t} (P_{\Omega} J_Z) + \nabla_Z \cdot (\dot{\vec{Z}} P_{\Omega} J_Z) \\ &= J_Z \left[\frac{\partial P_{\Omega}}{\partial t} + \dot{\vec{Z}} \cdot \nabla_Z P_{\Omega} \right] + \left[\frac{\partial J_Z}{\partial t} + \nabla_Z \cdot (\dot{\vec{Z}} J_Z) \right] P_{\Omega} \\ &= J_Z \frac{dP_{\Omega}}{dt}, \end{aligned}$$

where use has been made of Liouville's theorem (incompressibility of phase space)

$$\frac{\partial J_Z}{\partial t} + \nabla_Z \cdot (\dot{\vec{Z}} J_Z) = 0,$$

as markers follow Hamiltonian flow, described by Eqs. (2.18), (2.19) and (2.20). Therefore, the marker distribution is constant along marker trajectories, i.e.

$$\frac{dP_{\Omega}}{dt} = \frac{\partial P_{\Omega}}{\partial t} + \dot{\vec{Z}} \cdot \nabla_Z P_{\Omega} = 0. \quad (3.12)$$

A useful diagnostics of a PIC simulation is the distribution of marker count in the (s, v^2) -coordinate space. As markers are initially loaded with probability distribution P_Ω , denoting N_p as the total number of markers for the i^{th} species, the differential number of i^{th} species markers dN in the bin at (s, v^2) of differential area $ds dv^2$ is

$$\begin{aligned}
 dN &= N_p ds \int_0^{2\pi} d\theta^* \int_0^{2\pi} d\varphi J_s(s, \theta^*) dv_{\parallel} d\mu 2\pi B_{\parallel}^*(s, \theta^*, v_{\parallel}) P_\Omega \\
 &= \frac{N_p V'_s(s) ds}{V B_{\parallel}^* v_{\perp} (\pi \kappa_v v_{\text{th}})^2} dv_{\parallel} \frac{v_{\perp} dv_{\perp}}{B} 2\pi B_{\parallel}^* \\
 &= \frac{2\pi N_p V'_s ds}{V (\pi \kappa_v v_{\text{th}})^2} \frac{\pi dv^2}{2} \\
 &= ds dv^2 \frac{N_p}{V} \frac{V'_s(s)}{(\kappa_v v_{\text{th}}(s))^2}, \tag{3.13}
 \end{aligned}$$

where $V_s(s)$ is the configuration space volume enclosed by the magnetic surface labelled by s and

$$V'_s(s) = \frac{dV_s}{ds} = 2\pi \int_0^{2\pi} d\theta^* J_s(s, \theta^*). \tag{3.14}$$

3.1.3 Discretising δf

3.1.3.1 The phase-space volume element

The definition for the infinitesimal phase space volume occupied by the p^{th} marker at gyrocentre phase point \vec{Z}_p is the infinitesimal phase space volume around the p^{th} marker divided by the average number of marker in that volume,

$$\begin{aligned}
 \Omega_p &= \lim_{|\vec{\epsilon}| \rightarrow 0} \frac{\int_{\vec{Z}_p + \vec{\epsilon}} d\Omega}{N_p \int_{\vec{Z}_p + \vec{\epsilon}} d^5 Z P_\Omega} \\
 &= \frac{1}{N_p P_\Omega(\vec{Z}_p)} \\
 &= \frac{V B_{\parallel p}^* v_{\perp p} [\pi \kappa_v v_{\text{th}p}]^2}{N_p B_p}, \tag{3.15}
 \end{aligned}$$

with the subscript p indicating the evaluation of that function at \vec{Z}_p (except for N_p , which is a constant).

To ensure that all relevant regions of phase space are sampled at a given time, a useful diagnostic [52] is to evaluate numerically with the markers volumes of bins in phase space, and comparing these estimates to the corresponding exact analytical values. To this end, we consider the configuration space coordinates used by ORB5, (s, θ^*, φ) , with corresponding Jacobian $J_s(s, \theta^*)$. Here, s is the radial coordinate. Let $v^2 = v_{\parallel}^2 + 2\mu B$ be twice the kinetic energy per mass. The phase-space volume diagnostic involves binning in the two-dimensional (s, v^2) -space. The radial coordinate is $s \in [0, 1]$ discretised into n_s bins, whereas the energy per mass coordinate is $v^2 \in [0, 1.2\kappa_v^2 T_{\text{max}j}/m_j]$ is discretised into n_{v^2} bins. Here, $T_{\text{max}j}$ is the global maximum temperature at time $t = 0$ for the j^{th} species. In this work, we consider $(n_s, n_{v^2}) = (64, 64)$.

The marker estimate of the phase space region $\Gamma_{ij} = [s_i, s_{i+1}] \times [v_j^2, v_{j+1}^2]$, is simply given by

$$\Omega(i, j, t) = \sum_{p \in \Gamma_{ij}} \Omega_p(t). \quad (3.16)$$

where the sum is over all markers within the bin Γ_{ij} at time t . On the other hand, we can analytically exactly calculate the corresponding phase-space volume:

$$\begin{aligned} \Omega^{(a)}(i, j) &= \int_{\Gamma_{ij}} d\Omega \\ &= \int_{s_i}^{s_{i+1}} ds d\theta^* d\varphi J_s \int_{v_j}^{v_{j+1}} dv_{\parallel} d\mu J_v \\ &= \int_{s_i}^{s_{i+1}} ds V'_s(s) \int_{v_j}^{v_{j+1}} dv_{\parallel} dv_{\perp} \frac{2\pi B_{\parallel}^*}{B} v_{\perp} \\ &\equiv 2\pi \int_{s_i}^{s_{i+1}} ds V'_s(s) \int_{v_j}^{v_{j+1}} dv_{\parallel} dv_{\perp} v_{\perp} \\ &= 2\pi \int_{s_i}^{s_{i+1}} ds V'_s(s) \int_{v_j}^{v_{j+1}} dv v^2 \int_0^{\pi} d\zeta \sin \zeta \\ &= \frac{4\pi(v_{j+1}^3 - v_j^3)}{3} \int_{s_i}^{s_{i+1}} ds V'_s(s), \end{aligned} \quad (3.17)$$

where we have used Eq. (3.14), and ζ is the pitch angle. In the limit $N_p \rightarrow \infty$, one expects $\Omega(i, j, t) = \Omega^{(a)}(i, j)$ at all times t . In practice $\Omega(i, j, t)$ and $\Omega^{(a)}(i, j)$ differ, not only as a result of N_p being finite, but also because not all regions of phase space are initially sampled. Discretisation errors in the marker trajectory integration, the practical implementation of the heating operator and collision operators are some of the causes why the quality of marker sampling in critical regions of phase space may deteriorate over time. Comparing $\Omega^{(a)}(i, j)$ and $\Omega(i, j, t)$ provides a useful diagnostic of the quality of phase-space sampling.

3.1.3.2 Klimontovich distribution and marker w -weights

Consider the integral similar to Eq. (3.5) involving δf and using the sample mean Eq. (3.3) as the estimator,

$$\begin{aligned}
 I_{\delta f}(\vec{r}) &= \int d\Omega \delta f(\vec{Z}, t) A(\vec{Z}) \\
 &= \int d\Omega P_{\Omega}(\vec{Z}) \frac{\delta f(\vec{Z}, t) A(\vec{Z})}{P_{\Omega}(\vec{Z})}, \\
 \bar{I}_{\delta f}(\vec{r}) &= \frac{1}{N_p} \sum_{p=1}^{N_p} \frac{\delta f(\vec{Z}_p, t) A(\vec{Z}_p)}{P_{\Omega}(\vec{Z}_p)} \\
 &= \int d\Omega A(\vec{Z}) \sum_{p=1}^{N_p} \frac{\delta f(\vec{Z}_p, t)}{N_p J(\vec{Z}_p) P_{\Omega}(\vec{Z}_p)} \delta(\vec{Z} - \vec{Z}_p) \\
 &= \int d\Omega A(\vec{Z}) \sum_{p=1}^{N_p} \frac{\delta f(\vec{Z}_p, t)}{2\pi B_{\parallel p}^* N_p P_{\Omega}(\vec{Z}_p)} \delta(\vec{R} - \vec{R}_p) \delta(v_{\parallel} - v_{\parallel p}) \delta(\mu - \mu_p),
 \end{aligned} \tag{3.18}$$

where \vec{R}_p is Cartesian, and $d\Omega = 2\pi B_{\parallel}^* dv_{\parallel} d\mu d^3R$. We now define the Klimontovich distribution

$$\delta \hat{f}(\vec{R}, v_{\parallel}, \mu, t) = \frac{N_{\text{ph}}}{N_p} \sum_{p=1}^{N_p} \frac{w_p(t)}{2\pi B_{\parallel p}^*} \delta(\vec{R} - \vec{R}_p(t)) \delta(v_{\parallel} - v_{\parallel p}(t)) \delta(\mu - \mu_p(t)), \tag{3.19}$$

with N_{ph} is the total number of physical particles of the species for which δf is the fluctuation part of the distribution. It is given by

$$N_{\text{ph}} = \int ds d\theta^* d\varphi J_s(s, \theta^*) n_0(s), \tag{3.20}$$

with $n_0(s)$ the initial density profile prescribed by the user. The w -weight of the p^{th} marker weight is defined as:

$$w_p(t) = \frac{\delta f(\vec{Z}_p, t)}{N_{\text{ph}} P_{\Omega}(\vec{Z}_p)} = \frac{N_p}{N_{\text{ph}}} \delta f(\vec{Z}_p, t) \Omega_p, \tag{3.21}$$

where Eq. (3.15) was used². The introduction of N_{ph} is to normalise the w -weights so that they do not scale with N_{ph} . Inserting Eq. (3.19) into Eq. (3.18) leads to

$$\begin{aligned}
 \bar{I}_{\delta f} &= \int d\Omega \delta \hat{f} A(\vec{Z}) \\
 &= \int d\Omega A(\vec{Z}) \frac{N_{\text{ph}}}{N_p} \left[\sum_{p=1}^{N_p} \frac{w_p(t)}{2\pi B_{\parallel p}^*} \delta(\vec{R} - \vec{R}_p(t)) \delta(v_{\parallel} - v_{\parallel p}(t)) \delta(\mu - \mu_p(t)) \right] \\
 &= \frac{N_{\text{ph}}}{N_p} \sum_{p=1}^{N_p} w_p(t) A(\vec{Z}_p).
 \end{aligned}$$

²In ORB5, the phase-space volume assigned to the p^{th} marker is in fact defined such that $\Omega_p \leftarrow \Omega_p N_p / N_{\text{ph}}$ so that $w_p = \delta f(\vec{Z}_p, t) \Omega_p$.

It must be noted Eq. (3.19) is only defined under the integral $\int d\Omega$ over phase-space volume, and $\mathbf{E}[\bar{I}_{\delta f}] = I_{\delta f}$.

3.1.3.3 Marker p -weights

If the Klimontovich definition Eq. (3.19) were to be applied to the control variate f_0 , this would result in

$$\hat{f}_0(\vec{R}, v_{\parallel}, \mu, t) = \frac{N_{\text{ph}}}{N_p} \sum_{q=1}^{N_p} \frac{p_q(t)}{2\pi B_{\parallel}^*} \delta(\vec{R} - \vec{R}_q) \delta(v_{\parallel} - v_{\parallel q}) \delta(\mu - \mu_q),$$

with p -weights of the q^{th} marker defined similarly to Eq. (3.21),

$$p_q(t) = \frac{f_0(\vec{Z}_q, t)}{N_{\text{ph}} P_{\Omega}(\vec{Z}_q)} = \frac{N_p}{N_{\text{ph}}} f_0(\vec{Z}_q, t) \Omega_q. \quad (3.22)$$

The use of p -weights in tandem with w -weights in a PIC approach constitutes a ‘two-weight’ scheme. It is useful when collisions are considered (see Ref.[74]). As this work deals with collision-less dynamics, the ‘single-weight’ scheme is used. That is, δf is represented as Eq. (3.19), and f_0 as an analytical function. The use of p -weights is occasionally used to represent profiles in diagnostics only, e.g. Figs. 6.9 and 6.25.

3.1.3.4 Delta-f marker weights evolution

Taking the total time derivative of Eq. (3.21) and using Eqs. (2.31) and (2.24) leads to

$$\frac{d}{dt} w_p(t) = -\frac{N}{N_{\text{ph}}} \Omega_p \frac{d}{dt} f_0(\vec{Z}_p, t). \quad (3.23)$$

In anticipation of the adaptive f_0 scheme we have allowed for a time-dependent f_0 (see Sec. 3.2). This means that once loaded, each marker only needs to carry its associated initial phase-space volume Ω_p , which is given explicitly by Eq. (3.15), and remains constant along its trajectory. In ORB5, the time evolution of $w_p(t)$ is done in a time-splitting fashion, first solving for the homogeneous gyrokinetic Vlasov equation $df/dt = 0$, and then correcting w_p for sources S (see Eq. (2.24)). Therefore, for the first part, one has

$$\frac{d}{dt} w_p(t) = -\frac{N}{N_{\text{ph}}} \Omega_p \frac{d}{dt} f_0(\vec{Z}_p, t). \quad (3.24)$$

Given that $\Omega_p = \text{const}$, this leads to

$$\Delta w_p = -\frac{N}{N_{\text{ph}}} \Omega_p \Delta f_0(\vec{Z}_p, t), \quad (3.25)$$

where Δ stands here for the change in value along marker trajectories over a given time step. The actual implementation of Eq. (3.25) is referred to as the ‘direct- δf ’ approach [2], and it is used for all nonlinear simulations of this thesis. This approach avoids the explicit calculation of the time derivative df_0/dt on the r.h.s. of

Eq. (3.24), which involves the evaluation of profile gradients. This latter approach is termed the ‘standard δf ’ method. In this thesis, the standard δf approach is used in Ch. 5, and in linear simulations (to calculate maximum linear growth rates, for example), where the nonlinear terms of Eqs. (2.18) and (2.19) are dropped, i.e.

$$\left. \frac{d}{dt} w_p(t) \right|_0 = -\frac{N}{N_{\text{ph}}} \Omega_p \left. \frac{d}{dt} \right|_1 f_0(\vec{Z}_p, t). \quad (\text{linear simulations})$$

Note for this particular case that we define $\left. \frac{d}{dt} \right|_0 P_\Omega(\vec{Z}_p) = 0$ to be true, even though marker density is not conserved (c.f. Eq. (3.12)).

3.1.4 Relation between weight variance and field equation

Based on the discussion of Sec. 3.1.1, the measure of the weight variance gives an indication to the amount of statistical sampling noise accumulated in the simulation. To that end, we will discuss two diagnostics used in this work.

3.1.4.1 Signal-to-noise-ratio diagnostic

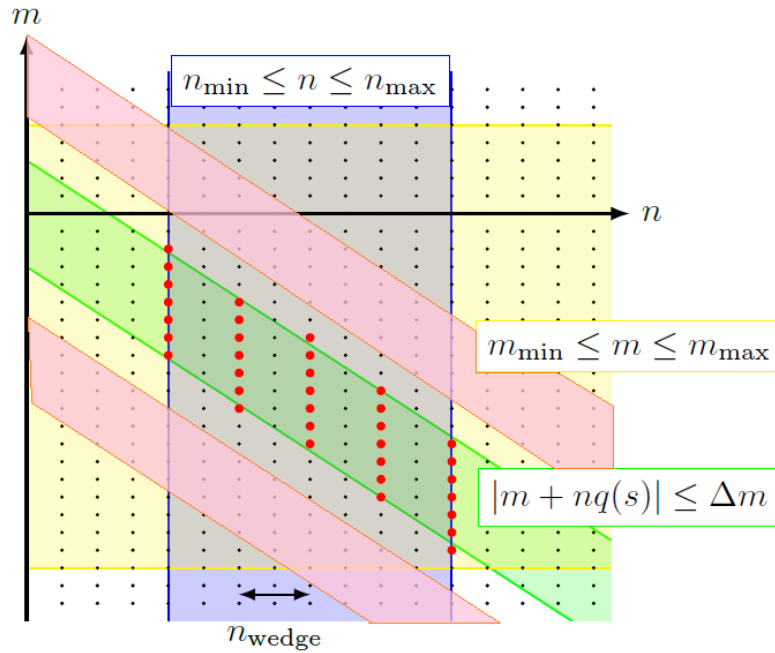


Figure 3.1: Fourier-filters for a fixed radial position s applied to the B-spline coefficients of the r.h.s. of the QNE. These are defined on a discrete grid of integer poloidal m and toroidal n Fourier modes. The band $\mathcal{F}_1 = |m + nq(s)| \leq \Delta m$ (green) of half-width Δm , indicates modes that are nearly field-aligned. Red dots represent the mode numbers chosen to be resolved, which are found in the overlap region of \mathcal{F}_1 and the box $(m, n) \in [m_{\min}, m_{\max}] \times [n_{\min}, n_{\max}]$. The pink side bands \mathcal{F}_2 are used for SNR diagnostics. They are of the same width, and are at a distance of $3\Delta m$ from centre to centre w.r.t. \mathcal{F}_1 , i.e. $\mathcal{F}_2 : |m \pm 3\Delta m + nq(s)| \leq \Delta m$.

A useful diagnostic derives from the discrete Fourier transform of the B-spline coefficients b_I, \hat{b}_{imn} , of the r.h.s. of the QNE, of Eq. (3.35). It can be shown [9] the

variance related to the finite sampling error is

$$\mathbf{Var}[b_I] = \frac{N_m}{N_p} G \sum_p w_p^2, \quad (3.26)$$

where N_m is the number of (m, n) Fourier modes that the simulation resolves, and G is a fixed simulation-dependent parameter (depends in particular on the order of splines considered in FEM). In order to separate the physical origin of the increase of $\sum w^2$ from the numerical one, we shall calculate the relative squared amplitudes $|b_I|^2$ related to field-aligned modes against non-field-aligned modes. This is in accordance with the gyrokinetic ordering $\mathcal{O}(k_{\parallel}/k_{\perp}) \sim \epsilon$, and the fact that non-field-aligned modes tend to be strongly Landau-damped. The field-aligned modes are thus described by a band \mathcal{F}_1 in the Fourier (m, n) -space defined by $|m + nq(s)| < \Delta m$, where $q(s)$ is the radially dependent safety factor, and Δm the half-width of \mathcal{F}_1 , a user-defined parameter taken to be $\Delta m = 5$ in this work, which was shown to be enough to converge the numerical results [45]. The $|b_I|^2$ amplitudes in \mathcal{F}_1 are thus termed the ‘signal’, though it still includes the discretised noise also present in the field-aligned modes [9]. Next, the ‘noise’ is described by the $|b_I|^2$ amplitudes in the band \mathcal{F}_2 , which are two side-bands of distance $3\Delta m$ apart from the centre of \mathcal{F}_1 , each of half-width Δm , i.e. $\mathcal{F}_2 : |m \pm 3\Delta m + nq(s)| \leq \Delta m$, see Fig. 3.1. Furthermore, all the (m, n) Fourier modes constituting signal and noise for this diagnostic lies in the intersect of regions $n \in [n_{\min}, n_{\max}]$ (purple) and $m \in [m_{\min}, m_{\max}]$ (yellow). $n_{\max} \leq N_{\varphi}/2$ and $m_{\max} \leq N_{\theta^*}$ are determined via the Nyquist limits, with N_{φ} and N_{θ^*} the number of toroidal and poloidal grid intervals, respectively³, in the FEM representation of ϕ . Given that sampling noise tends to in particular accumulate in the undamped zonal $(m, n) = (0, 0)$ component, it is interesting to separate it out from the signal. The construction of the signal-to-noise (SNR) diagnostic is thus

$$\begin{aligned} \text{signal} &= \frac{\sum_i \sum_{(m,n) \in \mathcal{F}_1} |\hat{b}_{imn}|^2}{\sum_i \sum_{(m,n) \in \mathcal{F}_1} 1}, \\ \text{signal without ZF} &= \frac{\sum_i \sum_{(m,n) \in \mathcal{F}_1 / (0,0)} |\hat{b}_{imn}|^2}{\sum_i \sum_{(m,n) \in \mathcal{F}_1 / (0,0)} 1}, \\ \text{noise} &= \frac{\sum_i \sum_{(m,n) \in \mathcal{F}_2} |\hat{b}_{imn}|^2}{\sum_i \sum_{(m,n) \in \mathcal{F}_2} 1}, \\ \text{SNR} &= \frac{\text{signal}}{\text{noise}}, \end{aligned} \quad (3.27)$$

$$\text{SNR without ZF} = \frac{\text{signal without ZF}}{\text{noise}}. \quad (3.28)$$

For ORB5 PIC simulations with $\Delta m = 5$, an SNR above the critical threshold of 10 was empirically found to be an indicative measure of the reliability of the simulated results [9, 44, 45].

3.1.4.2 Local f.s.a. weight standard deviation

The effectiveness of the adaptive control variate can be measured by estimating the standard deviation of the marker w -weights. The standard deviation indeed

³In linear simulations: $n_{\min} = n_{\max} = n$; nonlinear simulations: $n_{\min} = 0 < n_{\max}$, with $n_{\max} q(s_0)/s_0 \sim 1/\rho_*$.

provides a measure of the ratio $\|\delta f\|/\|f\|$, which should remain low for the δf -PIC scheme to be statistically advantageous over a full-PIC approach. The ultimate goal of introducing an adaptive control variate is thus to keep the standard deviation of the w -weights as low as possible throughout the simulation time. As a diagnostic, we thus calculate the standard deviation of the weights in different radial bins. Given a radial grid $\{s\}$, the i^{th} bin is defined as $s_i \leq s < s_{i+1}$, $\forall \theta^*$ and $\forall \varphi$. We then define the local weight standard deviations within each bin as follows:

$$(\sigma_w)_{\text{bin}} = \sqrt{\langle w^2 \rangle_{\text{bin}} - \langle w \rangle_{\text{bin}}^2}, \quad (3.29)$$

with $\langle w \rangle_{\text{bin}} = \sum_{p \in \text{bin}} w_p / N_{\text{bin}}$ and $\langle w^2 \rangle_{\text{bin}} = \sum_{p \in \text{bin}} w_p^2 / N_{\text{bin}}$ the expectation value of w and w^2 within that bin, respectively. Here, N_{bin} is the number of markers belonging to the bin. Note that, as the definition of w -weights given by Eq. (3.21) does not depend on the marker number N_p , one expects convergence of σ_w with N_p at a given time t .

In a collision-less PIC simulation without any dissipation, the variance of marker weights (not necessarily binned radially) will increase indefinitely due to phase space filamentation which in turn leads to increased statistical sampling noise accumulation [48]. Reaching quasi-steady state is therefore strictly speaking impossible. Even when simulations reach an apparent quasi-steady state, e.g. with roughly steady turbulent fluxes, noise continues to accumulate in higher velocity moments of δf and causes numerical problems for long times. As will be explained in Sec. 3.3, in our simulations, a dissipative term in the form of a Krook operator is used to control noise, and therefore limiting the growth of weight variance which can be seen as related to the fluctuation entropy $\delta S = \int d\Omega \delta f^2 / f_0$ [44]. For a sufficiently strong dissipation, weight variance is expected to level-off at quasi-steady state.

3.1.5 Solving the field equation with a B-spline finite element method

In ORB5, the field equations, i.e. the QNE and Ampère's law, are solved using the Galerkin formulation with B-spline finite elements. As this work considers only electrostatic dynamics, the only field equation that needs to be solved is the QNE for the electrostatic potential ϕ . Here, we will use the QNE with hybrid electrons, Eq. (2.38), as an example. The formulation for the case with fully adiabatic or drift kinetic electrons are simpler. For this discussion, we shall omit the explicit time dependence of ϕ for notation simplicity and assume one singly-charged ($Z = 1$) ion species. We first express Eq. (2.38) in the weak form, i.e. projected on a test

function $\hat{\phi}(\vec{r})$

$$\begin{aligned}
 & \int d^3r \left\{ \alpha_P \frac{en_{0e}}{T_{0e}} \left[\hat{\phi}(\vec{r}) - \langle \hat{\phi} \rangle(s) \right] \hat{\phi}(\vec{r}) + \frac{m_i n_{0i}}{eB^2} \nabla_{\perp} \hat{\phi}(\vec{r}) \cdot \nabla_{\perp} \phi(\vec{r}) \right\} \\
 = & \int d^3\Omega \left\{ \int \frac{d\alpha}{2\pi} \phi(\vec{r} + \vec{\rho}) \delta f_i(\vec{r}, v_{\parallel}, \mu) - \right. \\
 & \left. \phi(\vec{r}) \delta f_{e,T}(\vec{r}, v_{\parallel}, \mu) - \phi(\vec{r}) \delta f_{e,P}(\vec{r}, v_{\parallel}, \mu) \Big|_{(m,n)=(0,0)} \right\} \\
 \simeq & \sum_p^{N_{p,i}} \int \frac{d\alpha}{2\pi} \phi(\vec{R}_p + \vec{\rho}_p) w_{p,i} - \sum_p^{N_{p,e,T}} \phi(\vec{R}_p) w_{p,e,T} - \sum_p^{N_{p,e,P}} \phi(\vec{R}_p) \Big|_{(m,n)=(0,0)} w_{p,e,P}.
 \end{aligned} \tag{3.30}$$

Here, we have dropped the surface term resulting from the integration by parts of the ion polarisation density by assuming $\hat{\phi} = 0$ at the boundaries of the volume integration. The last equality in Eq. (3.30) is obtained using the marker representation of δf , Eq. (3.19). In the upgraded hybrid electron model, both the passing and trapped electrons have marker representation, whose weights are given by $w_{e,T}$ and $w_{e,P}$ respectively. The N_p values are the marker number for each species, which need not be equal. In the first term on the r.h.s. of Eq.(3.30), $\int d\alpha w_{p,i} \hat{\phi}(\vec{R}_p + \vec{\rho}_p)/2\pi$ represents the contribution of the p^{th} ion marker over corresponding gyro-ring $\vec{R} = \vec{R}_p + \vec{\rho}_p$. The evaluation of this quantity is done by building Larmor rings for each of the ion markers (see Sec. 3.1.6). Next, we define the B-spline finite element basis in the configuration space (s, θ^*, φ) to be

$$\Lambda_{ijk}(\vec{r}) = \Lambda_i(s) \Lambda_j(\theta^*) \Lambda_k(\varphi), \tag{3.31}$$

which is a tensor product of 1-dimensional basis functions relative to each of the three dimensions of configuration space. The number of Λ basis functions for each of the s -, θ^* - and φ -dimensions are N_s , N_{θ^*} and N_{φ} respectively. We then express the electrostatic potential ϕ in the space spanned by this basis

$$\phi(\vec{r}) = \sum_{i'=1}^{N_s+N_{\text{spl}}} \sum_{j'=1}^{N_{\theta^*}+N_{\text{spl}}} \sum_{k'=1}^{N_{\varphi}+N_{\text{spl}}} \bar{\phi}_{i'j'k'} \Lambda_{i'j'k'}(\vec{r}), \tag{3.32}$$

where $\bar{\phi}_{i'j'k'}$ are the coefficients of this decomposition. For this work, B-spline elements of order $N_{\text{spl}} = 3$ are considered. For the Galerkin approach, the test functions will be the same set as the basis functions: $\hat{\phi} = \Lambda_{ijk}(\vec{r})$. Continuing the development of Eq. (3.30) with this choice of $\hat{\phi}$ along with Eq. (3.32), using $I = (ijk)$ and $I' = (i, j', k')$ to lighten notation, leads to

$$\begin{aligned}
 & \sum_{I'} \int d^3r \left\{ \alpha_P \frac{en_{0e}}{T_{0e}} [\Lambda_{I'}(\vec{r}) - \langle \Lambda_{I'} \rangle(s)] \Lambda_I(\vec{r}) + \frac{m_i n_{0i}}{eB^2} \nabla_{\perp} \Lambda_{I'}(\vec{r}) \cdot \nabla_{\perp} \Lambda_I(\vec{r}) \right\} \bar{\phi}_{I'} \\
 = & \int \frac{d\alpha}{2\pi} \sum_p^{N_{p,i}} \Lambda_I(\vec{R}_p + \vec{\rho}_p) w_{p,i} - \sum_p^{N_{p,e,T}} \Lambda_I(\vec{R}_p) w_{p,e,T} - \sum_p^{N_{p,e,P}} \Lambda_I(\vec{R}_p) \Big|_{(m,n)=(0,0)} w_{p,e,P},
 \end{aligned} \tag{3.33}$$

which, defining b_I the r.h.s. of Eq. (3.33), can be expressed as a linear system to be solved for the B-spline coefficients $\bar{\phi}_{I'}$,

$$\sum_{I'} F_I^{I'} \bar{\phi}_{I'} = b_I, \quad (3.34)$$

To take advantage of the periodicity of the (θ^*, φ) -dimensions, we perform a discrete Fourier transform of Eq. (3.34). This in particular involves taking the DFT of the r.h.s. :

$$\begin{aligned} \hat{b}_{imn} &= \frac{1}{N_{\theta^*} N_{\varphi}} \sum_{j=0}^{N_{\theta^*} + N_{\text{spl}} - 1} \sum_{k=0}^{N_{\varphi} + N_{\text{spl}} - 1} b_{ijk} \exp \left[-2\pi i \left(\frac{mj}{N_{\theta^*}} + \frac{nk}{N_{\varphi}} \right) \right] \\ &= \int \frac{d\alpha}{2\pi} \sum_p^{N_{p,i}} \hat{\Lambda}_{imn}(\vec{R}_p + \vec{\rho}_p) w_{p,i} - \\ &\quad \sum_p^{N_{p,e,T}} \hat{\Lambda}_{imn}(\vec{R}_p) w_{p,e,T} - \sum_p^{N_{p,e,P}} \delta_{(0,0)}^{(mn)} \hat{\Lambda}_{imn}(\vec{R}_p) w_{p,e,P}, \end{aligned}$$

where m and n stand for the poloidal and toroidal Fourier mode numbers. $\hat{\Lambda}_{imn}$ is the discrete Fourier transform of the B-spline basis function in the poloidal and toroidal spline indices

$$\hat{\Lambda}_{imn} = \frac{1}{N_{\theta^*} N_{\varphi}} \sum_{j=0}^{N_{\theta^*} + N_{\text{spl}} - 1} \sum_{k=0}^{N_{\varphi} + N_{\text{spl}} - 1} \Lambda_{ijk} \exp \left[-2\pi i \left(\frac{mj}{N_{\theta^*}} + \frac{nk}{N_{\varphi}} \right) \right],$$

and $\delta_{(0,0)}^{(mn)}$ is the Kronecker delta. Eq. (3.34) then transforms to

$$\sum_{i'm'n'} \hat{F}_{imn}^{i'm'n'} \bar{\phi}_{i'm'n'} = \hat{b}_{imn}, \quad (3.35)$$

with

$$\hat{F}_{imn}^{i'm'n'} = \frac{1}{N_{\theta^*} N_{\varphi}} \sum_{j,j'=0}^{N_{\theta^*} + N_{\text{spl}} - 1} \sum_{k,k'=0}^{N_{\varphi} + N_{\text{spl}} - 1} F_{ijk}^{i'j'k'} \exp \left[-2\pi i \left(\frac{mj}{N_{\theta^*}} + \frac{nk}{N_{\varphi}} \right) \right] \cdot \exp \left[2\pi i \left(\frac{m'j'}{N_{\theta^*}} + \frac{n'k'}{N_{\varphi}} \right) \right].$$

Before solving Eq. (3.35) for $\bar{\phi}_{I'}$, a Fourier filter (see Sec. 3.1.4.1) is applied to both sides of Eq. (3.35). Taking the r.h.s. of Eq. (3.35) as an example, this means that

$$\hat{b}_{imn} \rightarrow \begin{cases} \hat{b}_{imn} & \text{for } |m + nq(s_i)| \leq \Delta m \\ 0 & \text{else,} \end{cases}$$

with s_i the radial coordinate that represents the radial position where the B-spline element $\Lambda_i(s)$ is centred.

This section is an overview of the solution method of the QNE. For a more detailed discussion, including evaluation of $F_I^{I'}$, toroidal mode parallelisation, and implementation of the upgrade hybrid electron model, the interested reader is invited to consult Refs. [8, 43, 54, 64].

3.1.6 Overview of ORB5

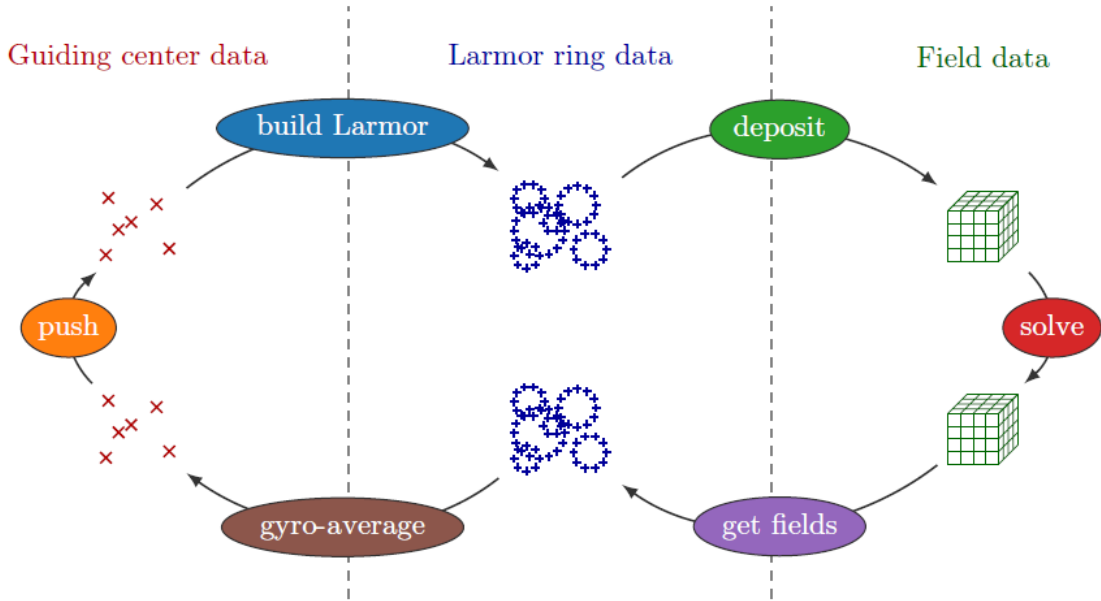


Figure 3.2: Overview of the ORB5 algorithm for 1 sub-step of a 4th order explicit Runge-Kutta (RK4) scheme. \times and $+$ represent marker data structure (gyro-centre and Larmor points respectively), and cubes represent fields on grid structure. Figure taken from Ref. [64].

Here, we briefly describe how the ORB5 code advances each species' distribution function f in a single time step. For more in-depth analysis, the interested reader is encouraged to read the theses [43, 52, 64]. A thorough overview is given in Ref. [54].

The sequence of operations in the time loop for evolving the markers according to the gyrokinetic Eqs. (2.18)-(2.20) is illustrated in Fig. 3.2. We begin the description of the time loop just after the pushing of markers. At this point the goal is to form the self-consistent fields, which requires the calculation of the gyrodensities (see Eq. (2.34)). To that end, the weight of each marker is uniformly distributed on N_L points on a Larmor ring ('build Larmor'). These rings have as centres the marker positions \vec{R}_p , and radii $\vec{\rho}_L$ determined by the markers' magnetic moment μ_p . N_L is determined in such a way as to ensure the distance between points on the circumference is roughly constant, and is thus dependent on the Larmor radius with the additional constraint of never being set below a minimum 4. For this work, the Larmor rings, a priori perpendicular to the magnetic field, are approximated to lie in the poloidal plane. After this, the $N_p \times N_L$ points are deposited ('deposit') on a 3-dimensional grid in (s, θ^*, φ) and the corresponding gyrodensities finally computed. Having formed the r.h.s., the QNE is back-solved ('solve') for the electrostatic potential ϕ . The process of back-solving involves the projection of the QNE on finite elements, and applying a Fourier filter (see Fig. 3.1). The subsequent remaining operations leading up to the marker push involves forming the gyroaveraged potential $\tilde{\phi}$ evaluated at marker positions, which is required in both Eqs. (2.18) and (2.19). The step 'get fields' evaluates the ϕ represented by FEM at the previous N_L Larmor points belonging to each marker. The 'gyro-average' operation appears as the reverse of 'build Larmor', that assigns the average of ϕ over the Larmor ring to its centre. Finally, each marker phase-space coordinate \vec{Z}_p is pushed via an explicit

RK4 scheme ('push'). To complete a full RK4 step, the whole cycle of Fig. 3.2 is repeated four times, one for each RK4 sub-step.

3.2 Adaptive background scheme

3.2.1 Motivation and idea

Let us start considering the estimator with the control variate, Eq. (3.7), as well as Eq. (2.27). As ORB5 is a δf PIC code, one may make use of the initial function f_{init} as control variate to δf . Such an estimator gives low variance values so long as the delta-f assumption Eq. (3.8) holds. In simulations describing collision-less physics, the canonical Maxwellian distribution give by Eq. (2.33), which is stationary state to the Vlasov Eq. (2.24), is usually considered as the initial distribution f_{init} . In this case Eq. (3.7) becomes:

$$\begin{aligned}\bar{I}_f &= \bar{I}_{\delta f} + I_{\text{init}}, \\ \bar{I}_{\delta f} &= \frac{1}{N_p} \sum_{p=1}^{N_p} \delta f(\vec{Z}_p, t) A(\vec{Z}_p),\end{aligned}\tag{3.36}$$

which one expects to be a good estimator⁴. The explicit evaluation of Eq. (3.36) using the Klimontovich distribution is given by Eq. (3.18).

For a typical flux-driven simulation, profiles exhibit $\mathcal{O}(1)$ deviation w.r.t. their initial values over transport time scales. Furthermore, $\mathcal{O}(1)$ variations of f are also found at the plasma edge, characterised by strong profile gradients where the relative fluctuation amplitude of density is high. Such situations lead to the violation of Eq. (3.8), and thus render the estimator defined by Eq. (3.36) inappropriate.

We now consider the possibility of a time-dependent control variate $f_0(\vec{Z}, t)$ with $f_0(\vec{Z}, 0) = f_{\text{init}}$, so that $f = f_0(t) + \delta f$ and revising our estimator of Eq. (3.7) to be

$$\begin{aligned}\bar{I}'_f &= \frac{1}{N_p} \sum_{p=1}^{N_p} \{ f(\vec{Z}_p, t) A(\vec{Z}_p) - [f_0(\vec{Z}_p, t) A(\vec{Z}_p) - \mathbf{E}[f_0 A](t)] \} = I_{\text{init}} + \bar{I}'_{\delta f} \\ \implies \bar{I}'_{\delta f} &= \frac{1}{N_p} \sum_{p=1}^{N_p} \{ f(\vec{Z}_p, t) A(\vec{Z}_p) - [f_0(\vec{Z}_p, t) A(\vec{Z}_p) - \mathbf{E}[f_0 A](t)] \} - \mathbf{E}[f_0 A](0),\end{aligned}\tag{3.37}$$

with $\mathbf{E}[f_0 A](0) = I_{\text{init}}$. Eq. (3.37) clearly reduces to Eq. (3.36) for a stationary control variate, i.e. $f_0(\vec{Z}, t) = f_{\text{init}}(\vec{Z})$. Defining $f_0(\vec{Z}, t) = f_0(\vec{Z}, 0) + \Delta f_0(\vec{Z}, t)$, we

⁴We have $\hat{I}_{\text{init}} = I_{\text{init}}$ as we assume that \tilde{f}_{init} can be analytically integrated, without the use of an estimator.

continue the development of Eq. (3.37),

$$\begin{aligned}
 \bar{I}'_{\delta f} &= \frac{1}{N_p} \sum_{p=1}^{N_p} \{ f_{\text{init}}(\vec{Z}_p) A(\vec{Z}_p) + \delta f(\vec{Z}_p, t) A(\vec{Z}_p) - [f_0(\vec{Z}_p, t) A(\vec{Z}_p) - \mathbf{E}[f_0 A](t)] \} - \\
 &\quad \mathbf{E}[f_0 A](0) \\
 &= \frac{1}{N_p} \sum_{p=1}^{N_p} \{ \delta f(\vec{Z}_p, t) A(\vec{Z}_p) + f_0(\vec{Z}_p, 0) A(\vec{Z}_p) - f_0(\vec{Z}_p, t) A(\vec{Z}_p) \} + \mathbf{E}[\Delta f_0 A](t) \\
 &= \frac{1}{N_p} \sum_{p=1}^{N_p} \{ \delta f(\vec{Z}_p, t) A(\vec{Z}_p) - \Delta f_0(\vec{Z}_p, t) A(\vec{Z}_p) \} + \mathbf{E}[\Delta f_0 A](t). \tag{3.38}
 \end{aligned}$$

Comparing Eq. (3.38) with Eq. (3.36), if we identify

$$\delta f'(\vec{Z}, t) = \delta f(\vec{Z}, t) - \Delta f_0(\vec{Z}, t), \tag{3.39}$$

so that for our new problem becomes

$$\bar{I}'_{\delta f} = \frac{1}{N_p} \sum_{p=1}^{N_p} \delta f'(\vec{Z}_p, t) A(\vec{Z}_p) + \mathbf{E}[\Delta f_0 A](t), \tag{3.40}$$

with variance

$$\mathbf{Var}[\bar{I}'_{\delta f}] = \frac{\mathbf{Var}[\delta f' A]}{N}. \tag{3.41}$$

Therefore, for a fixed marker number N_p , we can reduce the variance Eq. (3.41) of the new estimate by continuously ‘adapting’ f_0 in Eq. (3.39) to minimise $\mathbf{Var}[\delta f' A]$.

3.2.2 Starting equations

In this work, the approach of a time-dependent control variate is to only address the relaxation of profiles in the core, not in the case of $\mathcal{O}(1)$ fluctuations at the edge⁵. Allowing for $\mathcal{O}(1)$ variations of the background, assuming near-Maxwellian, we consider as time-dependent control variate to be

$$f_0(\vec{Z}, t) = f_M(\vec{Z}, t) = \frac{n_0(\psi, t)}{[2\pi T_0(\psi, t)/m]^{3/2}} \exp \left[-\frac{[v_{\parallel} - u_0(\psi, t)]^2/2 + \mu B(s, \theta^*)}{T_0(\psi, t)/m} \right]. \tag{3.42}$$

The subscript 0 denotes background⁶ quantities, and the n_0 , u_0 and T_0 are the f.s.a. gyrocentre background density, parallel velocity and temperature, respectively. With such an evolving control variate, the full distribution f is separated via the delta-f splitting

$$f = f_0 + \delta f. \tag{3.43}$$

⁵This is due to the fast time scales of high relative fluctuation amplitudes. No suitable control variate is thus available at any one period of time, unless the time step-size is severely limited

⁶The control variate does not necessarily correspond to the physical background. A discussion follows in Sec. 3.2.9.

Given f , this relation alone clearly does not uniquely set f_0 of the form Eq. (3.42), in other words $n_0(\psi, t)$, $u_0(\psi, t)$ and $T_0(\psi, t)$ remain undetermined. So as to avoid a secular growth of δf as a result of density and temperature profile relaxation as well as form the possible development of parallel flow, one could uniquely define the separation Eq. (3.43) by imposing the three constraints on δf :

$$\left\langle \int d^3v \delta f \begin{bmatrix} 1 \\ v_{\parallel} \\ v^2/2 \end{bmatrix} \right\rangle = 0, \quad (3.44)$$

In other words, allowing no growth in δf of f.s.a. mass, parallel momentum or kinetic energy. In this case, taking the same velocity moments and f.s.a. of Eq. (3.43) one then obtains

$$\begin{aligned} \left\langle \int d^3v f \right\rangle &= \left\langle \int d^3v f_0 \right\rangle = n_0 \left(1 + \frac{\hat{b} \cdot \nabla \times \hat{b}}{\Omega_c} u_0 \right) \\ \left\langle \int d^3v v_{\parallel} f \right\rangle &= \left\langle \int d^3v v_{\parallel} f_0 \right\rangle = n_0 \left[u_0 + \frac{\hat{b} \cdot \nabla \times \hat{b}}{\Omega_c} \left(\frac{T_0}{m} + u_0^2 \right) \right] \\ \left\langle \int d^3v \frac{v^2}{2} f \right\rangle &= \left\langle \int d^3v \frac{v^2}{2} f_0 \right\rangle = n_0 \left[\frac{3T_0}{2m} + \frac{u_0^2}{2} + \frac{\hat{b} \cdot \nabla \times \hat{b}}{\Omega_c} u_0 \left(\frac{5T_0}{2m} + \frac{u_0^2}{2} \right) \right], \end{aligned}$$

with terms multiple of $\hat{b} \cdot \nabla \times \hat{b}/\Omega_c$ appearing due to the velocity Jacobian (see Eqs. (2.22) and (2.23)). This clearly providing a set of three equations uniquely defining $n_0(\psi, t)$, $u_0(\psi, t)$ and $T_0(\psi, t)$. Such a rigid separation of f into f_0 and δf may be difficult to implement in practice. It is in fact advantageous to make use of the flexibility of the separation Eq. (3.43) and consider evolution equations for $n_0(\psi, t)$, $u_0(\psi, t)$ and $T_0(\psi, t)$, resulting from progressively feeding into the control variate any non-zero growth in δf of one of the three velocity moments on the r.h.s. of Eq. (3.44) as follows:

$$\begin{aligned} \frac{\partial}{\partial t} \left\{ n_0 \left(1 + \frac{\hat{b} \cdot \nabla \times \hat{b}}{\Omega_c} u_0 \right) \right\} &= \alpha_n \left\langle \int d^3v \delta f \right\rangle, \\ \frac{\partial}{\partial t} \left\{ n_0 \left[u_0 + \frac{\hat{b} \cdot \nabla \times \hat{b}}{\Omega_c} \left(\frac{T_0}{m} + u_0^2 \right) \right] \right\} &= \alpha_u \left\langle \int d^3v v_{\parallel} \delta f \right\rangle, \\ \frac{\partial}{\partial t} \left\{ n_0 \left[\frac{3T_0}{2m} + \frac{u_0^2}{2} + \frac{\hat{b} \cdot \nabla \times \hat{b}}{\Omega_c} u_0 \left(\frac{5T_0}{2m} + \frac{u_0^2}{2} \right) \right] \right\} &= \alpha_E \left\langle \int d^3v \frac{v^2}{2} \delta f \right\rangle. \end{aligned}$$

We now make a further simplification by dropping terms proportional to $\hat{b} \cdot \nabla \times \hat{b}/\Omega_c$, as it is predominantly small except near the magnetic axis (see Fig. 3.3) where fluctuations are also expected to be small. We therefore have

$$\frac{\partial n_0}{\partial t}(\psi, t) = \alpha_n Q_n(\psi, t), \quad (3.45)$$

$$\frac{\partial n_0 u_0}{\partial t}(\psi, t) = \alpha_u Q_u(\psi, t), \quad (3.46)$$

$$\frac{\partial}{\partial t} \left\{ \frac{3n_0 T_0}{2m} + \frac{1}{2} n_0 u_0^2 \right\}(\psi, t) = \alpha_E Q_E(\psi, t), \quad (3.47)$$

where we have made the assignment

$$Q_n = \left\langle \int d^3v \delta f \right\rangle, \quad Q_u = \left\langle \int d^3v v_{\parallel} \delta f \right\rangle, \quad Q_E = \left\langle \int d^3v \frac{v^2}{2} \delta f \right\rangle.$$

For notation simplicity for subsequent discussions, we define the l.h.s. of Eq. (3.47) as the time derivative of the kinetic energy (per mass)

$$E_{\text{kin}0} = \frac{3n_0T_0}{2m} + \frac{1}{2}n_0u_0^2. \quad (3.48)$$

We notice that Eqs. (3.45)-(3.47) for n_0 , u_0 and T_0 are coupled. Two methods of solution are used in this work, and are sketched in Sec. 3.2.3 and 3.2.4. Common to both methods is that the r.h.s. of Eqs. (3.45)-(3.47), i.e. $\{Q\}$ are time averaged (see Eq. (3.59)). Therefore, we set a time averaging window of duration $N_t\Delta t$, consisting of N_t time steps, in which $\{Q\}$ are accumulated in these N_t steps, and will be divided by N_t after. Eqs. (3.45)-(3.47) are then solved as an explicit Euler scheme of step size $N_t\Delta t$.

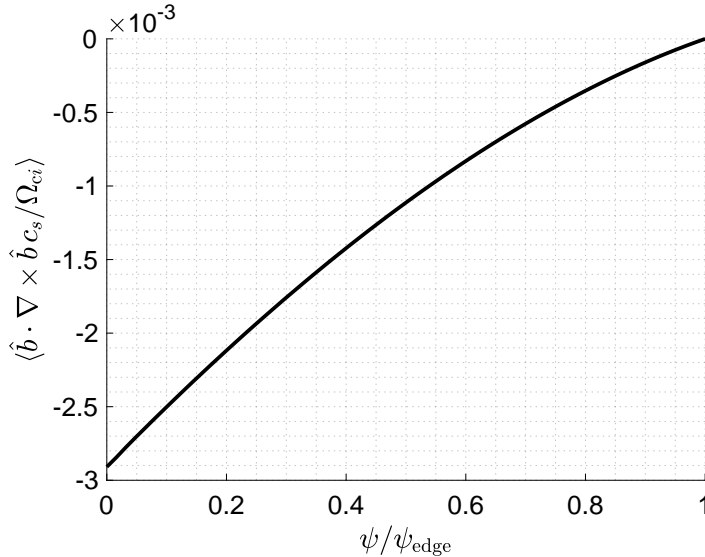


Figure 3.3: Flux-surface-averaged of $\hat{b} \cdot \nabla \times \hat{b} / \Omega_c$ for the singly charged ion, for the magnetic equilibrium geometry used in this thesis, i.e. TCV shot #43516.

3.2.3 Interleaved scheme

Equations (3.45)-(3.47) are solved sequentially. Such an execution is carried out throughout the simulation. Below is one cycle for the adaptation of the background gyrocentre density, parallel flow, and temperature, which spans a total time of $3N_t\Delta t$:

1. $Q_n \leftarrow 0$, do N_t time steps:
 - Advance markers according to Eqs. (2.18)-(2.20)
 - Estimate Q_n and accumulate
2. Calculate time averaged $Q_n \leftarrow Q_n / N_t$

3. Solve for $n_0^{(\text{new})} \leftarrow n_0 + \alpha_n N_t \Delta t Q_n$
4. $Q_u \leftarrow 0$, do N_t time steps:
 - Advance markers according to Eqs. (2.18)-(2.20)
 - Estimate Q_u and accumulate
5. Calculate time averaged $Q_u \leftarrow Q_u/N_t$
6. Solve for $u_0^{(\text{new})} \leftarrow u_0 + \alpha_n (N_t \Delta t Q_u)/n_0^{(\text{new})}$
7. $Q_E \leftarrow 0$, do N_t time steps:
 - Advance markers according to Eqs. (2.18)-(2.20)
 - Estimate Q_E and accumulate
8. Calculate time averaged $Q_E \leftarrow Q_E/N_t$
9. Solve for $T_0^{(\text{new})} \leftarrow T_0 + \Delta T_0$:

$$\begin{aligned} \frac{3n_0^{(\text{new})}}{2m} \frac{\partial T_0}{\partial t} + \frac{1}{2} n_0^{(\text{new})} (u_0^{(\text{new})})^2 &= \alpha_E Q_E \\ \implies \frac{3n_0^{(\text{new})}}{2m} \Delta T_0 &= \left[\alpha_E Q_E - \frac{1}{2} n_0^{(\text{new})} (u_0^{(\text{new})})^2 \right] N_t \Delta t \\ \Delta T_0 &= \frac{2m}{3n_0^{(\text{new})}} \left[\alpha_E Q_E - \frac{1}{2} n_0^{(\text{new})} (u_0^{(\text{new})})^2 \right] N_t \Delta t. \end{aligned}$$

3.2.4 Simultaneous scheme

Let us reconsider $Q_u = \langle \int d^3v v_{\parallel} \delta f \rangle$. It can be the case that even when δf has no parallel flow component δu , the existence of density perturbations δn , could contribute to $Q_u \neq 0$, thus leading to a change in u_0 if one naively applies #6 of the above scheme. This can also happen to the incorrect adaptation of T_0 due to nonzero δn and δu , which leads to $Q_E \neq 0$. The interleaved scheme can thus lead to distortion in the background profiles with time, as is demonstrated in App. C. Therefore, we seek to determine the individual components δn , δu and δT in terms of $\{Q\}$, and only consider these measures for the adaptation of n_0 , u_0 and T_0 respectively. Specifically, we seek background adaptive scheme of the form:

$$\frac{\partial n_0}{\partial t} = \alpha_n \langle \delta n \rangle, \quad \frac{\partial u_0}{\partial t} = \alpha_u \langle \delta u \rangle, \quad \frac{\partial T_0}{\partial t} = \alpha_E \left\langle \frac{\delta T}{m} \right\rangle.$$

Note that in this discussion all background profiles are flux-surface-averaged. To that end, we begin with the delta-f splitting: $f = f_0 + \delta f$, and seek to determine $\langle \delta n \rangle$, $\langle \delta u \rangle$, and $\langle \delta T \rangle$. Taking the 0th-order velocity moment, and then flux-surface-averaging for the density:

$$\langle n \rangle = n_0 + \langle \delta n \rangle, \quad (3.49)$$

and therefore,

$$\langle \delta n \rangle = Q_n.$$

For the next two velocity moments, for algorithmic simplicity we shall express them in the total f.s.a. density $\langle n \rangle$, as it is involved in higher order velocity moments and is invariant throughout the f.s.a. adaptation process. Taking the 1st-order velocity moment and subsequently flux-surface-averaging for the parallel flow:

$$\begin{aligned} nu &= (n_0 + \delta n)(u_0 + \delta u) \\ &= n_0 u_0 + \delta n u_0 + n \delta u \\ \langle nu \rangle &= n_0 u_0 + u_0 Q_n + \langle n \delta u \rangle, \end{aligned}$$

and therefore

$$\begin{aligned} Q_u &= u_0 Q_n + \langle n \delta u \rangle \\ \langle n \delta u \rangle &= Q_u - u_0 Q_n. \end{aligned} \quad (3.50)$$

Finally, for the 2nd-order velocity moment for the kinetic energy (per mass):

$$\begin{aligned} E_{\text{kin}} &= \frac{3}{2}(n_0 + \delta n) \left(\frac{T_0}{m} + \frac{\delta T}{m} \right) + \frac{1}{2}(n_0 + \delta n)(u_0 + \delta u)^2 \\ &= \frac{3}{2}n_0 \frac{T_0}{m} + \frac{1}{2}n_0 u_0^2 + \left(\frac{3}{2} \frac{T_0}{m} + \frac{1}{2} u_0^2 \right) \delta n + n u_0 \delta u + \frac{1}{2}n(\delta u)^2 + \frac{3}{2}n \frac{\delta T}{m}, \end{aligned}$$

and taking the flux-surface-average, and subsequently using Eq. (3.50) therefore leads to

$$\begin{aligned} Q_E &= \left(\frac{3}{2} \frac{T_0}{m} + \frac{1}{2} u_0^2 \right) Q_n + u_0 \langle n \delta u \rangle + \frac{1}{2} \langle n (\delta u)^2 \rangle + \frac{3}{2} \left\langle n \frac{\delta T}{m} \right\rangle \\ &= \left(\frac{3}{2} \frac{T_0}{m} + \frac{1}{2} u_0^2 \right) Q_n + u_0 (Q_u - u_0 Q_n) + \frac{1}{2} \left\langle \frac{(Q_u - u_0 Q_n)^2}{n} \right\rangle + \frac{3}{2} \left\langle n \frac{\delta T}{m} \right\rangle \\ \frac{3}{2} \left\langle n \frac{\delta T}{m} \right\rangle &= Q_E - \left(\frac{3}{2} \frac{T_0}{m} - \frac{1}{2} u_0^2 \right) Q_n - u_0 Q_u - \frac{1}{2} \frac{(Q_u - u_0 Q_n)^2}{\langle n \rangle}. \end{aligned} \quad (3.51)$$

In order to isolate $\langle \delta u \rangle$ in Eq. (3.50) and $\langle \delta T \rangle$ in Eq. (3.51), we make the approximation:

$$\begin{aligned} \langle \delta u \rangle &\approx \frac{Q_u - u_0 Q_n}{\langle n \rangle}, \\ \left\langle \frac{\delta T}{m} \right\rangle &\approx \frac{2}{3 \langle n \rangle} \left[Q_E - \left(\frac{3}{2} \frac{T_0}{m} - \frac{1}{2} u_0^2 \right) Q_n - u_0 Q_u - \frac{1}{2} \frac{(Q_u - u_0 Q_n)^2}{\langle n \rangle} \right]. \end{aligned} \quad (3.52)$$

Therefore, the following is one cycle for the adaptation of all three moments, which spans time $N_t \Delta t$:

1. $Q_n, Q_u, Q_E \leftarrow 0$, do N_t time steps:
 - Advance markers according to Eqs. (2.18)-(2.20)
 - Estimate Q_n, Q_u, Q_E and accumulate individually
2. Calculate time averages: $Q_n \leftarrow Q_n/N_t$, $Q_u \leftarrow Q_u/N_t$, $Q_E \leftarrow Q_E/N_t$

3. Calculate the correction terms:

$$\begin{aligned}\epsilon_u &\leftarrow -Q_n u_0 \\ \epsilon_E &\leftarrow -\left(\frac{3T_0}{2m} - \frac{1}{2}u_0^2\right) Q_n - u_0 Q_u - \frac{1}{2} \frac{(Q_u - u_0 Q_n)^2}{\langle n \rangle}\end{aligned}$$

4. Solve for $n_0^{(\text{new})} \leftarrow n_0 + \alpha_n N_t \Delta t Q_n$

5. Solve for $u_0^{(\text{new})} \leftarrow u_0 + \alpha_u N_t \Delta t (Q_u + \epsilon_u) / \langle n \rangle$

6. Solve for $T_0^{(\text{new})} \leftarrow T_0 + 2m\alpha_E N_t \Delta t (Q_E + \epsilon_E) / (3 \langle n \rangle)$

An alternative simultaneous scheme which does not involve the approximation Eq. (3.52) is presented in App. A. This alternative scheme did not show distinguishable results of Chs. 5 and 6 from the one presented here.

3.2.5 Application to a canonical Maxwellian as control variate

The adapted background profiles n_0 and T_0 obtained by integrating Eqs. (3.45) and (3.54) are expressed as a function of ψ (used in Ch. 5). However, this work also uses the *canonical* Maxwellian function as a control variate (for Ch. 6), i.e.

$$f_0(\vec{Z}, t) = \frac{n_0(\hat{\psi}_0, t)}{[2\pi T_0(\hat{\psi}_0, t)/m]^{3/2}} \exp\left[-\frac{[v_{\parallel} - u_0(\hat{\psi}_0, t)]^2/2 + \mu B(s, \theta^*)}{T_0(\hat{\psi}_0, t)/m}\right]. \quad (3.53)$$

Note that for this work $u_0(\hat{\psi}_0, 0) = 0$, thus at initial time Eq. (3.53) is still close to the gyrokinetic equilibrium of the unperturbed system, i.e. $f_0 \sim f_0(\hat{\psi}_0, \mathcal{E}, t)$ (see Sec. 2.4). In order to be able to use the canonical Maxwellian function as an adaptive control variate, we make the following assignments after solving Eqs. (3.45) and (3.54):

$$n_0(\hat{\psi}_0, t) \leftarrow n_0(\psi, t), \quad u_0(\hat{\psi}_0, t) \leftarrow u_0(\psi, t), \quad T_0(\hat{\psi}_0, t) \leftarrow T_0(\psi, t).$$

That is, the adapted canonical background profiles acquire the same functional form as that of the local profiles under the adaptive scheme. Note that a canonical Maxwellian with $n_0(\hat{\psi}_0, t)$ and $T_0(\hat{\psi}_0, t)$ reduces to a local Maxwellian with $n_0(\psi, t)$ and $T_0(\psi, t)$ in the limit $\rho_* \rightarrow 0$. This assignment slightly distorts the effective background gyrocentre density and temperature profiles, which are no longer simple magnetic flux functions but also acquire some poloidal angle dependence.

The reader is reminded that there is some flexibility in the choice of the background adaptation which is thus not unique. As long as the adaptation leads to a reduction in variance according to Eq. (3.41), the adaptive scheme will prove to have served its purpose.

3.2.6 No parallel flow adaptation

For the work done in this thesis, we will not consider any background parallel flow profile adaptation, $\alpha_u = 0$. The Maxwellian background is thus assumed having parallel velocity $u_0 = 0$. We further assume that

$$\left\langle \int d^3v v_{\parallel} \delta f \right\rangle(\psi, t) \ll \delta n(\psi, t) v_{\text{th}}(\psi, t)$$

on every ψ -surface. Under this assumption, the background is limited to the adaptation of its density and temperature profiles, and simplifies to

$$\frac{\partial}{\partial t} \left\{ \frac{3n_0 T_0}{2m} \right\} = \alpha_E Q_E. \quad (3.54)$$

Furthermore Steps #4-#6 and Step #5 are skipped for the interleaved and simultaneous schemes respectively.

3.2.7 Implementation of the adaptive scheme

Here, we discuss the implementation for the temperature adaptation scheme considering a density profile that is fixed in time. The adaptation scheme for the density is analogous. Consider two time-stamps t_i and $t_j = t_i + N_t \Delta t$, with an arbitrary time interval $N_t \Delta t$ (see Eq. (3.59)). The change in the temperature is done via the time-dependent background f.s.a. kinetic energy density, defined to be

$$E_{\text{kin0}}(\psi, t_j) - E_{\text{kin0}}(\psi, t_i) = \sum_{k=1}^{N_{\psi} + N_{\text{spl}}} \xi_k \Lambda_k(s),$$

where the change in E_{kin0} from $t = t_i$ to $t = t_j$ is expanded in terms of N_{spl} -order B-splines in the radial coordinate s , $\{\Lambda(s)\}$, with coefficients $\{\xi\}$ which need to be solved. The radial resolution is set by N_{ψ} , the number of radial intervals. Then, discretising Eq. (3.54) in time using a forward-Euler approach (first order accurate in t) leads to

$$\sum_{k=1}^{N_{\psi} + N_{\text{spl}}} \xi_k \Lambda_k(s) = \alpha_E N_t \Delta t \left\langle \int d^3v \frac{v^2}{2} \delta f(\vec{Z}, t_i) \right\rangle. \quad (3.55)$$

In order to solve Eq. (3.55) for $\{\xi\}$, consider the objective function O parameterised by τ ,

$$O(\{\xi\}, \tau) = \int d^3R \left\{ \frac{1}{2} \left(\alpha_E N_t \Delta t \left\langle \int d^3v \frac{v^2}{2} \delta f(\vec{Z}, t_i) \right\rangle - \sum_{k=1}^{N_{\psi} + N_{\text{spl}}} \xi_k \Lambda_k(s) \right)^2 + \frac{\tau}{2} \left(\sum_{k=1}^{N_{\psi} + N_{\text{spl}}} \xi_k \Lambda_k''(s) \right)^2 \right\}, \quad (3.56)$$

with $d^3R = J_s ds d\theta^* d\varphi$ representing the configuration space volume differential, and using the prime notation for the derivative of a function with respect to the

argument. Eq. (3.56) represents the error for the representation of Eq. (3.55), and τ is introduced as a penalty factor for the tension. This introduces smoothing into the background profile change. Now, minimising the error w.r.t. $\{\xi\}$ leads to

$$\begin{aligned}
 \frac{\partial \mathcal{O}}{\partial \xi_k} &= 0, \quad \forall k \\
 \sum_{k=1}^{N_\psi + N_{\text{spl}}} M_{lk}(\tau) \xi_k &= \alpha_E N_t \Delta t \int d^3 R \Lambda_l(s) \left\langle \int d^3 v \frac{v^2}{2} \delta f(\vec{Z}, t_i) \right\rangle \\
 &= \alpha_E N_t \Delta t \int d^3 R \Lambda_l(s) \frac{\int d\theta^* d\varphi J_s(s, \theta^*, \varphi) \int d^3 v v^2 / 2 \delta f(\vec{Z}, t_i)}{\int d\theta^{*\prime} d\varphi'' J_s(s, \theta^{*\prime})} \\
 &= \alpha_E N_t \Delta t \int d^3 R \Lambda_l(s) \int d^3 v \frac{v^2}{2} \delta f(\vec{Z}, t_i) \\
 &= \alpha_E N_t \Delta t \int d\Omega \Lambda_l(s) \frac{v^2}{2} \delta f(\vec{Z}, t_i),
 \end{aligned}$$

which can be written in compact matrix notation:

$$\mathbb{M}(\tau) \vec{\xi} = \vec{h}, \quad (3.57)$$

with solution $\vec{\xi} = \mathbb{M}^{-1} \vec{h}$. In the above relations, we have defined the matrix \mathbb{M} as the vector \vec{h} w.r.t. elements

$$\begin{aligned}
 M_{lk}(\tau) &= \int d^3 R \{ \Lambda_l(s) \Lambda_k(s) + \tau \Lambda_l''(s) \Lambda_k''(s) \}, \\
 h_l &= \alpha_E N_t \Delta t \int d\Omega \Lambda_l(s) \frac{v^2}{2} \delta f(\vec{Z}, t_i).
 \end{aligned}$$

Here, \mathbb{M} is the ‘mass matrix’ for the one-dimensional radial B-splines modified by the smoothing term (if $\tau \neq 0$). The integrals required for computing the coefficients are done based on the marker representation of δf , while the integral of M_{kl} is calculated via Gauss-Legendre quadratures. The B-spline expansion in Eq. (3.55) is represented on a uniformly spaced $\psi(s)$ -grid, which thus corresponds to a non-uniform grid in s with decreasing interval size going from the magnetic axis towards the plasma edge. This representation enables improved marker count per interval near the magnetic axis $\psi = 0$.

3.2.7.1 Homogeneous Neumann boundary condition on axis

We first transform the first B-spline elements near $s = 0$ from $\{\Lambda(s)\}_i^N$ to $\{\hat{\Lambda}(s)\}_j^{N'}$ so that functions expanded in such a set $\{\hat{\Lambda}(s)\}_j^{N'}$, $N' < N$ can conveniently be imposed the homogeneous Neumann boundary condition at $s = 0$. Such a condition reflects the continuity of the derivative of profiles across the magnetic axis. The transformation matrix \mathbb{C} ,

$$\hat{\Lambda}_i(s) = \sum_j^N C_{ij}^{(d)} \Lambda_j(s) \quad \forall i,$$

depends on the B-spline order d . Namely, for $d = 2, 3$,

$$\begin{aligned}\mathbb{C}^{(2)} &= \begin{bmatrix} 1 & 0 \\ 1 & 1 \end{bmatrix} \\ \mathbb{C}^{(3)} &= \begin{bmatrix} 1 & 0 & 0 \\ 0 & 1 & 0 \\ 1 & 0 & 1 \end{bmatrix}.\end{aligned}$$

Such transformation leaves only the first transformed element having non-zero derivative at $s = 0$, whose associated expansion coefficient will be set to zero.

The solution to $\{\xi\}$ of Eq. (3.57) is as follows. Firstly, the coefficients $\{\xi\}$ transform to $\{\hat{\xi}\}$ as

$$\begin{aligned}\sum_i \hat{\xi}_i \hat{\Lambda}_i &= \sum_j \xi_j \Lambda_j \\ &= \sum_{jk} \xi_j C_{jk}^{-1} C_{kl} \Lambda_l \\ &= \sum_j \xi_j C_{jk}^{-1} \hat{\Lambda}_k \\ \therefore \vec{\hat{\xi}} &= (\mathbb{C}^T)^{-1} \vec{\xi}\end{aligned}$$

Applying this transformation to the linear system leading to Eq. (3.57) leads to

$$\begin{aligned}\mathbb{M} \vec{\xi} &= \vec{h} \\ (\mathbb{C}^T)^{-1} \mathbb{M} \mathbb{C}^T (\mathbb{C}^T)^{-1} \vec{\xi} &= \vec{\hat{h}} \\ (\mathbb{C}^T)^{-1} \mathbb{M} \mathbb{C}^T \vec{\hat{\xi}} &= \vec{\hat{h}} \\ \vec{\hat{\xi}} &= \mathbb{C}^T (\hat{\mathbb{M}})^{-1} \vec{\hat{h}},\end{aligned}\tag{3.58}$$

where the first element of $\vec{\hat{h}} = (\mathbb{C}^T)^{-1} \vec{h}$ is set to zero, and the first row and column of $\hat{\mathbb{M}} = (\mathbb{C}^T)^{-1} \mathbb{M} \mathbb{C}^T$ has been set to zero, with the top-left element set to one, respectively, before the back-solve of Eq.(3.58). This indeed ensures the first element of $\vec{\hat{\xi}}$ is zero.

3.2.7.2 Time-averaging

Besides choosing sufficiently large radial intervals to increase the number of markers per radial bin, to further reduce marker sampling noise being incorporated into the adapted background profile, the linear system leading to Eq. (3.57) is only solved at periodic time intervals, within which $\int d\Omega \Lambda_l(s) \delta f(\vec{Z}, t)$ is time-averaged. Assuming uniform time-stepping $t_i = i\Delta t$ for some fixed time-step Δt , and let

$$\mathbb{E}_{(i,j)}[g(t)] = \frac{1}{j-i+1} \sum_{k=i}^j g(t_k),$$

for some function $g(t)$ of time. Then, if the fixed adaptive period is set to $N_t \Delta t$, i.e. $j = i + N_t$ in Eq. (3.55), from Eq. (3.57),

$$\xi_k = \alpha_E N_t \Delta t M_{kl}^{-1} \mathbb{E}_{(i,i+N_t)} \left[\int d\Omega \Lambda_l(s) \frac{v^2}{2} \delta f(\vec{Z}, t) \right].\tag{3.59}$$

The change in $E_{\text{kin}0}$ after every N_t^{th} time-step involves the combination of Eqs. (3.58) and (3.59). Assuming $\|\delta f\| < \|f_0\|$ at any point in time, it is necessary that

$$\alpha_E N_t \Delta t < 1. \quad (3.60)$$

In practice, N_t is fixed, and α_E is a fraction of the maximum linear growth rate γ_{max} , e.g. $N_t = 10$ and $\alpha_E = 0.1\gamma_{\text{max}}$.

3.2.8 Weight redefinition

After the adaptation step, the background will have changed either via n_0 or T_0 , or both. In order to ensure constancy of f along each of the p^{th} marker's trajectory, the marker weight w_p must have a change according to

$$\begin{aligned} \frac{d}{dt} f(\vec{Z}_p, t) &= \frac{d}{dt} [f_0(\vec{Z}_p, t) + \delta f(\vec{Z}_p, t)] \\ 0 &= \Delta f_0(\vec{Z}_p, t) + \Delta \delta f(\vec{Z}_p, t) \\ \Delta w_p &= -\Omega_p \Delta f_0(\vec{Z}_p, t), \end{aligned} \quad (3.61)$$

with⁷ $\Delta f_0 = f_0^{(\text{new})} - f_0^{(\text{old})}$.

3.2.9 Control variate and background

The discussion here supplement the discussion in Sec. 2.4. So far, the terms ‘control variate’ and ‘background distribution’ have been used interchangeably. Despite the time-averaging operator for the evolution of the ‘background’ profiles, the control variate defined via Eq. (3.42) or (3.53) in this work is not necessarily the physical background distribution. Firstly, we have assumed a Maxwellian form for our time-dependent control variate. This choice allows for straight-forward interpretation of the gyrocentre density, parallel flow, and temperature. Secondly, we have limited our adaptive control variate formalism to work with time-dependent f.s.a. profiles. Besides its simplicity, this has the benefit of having enough markers per radial bin, thus leading to accurate calculation of the r.h.s. of Eqs. (3.45)-(3.47). These restrictions on the control variate make it less likely to correspond to the physical background. On the other hand, if the delta-f assumption Eq. (3.8) is satisfied over turbulent time-scales, the distinction between adapted control variate and physical background becomes negligible.

3.2.10 Correction to the r.h.s. of the QNE

Consider again the singly charged perturbed ion gyrodensity term on the r.h.s. of the QNE,

$$\delta \tilde{n}_i(\vec{r}) = \frac{1}{2\pi} \int d\alpha d\Omega \delta[\vec{R} + \vec{\rho}_L(\vec{R}, \mu, \alpha) - \vec{r}] \delta f_i(\vec{Z}, t), \quad (3.62)$$

whose δf_i is represented by markers. According to Eq. (3.61), $\delta \tilde{n}_i(\vec{r})$ will change after adaptation. Since the adaptation scheme is numerical and the total density should

⁷Note that for a two-weight scheme with p and w weights: $\Delta w_p = -\Delta p_p$ (see Eq. (3.22)).

not change, this implies that $\tilde{n}_{0i}(\vec{r})$ will change as well. Therefore, a correction term is required on the r.h.s of the QNE (c.f. the second term of Eq. (3.40)). As $\delta f_i^{(\text{old})} = \delta f_i^{(\text{new})} + \Delta f_{0i}$, the ion gyrodensity with correction term is thus

$$\begin{aligned}\delta \tilde{n}_i(\vec{r}) &= \frac{1}{2\pi} \int d\alpha d\Omega \delta[\vec{R} + \vec{\rho}_L(\vec{R}, \mu, \alpha) - \vec{r}] [\delta f_i^{(\text{new})}(\vec{Z}, t) + \Delta f_{0i}(\vec{Z}, t)] \\ &= \frac{1}{2\pi} \int d\alpha d\Omega \delta[\vec{R} + \vec{\rho}_L(\vec{R}, \mu, \alpha) - \vec{r}] \delta f_i^{(\text{new})}(\vec{Z}, t) + \\ &\quad \tilde{n}_{0i}^{(\text{new})}(\vec{r}, t) - \tilde{n}_{0i}^{(\text{old})}(\vec{r}, t).\end{aligned}\tag{3.63}$$

The remainder of this section concerns the explicit calculation of the correction due to the ion background change $\tilde{n}'_{0i}(\vec{r}, t) - \tilde{n}_{0i}(\vec{r}, t)$. The corresponding term for the electron is similar, and in fact easier, as it does not involve gyroaveraging, in accordance to the drift-kinetic electron assumption.

3.2.10.1 Exact calculation of the correction term

As the QNE is solved by first projecting it onto B-spline basis elements

$$\Lambda_I(\vec{r}) = \Lambda_i(s)\Lambda_j(\theta^*)\Lambda_k(\varphi)$$

defined on a uniform spatial grid $\vec{r} = [s, \theta^*, \varphi]$ with index $I = [i, j, k]$, the evaluation of the correction term of Eq. (3.63) in the framework of the QNE, implies the evaluation of integrals of the form

$$\text{RHS}_I(t) = \int d^3r \Lambda_I(\vec{r}) \tilde{n}_0(\vec{r}, t).$$

Distinguishing $\vec{r} = [s, \theta^*, \varphi]$ and $\vec{R} = [S, \Theta^*, \Phi]$ as the field and gyrocentre spatial point respectively,

$$\begin{aligned}\text{RHS}_I(t) &= \frac{1}{2\pi} \int d^3r d\alpha d^3R d^3v \Lambda_I(\vec{r}) f_0(\vec{R}, v_{\parallel}, \mu) \delta[\vec{R} + \vec{\rho}_L(\vec{R}, \mu, \alpha) - \vec{r}] \\ &= \frac{1}{2\pi} \int d\alpha d^3R d^3v \Lambda_I(\vec{R} + \vec{\rho}_L) f_0(\vec{R}, v_{\parallel}, \mu) \\ \text{RHS}_{ijk}(t) &= \frac{1}{2\pi} \int d\alpha dS d\Theta^* d\Phi dv_{\parallel} d\mu \Lambda_i[S_L(S, \mu, \alpha)] \Lambda_j[\Theta_L^*(\Theta^*, \mu, \alpha)] \Lambda_k(\Phi) \cdot \\ &\quad J_s(S, \Theta^*) 2\pi B_{\parallel}^*(S, \Theta^*, v_{\parallel}) f_0(\vec{R}, v_{\parallel}, \mu) \\ &= \Delta\varphi \int d\alpha dS d\Theta^* dv_{\parallel} d\mu \Lambda_i(S_L) \Lambda_j(\Theta_L^*) J_s B_{\parallel}^* f_0(\vec{R}, v_{\parallel}, \mu),\end{aligned}\tag{3.64}$$

where use has been made of

$$\int_0^{2\pi} d\Phi \Lambda_k(\Phi) = \Delta\varphi,$$

for any k^{th} basis element Λ_k periodic in the φ -direction, with $\Delta\varphi$ the uniform grid spacing. The Larmor-averaging of the basis element $\Lambda_I(\vec{R} + \vec{\rho})$ is done only in the (s, θ^*) -plane, to be consistent with the formation of Larmor rings for the markers. The variables S_L and Θ_L^* of Eq. (3.64) are the (s, θ^*) -coordinates on those Larmor rings, and are given as follows.

The idea is that, first we transform the point (s, θ^*) on to a pseudo-Cartesian plane (ξ, η) , form the Larmor-rings, and then transforming points on those Larmor-rings back. The transformation is given by

$$\xi = s \cos(\theta^*) \quad \eta = s \sin(\theta^*),$$

with

$$\begin{aligned} \nabla \xi &= \nabla s \cos(\theta^*) - \nabla \theta^* s \sin(\theta^*) \\ \nabla \eta &= \nabla s \sin(\theta^*) + \nabla \theta^* s \cos(\theta^*). \end{aligned}$$

Then, the local Larmor vector on the (s, θ^*) -plane approximated to be perpendicular to \vec{B} , up to first order $\mathcal{O}(1/L_B)$, is given by

$$\vec{\rho}_L(\mu, \alpha) = \rho_L(\mu, \alpha) \left(\cos(\alpha) \frac{\nabla s}{|\nabla s|} + \sin(\alpha) \frac{\vec{B} \times \nabla s}{|\vec{B} \times \nabla s|} \right).$$

The points on the Larmor ring are then given by

$$\begin{aligned} \xi_L(S, \Theta^*, \mu, \alpha) &= \xi_{GC} + \vec{\rho}_L \cdot \nabla \xi|_{GC} \\ \eta_L(S, \Theta^*, \mu, \alpha) &= \eta_{GC} + \vec{\rho}_L \cdot \nabla \eta|_{GC} \\ \vec{\rho}_L \cdot \nabla \xi|_{GC} &= \rho_L \left[\cos(\alpha) \left(\cos(\Theta^*) |\nabla S| - S \sin(\Theta^*) \frac{\nabla S \cdot \nabla \Theta^*}{|\nabla S|} \right) - \right. \\ &\quad \left. S \sin(\Theta^*) \sin(\alpha) \frac{F}{J_s B |\nabla S|} \right] \\ \vec{\rho}_L \cdot \nabla \eta|_{GC} &= \rho_L \left[\cos(\alpha) \left(\sin(\Theta^*) |\nabla S| + S \cos(\Theta^*) \frac{\nabla S \cdot \nabla \Theta^*}{|\nabla S|} \right) + \right. \\ &\quad \left. S \cos(\Theta^*) \sin(\alpha) \frac{F}{J_s B |\nabla S|} \right], \end{aligned}$$

with the subscript GC representing the evaluation at the gyrocentre, and finally transforming back,

$$S_L(S, \Theta^*, \mu, \alpha) = \sqrt{\xi_L^2 + \eta_L^2}, \quad \Theta_L^*(S, \Theta^*, \mu, \alpha) = \arctan \left(\frac{\eta_L}{\xi_L} \right). \quad (3.65)$$

To proceed further with the integration of Eq. (3.64), let T_b be a f.s.a. temperature function to be assigned later. We then normalise the perpendicular and parallel velocities at fixed S , by defining the new variables

$$\lambda = \frac{\mu B}{T_b/m}, \quad \sigma^2 = \frac{v_{\parallel}^2}{2T_b/m}. \quad (3.66)$$

This leads to easy application of Gaussian quadrature formulas for their respective integration. Gauss-Laguerre and Gauss-Hermite quadratures are chosen for λ and σ due to their semi-infinite and infinite integration ranges, respectively. For a general function G , the Gauss-Laguerre and Gauss-Hermite quadratures are given by

$$\begin{aligned} \int_0^{\infty} d\lambda e^{-\lambda} G(\lambda, \dots) &\approx \sum_l w_l G(q_l, \dots), \\ \sum_l w_l &= 1, \end{aligned} \quad (3.67)$$

and

$$\begin{aligned} \int_{-\infty}^{\infty} d\lambda e^{-\sigma^2} G(\sigma, \dots) &\approx \sum_h w_h G(q_h, \dots), \\ \sum_h w_h &= \sqrt{\pi}, \end{aligned} \quad (3.68)$$

respectively. Here, $\{q\}$ and $\{w\}$ are respectively the quadrature point and weight sets. In the following, for ease of notation, we will use the indices l and h to indicate the type of quadrature used. Returning to Eq. (3.64),

$$\begin{aligned} \text{RHS}_{ijk}(t) &= \Delta\varphi \int d\alpha dS d\Theta^* dv_{\parallel} d\mu \Lambda_i(S_L) \Lambda_j(\Theta_L^*) J_s B_{\parallel}^* f_0(\vec{R}, v_{\parallel}, \mu, t) \\ &= \frac{\Delta\varphi}{2\pi\sqrt{\pi}} \int d\alpha dS d\Theta^* d\sigma d\lambda \left(\frac{2\pi T_b(\psi(S))}{m} \right)^{3/2} \\ &\quad \Lambda_i \left[S_L \left(S, \Theta^*, \frac{T_b(\psi(S))}{mB} \lambda, \alpha \right) \right] \Lambda_j \left[\Theta_L^* \left(S, \Theta^*, \frac{T_b(\psi(S))}{mB} \lambda, \alpha \right) \right] \\ &\quad \frac{J_s B_{\parallel}^* \left(S, \Theta^*, \sqrt{\frac{2T_b(\psi(S))}{m}} \sigma \right)}{B} f_0 \left(\vec{R}, \sqrt{\frac{2T_b(\psi(S))}{m}} \sigma, \frac{T_b(\psi(S))}{mB} \lambda, t \right) \\ &= \frac{\Delta\varphi}{2\pi\sqrt{\pi}} \sum_{lh} w_l e^{q_l} w_h e^{q_h^2} \int d\alpha dS d\Theta^* \left(\frac{2\pi T_b}{m} \right)^{3/2} \\ &\quad \Lambda_i [S_L(S, \Theta^*, \mu_l, \alpha)] \Lambda_j [\Theta_L^*(S, \Theta^*, \mu_l, \alpha)] \cdot \\ &\quad \frac{J_s B_{\parallel}^*(S, \Theta^*, v_{\parallel h})}{B} f_0(\vec{R}, v_{\parallel h}, \mu_l, t), \end{aligned} \quad (3.69)$$

where

$$\mu_l = \frac{T_b(\psi(S))}{m} q_l, \quad v_{\parallel h} = \sqrt{\frac{2T_b(\psi(S))}{m}} q_h \quad (3.70)$$

for notation simplicity.

3.2.10.2 Expansion approximation to the integral

The evaluation of Eq. (3.69) is computationally expensive. Namely, it takes $N_s^2 \times N_{\theta^*}^2 \times N_q^5$ integrand evaluations, where N_q is the average number of quadrature points per interval. The 5th power of N_q corresponds to the 5 dimensions of the $\{S, \Theta^*, v_{\parallel}, \mu, \alpha\}$ space. We now make the approximation, assuming a canonical Maxwellian background

$$\begin{aligned} f_0(\hat{\psi}_0, \mathcal{E}, t) &= \frac{n_0(\hat{\psi}_0, t)}{[2\pi T_0(\hat{\psi}_0, t)/m]^{3/2}} \exp \left[-\frac{\mathcal{E}}{T_0(\hat{\psi}_0, t)/m} \right] \\ &\approx \hat{f}_0(\hat{\psi}_0, \hat{\mathcal{E}}, t), \\ \hat{f}_0(\hat{\psi}_0, \hat{\mathcal{E}}, t) &= \sum_{xy}^{N_{\psi} N_{\mathcal{E}}} a_{xy}(t) \Lambda_x(\hat{\psi}_0) \Lambda_y(\hat{\mathcal{E}}) e^{-\hat{\mathcal{E}}}, \end{aligned} \quad (3.71)$$

with

$$\begin{aligned}\hat{\mathcal{E}} &= \frac{\mathcal{E}}{T_b(\hat{\psi}_0)/m}, \\ \mathcal{E} &= \frac{v_{\parallel}^2}{2} + \mu B(S, \Theta^*), \\ \hat{\psi}_0 &= \psi(S) + \frac{v_{\parallel} F(\psi(S))}{\Omega_c(S, \Theta^*)} - \text{sgn}(v_{\parallel}) \frac{m R_0}{e} \sqrt{2[\mathcal{E} - \mu B_{\max}(\psi(S))]} \text{H}(\mathcal{E} - \mu B_{\max}(\psi(S))).\end{aligned}$$

Looking at Eq. (3.71), the time dependence of f_0 is now only expressed via the $\{a_{xy}(t)\}$ coefficients. Then, after every adaptation step, one only needs to solve for these time-dependent coefficients via a cheap back-solve on a linear system, compared to solving the integral of Eq. (3.69). The reference function T_b is the same as that of Eq. (3.69). In Eq. (3.71), $\hat{\psi}_0$ and $\hat{\mathcal{E}}$ are treated as independent variables, spanning the space $[0, 1] \times [0, 1.2\kappa_v^2]$. The domain of $\hat{\psi}_0$ is restricted to $[0, 1]$, whereas the upper limit of $\hat{\mathcal{E}}$ is indeed 20% more than the limit of marker sampling at $v^2 \leq \kappa_v^2 v_{\text{th}}^2(S)$, defined using the initial temperature profile for the local thermal velocity $v_{\text{th}}(s) = T_0(\psi(s), t=0)/m$. This extension is to accommodate for large temperature deviations from $T_0(s, t=0)$ with simulation time. The number of basis functions in the $\hat{\psi}_0$ and $\hat{\mathcal{E}}$ dimensions are taken to be N_{ψ} and $N_{\mathcal{E}}$, respectively. The size of N_{ψ} and $N_{\mathcal{E}}$ is usually determined so that the maximum local fractional error of the approximation of Eq. (3.71) is taken to be less than 1%.

The time-dependent coefficients $\{a_{xy}(t)\}$ are retrieved by back-solving the linear system

$$\begin{aligned}& \sum_{x'y'} M_{xx'}^{(\hat{\psi}_0)} M_{yy'}^{(\hat{\mathcal{E}})} a_{x'y'}(t) \\ &= \int_0^1 d\hat{\psi}_0 \int_0^{1.2\kappa_v^2} d\hat{\mathcal{E}} \Lambda_{x'}(\hat{\psi}_0) \Lambda_{y'}(\hat{\mathcal{E}}) \frac{n_0(\hat{\psi}_0, t)}{[2\pi T_0(\hat{\psi}_0, t)/m]^{3/2}} \exp \left[-\hat{\mathcal{E}} \left(\frac{T_b(\hat{\psi}_0)}{T_0(\hat{\psi}_0, t)} - 1 \right) \right],\end{aligned}\tag{3.72}$$

with ‘mass matrices’ of size $N_{\psi} \times N_{\psi}$ and $N_{\mathcal{E}} \times N_{\mathcal{E}}$ are respectively

$$M_{xx'}^{(\hat{\psi}_0)} = \int_0^1 d\hat{\psi}_0 \Lambda_x(\hat{\psi}_0) \Lambda_{x'}(\hat{\psi}_0), \quad M_{yy'}^{(\hat{\mathcal{E}})} = \int_0^{1.2\kappa_v^2} d\hat{\mathcal{E}} \Lambda_y(\hat{\mathcal{E}}) \Lambda_{y'}(\hat{\mathcal{E}}).$$

By expressing f_0 as in Eq. (3.71), one needs to compute the time-independent integral only ‘once’, from Eq. (3.69)

$$\begin{aligned}\text{RHS}_{ijk}^{xy} &= \frac{\Delta\varphi}{2\pi\sqrt{\pi}} \sum_{lh} w_l w_h \int d\alpha dS d\Theta^* \left(\frac{2\pi T_b}{m} \right)^{3/2} \\ & \quad \Lambda_i[S_L(S, \Theta^*, \mu_l, \alpha)] \Lambda_j[\Theta_L^*(S, \Theta^*, \mu_l, \alpha)] \cdot \\ & \quad \frac{J_s B_{\parallel}^*(S, \Theta^*, v_{\parallel h})}{B} \Lambda_x(\hat{\psi}_0) \Lambda_y(\hat{\mathcal{E}}_{lh}) e^{-\hat{\mathcal{E}}_{lh} + q_l + q_h^2} \\ &= \frac{\Delta\varphi}{2\pi\sqrt{\pi}} \sum_{lh} w_l w_h \int d\alpha dS d\Theta^* \left(\frac{2\pi T_b(\psi(S))}{m} \right)^{3/2} \frac{J_s B_{\parallel}^*}{B} \\ & \quad \Lambda_i(S_L) \Lambda_j(\Theta_L^*) \Lambda_x(\hat{\psi}_0) \Lambda_y(\hat{\mathcal{E}}_{lh}) \cdot \exp \left[-\frac{\mathcal{E}_{lh}}{T_b(\hat{\psi}_0)/m} + \frac{\mathcal{E}_{lh}}{T_b(\psi(S))/m} \right],\end{aligned}\tag{3.73}$$

so that

$$\text{RHS}_{ijk}(t) \approx \sum_{xy} a_{xy}(t) \text{RHS}_{ijk}^{xy}. \quad (3.74)$$

Therefore, after every adaptation step, one needs to only evaluate Eqs. (3.72) and (3.74), both of which are numerically cheap.

Now, the determination of T_b remains to be addressed. One could fix T_b to the functional form of T_0 at time $t = 0$. However, looking at Eq. (3.71), the expansion gives a poor approximation for T_b very different from T_0 at later times, which will be true for an evolving background temperature T_0 . Therefore, the algorithm for computing the correction term of Eq. (3.63) requires one to periodically update T_b to have the functional form of the current T_0 through time. This involves the re-evaluation of Eqs. (3.73), though this could be done on a longer period compared to that of the background adaptation. The number of time steps after which Eq. (3.73) is re-evaluated is denoted by N_{eval} .

The algorithm described so far applies identically to the second term of the correction term in Eq. (3.63). The implementation in ORB5 stores the correction term in a buffer in a cumulative way, so that only one evaluation is required after every adaptation step.

Finally, for the case of a time-dependent local Maxwellian background,

$$f_0(\psi, \mathcal{E}, \mu, t) = \frac{n_0(\psi, t)}{[2\pi T_0(\psi, t)/m]^{3/2}} \exp\left[-\frac{\mathcal{E}}{T_0(\psi, t)/m}\right],$$

one just needs to replace all $\hat{\psi}_0$ terms with ψ in the algorithm described.

3.2.10.3 Coupled electron background density to ion gyrodensities

Consider the r.h.s. of the QNE involving a singly charged kinetic ion species and a fully drift-kinetic electron species after adaptive step, cross-referencing Eq. (3.63),

$$\begin{aligned} \delta \tilde{n}_i(\vec{r}) - \delta n_e(\vec{r}) &= \frac{1}{2\pi} \int d\alpha d\Omega \delta[\vec{R} + \vec{\rho}_L(\vec{R}, \mu, \alpha) - \vec{r}] [\delta f_i^{(\text{new})}(\vec{Z}, t) + \Delta f_{0i}(\vec{Z}, t)] - \\ &\quad \int d\Omega \delta[\vec{R} - \vec{r}] [\delta f_e^{(\text{new})}(\vec{Z}, t) + \Delta f_{0e}(\vec{Z}, t)] \\ &= \frac{1}{2\pi} \int d\alpha d\Omega \delta[\vec{R} + \vec{\rho}_L(\vec{R}, \mu, \alpha) - \vec{r}] \delta f_i^{(\text{new})}(\vec{Z}, t) + \\ &\quad [\tilde{n}_{0i}^{(\text{new})}(\vec{r}, t) - \tilde{n}_{0i}^{(\text{old})}(\vec{r}, t)] - \\ &\quad \int d\Omega \delta[\vec{R} - \vec{r}] \delta f_e^{(\text{new})}(\vec{Z}, t) - [n_{0e}^{(\text{new})}(\vec{r}, t) - n_{0e}^{(\text{old})}(\vec{r}, t)]. \end{aligned}$$

In this case, the correction term from the adaptation step is

$$[\tilde{n}_{0i}^{(\text{new})}(\vec{r}, t) - \tilde{n}_{0i}^{(\text{old})}(\vec{r}, t)] - [n_{0e}^{(\text{new})}(\vec{r}, t) - n_{0e}^{(\text{old})}(\vec{r}, t)]. \quad (3.75)$$

The expression above can be set to zero by having the change in electron background density equal to the change in ion background gyrodensity. Namely, for all times

(after $t = 0$), we enforce

$$\begin{aligned}
 n_{0e}(\vec{r}, t) &= \frac{1}{2\pi} \int d\alpha d\Omega \delta[\vec{R} + \vec{\rho}_L(\vec{R}, \mu, \alpha) - \vec{r}] f_{0i}(\vec{Z}, t) \\
 &= \frac{1}{2\pi} \int d\alpha dv_{\parallel} d\mu B_{\parallel}^*[\vec{r} - \vec{\rho}_L(\vec{R}, \mu, \alpha), v_{\parallel}] f_{0i}[\vec{r} - \vec{\rho}_L(\mu, \alpha), t] \\
 &\approx \frac{1}{2\pi} \int d\alpha dv_{\parallel} d\mu B_{\parallel}^*(\vec{r}, v_{\parallel}) f_{0i}[\vec{r} - \vec{\rho}_L(\vec{R}, \mu, \alpha), t],
 \end{aligned}$$

whose approximation in the last line being consistent with the building of Larmor-rings using the velocity Jacobian evaluated at gyrocentre positions. Introducing the substitutions, Eq. (3.66),

$$\begin{aligned}
 n_{0e}(\vec{r}, t) &= \frac{1}{2\pi^{3/2}} \int d\alpha d\lambda d\sigma \frac{B_{\parallel}^*[s, \theta^*, v_{\parallel}(\sigma)]}{B(s, \theta^*)} \left(\frac{2\pi T_b(\psi(s))}{m} \right)^{3/2} f_{0i}[\vec{r} - \vec{\rho}_L(\vec{R}, \mu(\lambda), \alpha), t] \\
 &= \frac{1}{2\pi^{3/2}} \int d\alpha \left(\frac{2\pi T_b(\psi(s))}{m} \right)^{3/2} \\
 &\quad \sum_{lh} w_l w_h e^{q_l} e^{q_h} \frac{B_{\parallel}^*(s, \theta^*, v_{\parallel h})}{B(s, \theta^*)} f_{0i}[s_L(s, \theta^*, \mu_l, \alpha), \theta_L^*(s, \theta^*, \mu_l, \alpha), t], \tag{3.76}
 \end{aligned}$$

where we have used quadratures Eqs. (3.67) and (3.68) for the velocity variables λ and σ integration, respectively. The s_L and θ_L^* expressions are given identically to the treatment leading up to Eq. (3.65), and the notation of Eq. (3.70) has been used.

Eq. (3.76) is much cheaper in terms of memory and computation as compared to that of Eq. (3.69). However, the electron background density profile used in this work is the f.s.a.. Therefore, we must have

$$n_{0e}(\psi, t) = \langle n_{0e}(\vec{r}, t) \rangle,$$

which will result in the cancellation of Eq. (3.75) only in the f.s.a. sense.

3.2.11 Update on the l.h.s. of the QNE

As background profiles are now time-dependent, this allows us to update the l.h.s. of the QNE. For this discussion, we shall use the form with electrons with hybrid response, Eq. (2.38) as an example as it contains all the relevant background terms,

$$\begin{aligned}
 &n_{\text{initi}}(\psi) + \nabla_{\perp} \cdot \left(\frac{m_i n_{\text{initi}}(\psi)}{e B^2} \nabla_{\perp} \phi \right) + \delta \tilde{n}_i \\
 &= n_{\text{inite}}(\psi) + \alpha_P \frac{e n_{\text{inite}}(\psi)}{T_{\text{inite}}(\psi)} (\phi - \langle \phi \rangle) + \delta n_{e,P}|_{(m,n)=(0,0)} + \delta n_{e,T} \tag{3.77}
 \end{aligned}$$

Here, we have rearranged the ion and electron contributions to the left and right of the equal sign respectively. We have also reintroduced the use of initial profiles, denoted by the superscript (init). Under the adaptive scheme, with the assignment $n_0(\psi, 0) = n_{\text{init}}$ for the respective species, Eq. (3.77) can be written equivalently as

$$\begin{aligned}
 &n_{i0}(\psi, t) + \nabla_{\perp} \cdot \left(\frac{m_i n_{\text{initi}}(\psi)}{e B^2} \nabla_{\perp} \phi \right) + \delta \tilde{n}_i^{(\text{new})} \\
 &= n_{e0}(\psi, t) + \alpha_P \frac{e n_{\text{inite}}(\psi)}{T_{\text{inite}}(\psi)} (\phi - \langle \phi \rangle) + \delta n_{e,P}^{(\text{new})}|_{(m,n)=(0,0)} + \delta n_{e,T}^{(\text{new})}. \tag{3.78}
 \end{aligned}$$

Perturbation quantities are now w.r.t. the updated background at time t . Since, Eqs. (3.77) and (3.78) are identical, they have the same solution ϕ . We recall that in ORB5 the second term on the l.h.s. of Eq. (3.78) is the linearised polarisation density. That is, n_{initi} has been used instead of $n_i(\vec{r}, t)$. This assumption becomes questionable in particular when profiles exhibit significant evolution from their initial values. In such situations, one would need for example to restart a completely new simulation, using the time-averaged final profiles of the old simulation as initial profile of the new one. This was done in the past, e.g. in Ref. [4]. The disadvantage is that the new simulation has to go again through the transient phase of growth, overshoot, saturation, before reaching a new quasi-steady state. An alternative is to periodically adapt the density appearing in the QNE:

$$\begin{aligned} & n_{i0}(\psi, t) + \nabla_{\perp} \cdot \left(\frac{m_i n_{i0}(\psi, t)}{eB^2} \nabla_{\perp} \phi \right) + \delta \tilde{n}_i^{(\text{new})} \\ = & n_{e0}(\psi, t) + \alpha_P \frac{en_{e0}(\psi, t)}{T_{e0}(\psi, t)} (\phi - \langle \phi \rangle) + \delta n_{e,P}^{(\text{new})}|_{(m,n)=(0,0)} + \delta n_{e,T}^{(\text{new})}. \end{aligned}$$

This requires rebuilding the matrix (see Eq. (3.34)) of the l.h.s. of the QNE every so often with the new background profiles n_0 and T_0 . For the ion case, we now see that a time-dependent background gyrocentre density adds nonlinearity to the polarisation density. As for the electrons, the interpretation of the time-dependent profiles in the adiabatic term is not straightforward. This is because updated profiles are derived from the contributions of both passing and trapped perturbed electrons. Hence, a more accurate change to the adiabatic term would require the distinction between passing and trapped background profiles. Nonetheless, for simplicity, this work does not make that distinction.

3.3 Heat sources and noise control

In this work, there are three inhomogeneous terms to the Vlasov equation used,

$$\frac{df}{dt} = \hat{S}_K + \hat{S}_H + S_B. \quad (3.79)$$

Here, \hat{S}_K is Krook operator that will serve as noise control. \hat{S}_H is a f.s.a. heating operator parameterised by user-defined density and temperature profiles. And γ_K is the source/sink that represents the buffer that damps all fluctuations at the $s = 1$ boundary. These operators will be discussed below. Under the direct- δf scheme (see Sec. 3.1.6) used in this work, the r.h.s. of Eq. (3.79) is implemented in a time-splitting fashion, one inhomogeneous term at a time.

3.3.1 Krook operator as noise control and heat source

In a PIC scheme, noise-control is essential to reduce the rate of statistical sampling noise accumulation when representing δf with markers, and is important to act as a source of dissipation to allow a source-less and collision-less system to reach quasi-steady state [48]. The noise control used in this work is in the form of a Krook operator,

$$\hat{S}_K(\vec{Z}, t) = -\gamma_K(f - f_K) + S_K^c \quad (3.80)$$

where f_K is a reference distribution function, which is usually taken to be the control variate $f_0(t)$ for noise control, which is not necessarily the initial equilibrium distribution in light of the adaptive scheme. The strength constant γ_K should not be too large as it will damp out essential physics from the time evolution, and not too small that it will be too weak as a noise control. A good compromise for γ_K is 10% of the maximum linear growth rate of the case under study. However, no matter how small γ_K is, over long simulation-times persistent profiles like the f.s.a. density and temperature profiles, as well as zonal flow structures, will be effected. Therefore, a correction term S_K^c is included in Eq. (3.80) to conserve the moments of density, parallel momentum, residual zonal flows, and the kinetic energy to machine precision on each flux surface. The method of calculation for correction terms is elaborated in Sec. 3.3.3.

For temperature-gradient-driven simulations in this work, the Krook operator is used as a nonlinear heat source with $f_K = f_{\text{init}}$, as

$$\begin{aligned}\hat{S}_K(\vec{Z}, t) &= -\gamma_K(f - f_{\text{init}}) + S_K^c \\ &= -\gamma_K[\delta f + f_0(t) - f_{\text{init}}] + S_K^c,\end{aligned}\quad (3.81)$$

where the extra term $f_0(t) - f_{\text{init}}$ accounts for the change in the background. Since Eq. (3.81) now serves as a heat source, S_K^c will not account for f.s.a. kinetic energy correction, but keep the density, parallel momentum and residual zonal flow conservation.

3.3.2 Fixed heat source and edge buffer sink

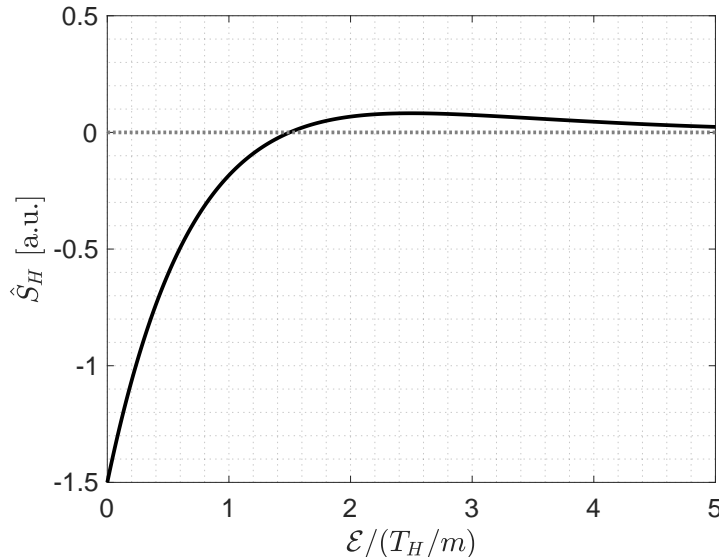


Figure 3.4: Amplitude of the f.s.a. heating operator $\hat{S}_H(\psi, \mathcal{E})$ of Eq. (3.82), at a fixed radial position ψ .

For flux-driven runs of this work, the f.s.a. heat source used is of the form

$$\hat{S}_H(\psi, \mathcal{E}) = \gamma_H G_H(\psi) \frac{1}{T_H(\psi)/m} \left(\frac{\mathcal{E}}{T_H(\psi)/m} - \frac{3}{2} \right) \frac{n_H(\psi)}{[2\pi T_H(\psi)]/m]^{3/2}} \exp\left(-\frac{\mathcal{E}}{T_H(\psi)/m}\right) + S_H^c, \quad (3.82)$$

with n_H and T_H the reference f.s.a. density and temperature profiles, G_H the radial profile for the heat source used for localised heating, and the constant γ_H its strength. The first term is proportional to the temperature derivative of a reference local Maxwellian function f_L , $\frac{\partial f_L}{\partial T_H}$. The consequence is that this term is not a source of density in the infinite marker limit,

$$\begin{aligned} \int d^3R \frac{\partial f_L}{\partial T_H} &= \frac{\partial}{\partial T_H} \int d^3R f_L \\ &= \frac{\partial}{\partial T_H} n_H(\psi) \\ &= 0. \end{aligned}$$

Nonetheless, like the Krook noise control operator of Eq. (3.80), we include a correction term S_H^c to ensure the conservation of not only the the parallel momentum and residual zonal flows, but also the density to machine precision on each flux surface.

Two insights can be made of \hat{S}_H . The first is that for a fixed radial position ψ , the amplitude of \hat{S}_H as a function of $\frac{\mathcal{E}}{T_H/m}$ is shown in Fig. 3.4. One can see that \hat{S}_H decreases the distribution function for gyrocentres with energies lower than the internal kinetic energy density at temperature T_H , $\mathcal{E} < 3T_H/(2m)$, and increases the distribution function of gyrocentres that are above this energy threshold. Secondly, again at fixed ψ , if we approximate the derivative $\frac{\partial}{\partial T_H}$ for Eq. (3.82) as

$$\hat{S}_H(\psi, \mathcal{E}) = \gamma_H G_H(\psi) \left. \frac{f_L(n_H, T + \Delta T) - f_L(n_H, T)}{\Delta T(\psi)} \right|_{T=T_H} + S_H^c,$$

we can interpret $\frac{G(\psi)}{\Delta T(\psi)}$ as the dimensionless radial positive envelope profile for heating, to increase the temperature from T_H to $T_H + \Delta T$. This also ensures that γ_H of Eq. (3.82) retains the correct units of Ω_{ci} .

Finally, to eliminate all turbulence at the edge, a (non-conserving) Krook buffer which acts as a sink in the form of

$$S_B(s) = -\gamma_B \left(\frac{s - s_B}{1 - s_B} \right)^4 \delta f \quad (3.83)$$

is used, with user-defined buffer radial edge s_B , and strength constant γ_B applicable only in $s \in [s_B, 1]$.

3.3.3 Source correction term

Let the correction term S^c be of the form [43]

$$S^c(\vec{Z}) = \sum_i^{N_{\text{mom}}} g_i(s) f_0(\vec{Z}) M_i(\vec{Z}), \quad (3.84)$$

with f_0 the control variate, and $\{M\}$ the set of moments from Table. 3.1 to be simultaneously conserved on each flux surface ψ . Here, we have omitted the explicit time dependence in Eq. (3.84), keeping in mind that Eqs. (3.80) and (3.82) are implemented in a time-splitting fashion after the marker push, and the re-evaluation of Eq. (3.84) needs to be done.

Like Eqs. (3.80) and (3.82), consider the inhomogeneous term of the Vlasov equation, of the form $\hat{S} = S + S^c$. The simultaneous conservation on each flux surface $\psi = s^2\psi_{\text{edge}}$ requires that

$$0 = \left\langle \int d^3v M_i(\vec{Z})(S + S^c) \right\rangle \quad \forall i$$

$$\sum_j^{N_{\text{mom}}} S_{ij}(s)g_j(s) = S_i(s) \quad \forall i, \quad (3.85)$$

with

$$S_{ij}(s) = \left\langle \int d^3v M_i M_j f_0 \right\rangle, \quad S_i(s) = - \left\langle \int d^3v M_i S \right\rangle.$$

The r.h.s. of the linear system of Eq. (3.85) is formed by binning the markers into radial bins $s \in [s_k, s_k + \Delta s]$, $\forall k$, and solving for the coefficients $\{g\}$ in each of those bins.

| Moment | Expression $M(\vec{Z})$ |
|-------------------|--|
| Density | 1 |
| Parallel velocity | v_{\parallel} |
| zonal flows | $\frac{v_{\parallel}}{B(s, \theta^*)} - \left\langle \frac{v_{\parallel}}{B(s, \theta^*)} \right\rangle_{\text{b.a.}}$ |
| energy per mass | $\frac{v_{\parallel}^2}{2} + \mu B(s, \theta^*)$ |

Table 3.1: Possible moments M to simultaneously conserve on every flux surface ψ via the correction term S^c . The operator $\langle \cdot \rangle_{\text{b.a.}}$ represents the bounce average.

3.4 Normalisations and transport measures

| Quantity | Reference unit |
|-----------------------------------|----------------|
| First ion mass | m_i |
| First ion charge | σ_i |
| Magnetic field at axis | B_0 |
| Electron temperature at $s = s_0$ | $T_{0e}(s_0)$ |

Table 3.2: Reference units of ORB5. $s = s_0$ is a user-specified reference flux surface label, $s_0 \in [0, 1]$.

| Quantity | Derived unit |
|---|------------------------------------|
| Ion cyclotron frequency | $\Omega_{ci} = \sigma_i B_0 / m_i$ |
| Ion sound speed at $s = s_0$ | $c_s = \sqrt{T_{0e}(s_0) / m_i}$ |
| Ion sound Larmor radius ρ_s | c_s / Ω_{ci} |
| j^{th} species volume-averaged density | \bar{n}_j |

Table 3.3: Common derived quantities of ORB5. The ion species is the reference (first) ion species of Tab. 3.2.

Table 3.2 shows the four reference units used in ORB5. Units for other quantities are derived from these. In view of the adaptive background scheme, the normalisation unit for temperature $T_{0e}(s_0)$ is specifically $T_{0e}(s_0, t = 0)$. Furthermore in this thesis, $T_{i0}(s_0, t = 0) = T_{0e}(s_0, t = 0)$ is always chosen. Tab. 3.3 shows examples of derived quantities and their respective units. For density normalisation, the average density of the j^{th} species is used, i.e.

$$\bar{n}_j = \frac{\int ds d\theta^* d\varphi J_s(s, \theta^*) n_{0j}(t = 0)}{\int ds d\theta^* d\varphi J_s(s, \theta^*)} = \frac{N_{\text{ph}j}}{V}, \quad (3.86)$$

with the integration done over the whole configuration space of total volume V , and Eq. (3.20) has been used. Note that this normalisation is unique to the j^{th} species, and uses the initial density $n_{0j}(t = 0)$ as reference. Under this normalisation, with δf_j approximated by markers Eq. (3.19),

$$\int d\Omega \delta \hat{f}_j = \frac{V}{N_{p,j}}.$$

| Quantity | ORB5 unit | Physical unit |
|--|---------------------------|------------------------------------|
| Shearing rate $\omega_{E \times B}$ | Ω_{ci} | c_s/a |
| Heat diffusivity χ | $\rho_s c_s$ | $\chi_{GB0} = \rho_s^2 c_s/a$ |
| Heat flux through surface $\langle \vec{q}_H \cdot \nabla \psi / \nabla \psi \rangle_S$ | $\bar{n} c_s T_{0e}(s_0)$ | $\bar{n} \chi_{GB0} T_{0e}(s_0)/a$ |
| Particle flux through surface $\langle \vec{\Gamma} \cdot \nabla \psi / \nabla \psi \rangle_S$ | $\bar{n} c_s$ | $\bar{n} \chi_{GB0}/a$ |

Table 3.4: Diagnostic quantities in ORB5 and physical units

We now define diagnostics commonly used in Chs. 5 and 6.

1. Zonal flow $E \times B$ shearing rate [77]:

$$\omega_{E \times B} = \frac{s}{2\psi_{\text{edge}} q(s)} \frac{\partial}{\partial s} \left(\frac{1}{s} \frac{\partial \langle \phi \rangle}{\partial s} \right) \quad (3.87)$$

2. Particle flux:

$$\vec{\Gamma} = \int d^3v \frac{-\langle \nabla \phi \rangle \times \vec{B}}{BB_{\parallel}^*} \delta f \quad (3.88)$$

3. Heat flux:

$$\begin{aligned} \vec{q}_{\text{kin}} &= \int d^3v \frac{mv^2}{2} \frac{-\langle \nabla \phi \rangle \times \vec{B}}{BB_{\parallel}^*} \delta f \\ \vec{q}_{\text{pot}} &= \int d^3v \sigma \phi \frac{-\langle \nabla \phi \rangle \times \vec{B}}{BB_{\parallel}^*} \delta f \\ \vec{q}_H &= \vec{q}_{\text{kin}} + \vec{q}_{\text{pot}} - \frac{5}{2} m v_{\text{th}}^2 \vec{\Gamma}. \end{aligned}$$

In diagnostics the average heat flux through a magnetic surface is usually shown. Let the averaging operator $\langle \cdot \rangle_S$ for a function G on a flux surface be

$$\langle G \rangle_S = \frac{\langle G |\nabla\psi| \rangle}{\langle |\nabla\psi| \rangle}. \quad (3.89)$$

The denominator represents the area of the flux surface in question. Note that Eq. (3.89) is not the same as the flux-surface average operator Eq. (2.12). The power through magnetic surface ψ is then defined to be

$$\left\langle \vec{q}_H \cdot \frac{\nabla\psi}{|\nabla\psi|} \right\rangle_S = \frac{\langle \vec{q}_H \cdot \nabla\psi \rangle}{\langle |\nabla\psi| \rangle}. \quad (3.90)$$

4. Heat diffusivity:

We start from its definition,

$$\begin{aligned} \vec{q}_H &= -n\chi\nabla T \\ \langle \vec{q}_H \cdot \nabla\psi \rangle &= -n\chi \frac{\partial T}{\partial\psi} \langle |\nabla\psi|^2 \rangle \\ \chi &= -\frac{\left\langle \vec{q}_H \cdot \frac{\nabla\psi}{|\nabla\psi|} \right\rangle_S \langle |\nabla\psi| \rangle}{n \partial T / \partial\psi \langle |\nabla\psi|^2 \rangle}, \end{aligned} \quad (3.91)$$

where use has been made of Eq.(3.89) and we assumed that χ is constant on flux surfaces.

5. Logarithmic gradient [75] of profile T , R/L_T :

$$\frac{R}{L_T} = \frac{R_0}{T} \frac{dT/d\psi}{dV_\psi/d\psi} \langle |\nabla\psi| \rangle, \quad (3.92)$$

where R_0 is the major radius, and V_ψ is the volume enclosed by the flux surface ψ .

Chapter 4

GKengine ITG adiabatic electrons

The GKengine code is used as a test bed for the adaptive scheme. Sec. 4.1 first introduces the code used in this chapter, along with its simplifying assumptions. Sec. 4.2 then presents a simplified version of the adaptive scheme for the background temperature in sheared-slab geometry. Sec. 4.3 gives an overview of the profiles and parameters that are used in this chapter. The main results are shown in Sec. 4.4, comparing the adaptive cases against the standard ones. Further analysis is done by varying parameters of the adaptive scheme to study their relative importance, including an attempt to increase heat transport by modifying the electron adiabatic response. Sec. 4.5 concludes this chapter with final remarks on the improvement brought by this simple temperature adaptation scheme. The contents of this chapter are largely based on Ref. [63].

4.1 Simplified physical model

The GKengine code [65] solves for the distribution function f of a singly charged ($Z = 1$) kinetic ion species via the gyrokinetic equation Eq. (2.24), with general source term. The electrons for this chapter are assumed to be adiabatic. The l.h.s. of Eq. (2.24) still reads as

$$\frac{df}{dt} = \left\{ \frac{\partial}{\partial t} + \frac{d\vec{R}}{dt} \cdot \nabla_{\vec{R}} + \frac{dv_{\parallel}}{dt} \frac{\partial}{\partial v_{\parallel}} + \frac{d\mu}{dt} \frac{\partial}{\partial \mu} \right\} f,$$

with gyrocentre coordinates $\vec{Z} = [\vec{R}, v_{\parallel}, \mu]$, where \vec{R} is the configuration space vector, v_{\parallel} the parallel velocity and $\mu = v_{\perp}^2/2B$ the magnetic moment per mass of the gyrocentre. The configuration space $\vec{r} = [x, y, z]$ has a 3D sheared-slab geometry which spans $\vec{r} \in [0, L_x] \times [0, L_y] \times [0, L_z]$, where the Cartesian coordinates $[x, y, z]$ can be related to the radial, poloidal, and toroidal directions, respectively, of a tokamak system. Periodic boundary conditions are thus imposed in the y - and z - directions, which span $L_y = \pi a$ and $L_z = 2\pi R_0$, respectively, with a the minor radius and R_0 the major radius. The sheared equilibrium magnetic field as illustrated in Fig. 4.1 is given analytically by

$$\begin{aligned} \vec{B}(x) &= B_y(x)\mathbf{e}_y + B_z\mathbf{e}_z \\ B\hat{b} &= B_z \left[\frac{L_y}{L_z q(x)} \mathbf{e}_y + \mathbf{e}_z \right], \end{aligned} \quad (4.1)$$

where \hat{b} is its direction, and $q(x)$ is the safety factor profile. Like $\vec{B}(x)$, all background profiles of this chapter will only depend on the radial position x , plus time t where relevant.

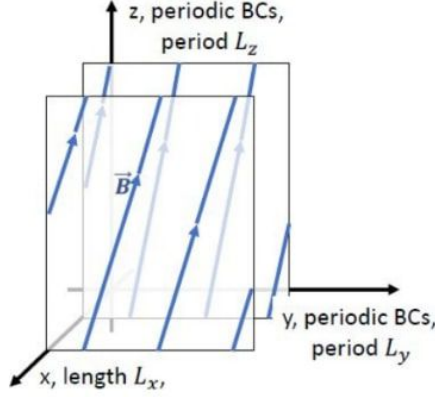


Figure 4.1: The sheared-slab magnetic geometry (see Eq. (4.1)) used for simulations of this chapter.

All fluctuations considered are electrostatic, and therefore the evolution of the gyrocentre phase space coordinates are given by

$$\begin{aligned} \frac{d\vec{R}}{dt} &= v_{\parallel} \hat{b} + \frac{\mu}{eB_{\parallel}^*} \hat{b} \times \nabla B + \frac{1}{B_{\parallel}^*} \hat{b} \times \nabla \tilde{\phi}, \\ \frac{dv_{\parallel}}{dt} &= -\frac{e}{m_i} \hat{b} \cdot \nabla \tilde{\phi}, \\ \frac{d\mu}{dt} &= 0. \end{aligned} \quad (4.2)$$

Here $B_{\parallel}^* = B[1 + m_i B'_y B_z v_{\parallel} / (eB^3)]$, and $\tilde{\cdot}$ is the gyroaveraging operator given by Eq. (2.21). The set of Eq. (4.2) is nonlinear as these equations depend on the self-consistent electrostatic potential $\phi(x, y, z)$ satisfying the quasi-neutrality equation, Eq. (2.39).

In order to simulate physics under strong profile gradients in quasi-steady state, heat sources are implemented to clamp ion temperature T_i at profile edges to prevent relaxation below critical gradients. This Krook-like source S_H of Eq. (3.81) with associated relaxation rate $\gamma_h(x)$ is stationary and radially dependent, maintaining over time the high and low ends of the T_i profile of the initial background distribution function $f_0(t = 0)$. Particle sources are not needed as there is no density profile relaxation. The assumed adiabatic electron response indeed enables no particle transport. Therefore, the correction term S_H^c of Eq. (3.84) to S_H includes the density and parallel momentum v_{\parallel} conservation. A Krook noise control operator S_K is also used here, with f_K the distribution function towards which it relaxes, a correction term S_K^c that conserves density, parallel momentum v_{\parallel} and energy v^2 .

Taken these sources together, the Vlasov equation, Eq. (2.24) expands to

$$\begin{aligned} &\left\{ \frac{\partial}{\partial t} + \frac{d\vec{R}}{dt} \cdot \nabla_{\vec{R}} + \frac{dv_{\parallel}}{dt} \frac{\partial}{\partial v_{\parallel}} + \frac{d\mu}{dt} \frac{\partial}{\partial \mu} \right\} f \\ &= -\gamma_h(x)[f - f_0(t = 0)] + S_H^c - \gamma_K(f - f_K) + S_K^c. \end{aligned}$$

4.2 Time-dependent control variate

The control variate for the work of this chapter has the form of a (local) Maxwellian function

$$\begin{aligned} f_0 &= f_M(X, v_{\parallel}, \mu, t) \\ &= \frac{n_{0i}(X)}{[2\pi T_{0i}(X, t)/m]^{3/2}} \exp\left[-\frac{v_{\parallel}^2/2 + \mu B(X)}{T_{0i}(X, t)/m_i}\right], \end{aligned} \quad (4.3)$$

with a background ion temperature profile $T_{0i}(X, t)$ as a function of the gyrocentre radial coordinate X and time t . Indeed, no density adaptation is necessary as no particle transport is expected. The time-dependence of f_0 thus only appears through $T_{0i}(X, t)$, which is governed by the ad-hoc equation, similar to Eq. (3.47),

$$\frac{\partial}{\partial t} \left(\frac{3}{2} n_{0i}(X) T_{0i}(X, t) \right) = \alpha_E \left\langle \int d^3v \left(\frac{v_{\parallel}^2}{2} + \mu B \right) \right\rangle, \quad (4.4)$$

which l.h.s. represents the variation in time of the background ion kinetic energy density $E_{kin0}(x, t)$ (per mass) related to f_0 ,

$$E_{kin0}(x, t) = \frac{3}{2} n_{0i}(x) T_{0i}(x, t),$$

with

$$T_{0i}(x, t) = T_{0i}(x, 0) + \delta T_{0i}(x, t)$$

and

$$\delta E_{kin0}(x, t) = \frac{3}{2} n_{0i}(x) \delta T_{0i}(x, t).$$

Here, $\delta E_{kin0}(x, t)$ and $\delta T_{0i}(x, t)$ are the deviations of the background ion kinetic energy and temperature profiles from their initial states $E_{kin0}(x, 0)$ and $T_{0i}(x, 0)$, respectively. The flux-surface-averaging operator $\langle \cdot \rangle$ in sheared-slab geometry simplifies (see Eq. (2.12)) to

$$\langle \phi \rangle(x, t) = \frac{1}{L_y L_z} \int_0^{L_y} dy \int_0^{L_z} dz \phi(x, y, z, t).$$

The explicit contributions from f_0 and δf to the QNE with an adiabatic electron response then becomes

$$\begin{aligned} & \frac{en_0(x)}{T_e(x)} [\phi(x, y, z, t) - \langle \phi \rangle(x, t)] - \nabla_{\perp} \cdot \left(\frac{m_i n_{0i}(x)}{e B^2(x)} \right) \\ &= \int \frac{d\alpha}{2\pi} \int d\Omega \delta[\vec{R} + \vec{\rho} - \vec{r}] \cdot [f_0(X, v_{\parallel}, \mu, t) - f_0(X, v_{\parallel}, \mu, 0) + \delta f(\vec{Z}, t)]. \end{aligned} \quad (4.5)$$

As with Eq. (2.34) the perpendicular gradient of Eq. (4.5), $\nabla_{\perp} \approx \nabla_{\text{pol}} = \mathbf{e}_x \partial_x + \mathbf{e}_y \partial_y$ has been approximated to the gradient in the (x, y) -plane (corresponding to the poloidal plane in a tokamak) due to the fact that micro-instabilities align along field lines and assuming $B_y/B_z = L_y/[L_z q(x)] \ll 1$. Since f_0 of Eq. (4.3) has an analytic form, the v_{\parallel} -integration is carried out analytically, and the μ - and α - integrations are done using quadratures. The convergence of this integration scheme is detailed in App. B. For this work, 30 quadrature points for each of these two dimensions were used.

4.3 Profiles and simulation parameters

Let the normalised radial coordinate be $s = x/L_x \in [0, 1]$. The profiles representing the initial unperturbed ion and electron background densities, n_0 , as well as their temperatures T_{0i} and T_{0e} , respectively, are parametrised by three parameters given by amplitude A , the normalised absolute maximum logarithmic gradient $\bar{\kappa}$, and the slope half-width $\bar{\Delta}$. For $s \in [0, 0.5]$, such a profile $G(s)$ is given explicitly by

$$G(s; \kappa, \Delta) = \begin{cases} A \exp\left(\frac{2\bar{\kappa}\bar{\Delta}}{3}\right) & 0 \leq s < s_0 - \bar{\Delta}, \\ A \exp\left[-\bar{\kappa}(s - s_0) + \frac{\bar{\kappa}(s - s_0)^3}{3\bar{\Delta}^2}\right] & |s - s_0| \leq \bar{\Delta}, \\ A \exp\left(-\frac{2\bar{\kappa}\bar{\Delta}}{3}\right) & s_0 + \bar{\Delta} < s \leq 0.5. \end{cases}$$

Note that this definition ensures that $g(s)$ and $\frac{dg}{ds}$ are both continuous. At the reference radial position $s = s_0$, it has a value of A , and its parabolic normalised logarithmic gradient peaks at this same point with value $\bar{\kappa}$.

The heat source radial profile γ_h is parameterised by the amplitude A_H , and the half-widths $\bar{\delta}_c$ and $\bar{\delta}_s$ of the clamp maximum and edge-slope regions, respectively., with $\bar{\delta}_c \geq \bar{\delta}_s$. This profile for $s \in [0.0, 0.5]$ is given explicitly by

$$\gamma_h(s; \bar{\delta}_c, \bar{\delta}_s) = \begin{cases} A_H & 0 \leq s < \bar{\delta}_c - \bar{\delta}_s \\ \frac{A_H}{2} \left[1 - \frac{3}{2} \left(\frac{s - \bar{\delta}_c}{\bar{\delta}_s} \right) + \frac{1}{2} \left(\frac{s - \bar{\delta}_c}{\bar{\delta}_s} \right)^3 \right] & |s - \bar{\delta}_c| \leq \bar{\delta}_s \\ 0 & \bar{\delta}_c + \bar{\delta}_s < s \leq \frac{1}{2} - (\bar{\delta}_c + \bar{\delta}_s) \\ \frac{A_H}{2} \left[1 + \frac{3}{2} \left(\frac{s - (1/2 - \bar{\delta}_c)}{\bar{\delta}_s} \right) - \frac{1}{2} \left(\frac{s - (1/2 - \bar{\delta}_c)}{\bar{\delta}_s} \right)^3 \right] & |s - (\frac{1}{2} - \bar{\delta}_c)| \leq \bar{\delta}_s \\ A_H & \frac{1}{2} - (\bar{\delta}_c - \bar{\delta}_s) < s \leq 0.5. \end{cases} \quad (4.6)$$

The noise control profile is uniform and is parameterised by as single parameter $\gamma_n = A_n$.

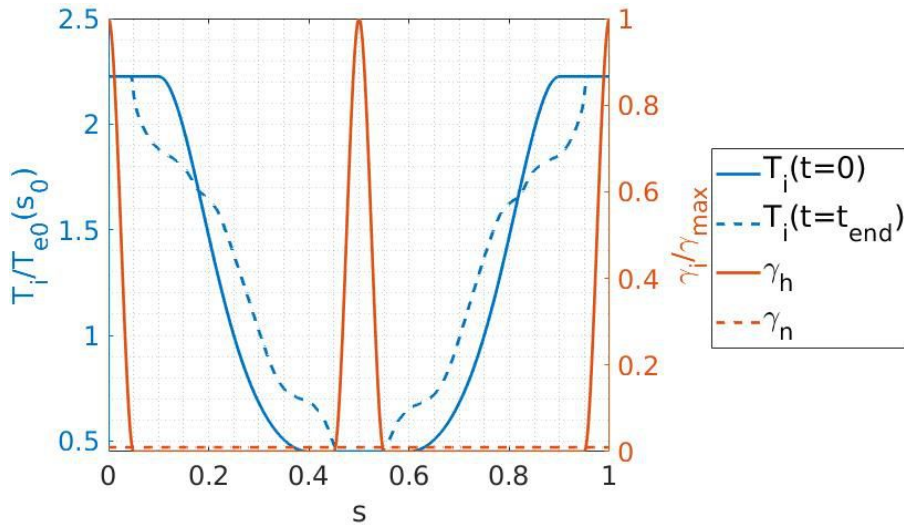


Figure 4.2: Symmetrised profiles used for this chapter. Blue: Initial (solid) and typical final (dashed) T_i . Red: Heat γ_h (solid) and noise control γ_n (dashed).

To avoid spurious marker build-up at the radial domain boundaries for long-time simulations with large κ under Dirichlet boundary conditions $\phi(s=0) = \phi(s=1) = 0$, all radial profiles are mirrored about $s = 0.5$, and periodic boundary conditions are imposed. Examples of such profiles, along with heat source and noise control operator profiles, are shown in Fig. 4.2. Henceforth for this chapter, only profiles from the left half will be shown, i.e. for $s \in [0.0, 0.5]$.

The GKengine code works in units such that time and speeds are normalised to $\Omega_c^{-1} = m_i/eB(s_0)$ and $c_s = \sqrt{T_e(s_0)/m_i}$ ($Z = 1$), representing the inverse ion cyclotron frequency and ion sound speed at $s_0 = 0.25$, respectively, which together gives the ion sound Larmor radius $\rho_s = c_s/\Omega_{ci}$ for units of length. The magnetic and potential fields are normalised to B_z , and $T_{0e}(s_0)/e$ respectively. To simulate slab-ITG instabilities, we use the major and minor radii values of $R_0 = 243.5\rho_s$ and $a = 66.4\rho_s$. The spatial domain is $L_x = 2a$ for an x -periodic profile, $L_y = \pi a$ and $L_z = 2\pi R_0$. The grid-cells number for ϕ is $(N_x, N_y, N_z) = (256, 512, 128)$. The time step used here is $\Delta t = 20\Omega_c^{-1} = 0.15L_x/c_s$. The safety factor is given by $q(s) = 1.25 + 12s^2$ for the half-domain $s \in [0.0, 0.5]$, and mirrored in the other half-domain. All normalised parameters describing profiles are converted to physical units via a multiplication/division by L_x . The initial profile gradients used in this paper are summarised in Tab. 4.1. These parameters correspond to $\eta_i(s_0) = \frac{\bar{\kappa}_T}{\bar{\kappa}_n} = 10$, and a peak value of ion temperature T_i logarithmic gradient of $|d \log T_i(s_0)/dx| = 4.0/a$, that is, $R_0/L_T = 14.6$.

| Parameter | Value |
|---------------------|-------|
| $\bar{\kappa}_n$ | 0.800 |
| $\bar{\delta}_n$ | 0.300 |
| $\bar{\kappa}_T$ | 8.000 |
| $\bar{\delta}_T$ | 0.150 |
| A_H/γ_{\max} | 1.000 |
| $\bar{\delta}_c$ | 0.025 |
| $\bar{\delta}_s$ | 0.025 |
| A_n/γ_{\max} | 0.030 |

Table 4.1: Equilibrium and heating profile parameters. Ions and electrons share identical equilibrium density and temperature profiles. The maximum linear growth rate $\gamma_{\max} = 1.169 \times 10^{-3}\Omega_{ci} = 0.155c_s/L_x$ is assumed, based on Fig. 4.3.

For the ‘toroidal’ direction (z), we chose to resolve modes in the range of $[n_{\min}, n_{\max}] = [0, 32]$, and ‘poloidal’ modes m determined by the field-aligned Fourier-filter $|nq(s) + m| \leq \Delta m$, with $\Delta m = 5$ [45]. All simulations are initialised with $f_{00} + \delta f(t=0)$. The initial background is taken to be $f_{00} = f_{M0}$, where $f_{M0} = f_M(\vec{R}, v_{\parallel}, \mu, 0)$. The control variate at initial time is also taken to be the initial background $f_0(t=0) = f_{00}$. $\delta f(t=0)$ represents a density perturbation of amplitude 10^{-4} and toroidal mode number $n = 7$ corresponding to the strongest growing linear mode. The poloidal modes initialised are those within the field-aligned filter at $s = s_0$, i.e. $|7q(s_0) + m| \leq 5$.

Unless otherwise stated, all cases in this chapter are run with $N_p = 256M$ (which is about 15 markers per cell) and adaptive background cases consider the relaxation rate $\alpha_E = 1.92\gamma_{\max}$. The number of time steps after which the background temperature profile is adapted via Eq. (4.4), is set to $N_\alpha = 10$ for all cases.

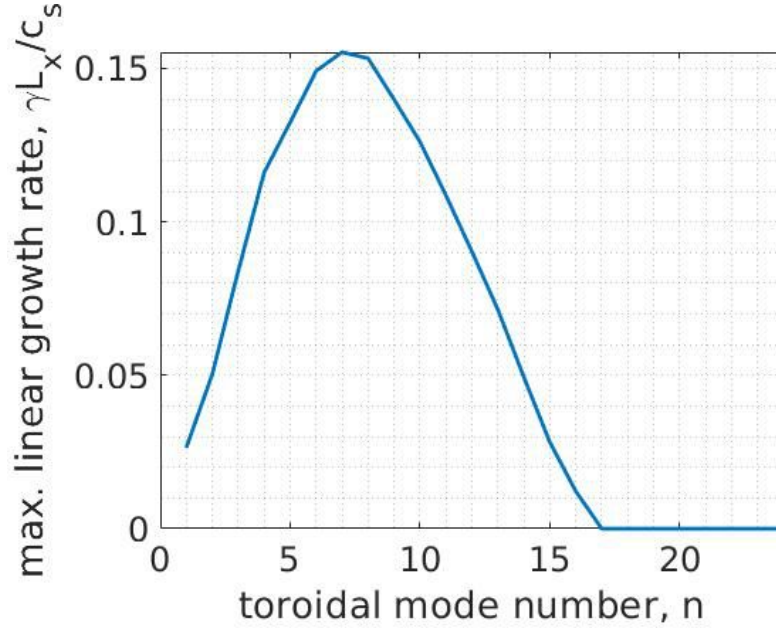


Figure 4.3: Maximum growth rate of linear modes as a function of each toroidal mode number n , for normalised ion temperature logarithmic gradient $a |d \log T_i / dx| = 4.0$ and $(d \log T_i / dx) / (d \log n / dx) = 10$. The poloidal mode number m is radially dependent and is determined by the Fourier filter.

4.4 Results

4.4.1 Marker convergence

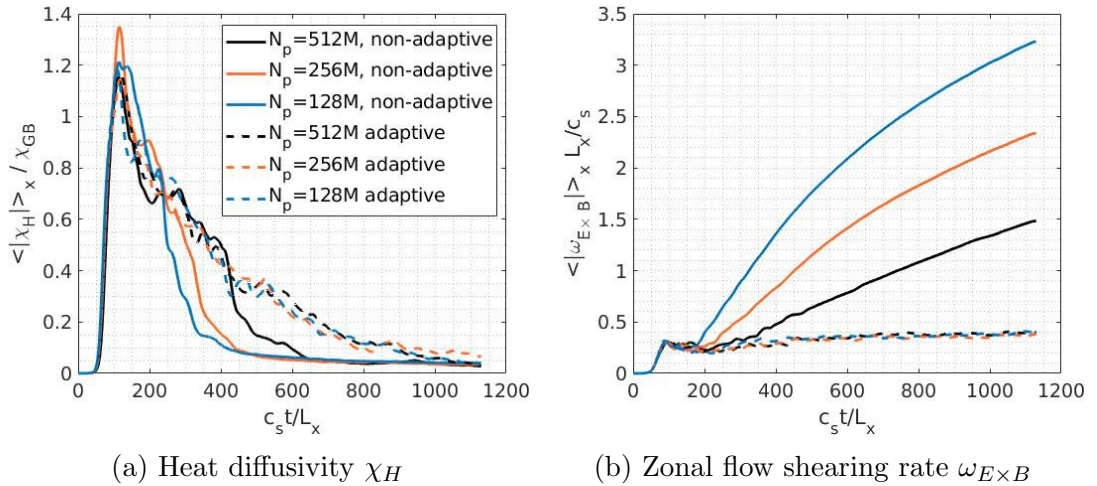


Figure 4.4: Time traces for various marker numbers, considering the non-adaptive and adaptive cases. The adaptive rate is set to $\alpha_E = 1.92 \gamma_{\max}$ where applicable. A moving time-averaging window of half-width $c_s t / L_x = 10$, which is equivalent to $\gamma_{\max} t = 1.6$, has been implemented.

Characteristic of all simulations is a turbulent burst in the initial phase of the simulation ($0 < c_s t / L_x < 300$) represented by a spike in the radially averaged heat

flux q_H and diffusivity χ_H , expressed by

$$\chi_H(t) = \left\langle \left| \frac{q_H(x, t)}{n_{0i}(x) \frac{\partial T_i(x, t)}{\partial x}} \right| \right\rangle_x.$$

χ_H is represented in gyroBohm units, $\chi_{GB} = \rho_s^2 c_s / L_x$ with reference to the radial position of steepest initial profile gradient, i.e. $s = s_0$. All radial averaging in this paper is done outside the heat source profile of Eq. (4.6), namely $s \in [0.025, 0.475] \cup [0.525, 0.975]$. Fig. 4.4 shows how turbulence is quenched for the non-adaptive cases by increasing zonal flow shearing rate $\omega_{E \times B}$. The latter is estimated by

$$\omega_{E \times B} = \frac{1}{B} \frac{d^2 \phi_{00}}{dx^2},$$

where, $\phi_{mn}(x)$ is in general the Fourier component of the electrostatic field corresponding to poloidal (y) mode m and toroidal (z) mode n , $\phi_{00}(x)$ thus being the zonal component. As can be seen in Fig. 4.4b, the very significant rise in $|\omega_{E \times B}|$ for non-adaptive simulations is dependent on the number of markers, N_p , and is thus of numerical origin. We note that even though the rise is reduced by increasing N_p , the simulation is far from having converged even for the largest $N_p = 512\text{M}$ considered. We interpret the rise in $|\omega_{E \times B}|$ as resulting from the statistical sampling noise accumulation in the zonal components, which are not physically damped [18]. As expected, the accumulated noise is highest for the case with lowest N_p . Corresponding un-physically large $\omega_{E \times B}$ levels lead to large eddy shearing and reduced transport. The time of χ_H collapse is correlated to $|\omega_{E \times B}|$, reaching a value comparable to $3\gamma_{\max} L_x / c_s$, thus the sequence of rises of $\omega_{E \times B}$ in Fig. 4.4b correspond to the sequence of falls of χ_H in Fig. 4.4a for the three non-adaptive cases. On the other hand, for the adaptive case, the converged results show that $\omega_{E \times B}$ increases at a much slower rate with time, resulting in a somewhat longer sustained flux. One notes that these converged fluxes nonetheless ultimately drop to zero as seen in Fig. 4.4a.

To further confirm that low marker numbers lead to an increase in zonal $\omega_{E \times B}$ levels due to noise accumulation, Fig. 4.5a shows the radially averaged absolute value of $\omega_{E \times B}$ at the initial time $t = 0$ against marker number N_p . All simulations are initialised with a density perturbation defined as including only $n \neq 0$ Fourier modes. Despite that, due to the finite and random marker number representation of δf , there is a resulting spurious finite zonal, $(m, n) = (0, 0)$, $\omega_{E \times B}$ profile, whose amplitude increases with decreasing number of markers as $\sim 1/\sqrt{N_p}$, as expected due to statistical sampling error. The magnitude of the corresponding zonal flow shearing rate $\omega_{E \times B}$ is then further increased at every time step. Thus, lower marker numbers lead to larger noise accumulation in $\omega_{E \times B}$ with time, which leads to Fig. 4.5b for end-time values of $\omega_{E \times B}$. Assuming linear increment, Fig. 4.5 indicates that the rate of increase of $\omega_{E \times B}$ is $d\omega_{E \times B}/dt \approx 2.12 \times 10^{-3} c_s^2 / L_x^2$ for $N_p = 256\text{M}$. For non-adaptive cases, the general trend of lower zonal $E \times B$ shearing with increasing N_p is apparent. The end-time $\omega_{E \times B}$ value is expected to plateau at higher N_p values, but this limit is not reached for the maximum marker number considered, $N_p = 512\text{M}$. This converged value would represent the zonal $\omega_{E \times B}$ derived from the physics of the problem, and not the result of the accumulation of noise. On the other hand, the adaptive cases show much lower and similar end-time $\omega_{E \times B}$ values throughout all N_p values considered in the different simulations.

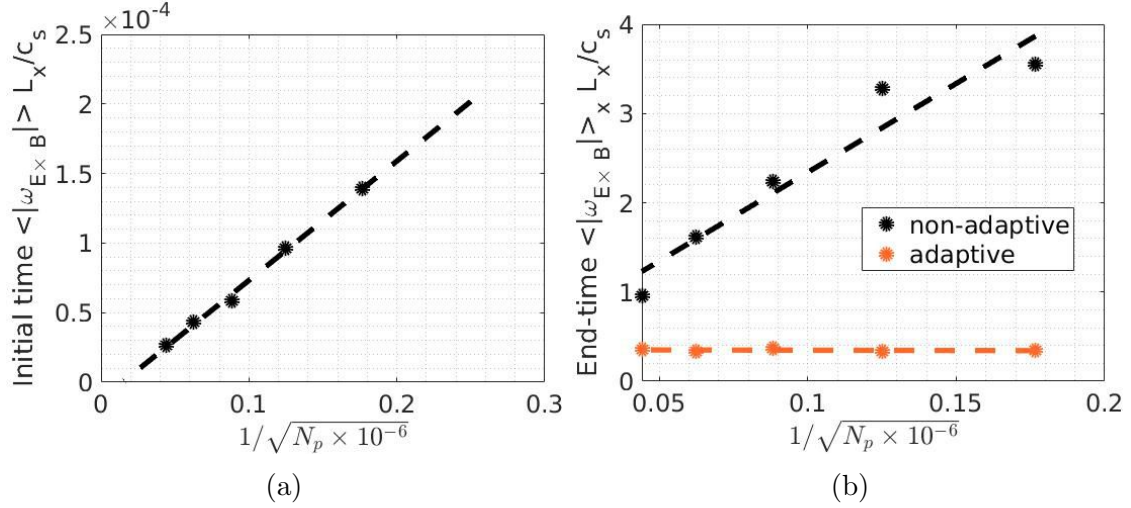


Figure 4.5: Radial averaged absolute value of the zonal flow shearing rate $\omega_{E \times B}$ at (a) initial time $c_s t/L_x = 0$ and (b) end-time $c_s t/L_x = 753$, as a function of the inverse square root of marker number N_p . The adaptive case (orange) adapts at a rate $\alpha_E = 1.92\gamma_{\max}$. All simulations are initialised with perturbations with toroidal mode $n \neq 0$.

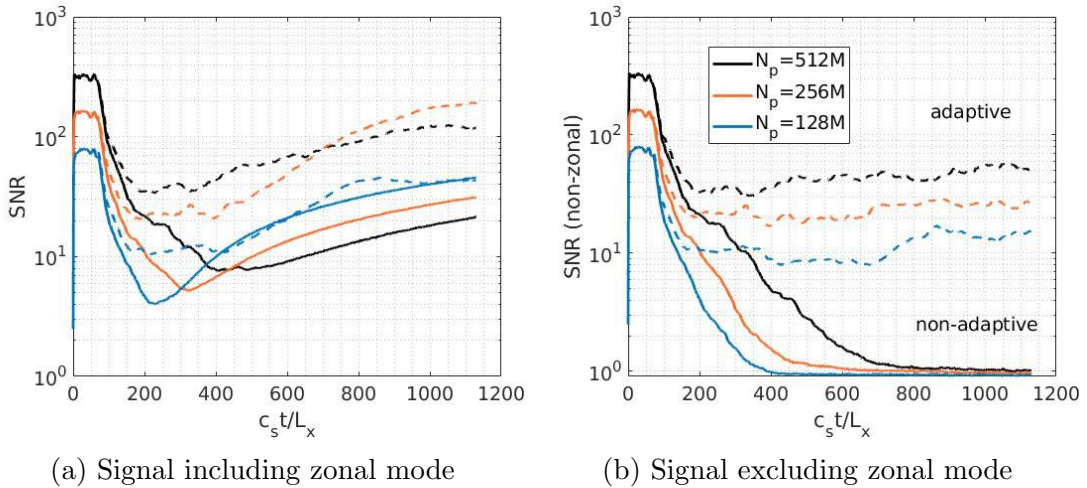


Figure 4.6: Signal-to-noise ratio (SNR) time traces for signal (a) including (see Eqs. (3.27)) and (b) excluding (see Eq. (3.28)), the $(m, n) = (0, 0)$ mode, for increasing marker number N_p , and considering both the non-adaptive (solid line) and adaptive (dashed line) cases.

From Fig. 4.6a, non-adaptive cases start from high SNR values and gradually drop to their respective lowest point after the initial burst $c_s t/L_x \sim 300$. N_p is reflected in the maximum of SNR values for each case, which the latter seem to scale as $1/N_p$. The adaptive cases follow a similar trend, but do not fall as low. From past works [62, 9], the rule-of-thumb SNR threshold of 10 is a value above which the results can be deemed reliable. Therefore, we can see that only the adaptive cases with $N_p = 256M, 512M$ meet this criterion throughout the whole simulation. All SNR values eventually rise with time, with the non-adaptive case at $N_p = 128M$ rising the quickest. This reflects the noise accumulation in the physically undamped

zonal component. Indeed, by subtracting the zonal component from the signal, Fig. 4.6b shows that the non-adaptive case with $N_p = 128M$ gives the lowest SNR value throughout the simulation. Thus, for this set of parameters, only the results from the adaptive case with $N_p = 256M$ or $N_p = 512M$ may be deemed reliable.

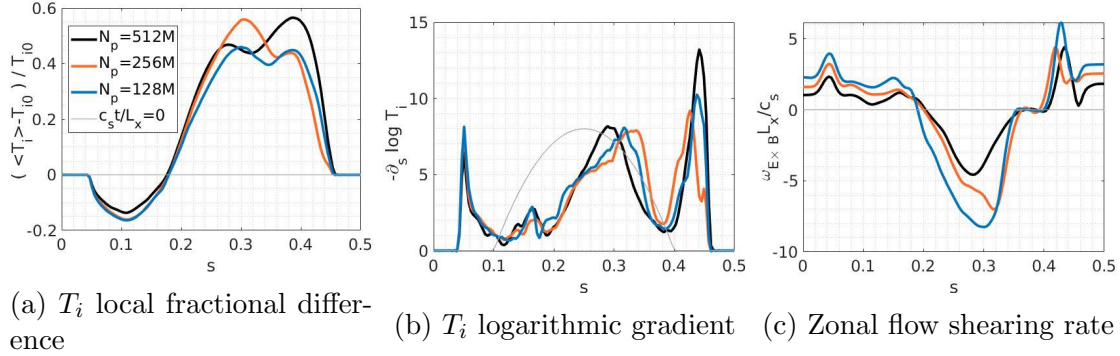


Figure 4.7: F.s.a. profiles at quasi-steady state averaged over a time interval of $c_s t / L_x \in [1030, 1130]$ for various marker numbers N_p under the non-adaptive scheme for the ion temperature (a) relative deviation with respect to background $[\langle T_i \rangle(s) - T_{0i}(s)] / T_{0i}(s)$ and its (b) logarithmic gradient $-\partial_s \log T_i(s)$, and the (c) zonal flow shearing rate $\omega_{E \times B}$.

Figs. 4.7 and 4.8 show the f.s.a. profiles at the end of the simulations for the zonal flow shearing rate $\omega_{E \times B}$, the ion temperature $\langle T_i \rangle$ relative deviation $(\langle T_i \rangle - T_{0i}) / T_{0i}$, and its logarithmic gradient for different total number N_p of markers, under the non-adaptive and adaptive cases, respectively. It should be noted that the maximum relative deviation value for T_i of around 60% in Fig. 4.7a for the non-adaptive cases challenges the δf assumption of $\|\delta f\| / \|f_0\| \ll 1$. For the adaptive case in Fig. 4.8a however, the relative deviation of $\langle T_i \rangle$ from the adapted background temperature $T_{0i}(t)$, which remains low at all times, qualifies. One notes also that the adaptive cases in fact resulted in f.s.a. T_i profiles with a larger deviation of 100%, from its initial state, as shown in Fig. 4.8b. This shows that the adaptive scheme appears to allow for simulations with more accurate profile evolution in case of large deviations, not afforded by the standard scheme. One notes also the development of strong T_i gradients at $s = 0.05$, just outside the heat source for the non-adaptive case (see Fig. 4.7). This is suspected to be related to spurious marker accumulation by error in drift calculation, whose magnitude reduces with increasing N_p . Under the adaptive scheme, this problem does not occur.

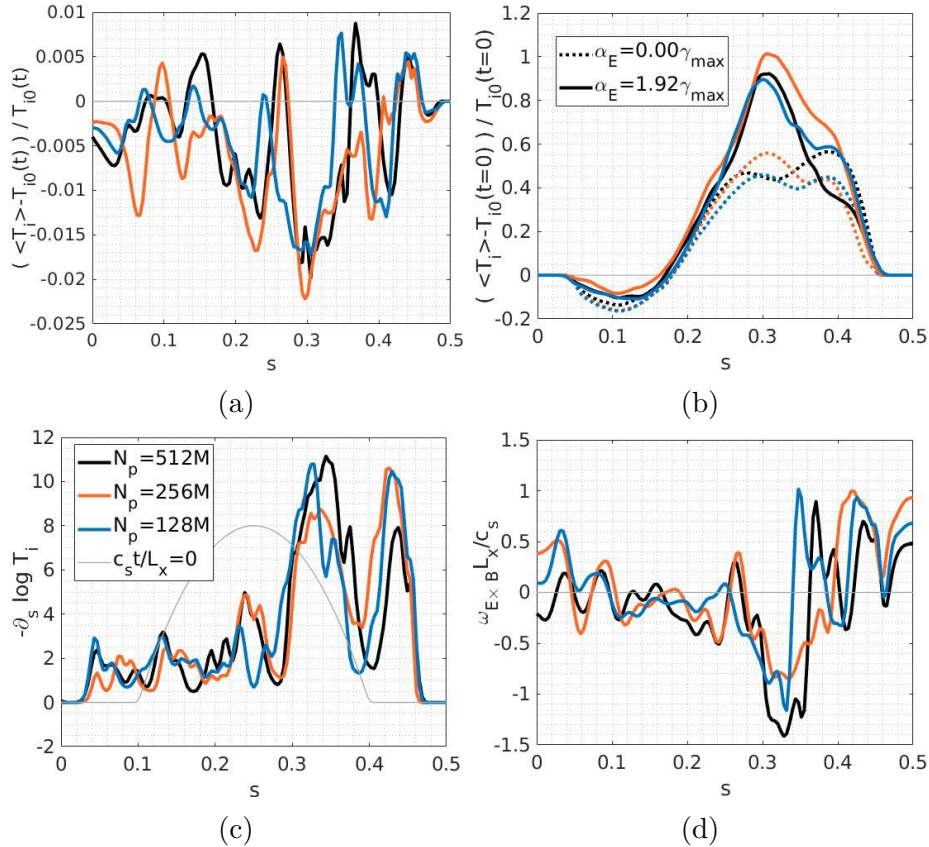


Figure 4.8: F.s.a. profiles at quasi-steady state averaged over a time interval of $c_s t/L_x \in [1030, 1130]$ for various marker numbers N_p under the adaptive scheme with adaptive rate $\alpha_E = 1.92\gamma_{\max}$ for the ion temperature (a) relative deviation with respect to adapted background, (b) relative deviation with respect to background at initial time $t = 0$, its (c) logarithmic gradient, and the (d) zonal flow shearing rate.

4.4.2 Adaptive control variate and noise control

Tentatively, two mechanisms contribute to the improvement of SNR with the adaptive scheme: (a) the adapted $f_0(t)$ as a good control variate; (b) the noise control operator S_n of the non-adapted scheme, which tends to bring f back¹ towards the initial distribution f_{00} , whereas in the adapted scheme it tends to relax f towards the time-evolved f_0 , which is closer to the time-averaged f , especially at late times. To study the relative importance of the adaptive scheme and the noise control, we varied in this section the control variate f_0 , both in the framework of the adaptive delta- f scheme, Eq. (2.31), and in the reference function f_n of the noise control operator i.e. $S_n = -\gamma_n(f - f_n)$.

All simulations begin with $f = f_{M0} + \delta f(t = 0)$, where $\delta f(t = 0)$ represents a small perturbation and the control variate f_0 is taken to be f_M (see Eq. (4.3)). By choosing different f_0 and f_n , four different adaptive scenarios can be constructed, depending on whether the adaptive scheme is used ($f_0 = f_{M0}$ or $f_0 = f_M(t)$) and whether adaptive noise control scheme is used ($f_n = f_{M0}$ or $f_n = f_M(t)$). Below, except for scenario 3, $f_M(t)$ adapts via T_{0i} from Eq. (4.3) according to Eq. (4.4).

¹Nonetheless, the noise control operator conserves lower order velocity moments (see Sec. ??)

1. non-adaptive δf scheme, non-adaptive f_n , labeled (no,no)

- $(f_0, f_n) = (f_{M0}, f_{M0})$

2. adaptive δf scheme, non-adaptive f_n , labeled (yes,no)

- $(f_0, f_n) = (f_M(t), f_{M0})$

3. non-adaptive δf scheme, adaptive f_n , labeled (no,yes)

- $(f_0, f_n) = (f_{M0}, f_M(t))$

- $f_n = f_0(t)$ is adaptive according to

$$\frac{\partial}{\partial t} \left(\frac{3}{2} n_{0i} T_{0i} \right) = \alpha_E \left\langle \int d\Omega [\delta f - (f_M(t) - f_{M0})] \right\rangle$$

- the adaptive scheme is run in the background to update $f_n = f_M(t)$, but the control variate $f_0 = f_{M0}$ remains time-independent.

4. adaptive δf scheme, adaptive f_n labeled (yes,yes)

- $(f_0, f_n) = (f_M(t), f_M(t))$

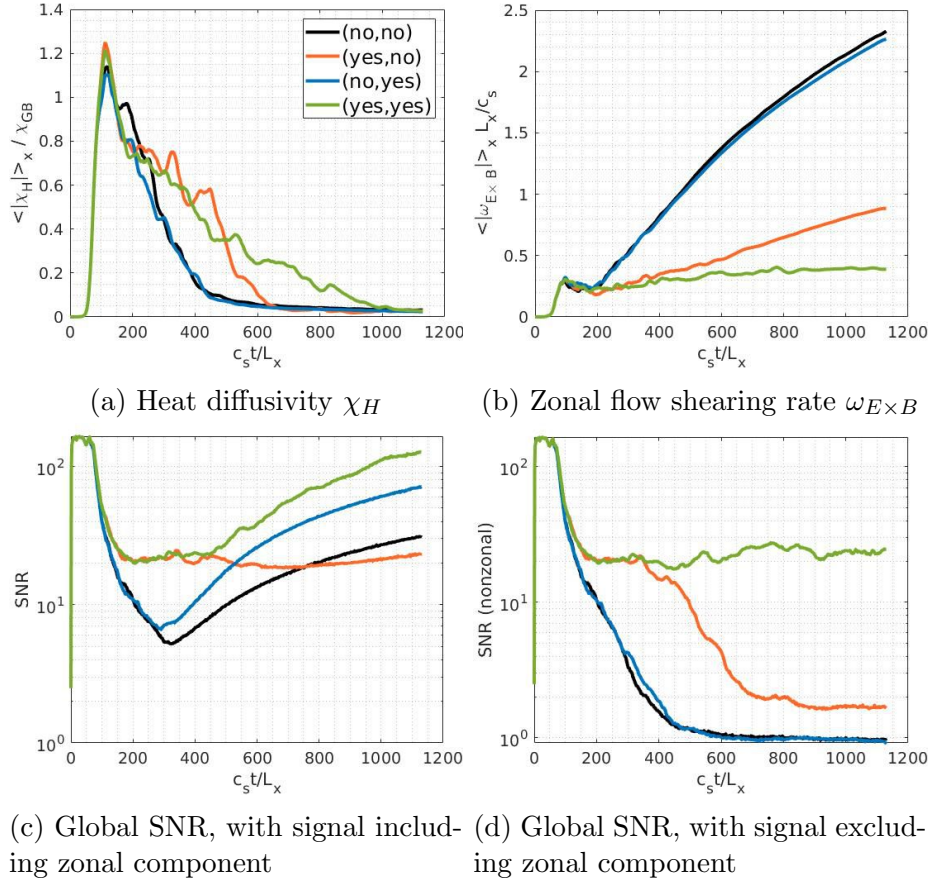


Figure 4.9: Diagnostics under four different adaptive scenarios (see description in text) for the radially averaged absolute (a) heat diffusivity χ_H and (b) zonal flow shearing rate $\omega_{E \times B}$, and the signal-to-noise (SNR) ratio with signal (c) including and (d) excluding, the $(m, n) = (0, 0)$ mode. Marker number set to $N_p = 256M$, and adaptive rate to $\alpha_E = 1.92\gamma_{\max}$ where applicable. A moving time-averaging window of half-width $c_s t / L_x = 10$ has been implemented.

Viewing the adaptive scheme as essentially a means to reduce noise, considering the different scenarios described allows one to determine which strategy is the most effective in this respect. Fig. 4.9 shows the effect of different adaptive scenarios on the simulation results. The adaptation of f_0 and/or f_n for the different scenarios are done at the same rate α_E . It can be seen that the full adaptive scheme with adaptive f_0 and f_n [scenario (yes,yes)], implying weight transfer from δf to f_0 of Eq. (3.61) and noise control only on the fluctuating part δf respectively, is necessary for effective noise control, as indicated by a reasonably high SNR value and a zonal flow shearing rate $\omega_{E \times B}$ value that does not increase indefinitely. For scenario (yes,no) with only the adaptive f_0 , noise control is effective only at an early stage when f is close to f_{M0} . As the former deviates away from the latter, S_n acts as a weak source, thus enlarging the δf component. The larger the portion of f that is represented by markers, the more noise accumulates. The weak improvement of scenario (no,yes), which is the stationary f_0 scheme with a time-dependent reference function $f_n = f_M(t)$, indicates that the improvement from weight transfer from δf to f_0 far out-weights an adaptive S_n .

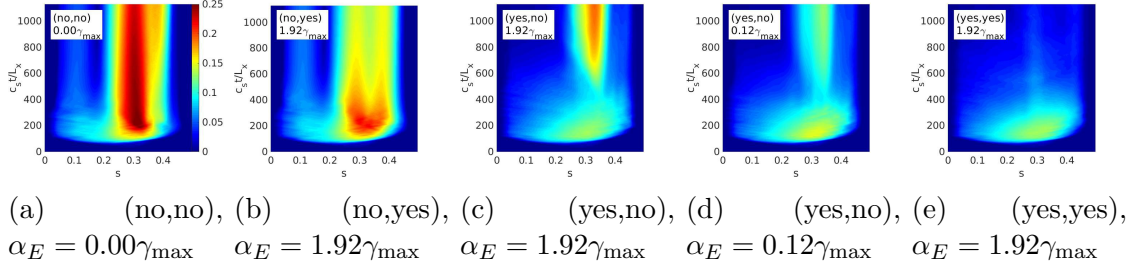


Figure 4.10: Local f.s.a. weight standard deviation σ_w through time under four different adaptive scenarios (see description in text), illustrated with the cases of (a) (no,no), (b) (no,yes) with $\alpha_E = 1.92\gamma_{\max}$, (c) (yes,no) with $\alpha_E = 1.92\gamma_{\max}$, (d) (yes,no) with $\alpha_E = 0.12\gamma_{\max}$, and (e) (yes,yes) with $\alpha_E = 1.92\gamma_{\max}$. σ_w is defined by $\sqrt{\sum_{p \in i} w_p^2 / N_i - (\sum_{p \in i} w_p / N_i)^2}$, with $N_i = N_p / N_x$ the average number of markers of the i^{th} radial bin, taken to be uniform for all bins. Marker number set to $N_p = 256\text{M}$. All figures share the same colour scale.

Noise can also be approached from the standard deviation of the f.s.a. weights σ_w , as shown in Fig. 4.10. Based on this measure, the full adaptive scheme (yes,yes) once again gives the best results, with low values of σ_w right after the burst at around $c_s t / L_x = 150$. One can see that σ_w as already plateaued for the non-adaptive case (no,no), whereas for the case (yes,no), the S_n acting as weak source continues to relax the distribution towards that at initial time. This is proved to be the case when see that a lower α_E value gives a smaller yet increasing σ_w value. Finally, the scenario (no,yes) with an adaptive noise control is able to continuously decrease σ_w values, but these values remain high after the burst, which may affect the results at late times.

A note on the inclusion of the $f_0(t) - f_0(t=0)$ term in Eq. (4.5) is in order. While some cases studied in this chapter do not involve a time-dependent background density, with reference to the full adaptive scheme [scenario (yes,yes)] described above, the exclusion of this extra term leads to a lower heat diffusivity, and a 17% increase in the zonal flow shearing rate at quasi-steady state, which in turn resulted in a lower final ion temperature deviation. Nonetheless, similar improvement in SNR and local f.s.a. weight standard deviation (see Fig. 4.10) have been observed.

4.4.3 Noise control strength and adaptive rate variations

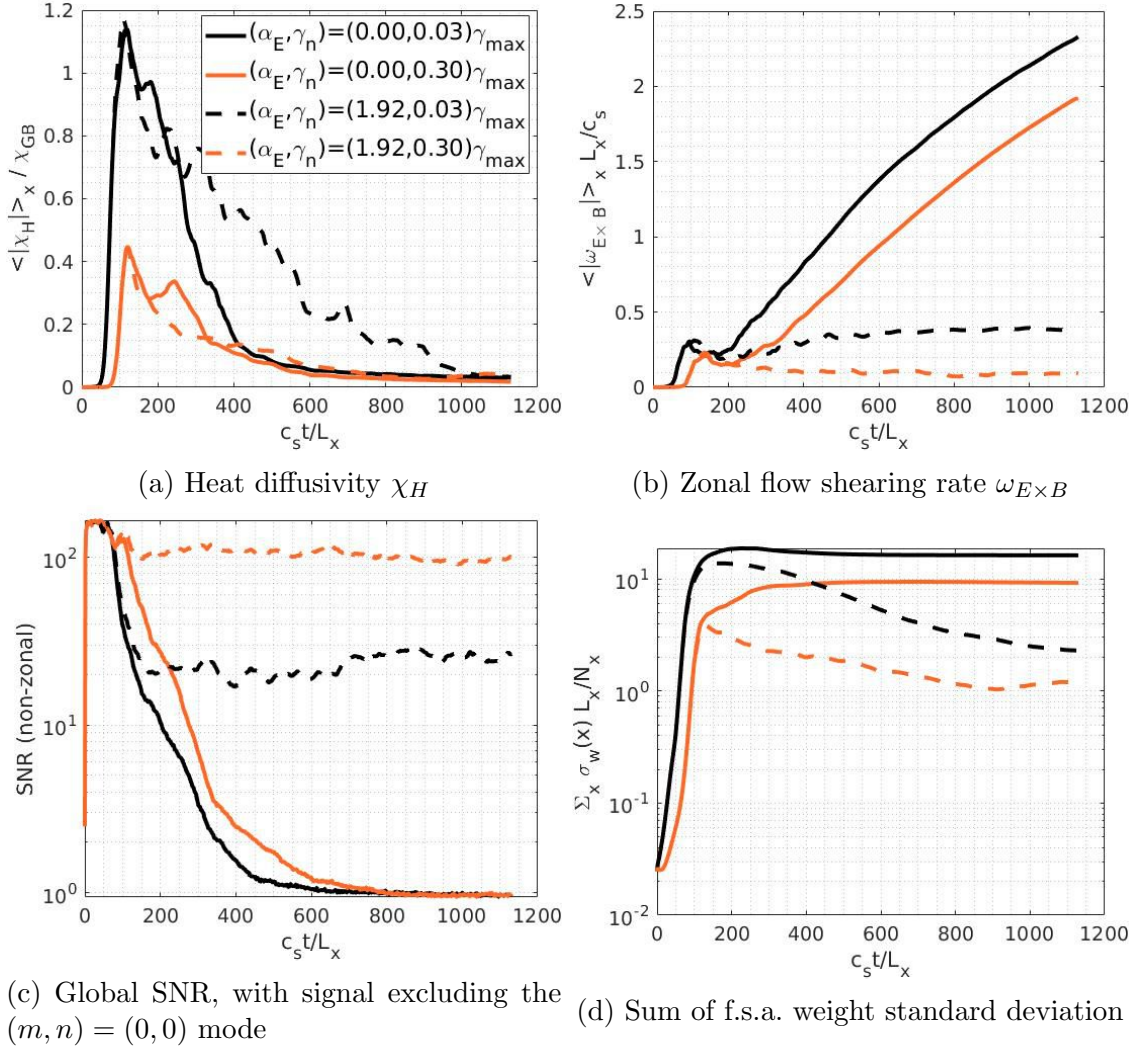


Figure 4.11: Diagnostics for various noise control strength γ_n considering both the non-adaptive and adaptive cases. Marker number set to $N_p = 256M$. The sum of f.s.a. weight standard deviation is calculated by summing the standard deviations of f.s.a. weights from each radial bin, and multiplying by the sum by L_x/N_x .

The purpose of the conservative noise control is to reduce the weight standard deviation at the expense of introducing numerical diffusion, thus affecting the validity of the simulation by adding artificial damping on the main instability drive and zonal flows. From Fig. 4.11a and 4.11b, it can be seen that at a larger γ_n value, both χ_H and $\omega_{E \times B}$ values are lower. Therefore, its amplitude γ_n should be adjusted just high enough to maintain a good SNR value throughout the simulation, taken in this work to be 10. Fig. 4.11c shows that $\gamma_n = 0.03\gamma_{\max}$ for the adaptive case is just enough, and it is this value of γ_n that is used in all other sections of the paper. For the non-adaptive case, it is seen that a high γ_n value only postpones the eventual decrease in SNR, implying that noise control alone, despite a time-dependent reference function f_n , is insufficient to prevent simulations being drowned in noise. Finally, the reduced weight standard deviation is shown in Fig. 4.11d. It is shown that S_n alone is insufficient to control noise to acceptable levels, while the adaptive

4.4. RESULTS

scheme is able to do so even in the presence of minimal noise control relaxation rate γ_n .

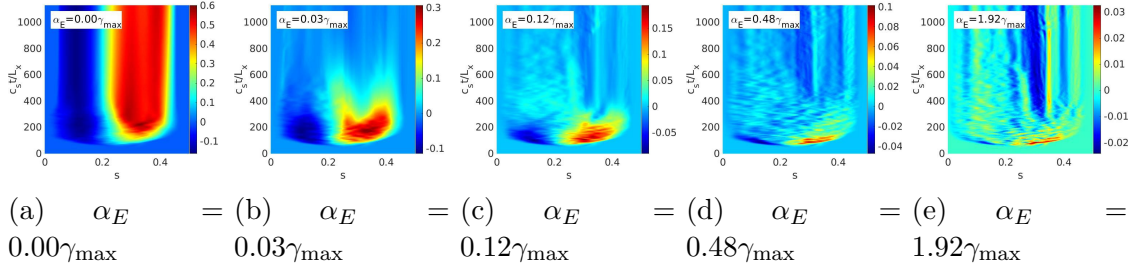
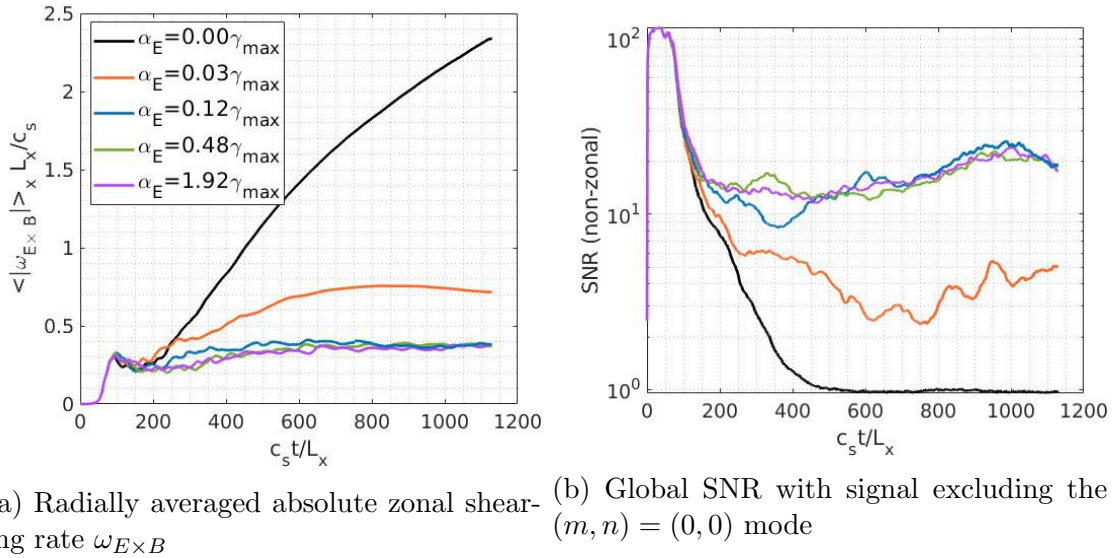


Figure 4.12: Time evolution of f.s.a. ion temperature relative deviation from its time-evolved adapted $T_{0i}(t)$, $(\langle T_i \rangle(x, t) - T_{0i}(x, t)) / T_{0i}(t)$ under various adaptive rates α_E . Marker number set to $N_p = 256M$.

Turning now to the choice of the adaptive rate α_E , from Eq. (4.4), the greater the α_E value, the greater the rate of transfer of the second velocity moment of the f.s.a. δf to the control variate, in this case, $f_0 = f_M(t)$. Fig. 4.12 shows that the maximum relative deviation of T_i from its time evolved adapted profile $T_{0i}(x, t)$ is lower with higher values of α_E . Also the decrease of the relative deviation after the initial burst is faster with increasing α_E . More specifically, Figs. 4.13a and 4.13b show that for $\alpha_E = 0.12\gamma_{\max}$ or higher, the simulation under given parameters is sufficient in terms of low zonal flow shearing rate $\omega_{E \times B}$ and high enough SNR values respectively. Therefore, under the parameters studied in this paper, any α_E value satisfying $\alpha_E > 0.12\gamma_{\max}$ and $\alpha_E N_\alpha \Delta t \leq 2$ gives results with the lowest noise accumulation. Here, N_α is the adaptation period.



(a) Radially averaged absolute zonal shearing rate $\omega_{E \times B}$

(b) Global SNR with signal excluding the $(m, n) = (0, 0)$ mode

Figure 4.13: Time traces with varying adaptation rates α_E . Marker number set to $N_p = 256M$.

4.4.4 Adjusting the f.s.a. potential term

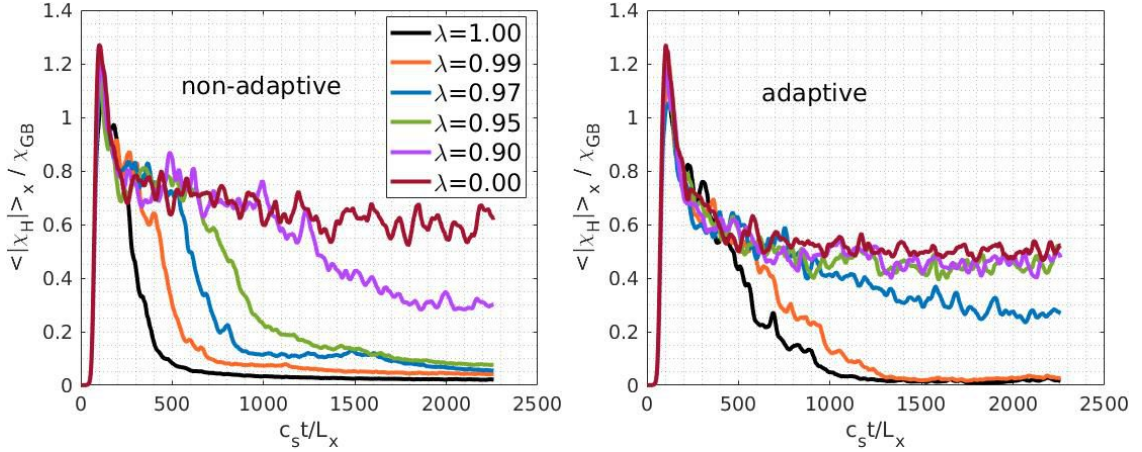
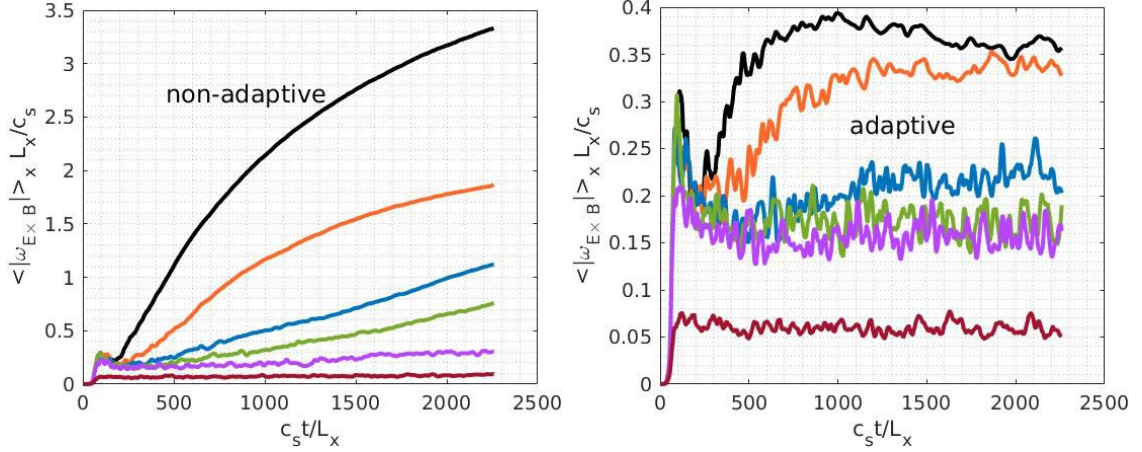
(a) Heat diffusivity χ_H : non-adaptive case(b) Heat diffusivity χ_H : adaptive case(c) Zonal flow shearing rate $\omega_{E \times B}$: non-adaptive case(d) Zonal flow shearing rate $\omega_{E \times B}$: adaptive case

Figure 4.14: Time traces under various tuning parameter λ (see Eq. (4.7)). The adaptive rate is set to $\alpha_E = 1.92\gamma_{\max}$. A moving time-averaging window of half-width $c_s t/L_x = 10$ has been implemented. Total number of markers is set to $N_p = 256M$.

In sheared-slab geometry with adiabatic electrons on the magnetic surfaces, ITG turbulence is strongly suppressed by zonal flows, resulting in a quasi-steady state with relatively low heat fluxes. In a real tokamak, much stronger heat fluxes and large relative fluctuation amplitudes are present in the plasma edge. In order to emulate such a situation but staying in slab geometry, the f.s.a. potential term $\langle \phi \rangle$ of the adiabatic electron response of Eq. (4.5) is tuned by defining a multiplicative parameter λ :

$$\begin{aligned}
 & \frac{en_0}{T_e} (\phi - \lambda \langle \phi \rangle) - \nabla_{\perp} \cdot \left(\frac{m_i n_0}{e B^2} \nabla_{\perp} \phi \right) \\
 &= \int d^3 R d\alpha dv_{\parallel} d\mu B_{\parallel}^* \delta[\vec{r} - (\vec{R} + \vec{\rho}_L(\mu, \alpha))] \times \\
 & [f_0(\vec{R}, v_{\parallel}, \mu, t) - f_0(\vec{R}, v_{\parallel}, \mu, 0) + \delta f].
 \end{aligned} \tag{4.7}$$

With $\lambda = 0.00$ [33, 79], the electrons respond adiabatically in all directions, i.e. not only in the magnetic surface, but also radially. This results in much lower $E \times B$ flows and thus higher turbulent heat fluxes.

Figure. 4.14 shows the effect of tuning λ on the heat diffusivity χ_H and zonal shearing rate $\omega_{E \times B}$. One can see that fluxes are sustained longer and higher due to a lower zonal flow shearing rate $\omega_{E \times B}$ from a greater attenuation of $\langle \phi \rangle$. This trend also exists for the adaptive cases, though $\omega_{E \times B}$ levels there are generally low as compared to the non-adaptive cases, see Fig. 4.14d. From Fig. 4.14b for the adaptive cases, the value of $\lambda = 0.95$ seems to be just sufficient to sustain the flux. Therefore, looking at the case of $\lambda = 0.95$ specifically, Fig. 4.15 shows that the result trend is similar to that of Fig. 4.4, albeit with lower levels of $\omega_{E \times B}$. Under this tuning, the non-adaptive cases (continuous lines) seem to evolve towards low χ_H values at long times, whereas the adaptive cases (dashed lines) are maintained at a higher χ_H value as compared to Fig. 4.4a. The adaptive cases seem to have converged already with $N_p = 128\text{M}$ markers whereas the non-adaptive case is still subject to collapse even with $N_p = 512\text{M}$ markers.

Fig. 4.16 shows that λ only affects the SNR values of the non-adaptive cases. Taking the standard non-adaptive case of $\lambda = 1.00$ as reference, the effect of higher attenuation of $\langle \phi \rangle$ only delays the eventual collapse of SNR values for each case, except for the case of complete $\langle \phi \rangle$ suppression, in which high SNR value and sustained flux (see Fig. 4.14a) are achieved. For a fixed value of $\lambda = 0.95$, besides the delayed fall of SNR values for the non-adaptive cases, Fig. 4.15b reflects the SNR value proportional to N_p relation, as was already shown in Fig. 4.6b. This convergence, instead of $\sqrt{N_p}$, is a result of taking the noise as a quadratic measure (see Eq. (3.27)).

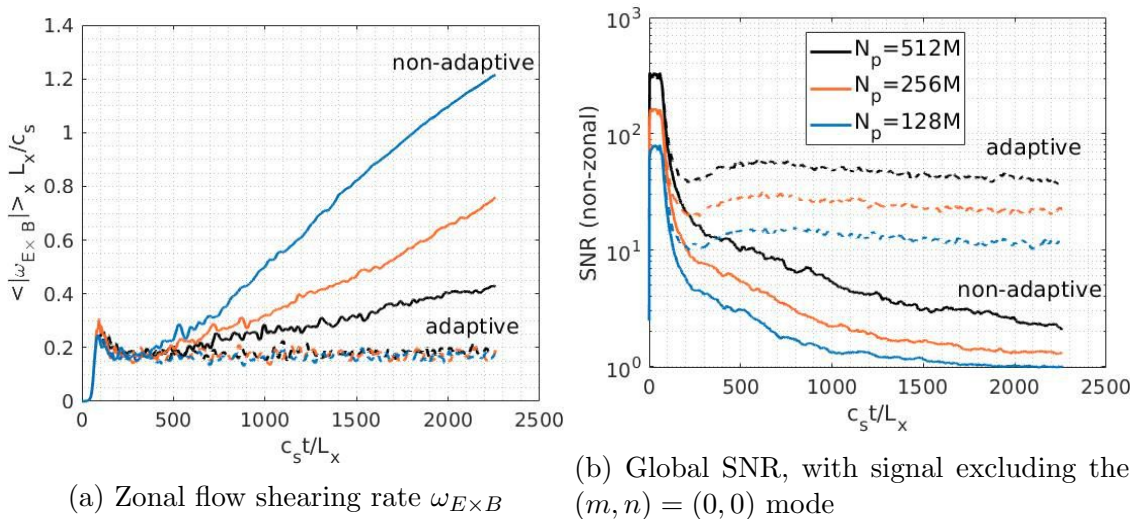


Figure 4.15: Time traces for various marker numbers N_p . The tuning parameter is set to $\lambda = 0.95$, and the adaptive rate is set to $\alpha_E = 1.92\gamma_{\max}$ where applicable. A moving time-averaging window of half-width $c_s t / L_x = 10$ has been implemented.

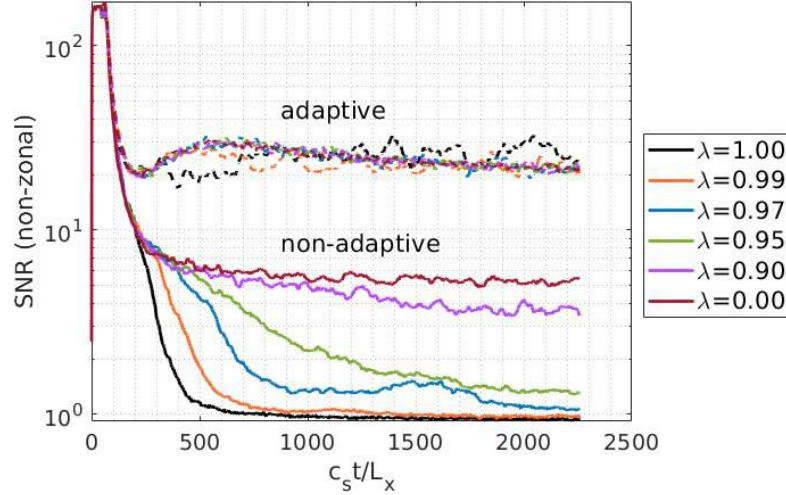


Figure 4.16: Global SNR time traces with signal excluding the $(m, n) = (0, 0)$ mode, under various tuning parameter λ (see Eq. (4.7)) considering the non-adaptive and the adaptive cases. Marker number set to $N_p = 256M$, and adaptive rate to $\alpha_E = 1.92\gamma_{\max}$ where applicable.

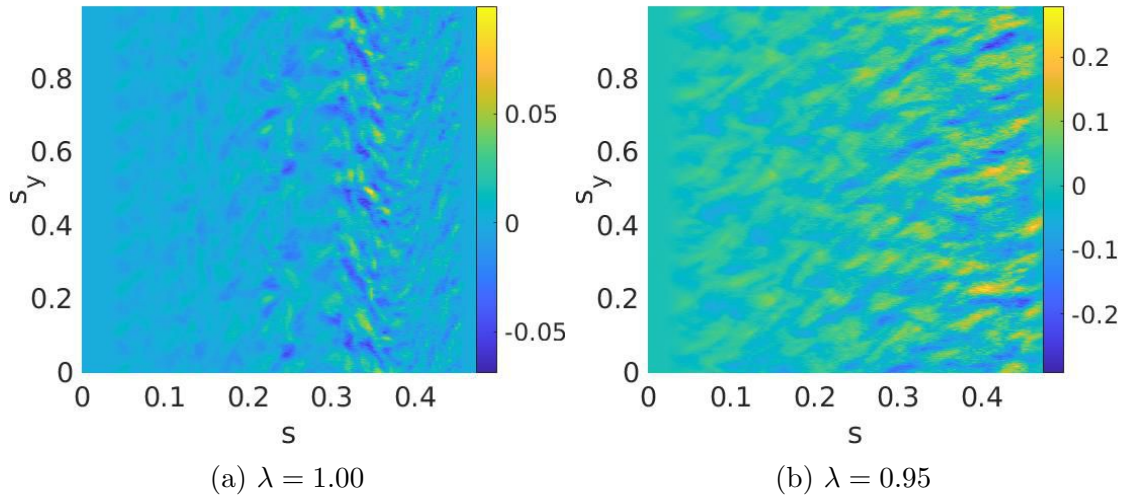


Figure 4.17: Time snapshot at $c_s t / L_x = 2259$ with tuning parameter λ of the ion temperature T_i relative non-zonal deviation on each magnetic surface, expressed by $(\delta T_i - \langle \delta T_i \rangle) / \langle T_i \rangle$, where $T_i = T_{0i} + \delta T_i$, integrated over the toroidal z direction. s_y is the normalised poloidal y axis. Both quasi-steady state cases have adaptive rate and marker number set to $\alpha_E = 1.92\gamma_{\max}$ and $N_p = 256M$, respectively.

We now consider simulations with $\lambda = 0.95$, which demonstrated high sustained flux for the adaptive cases for the following analysis. Fig. 4.17 shows that the fixed-time non-zonal T_i relative deviation across each magnetic surface increases towards the low-end of the $\langle T_i \rangle$ profile at quasi-steady state. The case with $\lambda = 0.95$ has relative deviation at least twice that of $\lambda = 1.00$, indicating the expected higher levels of turbulence. Since the adaptive scheme implemented in this work adapts its control variate T_{0i} by its f.s.a. values as shown in Eq. (4.4), it is not expected to further improve noise reduction for edge plasma simulations involving relative non-zonal deviation much higher than 25%. However, a similar adaptive scheme

could still be used for noise control, provided that f_0 is now a function of all spatial dimensions. This would allow for a transfer of non-zonal components of δf to f_0 , though with lower N_p statistics per spatial bin due to greater number of bins when implementing Eq. (4.4).

Under the same simulation parameters, Fig. 4.18 further shows that the relative fluctuation of T_i evaluated in an end-time window is derived mostly from its non-zonal variations. There, the curves are calculated as follows. Let the j -th flux tube on flux surface x occupy the space:

$$(y, z)_j \in \left[\begin{array}{l} \frac{B_y(x)z}{B_z} \leq y - j\Delta y < \frac{B_y(x)z}{B_z} + \Delta y \\ 0 \leq z < L_z \end{array} \right].$$

Visually, these N_y flux tubes are the straight blue lines of Fig. 4.1 of y -width Δy , spanning each $x = \text{constant}$ plane. The j -th flux tube gives the value $T_i(x, t; j)$. It is assumed that the plasma reaches thermal equilibrium instantly along the flux tube. Finally, let $\langle \cdot \rangle_t$ be the averaging in time for $t \in [t_1, t_2]$, and $\langle \cdot \rangle_{f.t.}$ be the flux-tube-average on the flux surface x , i.e.

$$\langle T_i(x, t; j) \rangle_{f.t.} = \frac{1}{N_y} \sum_{j=1}^{N_y} T_i(x, t; j).$$

Then, referring to Fig. 4.18,

$$\begin{aligned} \text{black} & : \frac{\sqrt{\langle \langle T_i \rangle^2(x, t) \rangle_t - \langle \langle T_i \rangle(x, t) \rangle_t^2}}{\langle \langle T_i \rangle(x, t) \rangle_t} \\ \text{orange} & : \frac{\sqrt{\langle \langle T_i^2(x, t; j) \rangle_{f.t.} \rangle_t - \langle \langle T_i(x, t; j) \rangle_{f.t.} \rangle_t^2}}{\langle \langle T_i(x, t; j) \rangle_{f.t.} \rangle_t}. \end{aligned} \quad (4.8)$$

For each fixed λ , the relative fluctuation when non-zonal variations are included gives a value at least twice as high as that of the case when only the f.s.a. values are considered. Consistent with Fig. 4.17, lower λ value gives higher fluctuation levels. These results summarily show that non-zonal fluctuations are dominant at quasi-steady state under current simulation parameters.

In conclusion, simulations using the adaptive scheme are shown to be better than the non-adaptive ones under all scenarios considered. To further test the advantage gained from the adaptive scheme under high fluctuation level scenarios would require simulating instabilities in toroidal geometry, which is the subject of Chs. 5 and 6. There, toroidal effects naturally results in higher fluxes and fluctuation levels, while zonal flows are an important factor determining the turbulent flux levels.

4.5 Conclusion

The advantage gained using a simple adaptive control variate for the δf scheme has been demonstrated in cases with high T_i gradients and simple physics in sheared-slab geometry. The necessary implementation of the boundary conditions and a stationary heat source has been done to further ensure simulations reach quasi-steady state in reasonable integration time. The mechanism of the adaptive scheme has been described in detail. Namely, the adaptation of T_i of the f.s.a. Maxwellian

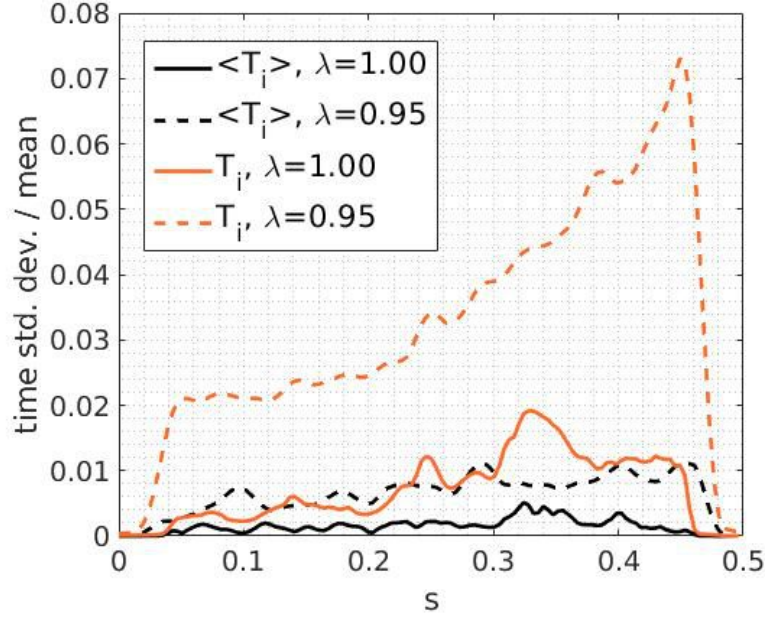


Figure 4.18: Relative fluctuation averaged over $c_s t / L_x \in [1807, 2259]$ of ion temperature T_i and its f.s.a. profile $\langle T_i \rangle$, as measured by its standard deviation over mean, see Eq. (4.8), for the cases of $\lambda = 1.00, 0.95$ with adaptive rate $\alpha_E = 1.92\gamma_{\max}$ and marker number $N_p = 256M$.

control variate $f_0 = f_M$ via a relaxation equation, through which a fraction of the ion kinetic energy density derived from the marker represented δf is periodically transferred to f_0 .

For the cases considered, the adaptive scheme has shown to reduce the ion temperature relative deviation with increasing adaptive rate. Maximum relative deviation of 1% has been achieved from 100% of the non-adaptive case. Due to spurious increase of the zonal flow shear with time, all non-adaptive cases show an eventual collapse of the heat flux. Under the adaptive scheme, not only is quasi-steady state achieved with non-collapsing heat fluxes, these fluxes have also been achieved using marker numbers as low as 1/4 of that required with the non-adaptive one, allowing for longer unquenched turbulence resulting in higher ion temperature deviation from its initial state. The scheme is further shown to be effective in reducing noise accumulation in the physically undamped zonal flow via the measure of $\omega_{E \times B}$. Such noise accumulation is shown to be the result of marker sampling. SNR values of adaptive simulations remain high for long integration times. In contrast, the eventual drop of SNR for the non-adaptive scheme is only postponed by increasing N_p .

We have then investigated further to determine if conservative noise control alone would suffice to produce a similar noise reduction advantage. Via a systematic separation of adaptation and noise control, it is shown that the scheme with an adaptive control variate $f_0 = f_M(t)$, coupled with a noise control operator S_n which relaxes f to the same f_0 , gives the best results. There, the former is proved to be more important than the latter in noise control. Moreover, it is shown that further increase in the strength of S_n not only unphysically damps zonal flows at early times, but also is only able to delay the latter's eventual indefinite rise due to noise accumulation. The adaptation of f_0 is therefore shown to be necessary, even with

an adaptation rate as low as $\alpha_E = 0.12\gamma_{\max}$.

To mimick prolonged fluxes and high fluctuation levels not afforded by slab-ITG, the $\langle\phi\rangle$ term of the adiabatic electron response in the quasi-neutrality equation is attenuated. Such a measure is done to better simulate edge-plasma conditions, despite testing the adaptive scheme in sheared-slab geometry. This chapter has shown that for slightly attenuated $\langle\phi\rangle$, the adaptive scheme exhibited improved noise control as before, for relative fluctuation in T_i as high as 20%. Such fluctuations are shown to be non-zonal. Therefore, it hints to a more sophisticated f_0 , which extends beyond a f.s.a. function that could prove to be useful for better noise control. Despite that, the adaptive scheme still gives SNR values orders of magnitude higher than that of the non-adaptive scheme, further increasing the credibility of simulated results.

Chapter 5

ITG turbulence with adiabatic electrons

In this chapter, the adaptive background temperature scheme used in the previous chapter to sheared-slab geometry is implemented in the ORB5 code in toroidal geometry. Instead of strong profile gradients, strong fluxes will be imposed, which results in large temperature profile deviation from its initial values, all done while still retaining the adiabatic electron assumption. This chapter first introduces the parameters and profiles in Sec. 5.1. Sec. 5.2 discusses the fixed heat source profile used to introduce high fluxes in the simulations. An overview of heat transport over long simulation times then discussed in Sec. 5.3. A discussion on the reduction of weight variance brought by the adaptive scheme follows in Sec. 5.4. In order to compare results of the standard and adaptive cases, time-evolved profile analysis is separated into two time windows. These results are discussed in Sec. 5.5. In Sec. 5.6, we then give a brief discussion on the limitations running simulations under the settings of this chapter for longer times.

5.1 Parameters and profiles

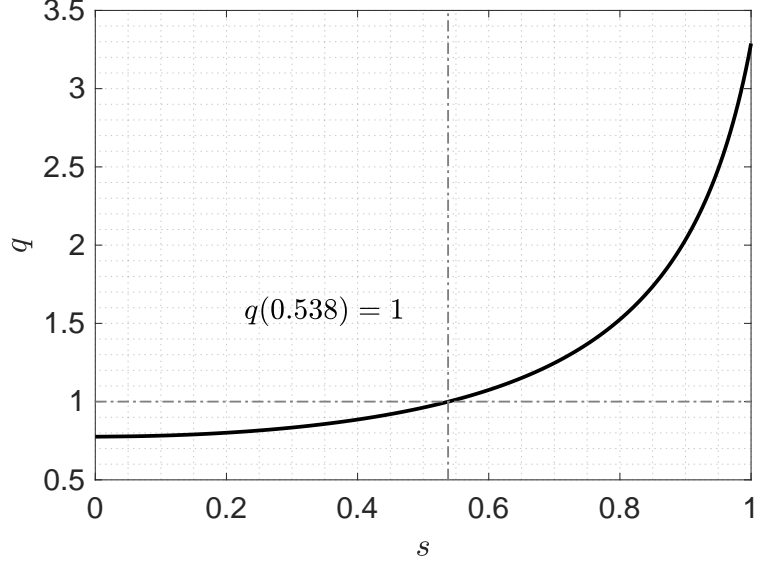


Figure 5.1: Safety factor profile for the TCV shot #43516 used in this work.

For all simulations from this chapter and subsequent ones, the ideal MHD equilibrium is computed by the CHEASE code [59] based on the TCV shot #43516. It has an aspect ratio of 3.64, an elongation of 1.44 and a triangularity of 0.20 at the last closed flux surface. Its safety factor is shown in Fig. 5.1, the $q = 1$ flux-surface is located at $s = 0.538$. The reference magnetic surface taken for normalisation is at $s_0 = 1$. For this chapter, we focus on turbulence driven by ITG modes. Therefore, we consider a singly charged ($Z = 1$) kinetic ion species, and an adiabatic electron species. $\rho_*(s_0) = \rho_i(s_0)/a = 1/245$, where $\rho_i(s) = \sqrt{T_{0e}(s)/m_i}$ is the ion sound Larmor radius, and a the minor radius.

The profile for the background density and temperature for the ions and electrons is described by the functional form of Eq. (5.1), designated by G .

$$G(\rho_V) = \begin{cases} g_0 + g_2 \rho_V^2 & \text{for } 0 \leq \rho_V \leq \rho_{\text{core}} \\ G_{\text{ped}} \exp[-\kappa_T(\rho_V - \rho_{\text{ped}})] & \text{for } \rho_{\text{core}} < \rho_V \leq \rho_{\text{ped}} \\ G_1 - \mu_G(\rho_V - 1) & \text{for } \rho_{\text{ped}} < \rho_V \leq 1 \end{cases}, \quad (5.1)$$

where ρ_V is the radial coordinate $\rho_V = \sqrt{V(\psi)/V(\psi_{\text{edge}})}$, with $V(\psi)$ the volume enclosed by the flux surface label ψ . g_0 and g_2 are coefficients determined such that G and $dG/d\rho_V$ are continuous at $\rho_V = \rho_{\text{core}}$, and $G_{\text{ped}} = G_1 + \mu_G(1 - \rho_{\text{ped}})$. Ions and electrons share the same functional from Eq. (5.1) for profiles of density n_{sp} and temperature T_{sp} , $sp = i, e$ respectively, whose parameters are shown in Tab. 5.1, and profiles illustrated in Fig.5.2.

| Parameter | Density | Temperature |
|----------------------|---------|-------------|
| ρ_{core} | 0.4431 | 0.4431 |
| ρ_{ped} | 0.8 | 0.8 |
| κ | 2.3 | 3.1 |
| μ | 5.0 | 12.0 |
| G_1 | 1.0 | 1.0 |

Table 5.1: Profile parameters of Eq. (5.1) for density and temperature profiles for both background ions and electrons.

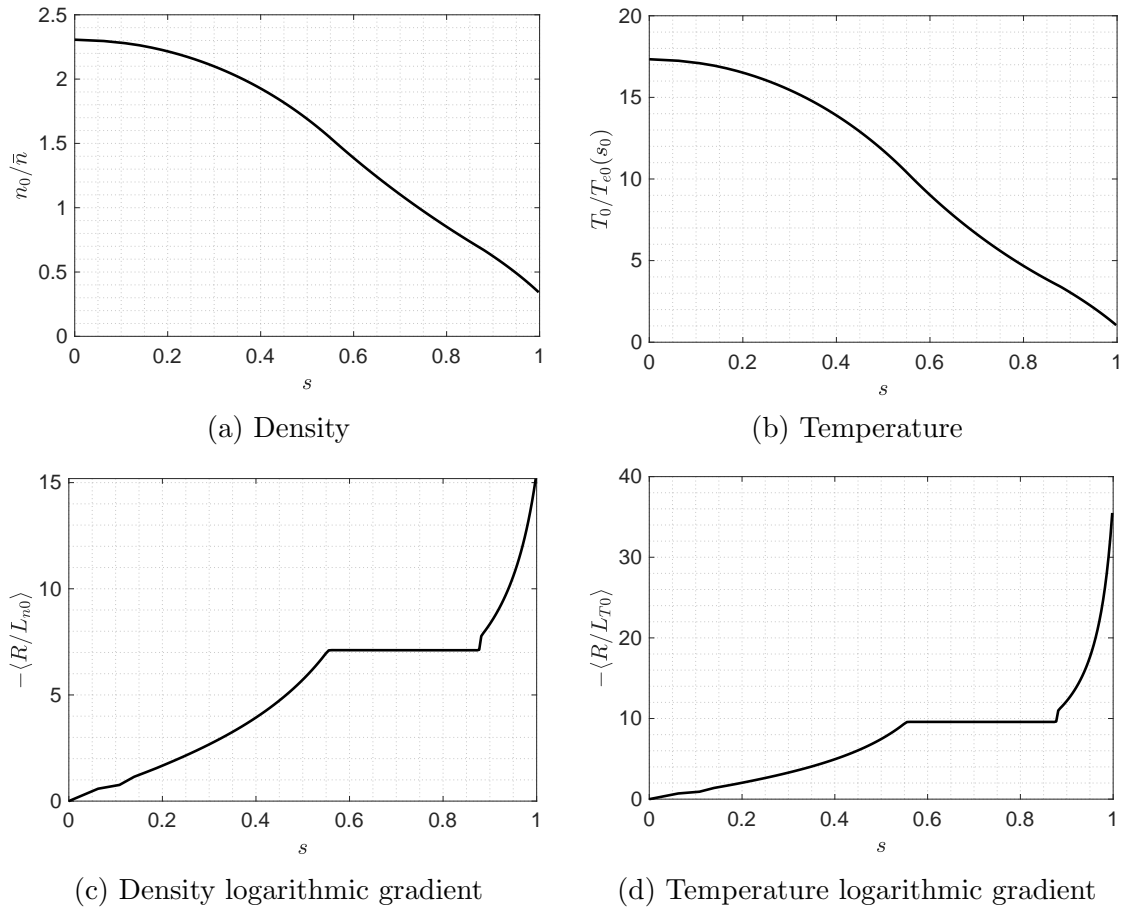


Figure 5.2: Initial gyrocentre density and temperature profiles and its logarithmic gradient for the ion and electrons used in Chs. 5 and 6.

The grid resolution for the radial s , poloidal θ^* and toroidal φ is taken to be $N_s \times N_{\theta^*} \times N_\varphi = 256 \times 512 \times 256$, where N represents the number of intervals. Toroidal modes in the range of $0 \leq n \leq 64$ will be simulated, with a Fourier filter half-width of $\Delta m = 5$, that is only poloidal modes $m \in [nq(s) - \Delta m, nq(s) + \Delta m]$ will be resolved (see Sec. 3.1.4.1). The time resolution is $\Omega_{ci}\Delta t = 20$, and the maximum linear growth rate is found to be $\gamma_{\text{max}}/\Omega_{ci} = 0.0085$ (see Fig. 5.3). The growth rates for the various n values are shown in Fig. 5.3.

Simulations are initially perturbed with a δf that represents a superposition of modes in $48 \leq m \leq 64$, $24 \leq n \leq 32$, with markers populating the velocity space up to $\kappa_V = 5$ (see Sec. 3.1.2). A Krook operator with strength $\gamma_n\Omega_{ci} = 0.00085$,

which is around $10\% \gamma_{\max}$, for either temperature gradient drive and/or noise control is always present. The specifications of the adaptive case of this chapter is shown in Tab. 5.2.

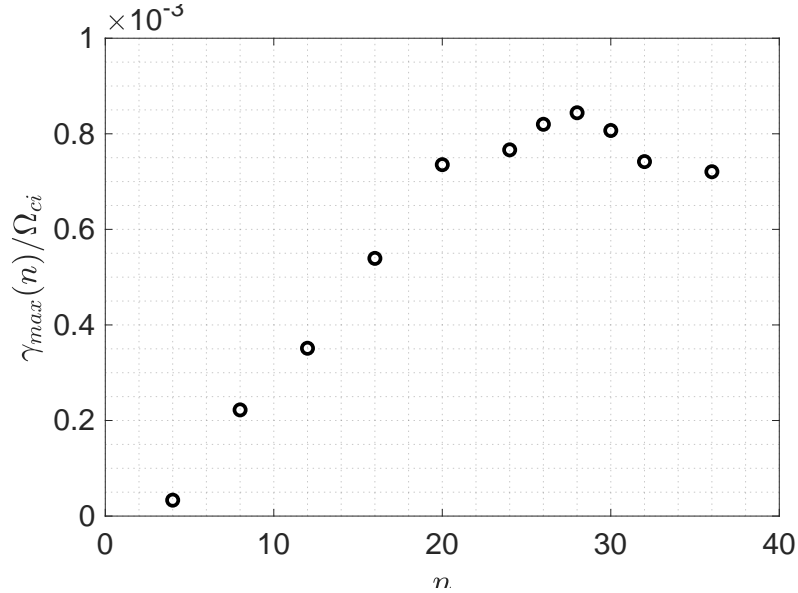


Figure 5.3: Maximum linear growth rate for each toroidal mode number n . The maximum linear growth rate over all n is found to be $\gamma_{\max}/\Omega_{ci} = 0.00084$ ($\gamma_{\max}a/c_s = 0.2$) for $n = 28$.

| Parameter | Value | Reference |
|---|----------------------------------|----------------------|
| scheme | simultaneous | Sec. 3.2.4 |
| control variate | local | Eq. (3.42) |
| adaptive rate, α | $1.7 \times 10^{-4} \Omega_{ci}$ | $20\% \gamma_{\max}$ |
| time-averaging period, N_t | 50 | Eq. (3.59) |
| background profile grid resolution, N_ψ | 128 | Eq. (3.55) |
| background profile B-spline order, N_{spl} | 3 | Eq. (3.55) |
| QNE r.h.s. calculation | exact | Sec. 3.2.10.1 |

Table 5.2: Parameters of the adaptive scheme used in this chapter. Adaptive rate α is common for both gyrocentre density α_n and energy (temperature) α_E

The choice of using a local control variate and a ‘simultaneous’ scheme of adaptation (see Sec. 3.2.4) in this chapter is due to an unresolved numerical instability, which occurs specifically when using adiabatic electrons and a canonical control variate. This issue is briefly explored in App. C. As the background is now a local Maxwellian function, we employ the standard δf scheme (see Sec. 3.1.3.4) and neglecting the neoclassical term, i.e. $\left. \frac{df_0}{dt} \right|_0 = 0$ (see Sec. 2.4).

5.2 Heat source radial profile

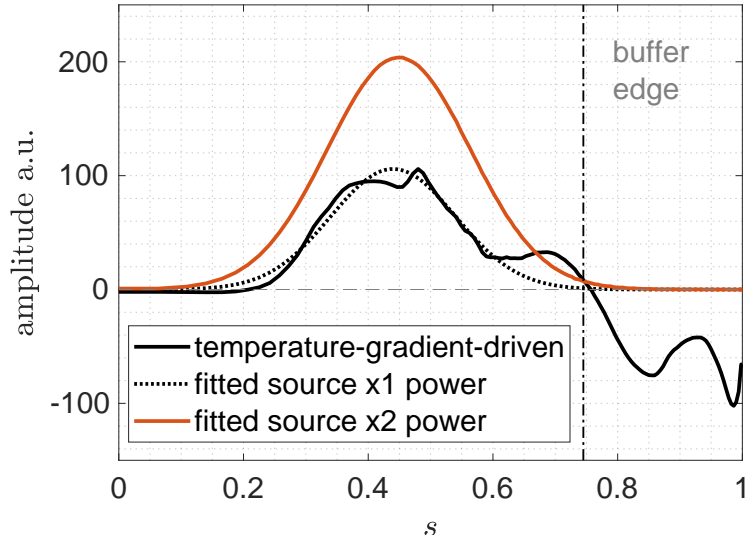


Figure 5.4: Fixed heat source profile (see Eq. (3.82)) $G_H(\psi)$ (dotted line) fitted to the effective flux-surface- and time- averaged heat source of the temperature-gradient-driven run (black solid line) using the standard case with $N_p = 256M$. The orange line shows the source profile with twice the power, which is used for this chapter. Buffer edge is taken to be $s_b = 0.745$ (see Eq. (3.83)).

A specification of the radial ion heat source is required to run flux-driven simulations. To that end, under the parameters of this chapter, we first run a ‘temperature-gradient-driven’ simulation till it reaches quasi-steady state. This involves using the Krook operator Eq. (3.81) as both noise control and heat source, accomplished by not imposing the conservation of energy on each flux surface. The resulting end-time radial distribution of the heat source is time averaged in an appropriate time window to average out fluctuations. The aforementioned profile is shown in Fig. 5.4 as the black solid curve.

We fit a Gaussian curve to the single positive amplitude near the core peaked around $s = 0.4$, illustrated with the dotted curve of Fig. 5.4. Indeed, the profiles of Eq. (5.1) used in this work are chosen in such a way so that it results in a single dominant heating source near the core. The Gaussian fit for the peak heat source is done in such a way as to equate the power of the heat source in the positive region ($s \lesssim 0.75$). Furthermore, as the aim of this work is to verify the effectiveness of the adaptive background scheme under large ion temperature profile deviation, we use as heat source a profile with twice the power, which is shown as the orange curve in Fig. 5.4. Towards the edge, we approximate the heat sink with a buffer of Eq. (3.83) with edge $s_b = 0.745$, as indicated by the vertical dashed line of Fig. 5.4. With such an edge, we have found that the buffer amplitude of $\gamma_b = 10\% \gamma_{\max}$ is adequate to suppress fluctuations almost completely at $s = 1$.

Finally, for flux-driven runs the Krook operator Eq. (3.80) is resumed to be used only for noise control. A summary of the various parameters used for the sources/sinks are shown in Tab. 5.3.

| Parameter | Value |
|--------------------------|-------|
| γ_n/γ_{\max} | 0.100 |
| γ_b/γ_{\max} | 0.100 |
| s_b | 0.745 |

Table 5.3: Parameters relating to sources of Eqs. (3.80) and (3.83) used in this chapter.

For the simulations of this chapter, we split the analysis of the results in two separate time windows. This is because adaptive cases allow for a much longer simulation time. The first time window is $c_s t/a \in [1225, 1430]$. This time allows us to compare results from both the standard and adaptive cases. The second time window $c_s t/a \in [4697, 4902]$ which is on average twice the simulation time of the first, is to analyse results of the adaptive cases at late times.

5.3 Heat transport

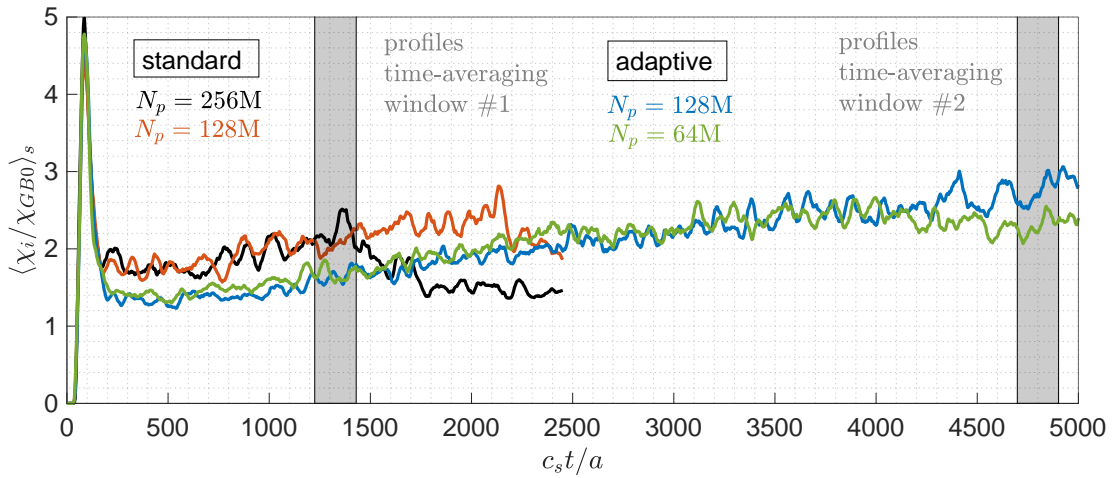


Figure 5.5: Radially averaged $s \in [0.7, 0.9]$ ion heat diffusivity for various marker numbers N_p under the standard and adaptive schemes. Grey shaded areas represent two time windows for profile analysis, considered in Sec. 5.5.

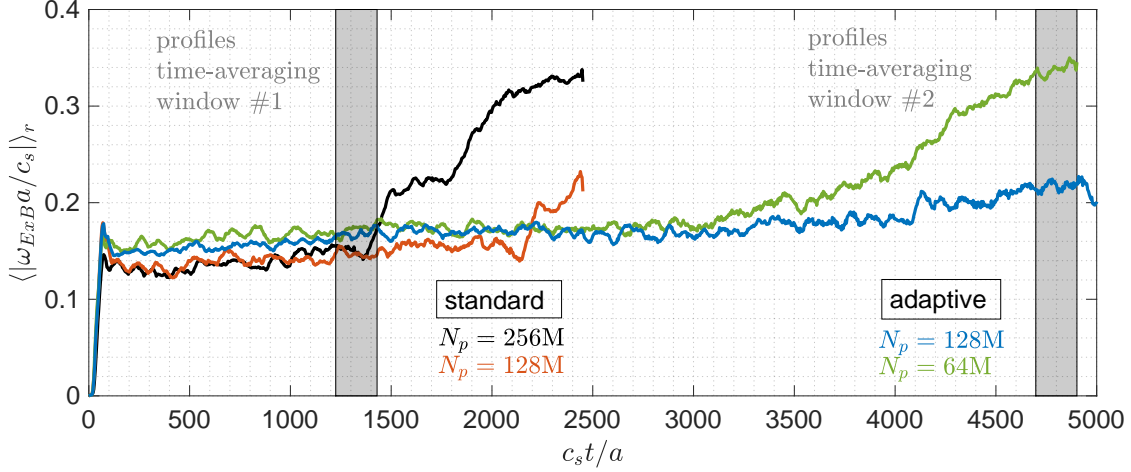


Figure 5.6: Time dependence of absolute value of the radially averaged $s \in [0.7, 0.9]$ zonal flow shearing rate $\omega_{E \times B}$. Grey shaded areas represent two time windows for profile analysis, considered in Sec. 5.5.

Figure. 5.5 shows the radially averaged $s \in [0.7, 0.9]$ ion heat diffusivity χ_i time traces. This radial average window corresponds to the flat logarithmic gradient of ion temperature (see Fig. 5.2d). We see that just after the initial burst at $c_s t / a \simeq 100$, both the standard and adaptive cases converge to different χ_i values, with the results of standard cases at $0.5\chi_{GB0}$ higher than that of the adaptive cases. In $c_s t / a \in [100, 1300]$, χ_i of all cases steadily increases, after which the results for the standard cases diverges. The results of the adaptive cases however continue to increase at the same rate.

The difference in χ_i values between the standard and adaptive scheme can be explained by the difference in zonal flow shearing rate $\omega_{E \times B}$. Fig. 5.6 shows the radially averaged $s \in [0.7, 0.9]$ absolute value of $\omega_{E \times B}$. We see that for the time $c_s t / a \in [100, 1400]$, the results under the standard scheme gives consistently lower $|\langle \omega_{E \times B} \rangle_r|$. The higher shearing rate under the adaptive scheme shears turbulent eddies at a higher rate, thereby more effectively suppressing turbulence, which leads to a lower heat transport indicated by a lower χ_i . Fig. 5.6 explains the divergence in results for the standard cases. Compared with the case with $N_p = 128M$ markers, the case with $N_p = 256M$ exhibits a sudden increase in $|\langle \omega_{E \times B} \rangle_r|$, thereby reducing its heat diffusivity significantly. To investigate this difference between the cases with $N_p = 128M$ and $N_p = 256M$ under the standard scheme further, Fig. 5.7 shows the time evolution of the $\omega_{E \times B}$ profile for all cases discussed. Comparing Figs. 5.7a and 5.7b, we see that the increase of $|\langle \omega_{E \times B} \rangle_r|$ for standard case with $N_p = 256M$ is due to the radially outward migration of the $\omega_{E \times B}$ corrugation near the $q = 1$ flux surface. Whereas for the standard case with $N_p = 128M$, this migration is slower. On the contrary, the results of $N_p = 128M$ and $N_p = 64M$ under the adaptive scheme exhibit stationary $\omega_{E \times B}$ corrugation structure around $q = 1$ flux surface at all times, shown in Figs. 5.7c and 5.7d respectively. For all cases of Fig. 5.7, the negative $\omega_{E \times B}$ at the edge $s = 0.9$ is due to the buffer used.

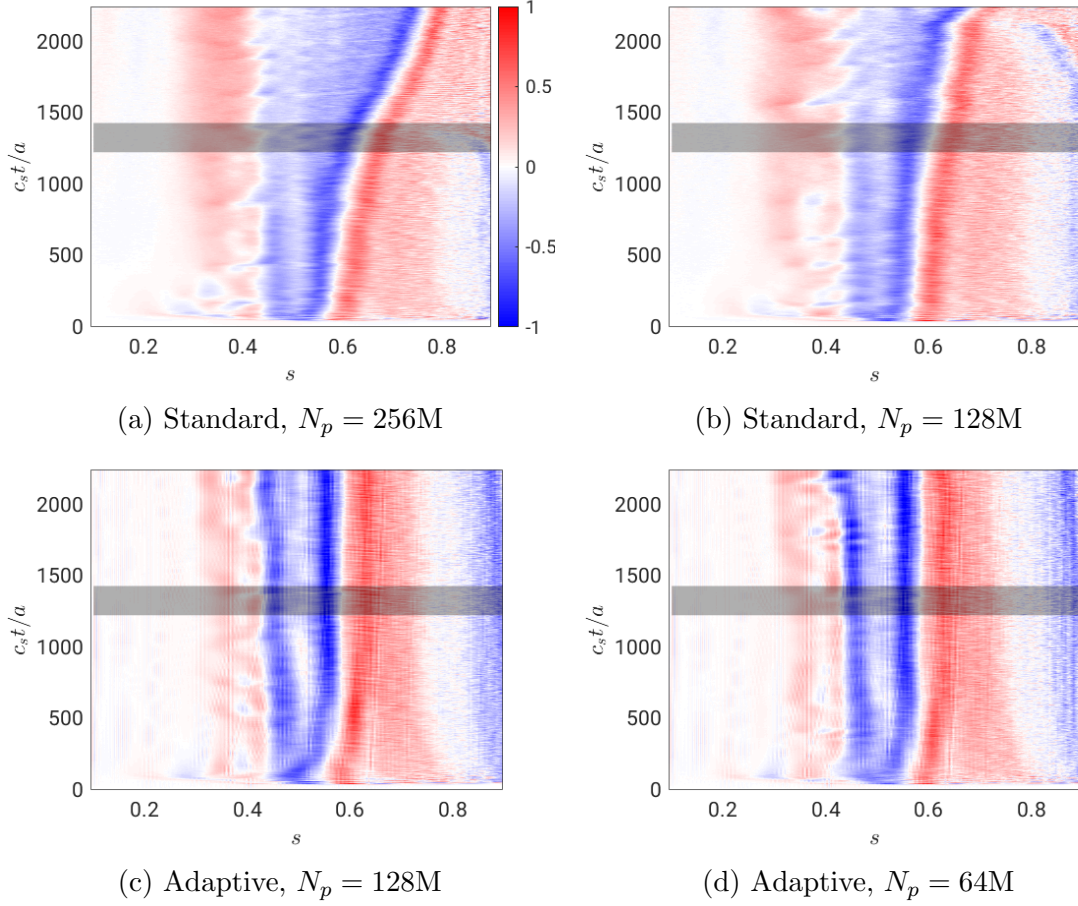


Figure 5.7: Time evolution up to $c_s t/a = 2451$ of the radial profile of the zonal flow shearing rate, $\omega_{E \times B}(s, t)$, for various marker numbers N_p under the standard and adaptive schemes. Grey area indicates the first profile time-averaging window $c_s t/a \in [1225, 1430]$. All plots share the same colour scale.

5.4 Weight variance measure

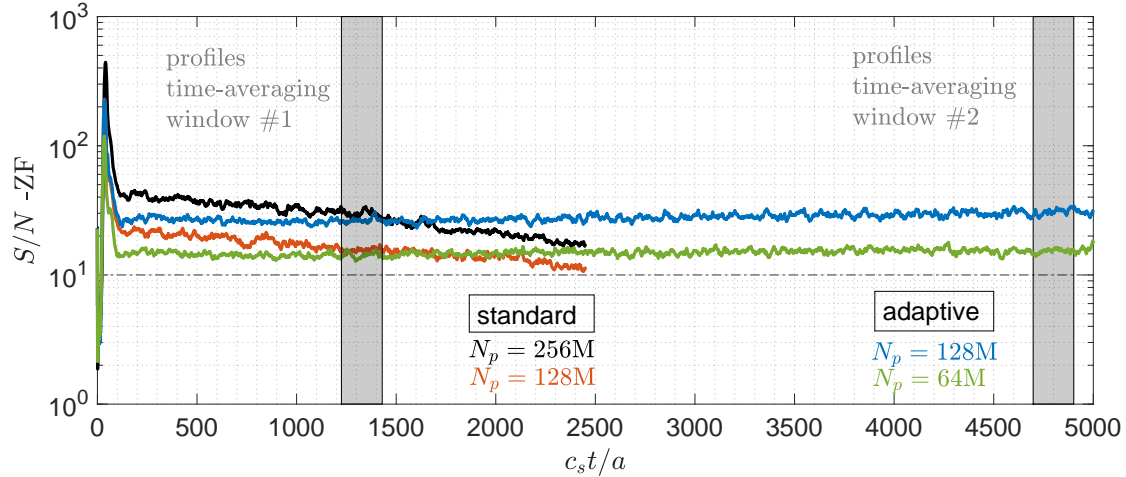


Figure 5.8: Time dependence of global Signal-to-Noise Ratio (SNR) values, for various marker numbers N_p under the standard and adaptive schemes. The signal excludes the zonal component $(m, n) = (0, 0)$. Horizontal dashed line indicates the empirically set minimum value of 10 for quality simulations. Grey shaded areas represent two time windows for profile analysis, considered in Sec. 5.5.

The difference between the results of the standard and adaptive schemes is attributed to a statistical noise problem, diagnosed by the marker weight variance. Fig. 5.8 shows the time traces of the global Signal-to-Noise-Ratio (SNR) value for all cases discussed. The SNR values shown here do not include the zonal component $(m, n) = (0, 0)$ in its signal (see Eq. (3.28)). The SNR values which includes this is consistently higher by 20% for all cases. Considering first the standard cases (black and orange), after the initial burst at $c_s t/a \simeq 100$, both standard cases have SNR values steadily decrease. This is because, as the temperature profile increasingly deviates from its initial values, the δf component gets increasingly large. Furthermore, the magnitude of the SNR values scales with N_p . The empirically chosen [9] minimum value of SNR of 10 for quality simulations motivate of the first time window $c_s t/a \in [1225, 1430]$. Nonetheless, the divergence between results at $N_p = 128M$ and $N_p = 256M$ under the standard scheme (see Figs. 5.7a and 5.7b) suggests that the results may already have drown in noise by this simulation time.

We now turn to the adaptive case of Fig. 5.8. Once again, we see the N_p scaling of the respective SNR values. The main difference between standard and adaptive cases is that the SNR values of the adaptive case maintain steady values, after the initial burst at $c_s t/a \simeq 100$. The SNR values of the adaptive cases are maintained at constant values because the weights are being continuously reduced by the background f_0 with an adaptive temperature. The SNR diagnostic is only indicative, and other PIC simulation quality diagnostics exist, to which we now discuss.

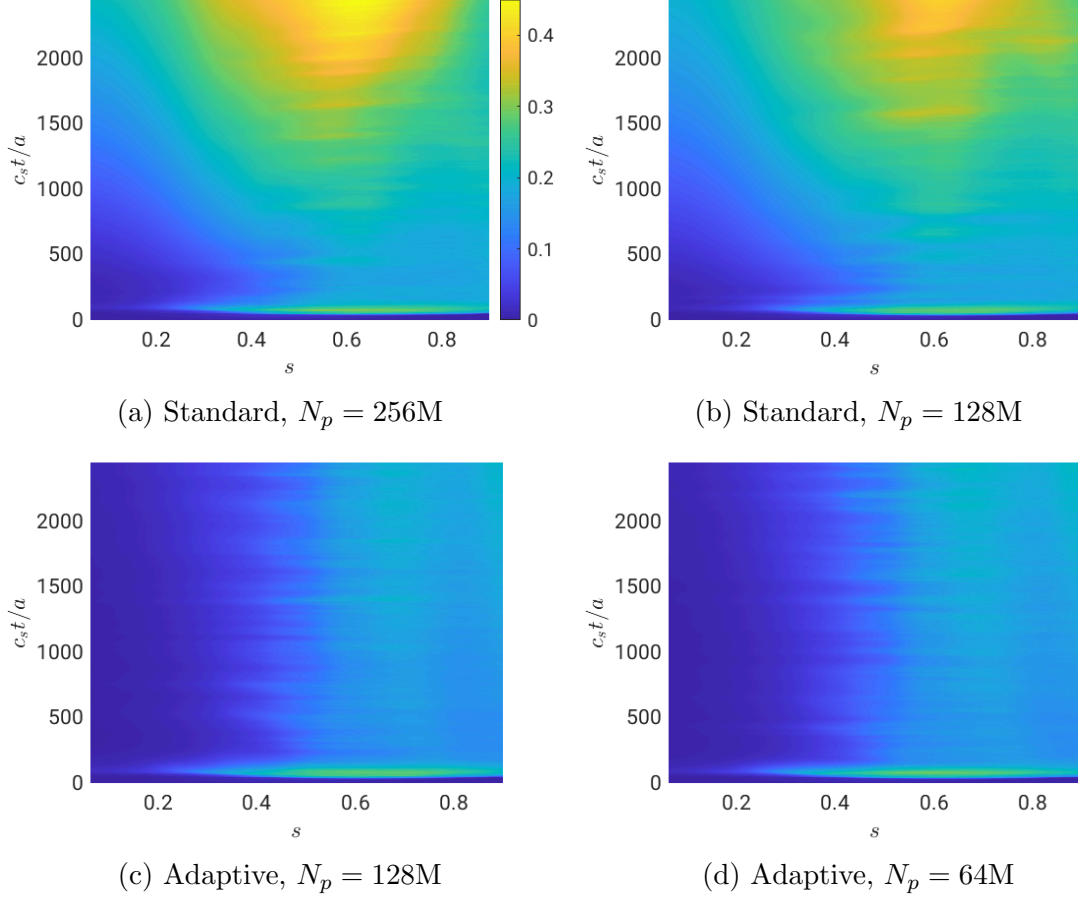


Figure 5.9: Time evolution of the ion f.s.a. weight standard deviation profiles $\sigma_w = \sqrt{\langle w^2 \rangle - \langle w \rangle^2}$. All plots share the same colour scale.

Figure 5.9 shows the time evolution of the radial-bin-wise weight standard deviation $\sigma_w(s) = \sqrt{\langle w^2 \rangle(s) - \langle w \rangle^2(s)}$ for all cases discussed. Common to all cases is the sudden increase in σ_w at $c_s t/a \simeq 100$ corresponding to the initial burst. Also, there are small bursts in σ_w throughout simulation time. Considering first the standard cases of Figs. 5.9a and 5.9b with marker numbers $N_p = 256\text{M}$ and $N_p = 128\text{M}$, we see that σ_w continuously increases with time, with maxima at $s \simeq 0.6$. Given a high enough N_p , σ_w values should converge to the same amplitude, which is not entirely the case for Figs. 5.9a and 5.9b. Turning now to the adaptive case of Figs. 5.9c and 5.9d with $N_p = 128\text{M}$ and $N_p = 64\text{M}$, we see that after the initial burst, σ_w values are kept low and quasi-constant. To determine how much improvement the adaptive scheme brings us, Fig. 5.10 shows the s -cuts at $s = 0.6$ for Fig. 5.9 where the σ_w peak of the standard cases are located. The σ_w values of the standard cases are seen to increase almost linearly in time, at a much higher rate than the adaptive cases. At time $c_s t/a \simeq 2500$, the σ_w values of the adaptive cases are at least twice smaller than the standard cases. For the standard cases, we see that the σ_w values are not entirely converged between $N_p = 256\text{M}$ (black) and $N_p = 128\text{M}$ (orange) at late times. Furthermore, the σ_w values of the adaptive scheme have converged in N_p , and exhibit smaller bursts as compared to the standard cases.

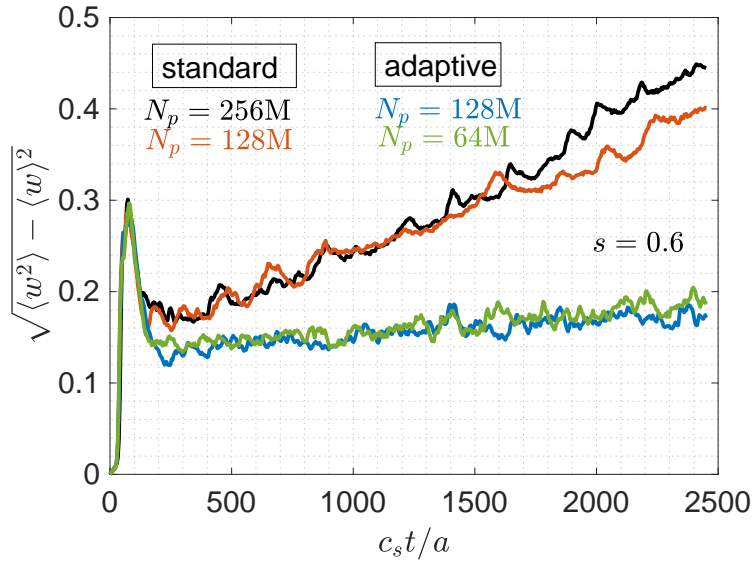


Figure 5.10: F.s.a. weight standard deviation profiles $\sigma_w(s) = \sqrt{\langle w^2 \rangle(s) - \langle w \rangle^2(s)}$ at $s = 0.6$, for various marker numbers under the standard and adaptive schemes.

5.5 Profile evolution

In this section, we discuss the time averaged f.s.a. profiles of the two time averaging windows as indicated in Fig. 5.5.

5.5.1 Time window #1

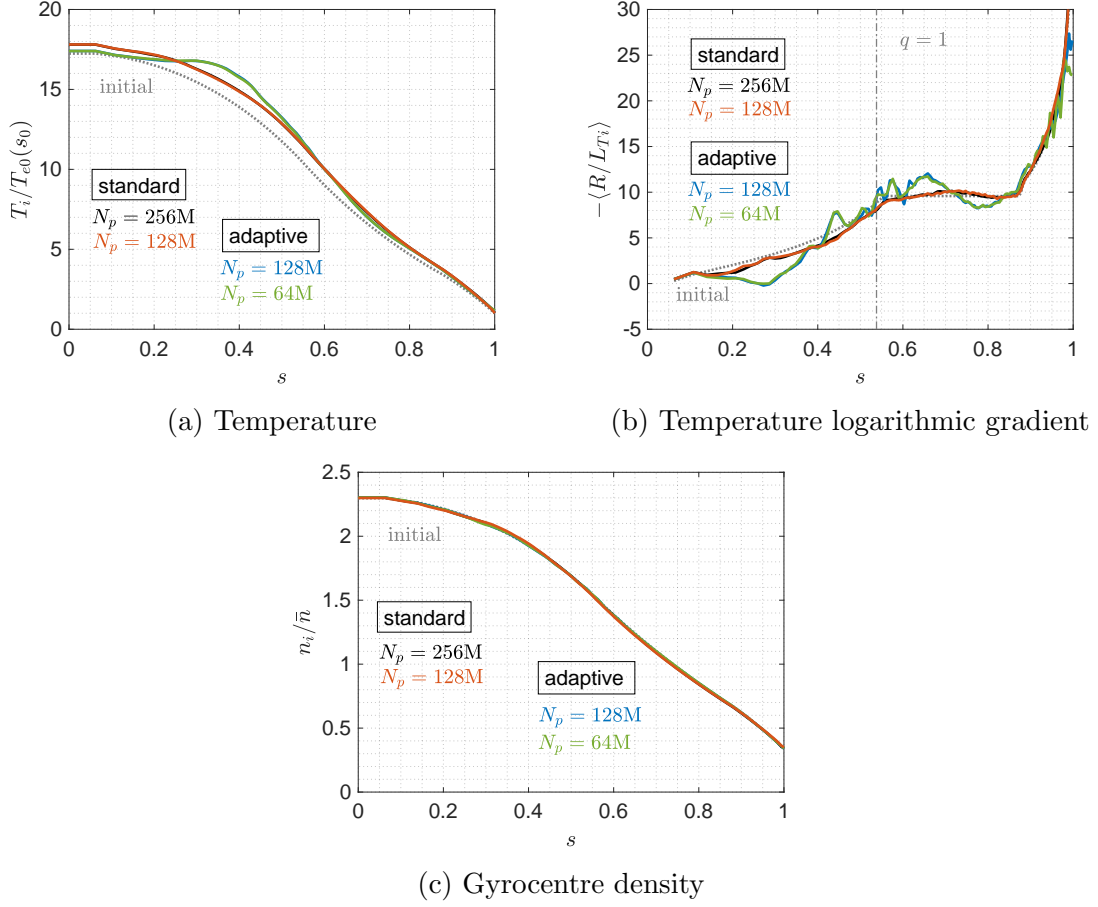


Figure 5.11: Time averaged $c_s t/a \in [1225, 1430]$ of f.s.a. ion gyrocentre profiles, for various marker numbers N_p under the standard and adaptive schemes. The dotted lines indicate the initial profiles.

Figure 5.11 shows the time and f.s.a. averaged ion gyrocentre profiles in the time window $c_s t/a \in [2246, 2451]$ for all cases discussed. These profiles are plotted by binning the sum of p and w weights (see Eqs. (3.21) and (3.22)) into radial bins. For the adaptive cases, the background profiles come so close to the total profiles that they would superimpose at the scale of the plots (not shown). Fig. 5.11a shows the ion temperature. We first note that the results under the respective schemes seem to have converged in N_p . The main difference is that under the standard scheme (black and orange), we see a significant increase of ion temperature near the magnetic axis. The time-averaged temperature profile of the standard cases are shifted almost globally upwards, with smallest increase at the edge. The results of the adaptive case (blue and green), on the other hand, exhibit a temperature peak at $s \simeq 0.35$, with almost no evolution at the magnetic axis. These trends are reflected in the logarithmic gradient of the ion temperatures shown in Fig. 5.11b. Focusing first on the standard cases, we see that the logarithmic gradient remains almost unchanged except for the flat region $s \in [0.6, 0.9]$. There, we see an increase towards the edge. This increase is consistent with the higher ion heat diffusivity χ_i values exhibited in Fig. 5.5 for the standard cases. The results under the adaptive

scheme are very different, in that they exhibit, on top of an increased logarithmic gradient, gradient corrugations around the $q = 1$ flux surface. Analysis on the cause of such corrugation, which also occurs only under the adaptive scheme, has not been done by the author. Lowest order Mode-Rational-Surfaces (MRSs) have a role in creating mini-barriers with corrugated zonal flow shearing rate [1] (see Fig. 5.12). However, it was shown in Ref. [20] that the non-adiabatic dynamics of the passing electrons is essential in producing sharp corrugations near MRSs, and here we do not include this dynamics. Another feature exhibited by the adaptive cases is the negative peak at $s \simeq 0.3$, which corresponds to the rise in temperature away from the magnetic axis, shown in Fig. 5.11a. Finally, under the adiabatic electron assumption, one expects no particle transport as the perturbation field is in phase with the perturbed density. Thus, unless polarisation density is large, one expects no evolution of the gyrocentre density profile. Fig. 5.11c shows the time-averaged ion gyrocentre density profile for all cases discussed. For all case, the density profiles appears to have no evolution, expect for the region $s \in [0.1, 0.25]$. In this region, the results for the standard cases deviate more from the initial values, but improves with increasing marker number. The adaptive cases on the other hand show even smaller deviation, with results converged in N_p .

To further investigate the corrugation in the logarithmic gradient of the ion temperature under the adaptive scheme (see Fig. 5.11b), Fig. 5.12 shows the time-averaged $c_s t/a \in [2246, 2451]$ zonal flow shearing rate profile $\omega_{E \times B}$ for all cases discussed. Here, we can see that the adaptive cases (blue and green) do exhibit strong shearing rate near the $q = 1$ flux surface, whereas it is absent under the standard scheme because the $\omega_{E \times B}$ structure has drifted radially outwards as shown in Fig. 5.12 at $s \simeq 0.7$ and $s \simeq 0.65$ for the standard cases with $N_p = 256M$ (black) and $N_p = 128M$ (orange) respectively.

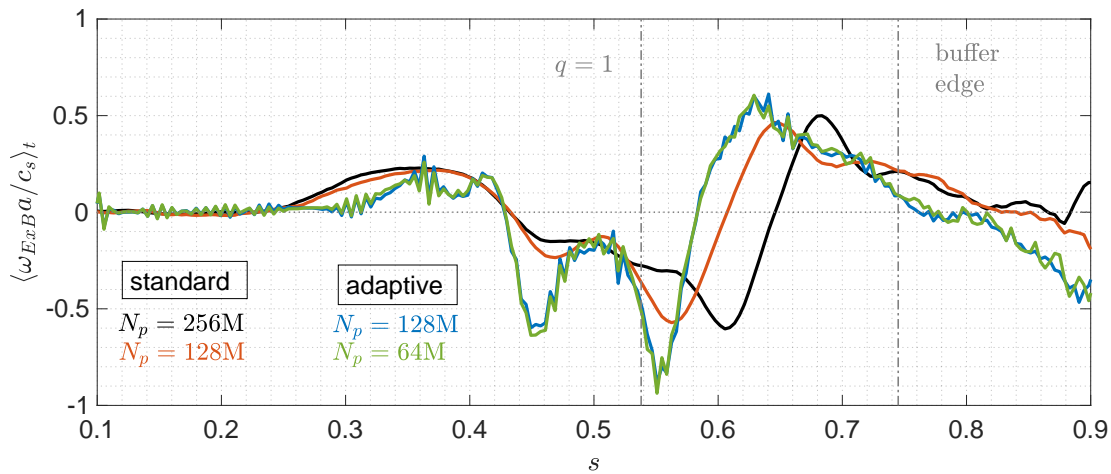


Figure 5.12: Radial profile of the time-averaged $c_s t/a \in [2246, 2451]$ zonal flow shearing rate $\omega_{E \times B}$, for various marker numbers under the standard and adaptive schemes.

5.5.2 Time window #2

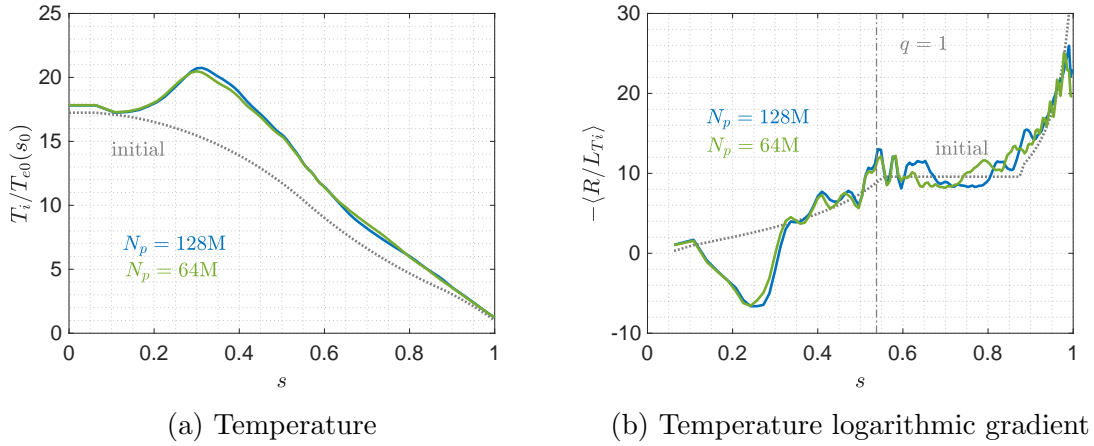


Figure 5.13: Time averaged $c_s t/a \in [4697, 4902]$ of f.s.a. ion gyrocentre temperature profile and its logarithmic gradient, for marker numbers $N_p = 128M$ and $N_p = 64M$ under the adaptive scheme. Dashed lines show profiles at initial time.

Figure 5.13 shows the time- and flux-surface- averaged ion temperature profiles after twice the amount of simulation time past when the profiles of Fig. 5.11 was averaged. Only adaptive cases are shown here, as the quality of standard cases have deteriorated (simulation crashed) by $c_s t/a \simeq 2500$ (see Fig. 5.8). Once again results of adaptive cases are converged in marker number N_p . Considering first Figs. 5.11a and 5.13a, we see that the temperature peak at $s \simeq 0.35$ has increased by 25%. The slight increase around $s \in [0, 0.1]$ is due to the corruption of phase-space volume sampled, which gets worse with simulation time¹. Considering now Fig. 5.13b with reference to 5.11b, the only difference is that the increased peak at $s \simeq 0.35$ has led to a more negative logarithmic gradient profile of the temperature. The corrugation structure around the $q = 1$ flux surface remains unchanged with simulation time.

We now turn to the time-evolved ion gyrocentre density, as shown in Fig. 5.14a. We note that the gyrocentre density values have approximately no deviation from the previous time window (see Fig. 5.11c). On the other hand, one notices strong corrugation in the logarithmic gradient profile of the density, as shown in Fig. 5.14b. The location of maximum corrugation amplitudes occurs around the $q = 1$ flux surface, and spreads radially inwards. Though not shown here, these corrugations grow with simulation time up to the current time averaging window $c_s t/a \in [4697, 4902]$. Further work is necessary in order to analyse the cause of these corrugations, which are probably unphysical. These high radial wavenumber k_r variations in the density profile might challenge the assumption on the use of the long-wavelength approximation for the ion polarisation density term in the QNE (see Eq. (2.34)). Work [20] has indeed been done to implement an arbitrary wavelength solver due to corrugation structures around MRSs. This leads to the discussion on the limitations of simulation setup of this chapter for long simulation time integration of the adaptive cases.

¹A detailed analysis of this phenomenon follows in Sec.6.3.7.2.

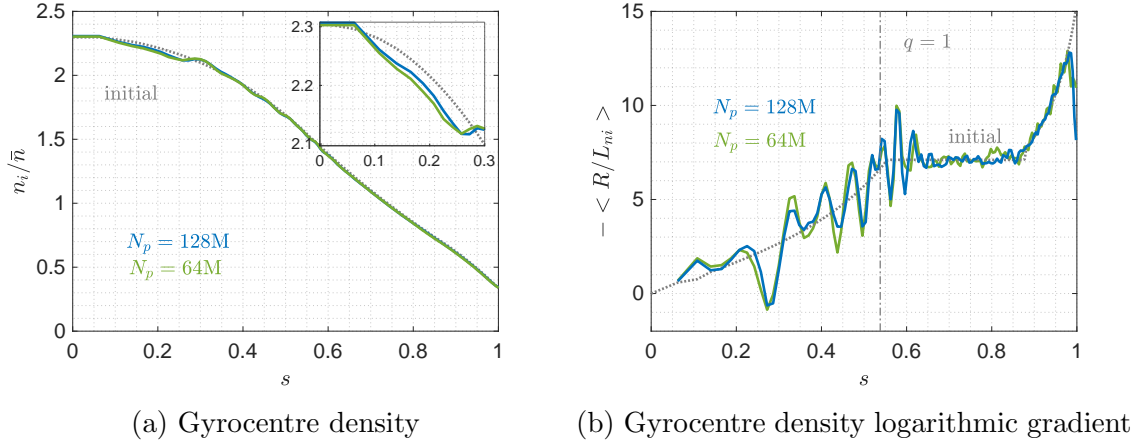


Figure 5.14: Time averaged $c_s t/a \in [4697, 4902]$ of f.s.a. ion gyrocentre density profiles and its logarithmic gradient, for marker numbers $N_p = 128\text{M}$ and $N_p = 64\text{M}$ under the adaptive scheme. Time-evolved background quantities contributed by f_0 are not shown, as they coincide with the full measure contributed by $f_0 + \delta f$.

5.6 Limitations of long time simulations

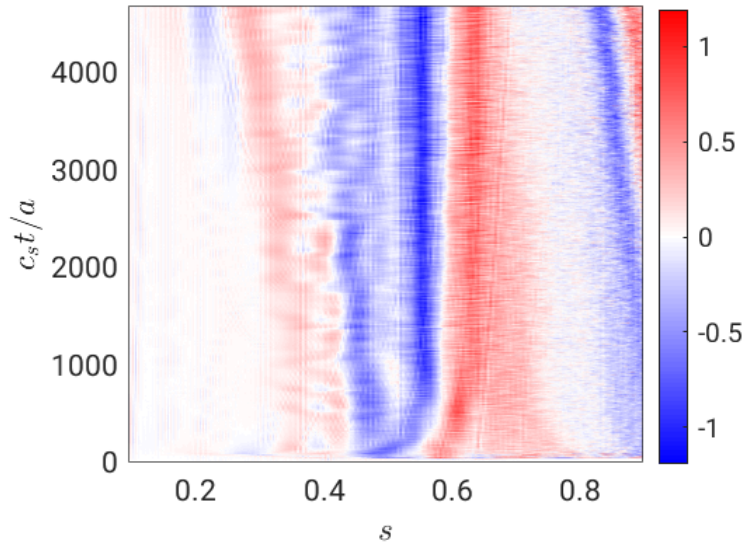


Figure 5.15: Time evolution up to $c_s t/a = 4902$ of the radial profile of the zonal flow shearing rate, $\omega_{E \times B}(s, t)$, for marker numbers $N_p = 128\text{M}$ under the adaptive scheme.

Figure 5.15 shows the time evolution of the radial profile of the zonal flow shearing rate of the adaptive case with $N_p = 128\text{M}$ markers. This is an extended result of Fig. 5.7c. Here, we see that while the main corrugation structure of $\omega_{E \times B}$ at the $q = 1$ flux surface $s = 0.538$ remains, a perturbation resulting from the edge buffer appears to drift radially inwards. Over long simulation times, this density perturbation will interact with the corrugation structure, thereby destroying it. Under strong fluxes in simulations of this chapter, a study on the length of the buffer

region s_b along with its strength γ_b on the effects of such radially inward drifting perturbations has yet to be conducted.

Finally, we consider the issue of phase-space volume sampling. At the beginning of every simulation, markers are uniformly distributed in configuration space and in the half-disc in velocity space $(v_{\parallel}, v_{\perp})$ of radius $\kappa_v v_{\text{thi}}(s)$ with $v_{\text{thi}}(s)$ the local ion sound velocity at initial time (see Eq. (3.11)). Each marker thus has a phase-volume element with which it occupies (see Eq. (3.15)). As simulation time passes, markers will be pushed in magnetic coordinates (s, θ^*, φ) via the gyrokinetic equations Eqs. (2.18)-(2.20), while phase-space volume evolves as an ‘incompressible fluid’ (see Eq. (3.12)). Near the magnetic axis, in order to avoid the singularity at $s = 0$ for the θ^* evolution (see Eq. (2.19)), a coordinate transformation is done in ORB5, from magnetic coordinates to a pseudo-Cartesian (ξ, η) , for markers within the radial region $s < s_{\text{push}}$ from the magnetic axis. As markers being pushed in (ξ, η) do not lead to accurate calculation of radial drifts ds/dt , it turns out that this leads to an accumulation of markers in the $s < s_{\text{push}}$ region. This is especially true for high-energy markers, as the error committed in the RK4 scheme is larger. Fig. 5.16 shows the ion marker count distribution difference from that at $t = 0$, over the reduced (radius,energy) (s, v^2) -phase space. The black dashed line indicates the boundary of the initially loaded markers, capped by $\kappa_v^2 v_{\text{thi}}^2(s)$. We first note the expected marker diffusion across this boundary, indicated by the blue regions just under the dashed line and red just above. We also see an accumulation of markers at low energy around $s \in [0.3, 0.7]$. Further diagnostic done for phase-space volume show that these migrations seem to still preserve the incompressibility of the phase-space. Finally, we notice the high-energy ion marker accumulation just within the radial region in which markers are pushed in (ξ, η) . This accumulation will be shown to corrupt phase-space volume in this region. It also explains to a certain extent the slight elevation of the ion temperature profiles in Figs. 5.11a and 5.13a. A more thorough analysis of the cause and potential solutions for this problem will be addressed in Sec. 6.3.5, where we will instead observe high-energy electron accumulation, and not for the ions.

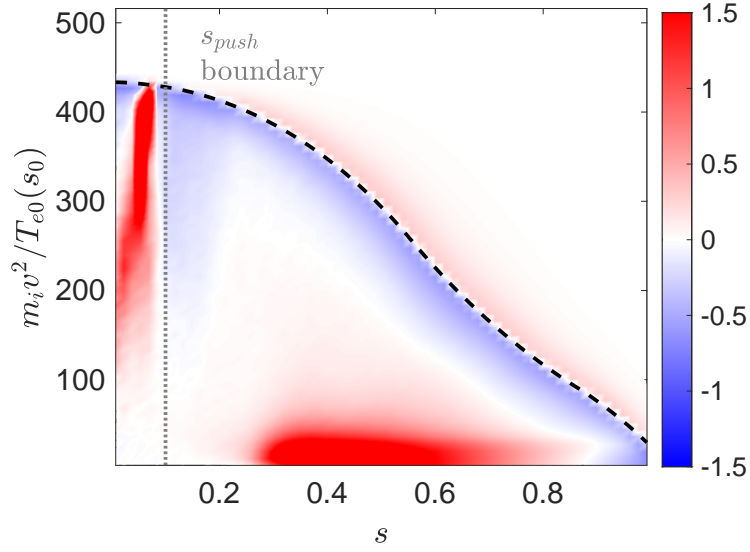


Figure 5.16: Ion marker count fractional difference $\Delta N v_{\text{th}}^2(s)/V_s(s)N_{\text{max}}(t=0)$ at time $c_s t/a = 4902$, with $N_p = 128\text{M}$ under the adaptive scheme. $N_{\text{max}}(t=0)$ indicates the global maximum marker number per bin at initial time $t=0$. s_{push} is the flux surface which pseudo-cartesian coordinates are used.

Chapter 6

Mixed TEM/ITG regime in TCV

The use of the adaptive scheme is further extended to include density and temperature background profile adaptation of ions and electrons separately. The assumption on fully adiabatic electrons of Ch. 5 is now relaxed, and the upgraded hybrid response of the electrons is adopted. This allows for both density and temperature evolution. The ultimate goal of this part of the thesis is to run flux-driven mixed ITG-TEM regime turbulence simulations. To that end, this chapter begins by defining the initial background profiles in Sec. 6.1. Sec. 6.2 describes the first phase of the stated goal: derive a source profile for the flux-driven runs, by first conducting temperature-gradient-driven simulations. The adaptive scheme of this section is thus limited to density adaptation only. This section also introduces the main diagnostics that are used throughout the chapter. Discussions on flux-driven runs are contained in Sec. 6.3. It begins by describing the heat source profile derived from the previous section, and gives an overview of the transport processes over the whole simulated time. The results of this second phase are split into two time windows. Sec. 6.3.4 discusses the first time window in which results of the standard and adaptive schemes are compared. Sec. 6.3.5 investigates the problem of the observed accumulation of high-energy electrons at the magnetic axis, and Sec. 6.3.6 describes the various implementations of the r.h.s. correction of the QNE. This chapter finishes with a discussion of the results under the adaptive scheme in the second time window in Sec. 6.3.7, with some concluding remarks in Sec. 6.4.

6.1 Parameters and profile

All simulations of this chapter use the the ideal MHD equilibrium of Ch. 5, i.e. the TCV shot #43516. The gyrokinetic equilibrium density and temperature profiles for both ions and electrons are still that of Eq. (5.1) with the parameters shown in Tab. 6.1, and illustrated in Fig. 6.1.

The grid resolution and the modes to be resolved within the Fourier filter are identical to Ch. 5. The electron mass is taken to be $m_e/m_i = 1/200$, contributing with a hybrid response to the QNE. The time resolution is set to $\Omega_{ci}\Delta t = 1.0$ ($c_s\Delta t/a = 4.1 \times 10^{-3}$), and the maximum linear growth rate is taken to be $\gamma_{\max}/\Omega_{ci} = 0.0038$ ($\gamma_{\max}a/c_s = 0.931$). The growth rates for the various toroidal modes n are shown in Fig. 6.2.

| Parameter | Ions | | Electrons | |
|----------------------|---------|-------------|-----------|-------------|
| | Density | Temperature | Density | Temperature |
| ρ_{core} | 0.4016 | 0.4016 | 0.4016 | 0.4016 |
| ρ_{ped} | 0.8 | 0.8 | 0.8 | 0.8 |
| κ | 2.3 | 2.3 | 2.3 | 2.5 |
| μ | 5.0 | 6.0 | 5.0 | 10.0 |
| G_1 | 1.0 | 1.0 | 1.0 | 1.0 |

Table 6.1: Profile Eq. (5.1) parameters for initial density and temperature for both background ions and electrons.

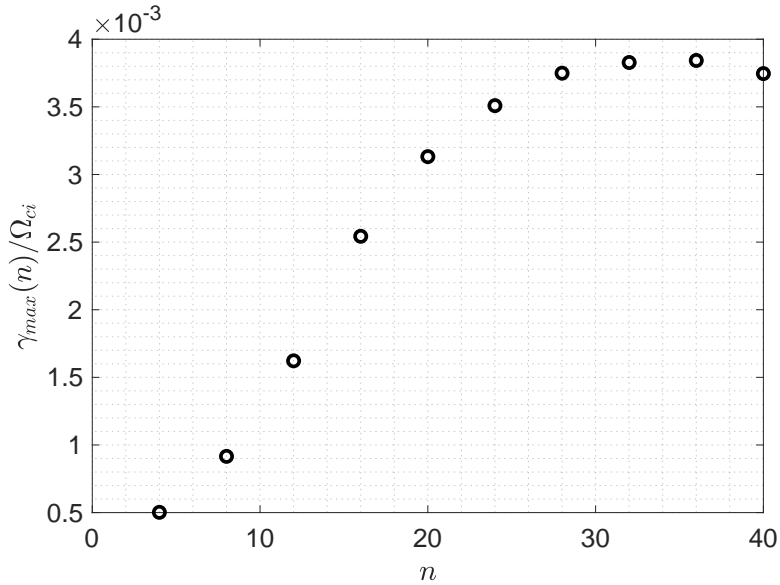


Figure 6.2: Maximum linear growth rate for each toroidal mode number. Maximum linear growth rate is found to be $\gamma_{\text{max}}/\Omega_{ci} = 0.0038$ ($\gamma_{\text{max}}a/c_s = 0.931$).

Simulations are initially perturbed with a $\delta f(t=0)$ set as white noise¹, with markers populating the velocity space up to $\kappa_V = 5$ (see Sec. 3.1.2). The Krook operator Eq. (3.80) with strength $\gamma_K\Omega_{ci} = 4.2 \times 10^{-4}$ ($\gamma_K a/c_{s0} = 0.103$), which is around 11% γ_{max} , for either temperature gradient drive and/or noise control, is always present throughout the whole simulation volume.

For this chapter, unless stated otherwise, all time traces have a moving time averaging window of $c_s\Delta t/a = 4.085$. Radial averages of profiles are taken to be for $s \in [0.7, 0.9]$, which is within the constant logarithmic gradient regions in the initial profiles, see Fig. 6.1. Marker numbers N_p are displayed in millions (M). Comparisons will be made between the standard case with $N_p = 256\text{M}, 128\text{M}$ and the adaptive case with $N_p = 128\text{M}, 64\text{M}$. All adaptive cases have parameters as shown in Tab. 6.2. Adaptive scheme using the simultaneous scheme (see Sec. 3.2.4) are indistinguishable with the results shown here under the current plot resolution. Corrections to the r.h.s. of the QNE Eq. (2.36) resulting from/related to the evolution of the background distribution is done by exact integration of the change in each species' background gyrodensity (see Sec. 3.2.10.1), except in Sec. 6.3.6, where

¹White noise initialisation for $\delta f(t=0)$ is done by setting the marker weights $w = 5 \times 10^{-4}(2U-1)$, where U is a unit uniform random number

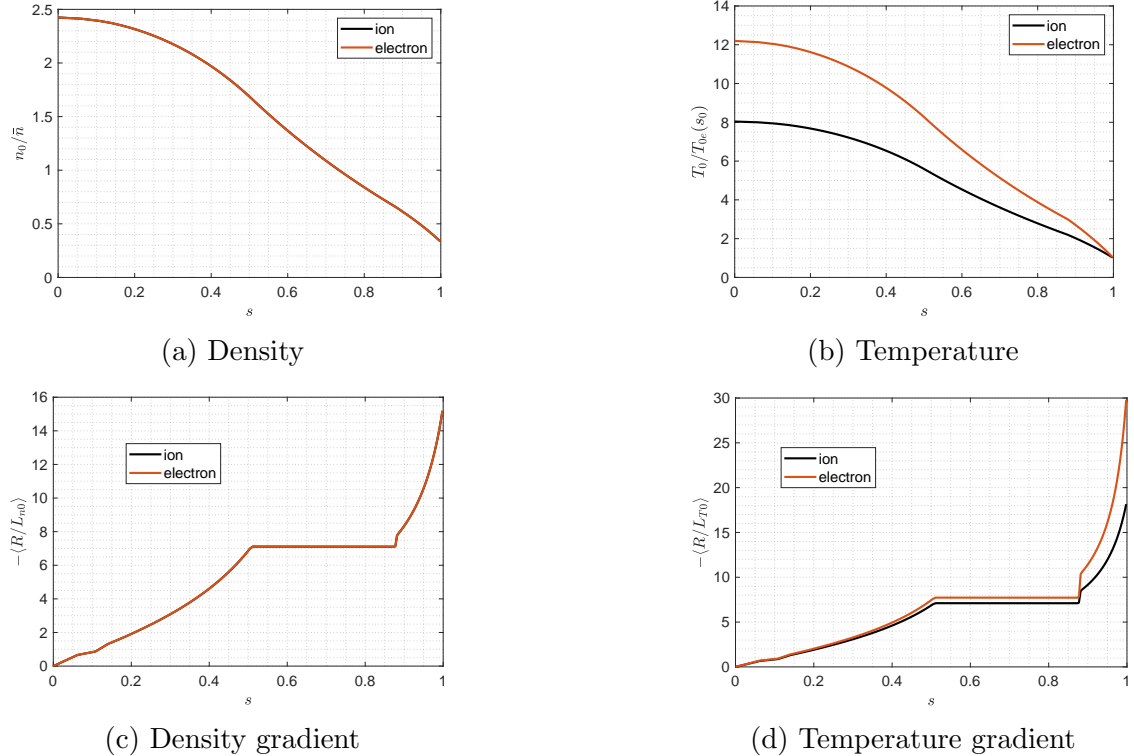


Figure 6.1: Initial density and temperature profiles of both ions and electrons as well as corresponding logarithmic gradients.

other calculation methods are compared. Adapted electron profiles include contributions from both passing and trapped electrons. In all simulations, markers are loaded only once at initial time $t = 0$.

| Parameter | Value | Reference |
|--|----------------------------------|----------------------|
| scheme | interleaved | Sec. 3.2.3 |
| control variate | canonical | Eq. (3.53) |
| adaptive rate, α | $3.8 \times 10^{-4} \Omega_{ci}$ | $10\% \gamma_{\max}$ |
| time-averaging period, N_t | 100 | Eq. (3.59) |
| background profile grid resolution, N_ψ | 64 | Eq. (3.55) |
| background profile B-spline order | 3 | Eq. (3.55) |
| QNE r.h.s. calculation | exact (unless otherwise stated) | Sec. 3.2.10.1 |

Table 6.2: Parameters of the adaptive scheme for both ions and electrons used in this chapter. Adaptive rate α is common for both gyrocentre density α_n and energy (temperature) α_E . Temperature adaptation is only done for Sec. 6.3.

6.2 Temperature-gradient-driven simulation

In order to prevent f.s.a. temperature profile relaxation, we use the Krook operator Eq. (3.80) as a δf dependent heating operator for each species. This is accomplished by not conserving the energy moment on each flux surface, thus damping δf so that $f(t)$ is restored towards the target (initial) f.s.a. temperature profile. The heating strength γ_K must be low enough to avoid unphysical damping of turbulence, and high

enough to ensure noise control. The consequence of choosing low values of γ_K is some level of relaxation of profiles w.r.t. reference ones. Since simulations presented in this chapter involves hybrid electrons, density transport is expected as the potential and density perturbations are no longer in phase. The Krook heating operator allows for an unrestricted density evolution by conserving the f.s.a. density. For the adaptive cases, background temperatures are not adapted as only small deviation is expected in these temperature gradient driven simulations. Quasi-steady state is found to have reached at $c_s t/a \approx 300$.

6.2.1 Heat and particle transport

The simulations of this chapter use the hybrid electron model. That is, all passing and trapped electrons are evolved according to the drift-kinetic trajectories. However, only the associated kinetic contribution to the r.h.s. of the QNE of the trapped electrons is considered while the passing contribution is set to be adiabatic, except for zonal contribution. Furthermore note that electrons can be trapped/detrapped, not only as a result of collisions, but also due to $E \times B$ parallel non-linearity. Given that one enforces the contribution to the QNE from passing electrons to be adiabatic, one expects their distribution (evolved kinetically) to confirm this, else the model is questionable. Non-zero contributions to fluxes from passing electrons provides a measure of un-adiabaticity. Fig. 6.3 shows heat transport measured according to the corresponding heat diffusivity (Eq. (3.91)) for ions χ_i , trapped electrons $\chi_{e,T}$, as well as total electrons (passing + trapped) $\chi_{e,P} + \chi_{e,T}$. Specifically, the trapped electron heat diffusivity $\chi_{e,T}$ is given by

$$\chi_{e,T} = \frac{\left\langle \bar{q}_{H,e}^{(\text{trapped})} \cdot \nabla \psi \right\rangle}{n_e dT_e / d\psi \langle |\nabla \psi|^2 \rangle},$$

where $\bar{q}_{H,e}^{(\text{trapped})}$ is the trapped electron heat flux. n_e and T_e are the density and temperature profiles of all (passing and trapped) electrons respectively.

Figure. 6.3a illustrates the radially-averaged ion heat diffusivity χ_i . In quasi-steady state, χ_i is maintained constant with intermittent turbulent bursts. As shown in Fig. 6.3b, the heat diffusivity of the electrons χ_e behaves similarly. Although at early times $c_s t/a \lesssim 100$, one has $\chi_e > \chi_i$, reflecting that turbulence is at first dominantly driven by TEM. At later times, $\chi_i \sim \chi_e$, consistent with a mixed ITG/TEM turbulence drive. Note that trapped electrons (dashed curves) contribute to only a fraction of the total electron heat flux. This is an indication that the passing electron contribution is non-zero, and their response is therefore not truly adiabatic, as assumed in the hybrid electron model. This discrepancy is probably enhanced due to the large electron mass used in this work $m_e/m_i = 1/200$. Fig. 6.3c shows the heat diffusivity ratio χ_i/χ_e for χ_e including both the passing + trapped contributions of electrons (solid curves) and trapped only (dotted curves) respectively. One can estimate the contribution of passing electrons to be about 40% of the total heat flux of this species. Fig. 6.3c also confirms that simulation has turbulence driven at early times by trapped-electron-modes (TEM) ($\chi_i/\chi_e < 1.0$), but driven in a 50% – 50% ITG-TEM mixed regime at quasi-steady state ($\chi_i/\chi_e \approx 1.0$).

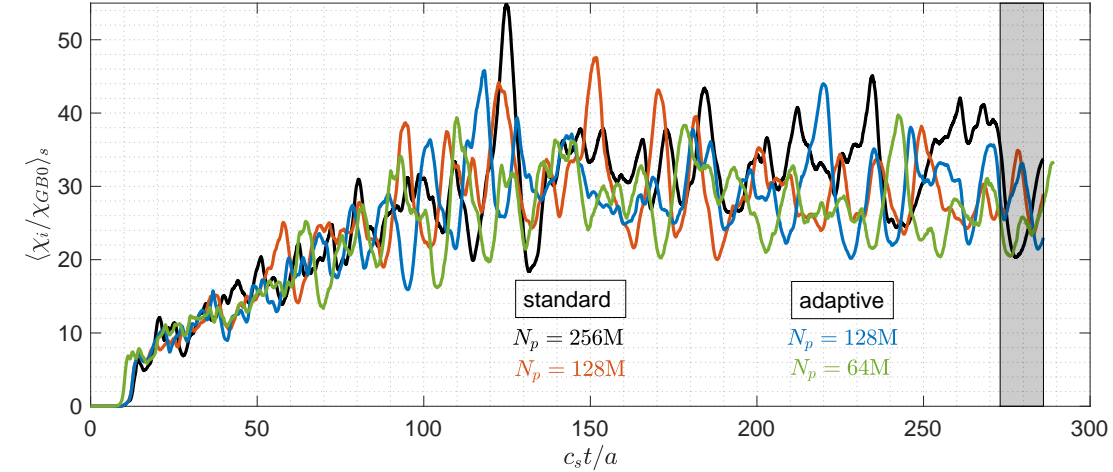
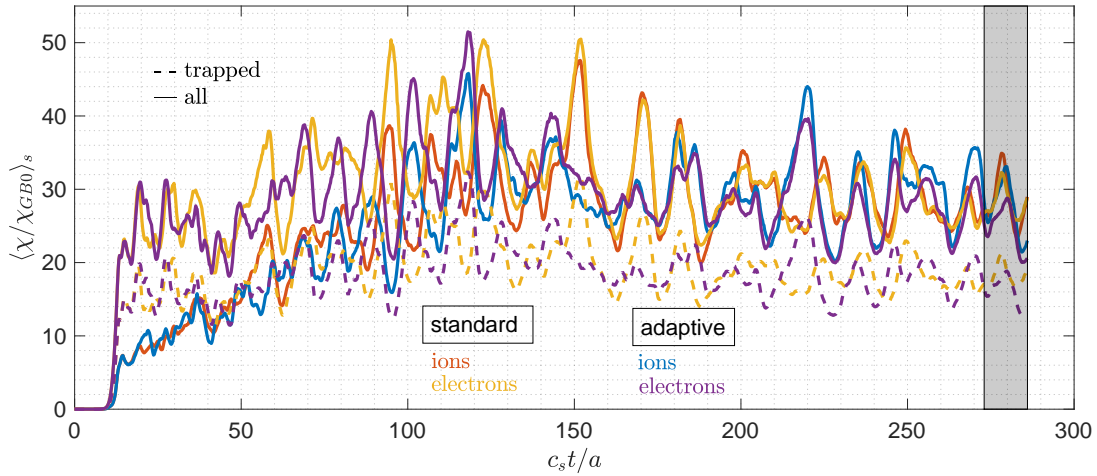
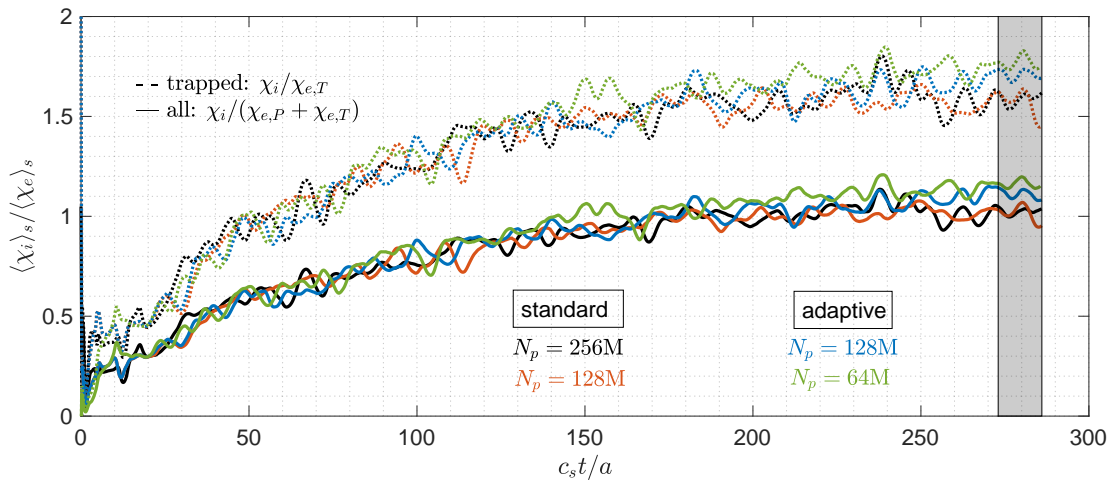

 (a) Ion heat diffusivity χ_i

 (b) Ion and electron heat diffusivities with $N_p = 128M$

 (c) Heat diffusivity ratio χ_i / χ_e

Figure 6.3: Radially averaged $s \in [0.7, 0.9]$ heat diffusivities χ and heat diffusivity ratio χ_i / χ_e , for various marker numbers N_p under the standard and the adaptive schemes. Subscripts P and T for the electron heat diffusivity χ_e represent passing and trapped contributions respectively. The grey time window is used to plot time-averaged profiles of Figs. 6.9 and 6.10.

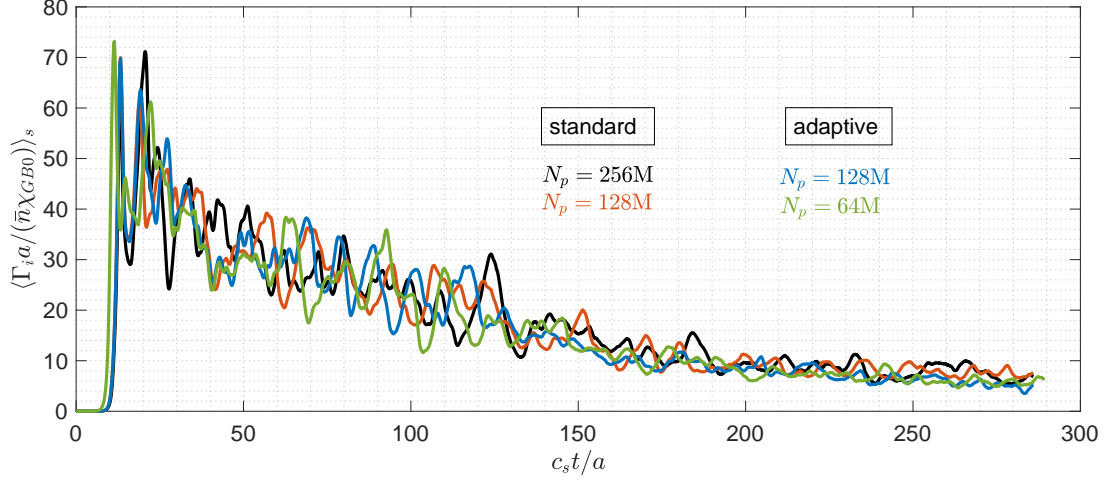
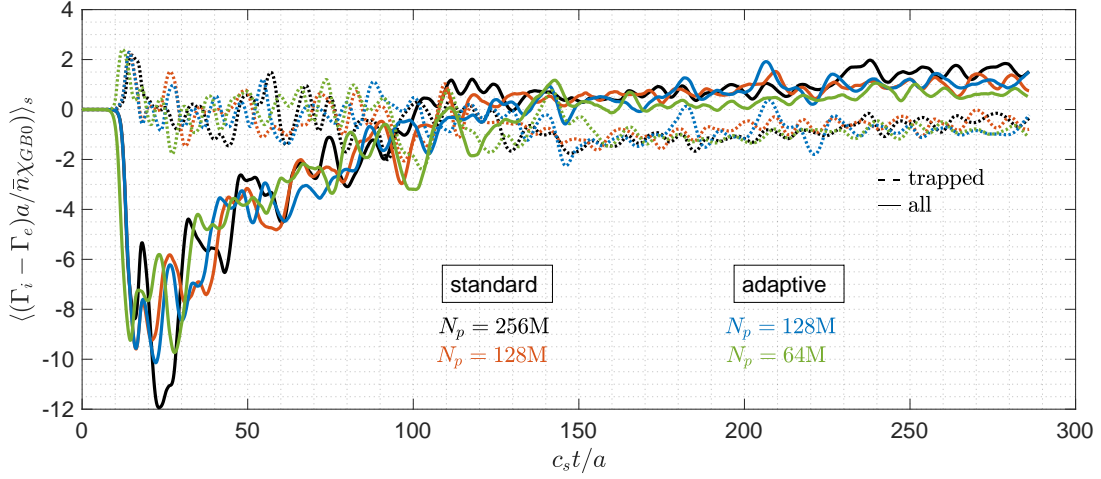

 (a) Ion gyrocentre flux Γ_i

 (b) Particle flux difference $\Gamma_i - \Gamma_e$

Figure 6.4: Time traces of radially averaged $s \in [0.7, 0.9]$ ion gyrocentre flux as well as ion-electron gyrocentre flux difference $\Gamma_i - \Gamma_e$, for various marker numbers N_p under both the standard and the adaptive schemes. 'trapped' and 'passing+trapped' curves use χ_e contributed by trapped only and passing and trapped electrons, respectively.

The presence of drift-kinetic electrons allows for particle transport as the density and potential fluctuations are not necessarily in-phase. Fig. 6.4a shows the ion gyrocentre flux Γ_i for all cases considered. Once again, the results under the standard and adaptive schemes are similar. As expected, Γ_i reduces to negligible values (i.e. $\sim 5\%$ of initial peak flux) as the system reaches quasi-steady state. As quasi-neutrality is imposed, the ion and electron particle fluxes is expected to be ambipolar, i.e. exactly equal. The f.s.a. gyrocentre fluxes will however only be equal when averaged over a time window. Indeed, the f.s.a. particle and gyrocentre fluxes differ by the polarisation drift contribution which cancels averaged over time[11, 20]. Fig. 6.4b shows the difference between these fluxes $\Gamma_i - \Gamma_e$. We see that particle fluxes of ions and trapped electrons are roughly equal throughout time. Consistent with QNE including zonal ($n = 0$) contribution of all electrons (passing+trapped), one expects that ambipolarity is ensured by electron flux including

both trapped + passing contributions as well. Nonetheless according to Fig. 6.4b, the difference between the gyrocentre fluxes $\Gamma_i - \Gamma_e$ seem to converged to a value of $\Gamma_i - \Gamma_e = 1\bar{n}\chi_{GB0}/a$.

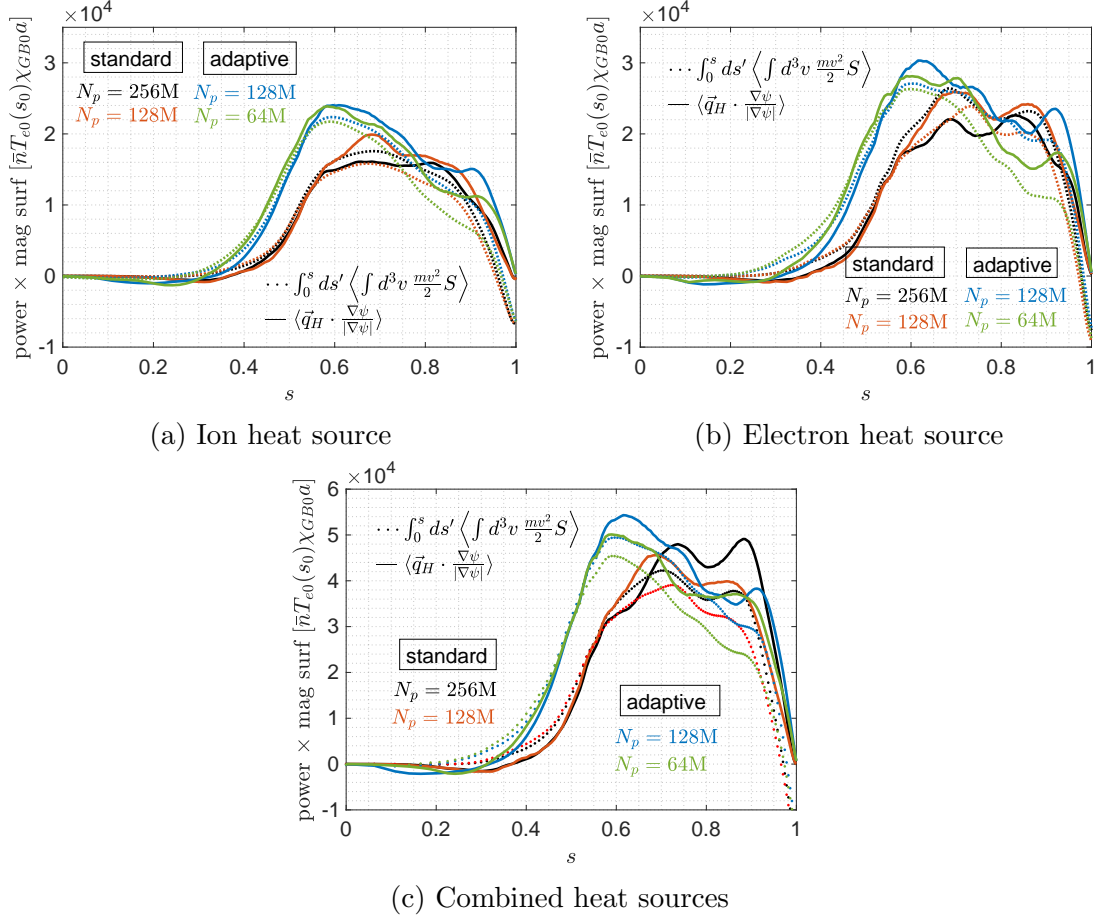


Figure 6.5: Time-averaged volume integrated heat source $\int_0^s ds' \langle \int d^3v \frac{mv^2}{2} S \rangle$ and heat flux through flux surface $\langle \vec{q}_H \cdot \frac{\nabla\psi}{|\nabla\psi|} \rangle$, for various marker numbers N_p under the standard and the adaptive schemes. The electron heat flux includes both passing and trapped contributions. The time averaging window is taken to be $c_s t/a \in [273, 286]$.

Finally, at quasi-steady state the volume integrated and time-averaged heat sources should be balanced by the time-averaged heat flux passing through the magnetic surface which encloses the considered volume. Fig. 6.5 show such balance for both the ions and electrons, separately and combined, for the time window indicated by the grey shaded region of Fig. 6.3. The volume integrated heat source (dotted curves) is estimated by binning weight variations per unit time resulting from the heating operator (see Eq. (3.81)) on a ψ grid. As we can see, these time-averaged quantities are approximately equal in the species-separated cases. The adaptive scheme seems to lead to a larger and radially wider heat source as compared to the standard approach. The Krook operator acts differently for both standard and adaptive cases as the correction term $S_{K^c}^c$, which conserves the f.s.a. density, parallel velocity and zonal flow, is calculated based on the binning of marker weights, which are different between both schemes. That is, weight amplitudes along with their variance are usually smaller under the adaptive scheme as compared to that

under the standard scheme. Therefore, though f.s.a. kinetic energy is conserved up to machine precision in each radial bin, the variance in these bin will be larger under the standard scheme. This will be confirmed by the analysis of the Signal-to-Noise Ratio (see Sec. 6.2.2).

6.2.2 Signal-to-noise and weight variance

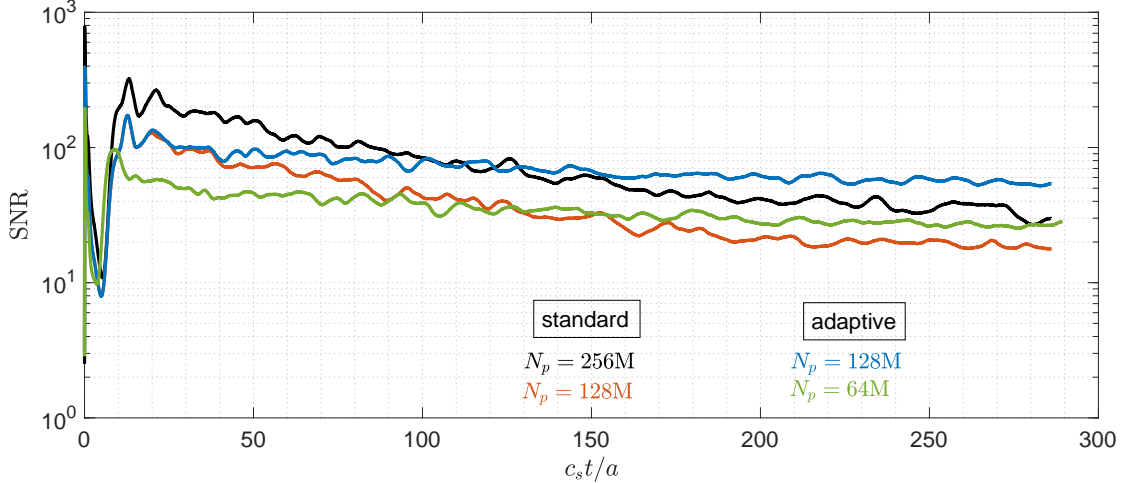


Figure 6.6: Time dependence of global Signal-to-Noise ratio (SNR) values, for various marker numbers N_p under the standard and the adaptive schemes. The signal includes the zonal component $(m, n) = (0, 0)$.

We now turn to the diagnostics relating to weight variance. Fig. 6.6 shows the global Signal-to-Noise Ratio (SNR) (see Eq. (3.27)) value time trace for all four cases discussed in this chapter. One observes firstly that for a given scheme (standard or adaptive), the SNR values scale roughly as N_p after the initial burst at around $c_s t/a = 10$, as this diagnostic uses the square of the spline coefficient amplitudes \hat{b}_{imm} of the r.h.s. of the QNE (see Sec. 3.1.4.1). That is, \hat{b}_{imm} scales as N_p^0 and $1/\sqrt{N_p}$ in the signal \mathcal{F}_1 and noise \mathcal{F}_2 , respectively (see Fig. 3.1). Focusing then on the standard cases, we see that the SNR values continue to drop as simulation time passes. As the noise is proportional to the weights squared, Eq. (3.26), as the system approaches quasi-stead state characterised by absence of secular profile evolution, the rate of drop is expected to reduce. Towards the end of the simulations for the standard cases, the simulation is deemed to be drowned in noise, and a restart (resampling of markers) would be required. For the adaptive cases, SNR values are maintained at a nearly constant level over long times as long as our computing resources allowed us to follow only a small drop after the initial burst. Comparing the standard and adaptive cases, we see that after around $c_s t/a = 140$, adaptive cases with half the number of markers compared to the standard cases already present larger SNR values. At the end of simulations $c_s t/a \approx 280$, the adaptive case with $N_p = 64M$ has an SNR value as high as the $N_p = 256M$ non-adaptive case. For this particular temperature-gradient-driven study, the considered N_p values have been chosen such that all cases maintain acceptable SNR values over at least the length of the simulation. This is done to allow for comparison between results from the standard and adaptive cases.

SNR values of the standard cases will usually continue to drop, while those of the adaptive cases are maintained approximately at a constant value.

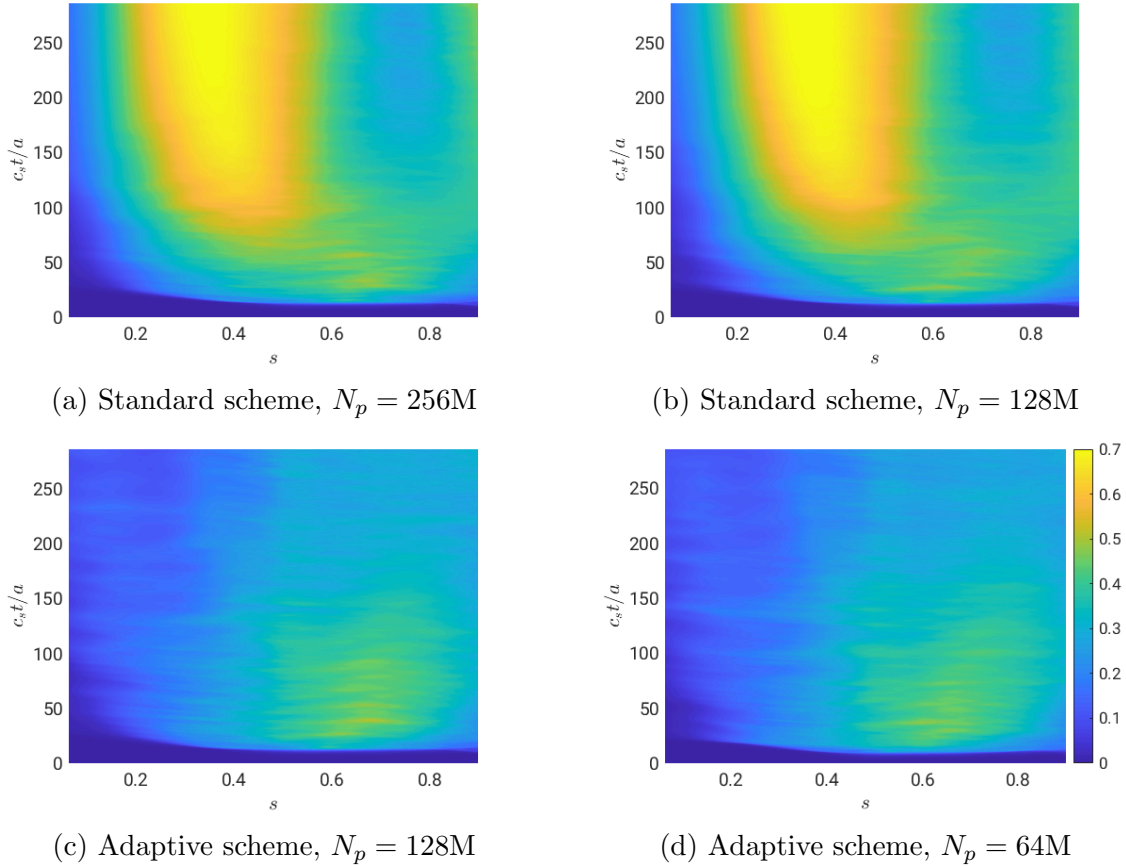


Figure 6.7: Time evolution of ion f.s.a weight standard deviation profiles $\sqrt{\langle w^2 \rangle - \langle w \rangle^2}$. All plots share the same colour scale. Corresponding results for electrons give similar trends.

Taking a closer look at how the local f.s.a. weight standard deviation σ_w (see Eq. (3.29)) changes, Fig. 6.7 shows the time evolution of the ion $\sigma_w(s_{\text{bin}})$ for the consider standard and adaptive cases. We first note that for the standard cases the ion σ_w is greatest around $s = [0.3, 0.5]$. Comparing Figs. 6.7a and 6.7b, for cases with marker numbers $N_p = 256M$ and $N_p = 128M$ respectively, we can deduce that σ_w is converged with N_p . Comparing with Fig. 6.9. This radially local increase of σ_w can be explained by local density profile deviations (see Fig. 6.9), which leads to generally large local weights $\{w\}$. On the other hand, the adaptive cases Figs. 6.7c and 6.7d show reduced σ_w . The location of maxima for these cases are also located at $s \in [0.6, 0.7]$. σ_w of the adaptive cases are gradually reduced with time as the control variate, i.e. the background f.s.a ion density profile adapts.

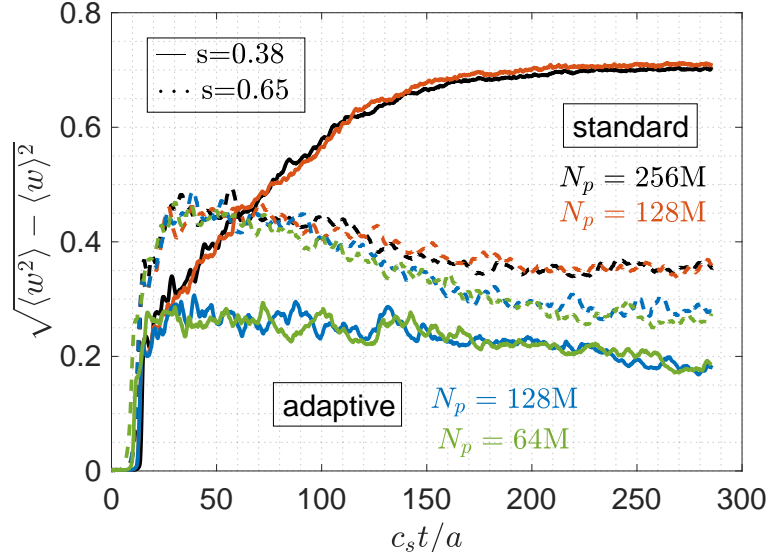


Figure 6.8: s -cuts of ion f.s.a. weight standard deviation profiles $\sigma_w = \sqrt{\langle w^2 \rangle - \langle w \rangle^2}$. Electrons give similar trends.

To compare the amount of reduction in σ_w as a result of an adaptive control variate, Fig. 6.8 shows radial s -cuts at locations $s = 0.38, 0.65$, of the results of Fig. 6.7. Focusing first on the $s = 0.38$ cut corresponding to the peak σ_w of the standard cases, we see that the adaptive scheme (blue and green) reduces this value by about 3-fold. In fact, the result from the adaptive case seem to further decrease with time. The $s = 0.65$ cut corresponds to the location of maximum for the adaptive cases. We see that, though σ_w is small, with reference to the standard cases, the adaptive control variate nonetheless further reduces this value. Though not shown here, the σ_w results for the electrons, corresponding to Figs. 6.7 and 6.8, give similar trends.

6.2.3 Profile evolution

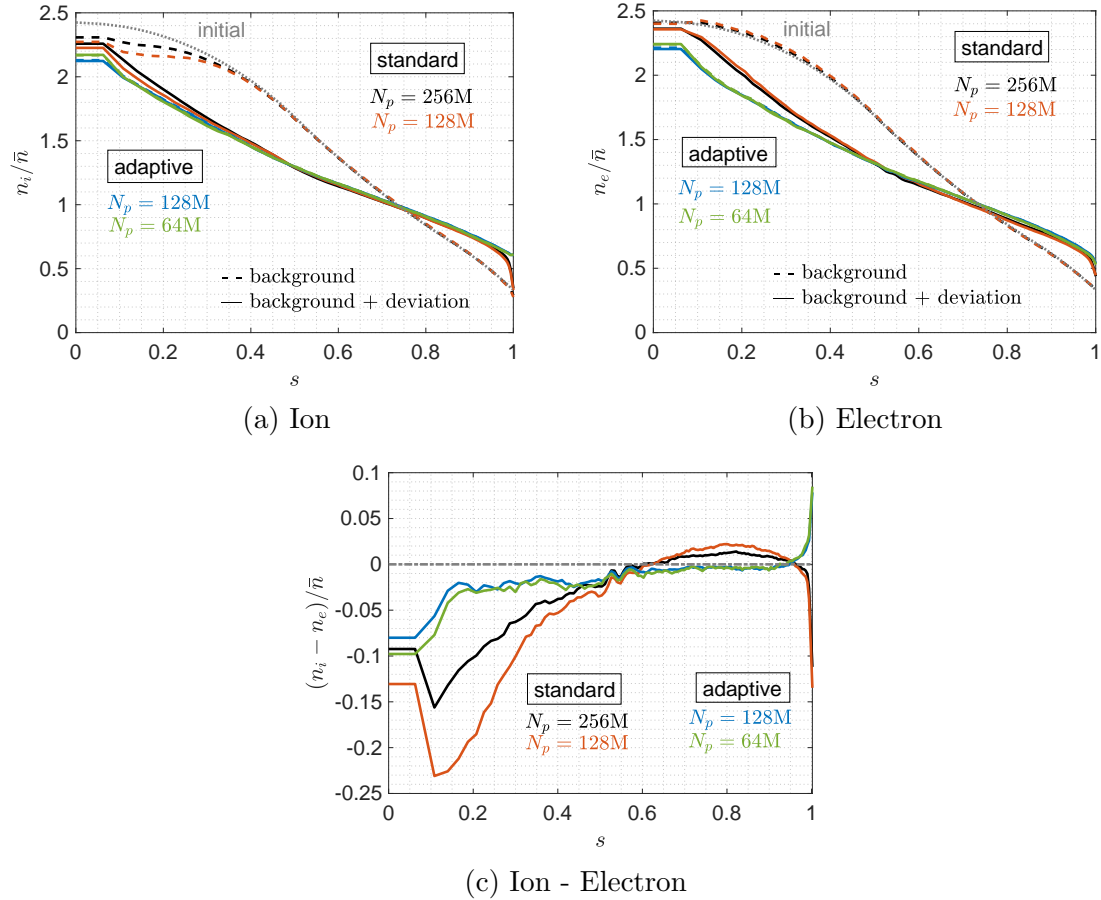


Figure 6.9: End-time time-averaged $c_s t/a = [273, 286]$ gyrocentre density profiles, for various marker numbers N_p under the standard and adaptive schemes. ‘background’ and ‘background + deviation’ represent the profile contributed by f_0 and $f_0 + \delta f$, respectively. (c) shows gyrocentre density difference contributed by $f_0 + \delta f$.

Looking first at the final radial electron density profile in Fig. 6.9b, we can see that the adaptive cases allowed for a larger density deviation compared to all standard cases. Also, the background densities of the adaptive cases represented as dashed lines actually coincide with the end-time total (background plus deviation) densities, as they are being adapted at a sufficiently high rate.

A similar analysis can be done for the ion gyrocentre density of Fig. 6.9a. Comparing with Fig. 6.9b, the ion gyrocentre density evolution does not have to be exactly equal to that of the electrons as the ion polarisation density and FLR contributions are not included, which actually represent a significant fraction of the total density, see Fig. 6.9c. This applies especially around $s = 0.1$. Gyrocentre profiles of Figs. 6.9a and 6.9b are the fully relaxed profiles corresponding to the zero particle flux condition (see Fig. 6.4b). Nonetheless, we see better equality between the gyrocentre densities of ions and electrons under the adaptive scheme. It is interesting to observe that near the magnetic axis, the background densities of the standard cases which a priori do not evolve do not coincide with the initial density when constructed using p -weights, i.e. $f_0(\vec{Z}_p)\Omega_p$. Under this construction, lower N_p

results in a larger discrepancy. This is because the profiles shown in Fig. 6.9, and all subsequent radial profiles are represented, only as diagnostics, by marker sampling on radial bins and not analytical functions. The background density deviation for the standard cases could be explained (see Sec. 6.2.5) by phase-space volume not being conserved for low energy markers near the magnetic axis. This problem is more pronounced for the ions than the electrons. As will be shown, this problem is not present for simulations under the adaptive scheme.

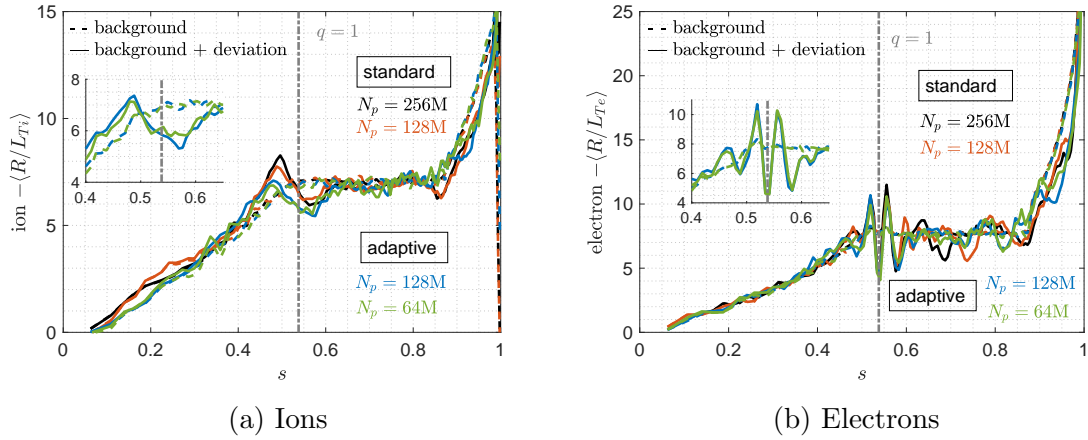


Figure 6.10: Time-averaged $c_s t/a \in [273, 286]$ logarithmic gradient profiles of gyrocentre temperature, for various marker numbers N_p under the standard and adaptive schemes. ‘background’ and ‘background + deviation’ represent the profile contributed by f_0 and $f_0 + \delta f$, respectively.

Figure 6.10 shows the end-time logarithmic gradients profiles of gyrocentre temperature for both ions and electrons. As these simulations are temperature-gradient-driven, only a weak relaxation is expected. It is interesting to note the corrugation of the gradients around $s = 0.55$ for both ions and electrons, though more severe for the latter. This region is close to the $q = 1$ rational flux surface (see Fig. 5.1). For both species, the corrugation is only captured by the δf component even with the adaptive scheme, as the background temperature is not adapted in these temperature-gradient simulations, only the density profile is adapted. The deviation in the ion gradient near the magnetic axis $s \in [0, 0.3]$ in the standard cases is once again due to low local marker sampling statistics.

6.2.4 Zonal flow shearing rate

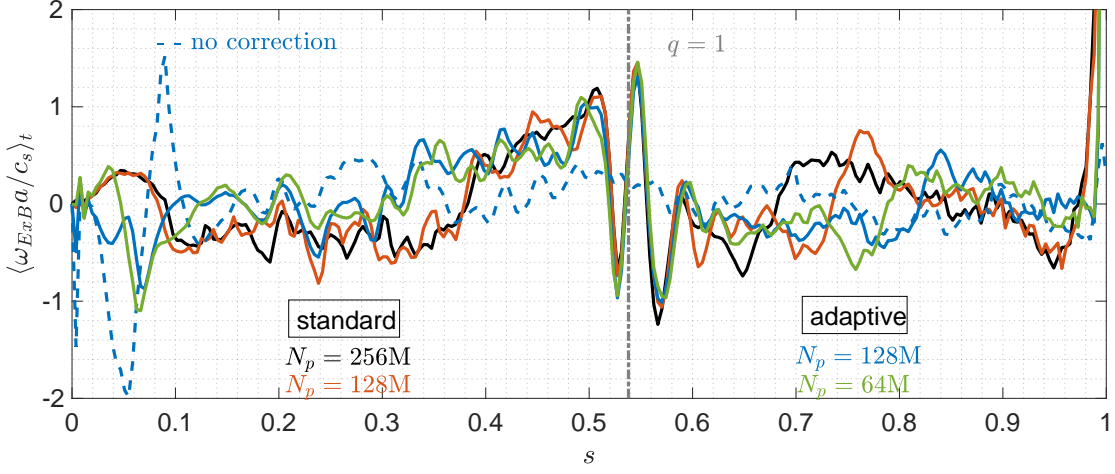
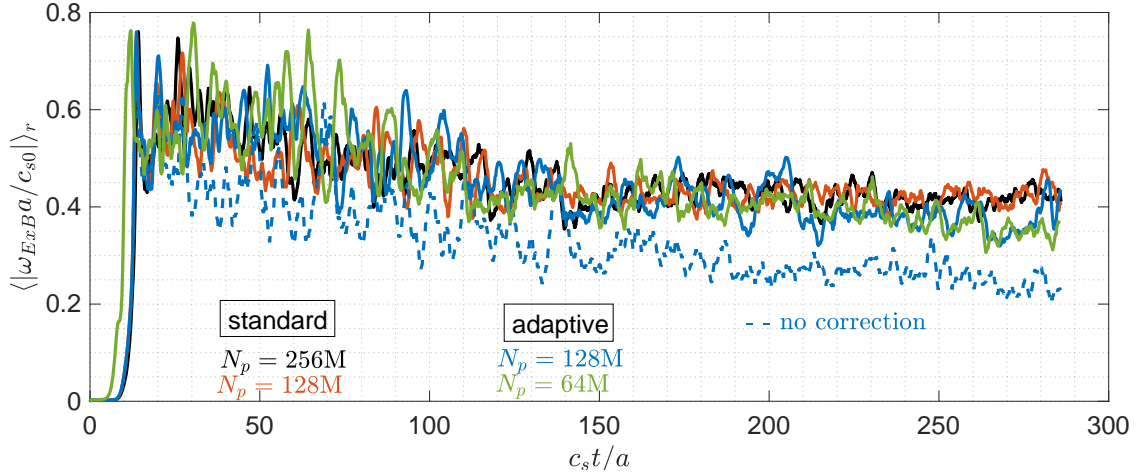
(a) Time-averaged zonal flow shearing rate $\langle \omega_{E \times B} \rangle_t$ (b) Radially averaged absolute value of zonal flow shearing rate $\langle |\omega_{E \times B}| \rangle_r$

Figure 6.11: $E \times B$ zonal flow shearing rate $\omega_{E \times B}$, for various marker numbers N_p under the standard and the adaptive schemes. ‘correction’ refers to the r.h.s. of the QNE. The time-averaging window for (a) is $c_s t/a \in [274, 286]$ and the radial averaging window for (b) is $s \in [0.1, 0.9]$.

Figure 6.11a shows the zonal flow shearing rate $\omega_{E \times B}$ profile, time averaged over the interval $c_s t/a \in [274, 286]$ from both the standard and adaptive schemes. The results from the adaptive scheme with QNE r.h.s. correction coincide with results obtained using the standard approach around the $q(s = 0.538) = 1.0$ region, characterised by a well defined corrugation. For the adaptive case without the correction (dashed blue curve), compared to the other simulations we see that it does not include the corrugation at $q = 1.0$ and has globally lower $\omega_{E \times B}$ amplitudes as can be seen by the time traces of Fig. 6.11b. Even in the expected quasi-steady state, this case with no correction presents decreasing radially averaged shearing rate $\langle |\omega_{E \times B}| \rangle_r$ seem to continue to have even smaller $\omega_{E \times B}$.

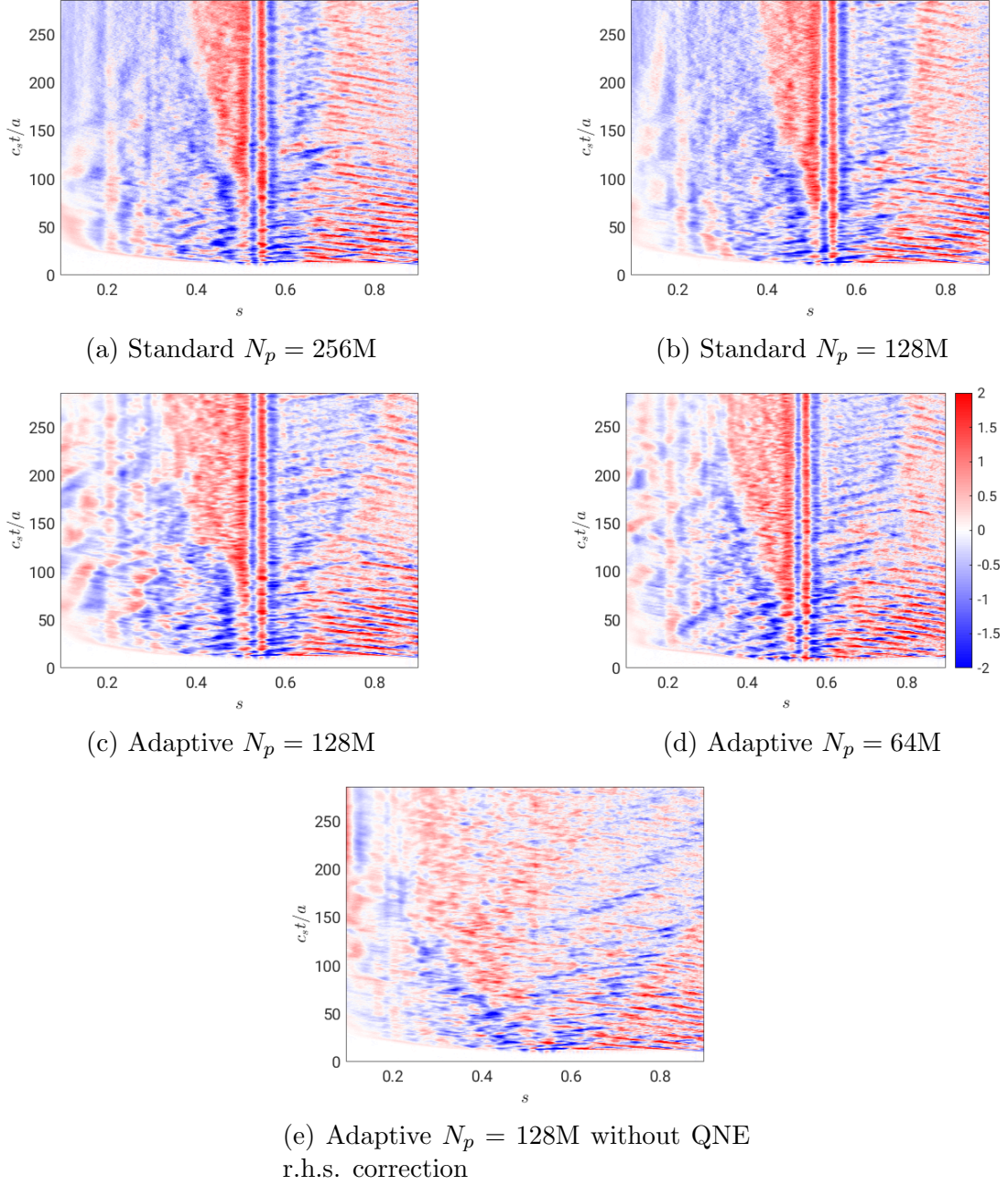


Figure 6.12: Time evolution of zonal flow shearing rate profile $\omega_{E \times B}(s, t)$, for various marker numbers N_p under the standard and the adaptive schemes. All plots share the same colour scale.

To further illustrate the differences between all cases, Fig. 6.12 shows the time evolution of the $\omega_{E \times B}$ radial profile. The first point to note is that negative (blue) and positive (red) $\omega_{E \times B}$ corresponds to an outward and inward direction of avalanches respectively, in agreement with Ref. [61]. As we can see, cases under the adaptive scheme with the r.h.s. correction exhibit outward travelling avalanches that extend more to the right of $s = 0.55$ as compared to the standard cases. These adaptive cases also show prolonged intermittent inward travelling avalanches around $s \in [0.1, 0.3]$. Nonetheless, for all cases discussed, except for the adaptive case without correction, the magnitude of the local $\omega_{E \times B}$ remains similar in the final phase

of the simulation, as already shown in Fig. 6.11a.

Henceforth, all adaptive scheme results presented in this thesis will involve the r.h.s. correction term. Thus far, the calculation of this term is based on the exact method of Sec. 3.2.10.1. No noticeable difference was found between the various methods (see Sec. 3.2.10.1, 3.2.10.2 and 3.2.10.3), as will be shown in Sec. 6.3.6.

6.2.5 Phase-space volume diagnostic

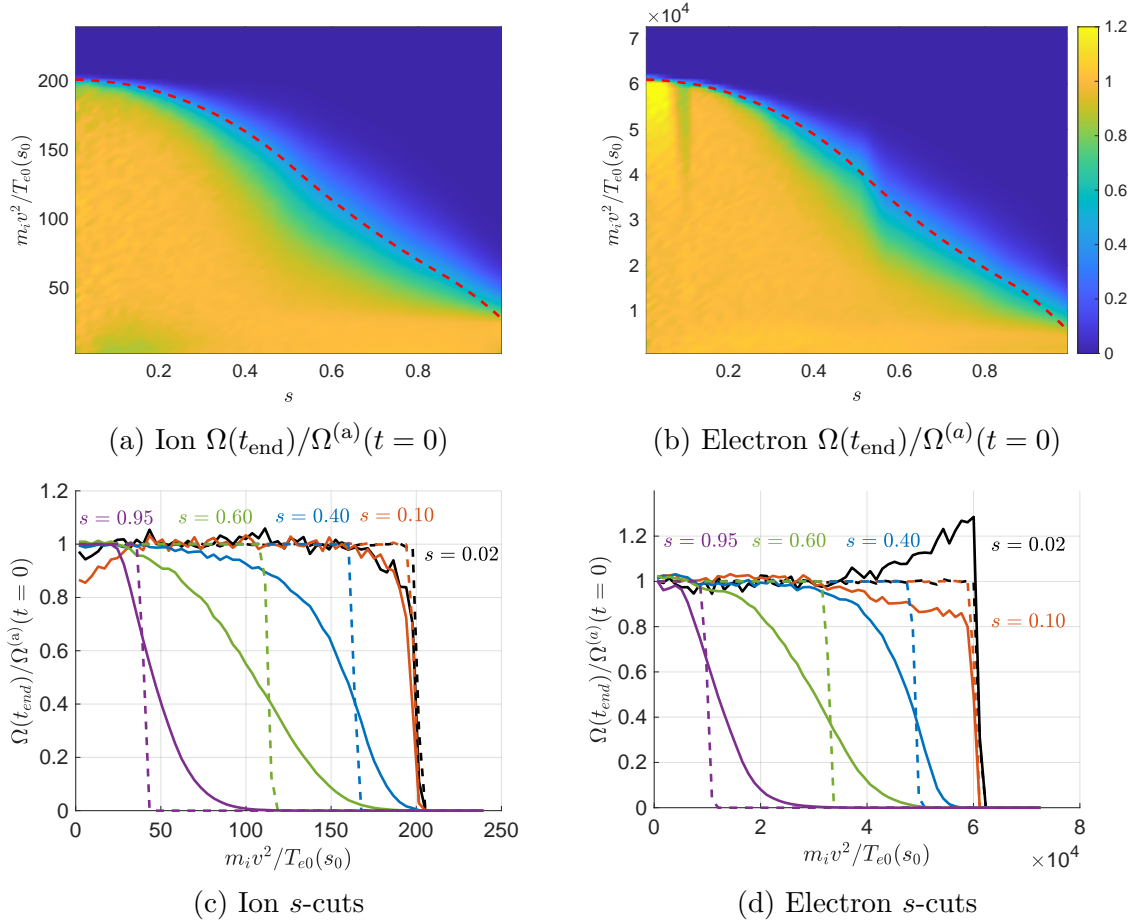


Figure 6.13: Phase-space volume diagnostic applied to Cartesian bins in (s, v^2) space for the standard case with $N_p = 128\text{M}$ at $c_s t_{\text{end}}/a = 286$. Shown is the ratio $\Omega(t_{\text{end}})/\Omega^{(a)}$, of which values near 1 reflect good sampling, while ratios deviating significantly from 1 reflect poor/deficient sampling. The red dashed line on the contour plots indicate the energy upper-bound during initial marker loading, given by $m\kappa^2 v_{\text{th}}^2(s)$. As $\Omega^{(a)}$ appears in the denominator, it is taken without the v^2 -cut-off to avoid singularities (see Eq. (3.17)). The dashed lines in (c) and (d) are taken at $t = 0$.

At the beginning of each simulation, markers representing gyrocentres are populated in phase-space according to Eq. (3.17). This means that in velocity space, markers are initially distributed uniformly in the two-dimensional semi-circular domain of radius $\kappa_v v_{\text{th}}$ in the $(v_{\parallel}, v_{\perp})$ -plane: $v_{\parallel}^2 + v_{\perp}^2 \leq \kappa_v^2 v_{\text{th}}^2$ with $v_{\perp} \geq 0$. In configuration space, markers are initially distributed uniformly (see Sec. 3.1.2). As the simulation

evolves over time, markers move in phase space governed by the gyrokinetic equations of motion Eqs. (2.18)-(2.20), and the overall marker distribution should behave like an incompressible fluid (Eq. (3.12)). Due to RK4 time-integration inaccuracies, markers will deviate from their characteristic trajectories, and phase space may not be well sampled with simulation time. This is particularly true near the magnetic axis $r = 0$ where, according to the current loading, there are very few markers per s -bin. We now employ the phase-space volume diagnostic described in Sec. 3.1.3.1. We divide Ω by its initial value $\Omega^{(a)}(t = 0)$ to even out an otherwise large Ω variation for better illustration, and it also gives a better gauge of fractional change.

Figure. 6.13 shows the phase-space volume diagnostic, at time $c_s t/a = 286$, for the ions and electrons under the standard scheme. To aid analysis, various radial s -cuts are also shown. Focusing first on the ions shown in Figs. 6.13a and 6.13c, we notice the expected phase-space diffusion near the step-like upper boundary of the initial marker loading in velocity space, represented by the dashed red line in the contour plot. This diffusion is particularly high around $s = 0.6$. As the current case study does not exhibit large temperature profile variations, this should not result in under-sampling for high energy markers. Next, we observe a strange lack of sampling of the ion phase-space at very low energies around $s = 0.1$. This is the result of either markers migrating away from said region and not being replaced by new ones, or the incompressibility of phase-space Eq. (3.12) being violated. We now turn to the electron phase-space diagnostic shown in Figs. 6.13b and 6.13d. Once again, we note the diffusion at the high velocity cut-off. The ‘kink’ in the radial diffusion pattern at $s \sim 0.5$ coincides with the corrugation in the electron temperature logarithmic gradient (see Fig. 6.10b). We also note an over-sampling at high energies near the magnetic axis (below $s = 0.1$). However, no under-sampling at low energies near magnetic axis is seen as for the ions. However, there is a dent in the distribution at high energies at $s = 0.1$. This is related to how ORB5 uses different coordinates near axis for particle orbit time-integration, which will be further explained in Sec. 6.3.5.

To further analyse the respective sampling problems of ions and electrons near axis under the standard scheme, we look into the actual marker distribution by diagnosing the actual marker count in different phase-space bins, shown in Fig. 6.14. The marker count is normalised by $V_s(s)/v_{th}^2(s)$ to display a uniform distribution at loading, i.e. such that $N(t = 0)v_{th}^2/V_s$ is a constant, the global bin maximum of which is $N_{max}(t = 0)$ (see Eq. (3.13)). Here, N is the number of markers in each bin. The common feature of both species is that we do see the expected marker diffusion across the high velocity loading boundary. We also see an accumulation of markers at low energies in the region $s \in [0.1, 0.8]$, with the accumulation of ion markers stronger than that of electrons. This has already been observed in Ref. [8]. Focusing now on the ions represented by Fig. 6.14a, we do not see a lack of markers at the under-sampling region near axis of Fig. 6.13a. For the case of the electrons, we see an accumulation of markers at high energies around $s < 0.1$. This accumulation of markers is however unphysical as associated phase-space volume is too large according to Fig. 6.13b. As mentioned, this will be discussed in Sec. 6.3.5.

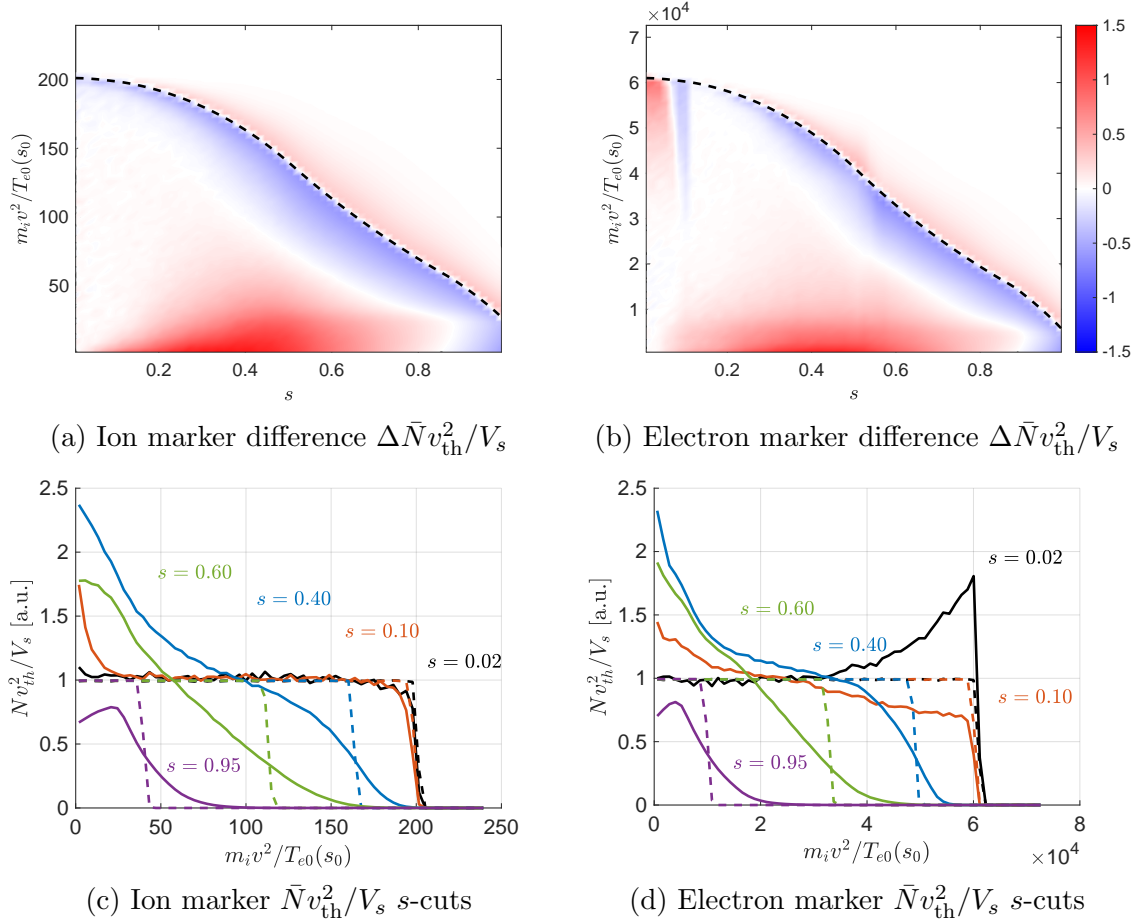


Figure 6.14: Normalised marker count $\bar{N} = N/N_{\text{max}}(t = 0)$ for the standard case with $N_p = 128\text{M}$ at time $c_s t/a = 286$. Here, $N_{\text{max}}(t = 0)$ is the global maximum marker count per (s, v^2) -bin at initial time $t = 0$. (a) and (b) show marker count differences $\Delta \bar{N} = \bar{N}(t_{\text{end}}) - \bar{N}(t = 0)$. Subplots (c) and (d) show different s -cuts at time $t = 0$ (dashed lines) and at t (full lines).

Having discussed the phase-space diagnostic and marker distribution results for the standard case with $N_p = 128\text{M}$, we now consider the result for the adaptive case with $N_p = 128\text{M}$, shown in Figs. 6.15 and 6.16. We once again observe the diffusion of phase-space volume and markers across the high velocity loading threshold for both ions and electrons. Looking in particular at Figs. 6.15d and 6.16d, the problem of electron marker accumulation at high energies towards the left of $s = 0.1$ with unphysical increase of associated phase-space volume is also present for the adaptive case. Looking at Fig. 6.15a, the under-sampling problem for ions at lower energies near the magnetic axis seen in the standard case is not however present here. The main difference is revealed by comparing N s -cuts of Figs. 6.14c and 6.16c for the standard and adaptive cases, respectively. Focusing in particular on the $s = 0.02$ (black) curves, we see that there is an accumulation of markers at lower energies for the adaptive case, which is not observed for the standard case. This accumulation also spreads over a wider radial region, e.g. compare Figs. 6.14a, 6.14b against 6.16a, 6.16b. This higher accumulation of the adaptive case clearly compensates for the under-sampling problem of ion observed in Fig. 6.13a.

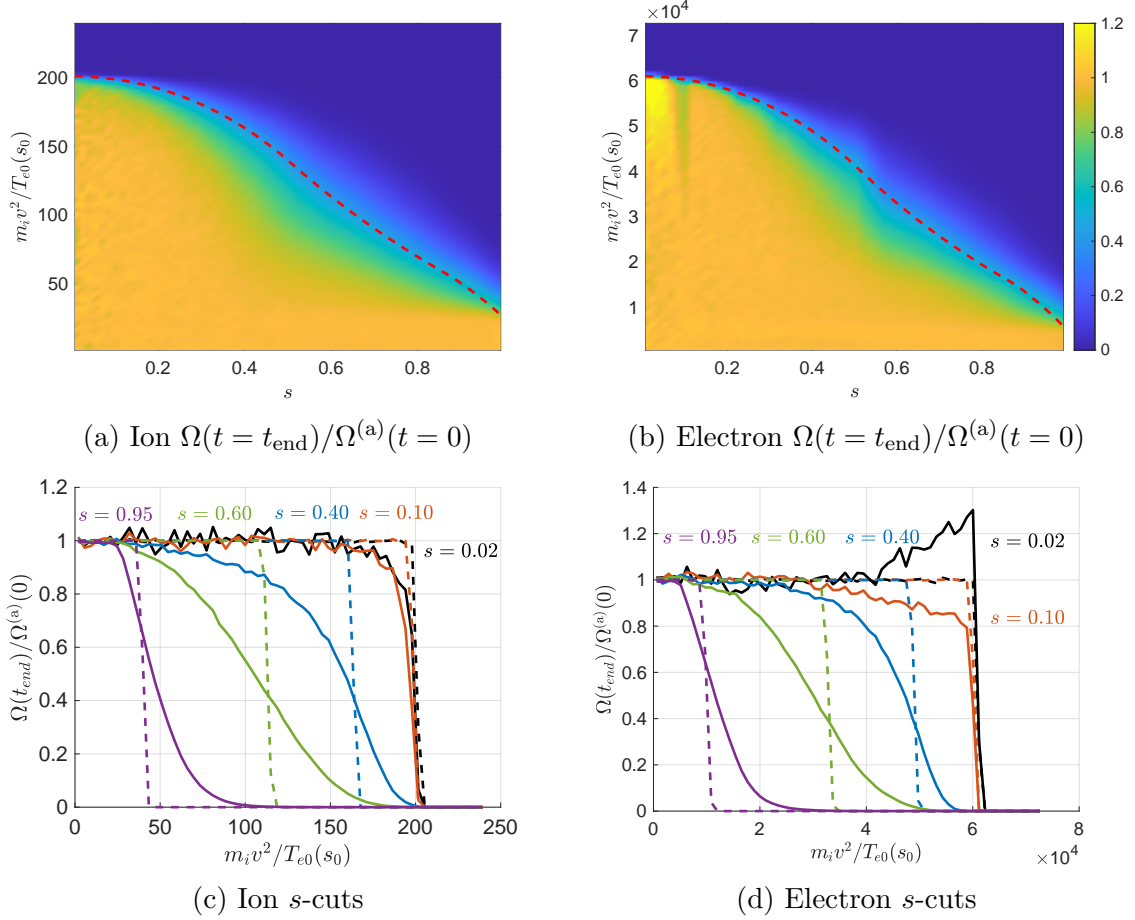


Figure 6.15: Phase-space volume diagnostic applied to Cartesian bins in (s, v^2) space for the adaptive case with $N_p = 128\text{M}$ at $c_s t_{\text{end}}/a = 286$. Shown is the ratio $\Omega(t_{\text{end}})/\Omega^{(a)}$, of which values near 1 reflect good sampling, while ratios deviating significantly from 1 reflect poor/deficient sampling. The red dashed line on the contour plots indicate the energy upper-bound during initial marker loading, given by $m\kappa^2 v_{\text{th}}^2(s)$. As $\Omega^{(a)}$ appears in the denominator, it is taken without the v^2 -cut-off to avoid singularities (see Eq. (3.17)). The dashed lines in (c) and (d) are taken at $t = 0$.

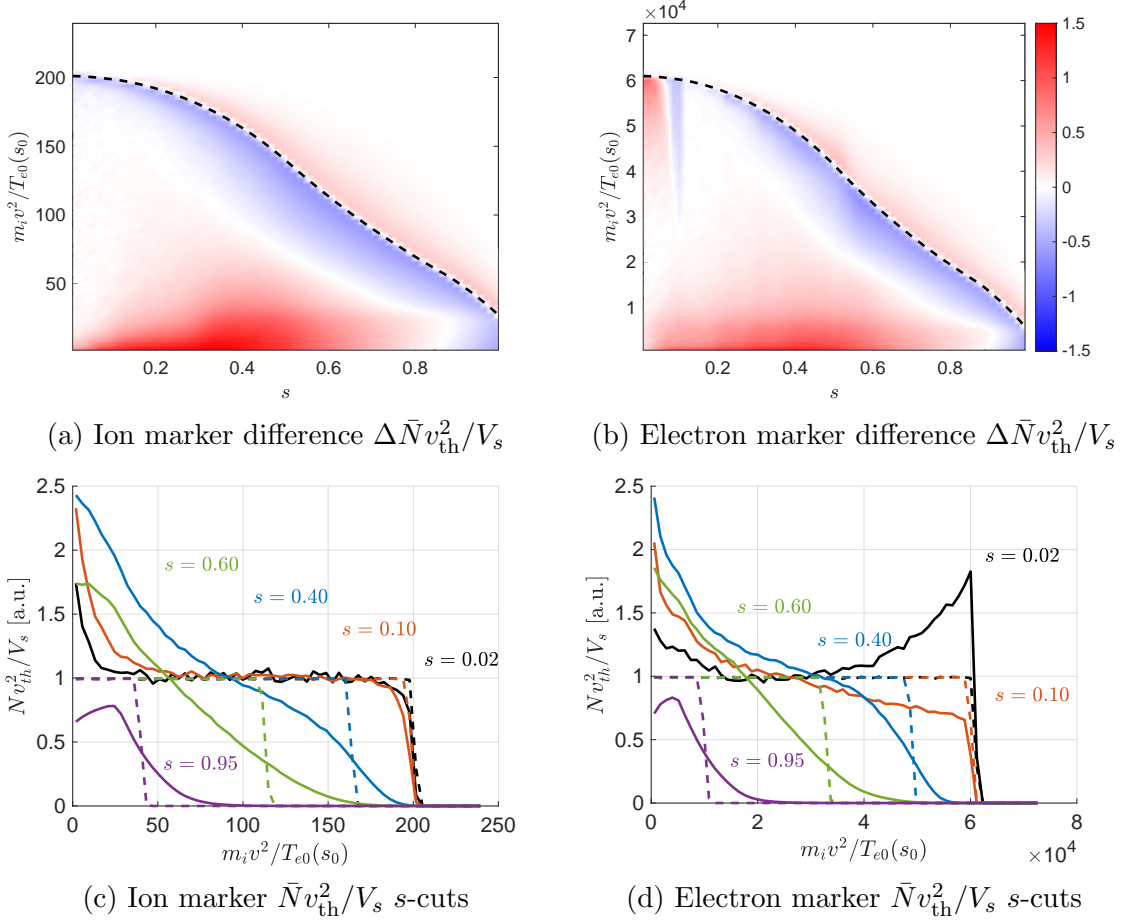


Figure 6.16: Normalised marker count $\bar{N} = N/N_{\text{max}}(t = 0)$ for the adaptive case with $N_p = 128\text{M}$ at time $c_s t_{\text{end}}/a = 286$. Here, $N_{\text{max}}(t = 0)$ is the global maximum marker count per (s, v^2) -bin at initial time $t = 0$. (a) and (b) show marker count differences $\Delta\bar{N} = \bar{N}(t_{\text{end}}) - \bar{N}(t = 0)$. Subplots (c) and (d) show different s -cuts at time $t = 0$ (dashed lines) and $t = t_{\text{end}}$ (full lines).

6.3 Flux-driven simulations

6.3.1 Heat source radial profile

In order to run flux-driven simulations with similar quasi-steady state with that of the previous temperature-gradient-driven runs of this chapter, the effective f.s.a. heat source resulting from the Krook operator Eq. (3.81) will be replaced by the fixed heat source operator Eq. (3.82). This is done separately for each species (ions and electrons). The radial heat source profile $G_H(\psi)$ of Eq. (3.82) is approximated by fitting a Gaussian function around the peak of the time-averaged effective heat source of the gradient-driven run, considering here the standard case with $N_p = 256\text{M}$. The sink at the edge will be replaced by a non-conserving Krook buffer Eq. (3.83). The effective heat source/sink profile in the gradient-driven simulations is estimated by flux surface and time averaging the second order velocity moment of the Krook operator Eq. (3.81), $\left\langle \left\langle \int d^3v \frac{mv^2}{2} \hat{S}_n \right\rangle \right\rangle_t$. An example of the heat source profile for each species is shown in Fig. 6.17. The peaks of the fitted Gaussian are lower than the corresponding peaks of the source profiles of the gradient-driven runs to ensure

that the area under the curves (heating powers) are approximately equal. The radial regions where the fitted curve is above (below) the heat source will tend to result in an increase (decrease) of the quasi-steady state temperature profile. The dashed lines represent the beginning of the buffer region. It is found that a relaxation rate for the Krook buffer of $\gamma_B = 10\% \gamma_{\max}$ (see Eq. (3.83)) is sufficient to efficiently damp all turbulence at the edge given the strength of the considered heat sources.

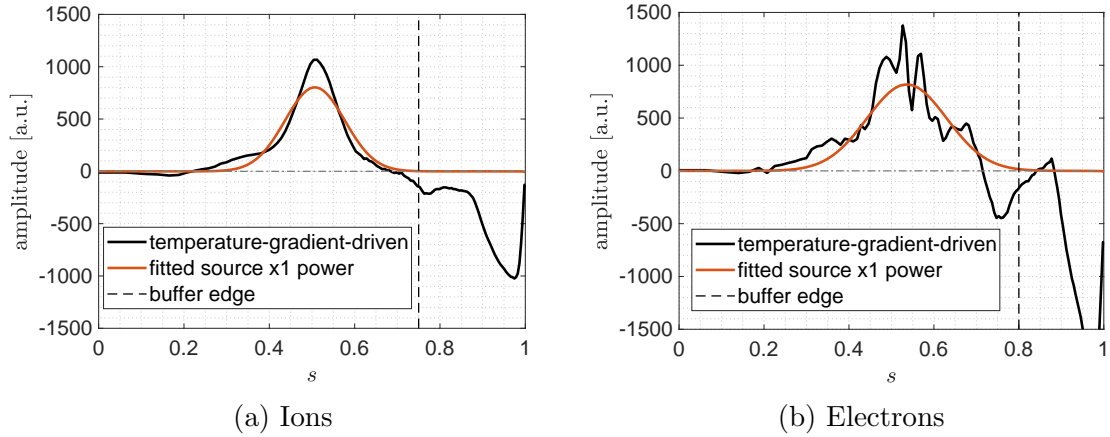


Figure 6.17: Fixed heat source profiles $G_H(\psi)$ (orange) for the flux-driven simulations fitted to the effective flux surface and time-averaged heat source of the temperature-gradient-driven run using the standard case with $N_p = 256M$. Buffer edges for the ions and electrons are taken to be $s_B = 0.75$ and $s_B = 0.80$, respectively (see Eq. (3.83)).

The subsequent flux-driven simulations discussed in this chapter are run with these fixed heat sources till they reach quasi-steady state, or for as long as is appropriate based on a single initial marker loading. Whether the former is reached is judged by comparing the power through magnetic surfaces calculated from the fluxes and the volume-integrated heat source and identifying when they become equal. As will be shown, despite the approach taken to set these heat sources, they result in large f.s.a. density and temperature profile deviations, thus prohibiting standard runs from reaching quasi-steady state. In order to allow for comparison between results under the standard and the adaptive schemes, we split the analysis of the results into two sections, Secs. 6.3.4 and 6.3.7. They correspond respectively to the two time windows represented by shaded grey areas of the time traces of Fig. 6.18. The first time window then contains transient profiles under the standard and adaptive schemes, while the second time window contains only profiles under the adaptive scheme at quasi-steady state.

6.3.2 Transport time traces

Figure 6.18a shows the ion heat diffusivity χ_i for all cases. The first observation to be made is that under the respective standard and adaptive schemes, all results have converged in N_p . Secondly, χ of the adaptive case are consistently higher than that of the standard cases. This is especially obvious at comparing the standard case with $N_p = 256M$ and any of the adaptive cases for times $c_s t/a \gtrsim 700$, for which one approaches a quasi-steady turbulent state. Note that the latter have 1.5-times

the χ of the former. This is despite the fact that the adaptive cases exhibit lower temperature gradients in $s \in [0, 7, 0.9]$ (see Fig. 6.37) as compared to the standard case. This difference between results of the two schemes can be explained by looking at the shearing rate. Fig. 6.19 shows the $s \in [0.7, 0.9]$ radially averaged absolute value of the $E \times B$ zonal flow shearing rate $\omega_{E \times B}$ for all the cases discussed. We see that the shearing rate for the standard cases are consistently lower than that of the adaptive cases. As $\omega_{E \times B}$ amplitudes indicate the rate of turbulent eddies shearing, higher $\omega_{E \times B}$ amplitudes of the standard case suppress turbulence more than in the adaptive cases at $s \in [0.7, 0.9]$. This thus explains the consistent higher χ_i of the adaptive cases as compared to the standard cases (see Fig. 6.18a). As the system finally reaches quasi-steady state for $c_s t/a \gtrsim 1000$, simulations under both standard and adaptive schemes show signs of asymptoting to the same χ and $|\omega_{E \times B}|$ values. This is not conclusive as a standard simulation with $N_p > 256\text{M}$ needs to be run for an even longer simulation time in order to reach quasi-steady state for comparison with the adaptive cases presented here.

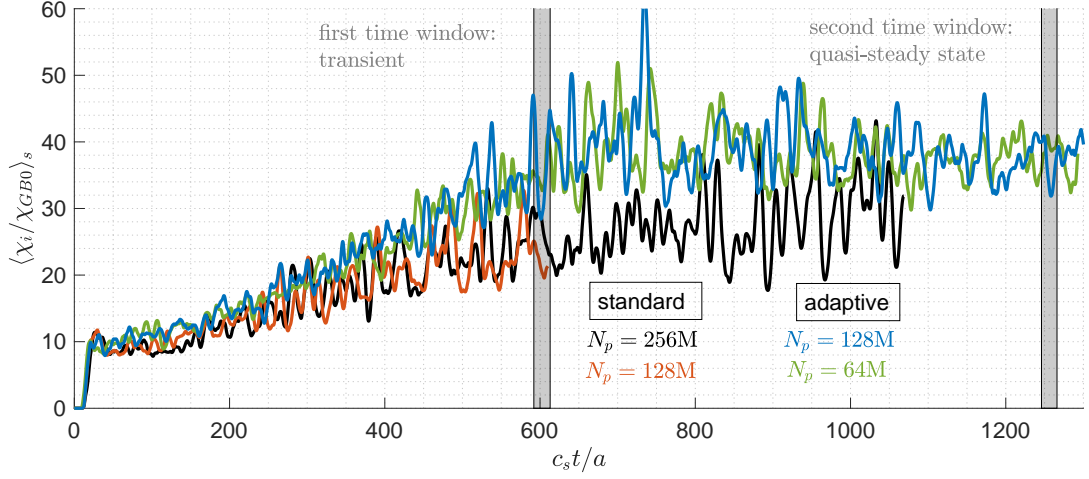
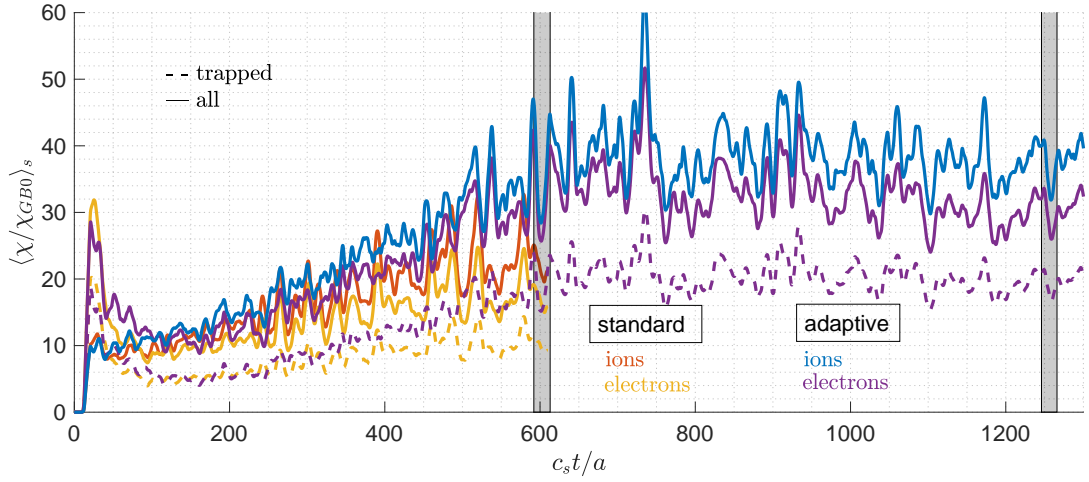
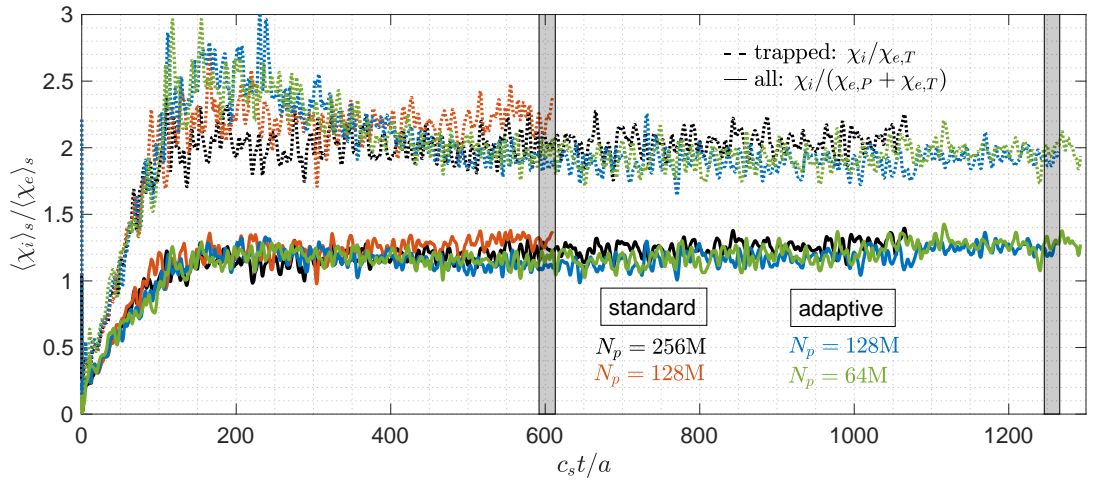
(a) Ion heat diffusivity, χ_i (b) Ion and electron heat diffusivities with $N_p = 128M$ (c) Heat diffusivity ratio, χ_i / χ_e

Figure 6.18: Radially averaged $s \in [0.7, 0.9]$ ion and electron heat diffusivities as well as ion-electron heat diffusivity ratio χ_i / χ_e , for various marker numbers N_p under the standard and the adaptive schemes. 'trapped' and 'all' curves use χ_e contributed by trapped only and passing and trapped electrons, respectively. Grey shaded areas represent two time windows for profile analysis, given in Sec. 6.3.4 and 6.3.7 respectively.

6.3. FLUX-DRIVEN SIMULATIONS

To see how electron diffusivity χ_e compares to χ_i , Fig. 6.18c shows the ratio χ_i/χ_e for all cases considered. Dashed and solid curves represent χ_e contributed by trapped, and passing and trapped, electrons respectively. During $c_s t/a \in [0, 100]$, the edge (at $s \in [0.7, 0.9]$) with almost constant gradient is predominantly driven by trapped electron modes (TEM). From $c_s t/a = 200$ onwards, the system is in a mixed regime of instabilities driven by TEM and Ion-Temperature-Gradient (ITG) modes. In the latter, χ_i and χ_e go in-step. The discrepancy between different converged values of χ_e with and without passing electrons contribution might be due to the large electron mass used in this work, $m_e/m_i = 1/200$. Studies with more realistic values of m_e should be conducted to investigate passing electron contribution to transport.

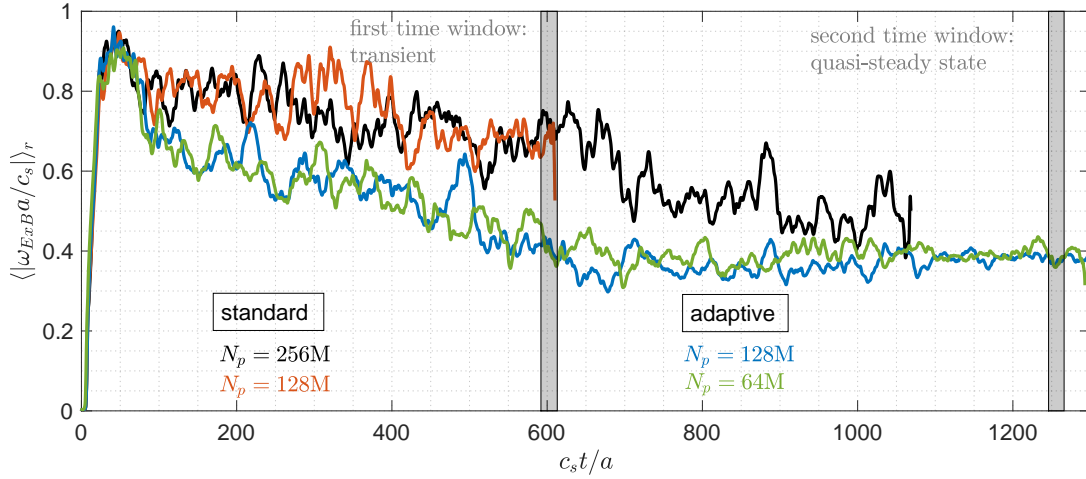


Figure 6.19: Radially averaged $s \in [0.7, 0.9]$ absolute value of the $E \times B$ zonal flow shearing rate $\omega_{E \times B}$, for various marker numbers N_p under the standard and the adaptive schemes. Grey shaded areas represent two time windows for profile analysis, given in Secs. 6.3.4 and 6.3.7 respectively.

As the system approaches quasi-steady state, with the buffer being the only source/sink of particles, the particle flux reduces and plateaus to low values, as shown in Fig. 6.20 for the ion gyrocentre flux Γ_i . All cases, whether under the standard or adaptive scheme, show no distinction in the reducing trend of Γ_i . To ensure quasi-neutrality, ion gyrocentre flux Γ_i should approximately cancel the electron flux Γ_e (with near perfect cancellation with ion particle flux). Fig. 6.20b shows the difference between between Γ_i and Γ_e . We see that quasi-steady state reached by the adaptive scheme, there is good cancellation for Γ_e contributed only by the trapped electrons. Contribution of passing electrons is once again expected to reduce with decreasing m_e/m_i .

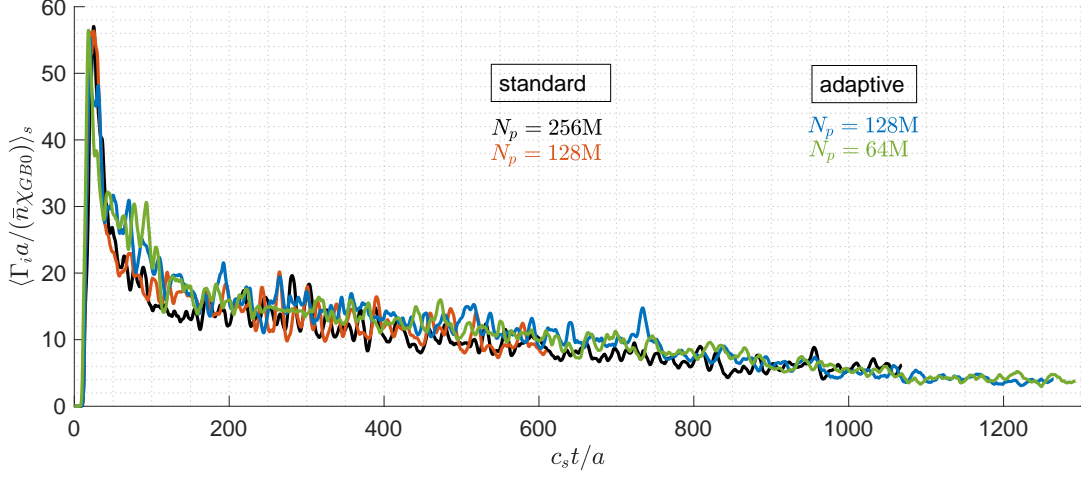
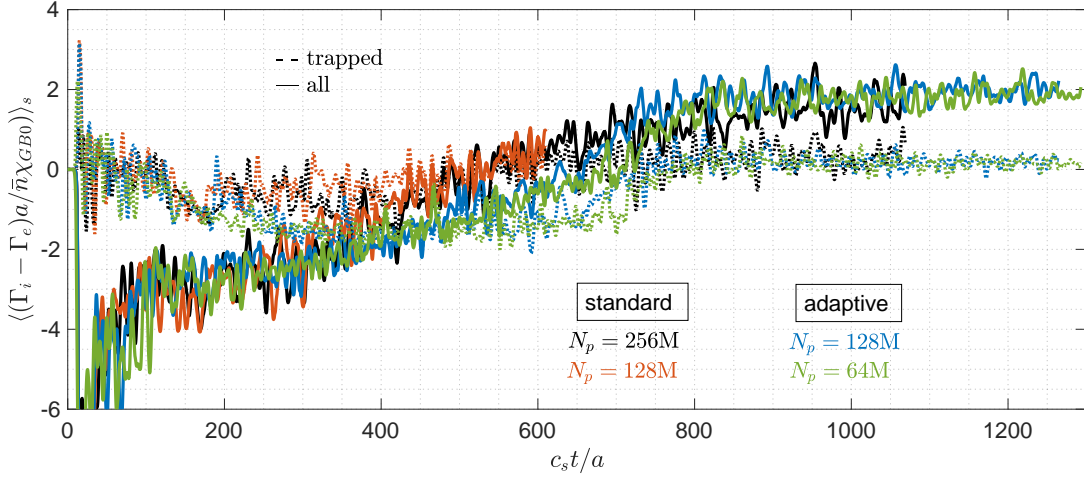
(a) Ion gyrocentre flux, Γ_i (b) Particle flux difference, $\Gamma_i - \Gamma_e$

Figure 6.20: Radially averaged $s \in [0.7, 0.9]$ ion gyrocentre flux and ion-electron particle flux difference, for various marker numbers N_p under the standard and the adaptive schemes. 'trapped' and 'passing+trapped' curves use χ_e contributed by trapped only and passing and trapped electrons, respectively.

6.3.3 Weight variance

We now examine how the adaptive scheme reduces weight standard deviation $\sigma_w(s_{\text{bin}})$ of Eq. (3.29). We begin by comparing σ_w radial profiles for cases of varying marker numbers N_p and using either a fixed or an adaptive background. Fig. 6.21 shows σ_w for all cases with marker number $N_p = 128M$, up to a simulation time of $c_s t / a = 600$. From Figs. 6.21a and 6.21b, we see that both the ions and electrons have similar trend in σ_w under the standard scheme. Though not shown, these σ_w values have converged with marker numbers for both species, just like in Fig. 6.7 for the ions. The radial location of increasing maxima for both the ions and electrons are once again located where profile deviation is the greatest. For gradient simulations of Sec. 6.2, it is only the density profiles of both the ions and electrons that deviated significantly from its initial values. Whereas for the flux-drive cases of this section, the temperature profiles for both species also evolve. This explains the

wider radial region $s \in [0.2, 0.8]$ of maxima of σ_w for both the ions and electrons for the flux-driven case, e.g. compare Figs. 6.7b and 6.21a. Turning now to the flux-driven case with marker number $N_p = 128M$ under the adaptive scheme, we see in Figs. 6.21c and 6.21d that the maxima for both the ions and electrons occurs at around $s \in [0.4, 0.8]$. The main difference between the standard and adaptive cases is that σ_w for the adaptive case does not increase indefinitely. This is due to the adaptive control variate, with adaptive density and temperature profiles. Furthermore for the adaptive cases, we see a drop in σ_w for the electrons that is around $c_s t/a = 50$, compared to that of the ions, where σ_w is gradually decreased. This can be explained by analysing Fig. 6.18b, where we see that for $c_s t/a \in [0, 50]$, the electron diffusivity χ_e is more than 200% that of the ion χ_i . This suggests a quicker evolving electron temperature profile T_e during this period. Thus, as the adaptive rate is sufficiently high for this case, the electron σ_w is reduced at a shorter time scale.

To estimate the improvement via an adaptive control variate, Fig. 6.22 shows radial s -cut $s = 0.534$, where maxima of all cases illustrated in Fig. 6.21 coincide. Here, we see that the adaptive case have 15% the value of σ_w compared to that of the standard cases. Furthermore, at $c_s t/a = 600$, σ_w for the standard cases still increase linearly, while that of the adaptive cases exhibit a steady value of around 0.2.

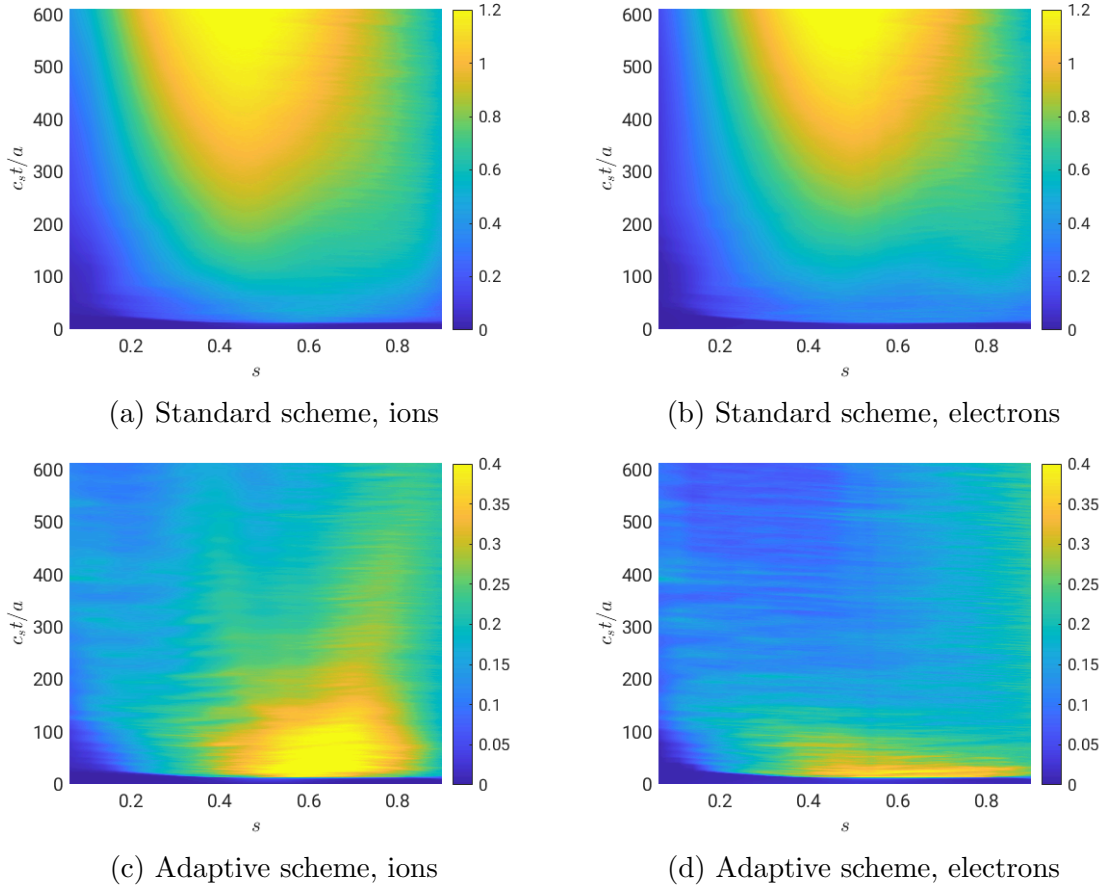


Figure 6.21: F.s.a. weight standard deviation profiles $\sigma_w(s) = \sqrt{\langle w^2 \rangle(s) - \langle w \rangle^2(s)}$ for marker number $N_p = 128M$, under both the standard and adaptive schemes.

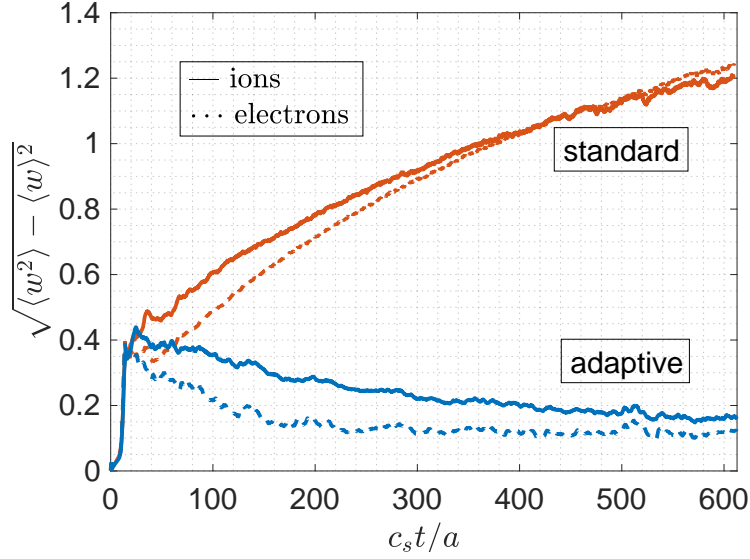


Figure 6.22: F.s.a. weight standard deviation profiles $\sigma_w(s) = \sqrt{\langle w^2 \rangle(s) - \langle w \rangle^2(s)}$ at $s = 0.534$ for marker number $N_p = 128\text{M}$, under both the standard and adaptive schemes.

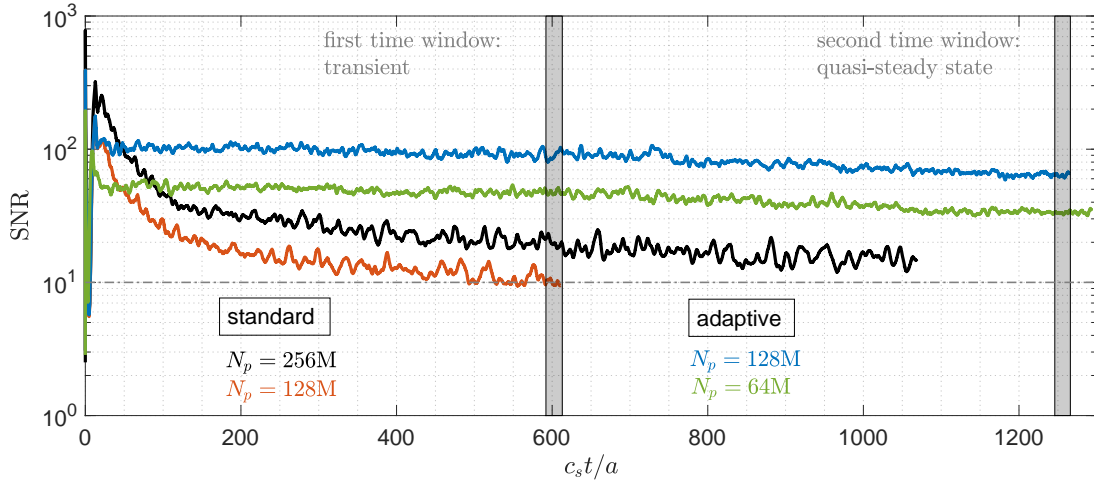


Figure 6.23: Time dependence of global Signal-to-Noise Ratio (SNR) values, for various marker numbers N_p under the standard and the adaptive schemes. The signal includes the zonal component $(m, n) = (0, 0)$. Horizontal dashed line indicates the empirically set minimum value of 10 for quality simulations. Grey shaded areas represent two time windows for profile analysis, considered in Secs. 6.3.4 and 6.3.7 respectively.

Next, we look at radially averaged measures of squared weight w^2 via the Signal-to-Noise Ratio (SNR) values. Fig. 6.23 shows the SNR time trace for all cases discussed in this section. These results include the zonal component in the signal (see Eqs. (3.27) and (3.28)). The corresponding values without the zonal component are about 10% lower for all cases and for all times. The SNR values of the two standard cases with $N_p = 256\text{M}$ (black) and $N_p = 128\text{M}$ (orange) can be seen to fall continuously with similar rates as simulation time passes. The gain in SNR

value achieved by increasing N_p is proportional to N_p , owing to the fact that this diagnostic is based on fluctuation amplitudes and in particular the noise estimate which scales as $1/N_p$ (see Sec. 3.1.4.1). Simulations are stopped when SNR values reach the empirically set minimum threshold of 10 due to degrading simulation quality. With this trend, we can predict that a simulation with $N_p = 512\text{M}$ would get us to a simulation time comparable to the adaptive case with $N_p = 64\text{M}$ shown here. The adaptive cases have their SNR values drop at a much lower rate compared to the standard cases. This drop happens mostly at the initial phase $c_s t/a \lesssim 50$ of the simulation when profiles evolve the most. This drop rate is once again similar for the cases of $N_p = 128\text{M}$ and $N_p = 64\text{M}$. This rate of SNR value reduction could be somewhat further reduced by increasing the adaptation rates α_n and α_E , though improvements via increasing adaptive rates are marginal. This is because the adaptive scheme discussed in this work is based on a f.s.a. control variate. Any variation of weights in the poloidal direction for example will not be accounted for. Nonetheless, for the cases study of this chapter, we see a simulation run with $N_p = 64\text{M}$, or even potentially $N_p = 32\text{M}$, gives us results otherwise, i.e. with standard scheme, only obtained with at least $N_p = 512\text{M}$.

6.3.4 Transient results: first time window

6.3.4.1 Profiles

Figure 6.24 shows the time-averaged gyrocentre densities of the ions and electrons. Focusing first on Fig. 6.24a for ions, we can see that at the considered stage of the simulation, the non-adapted background density of the standard case has a lower value near the magnetic axis as compared to the initial profile, which should not be the case. This was already observed with the gradient-driven simulations of Sec. 6.2.3. But for the current considered flux-driven runs, the drop in background density for both standard cases is more severe, with the case with a higher marker number $N_p = 256\text{M}$ being slightly better than that with $N_p = 128\text{M}$. This is once again due to the ‘hole’ developing in the ion phase space volume, as will be discussed later together with Fig. 6.27 in Sec. 6.3.4.2. The f_0 contributed density (dashed curve) of the adaptive cases is on top of the one including the δf contribution, which indicates that the time-dependent background density has captured the total density evolution correctly.

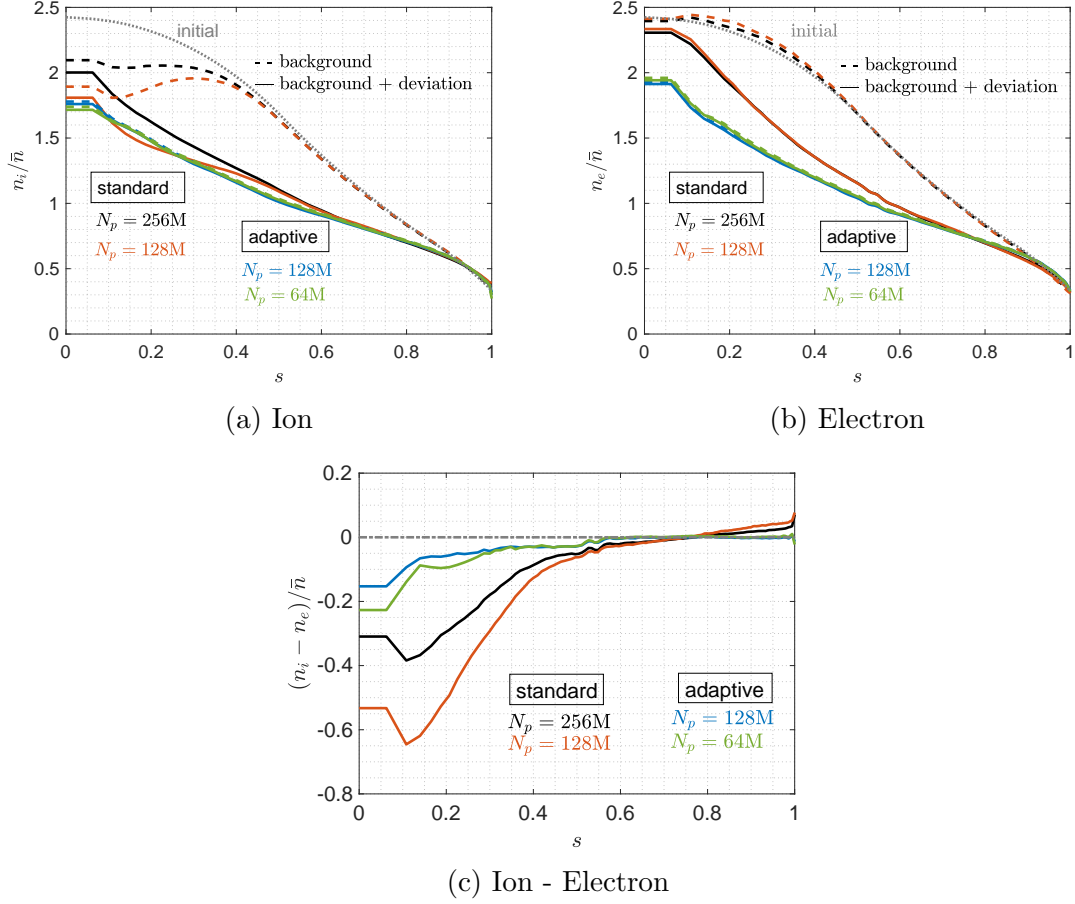


Figure 6.24: Time-averaged $c_s t/a = [592, 613]$ gyrocentre density profiles, for various marker numbers N_p under the standard and adaptive schemes. ‘background’ and ‘background + deviation’ represent the profile contributed by f_0 and $f_0 + \delta f$, respectively. (c) shows gyrocentre density difference contributed by $f_0 + \delta f$. All profiles are the result of binning markers with the appropriate weights, $f_0 \Omega$ and w for f_0 and δf contributions respectively.

Turning now to Fig. 6.24b, we first note that the deterioration of the electron background density near the magnetic axis for the standard cases is once again (as for gradient-driven runs) not as severe as that of the ions. We also see that the density of the standard and adaptive cases respectively converge to different values. Given the fact that the electron $f_0 + \delta f$ density of the standard scheme appear converged w.r.t. N_p , we conclude that the discrepancy between the ion densities with $N_p = 128M$ and $N_p = 256M$ for the standard case is due to the aforementioned deterioration in ion phase space volume. The difference between the ion gyrocentre and electron densities is accounted for by the ion polarisation density and ion FLR contributions. Fig. 6.24c shows the difference between ion gyrocentre and electron densities, where we see a larger difference between these densities for the standard scheme. And between these standard cases, the case with $N_p = 128M$ shows a larger density difference as compared to that with $N_p = 256M$, thus indicating that this density difference is partly due to sampling noise. On the other hand, we see that the results of the adaptive scheme is mostly converged in N_p . The larger difference between the densities for the standard case than the adaptive case is already hinted at in Fig.6.19. Though the radial average is not taken near the magnetic axis, a high

shearing rate of the standard case is indicative of a large ion polarisation density contribution to the ion density.

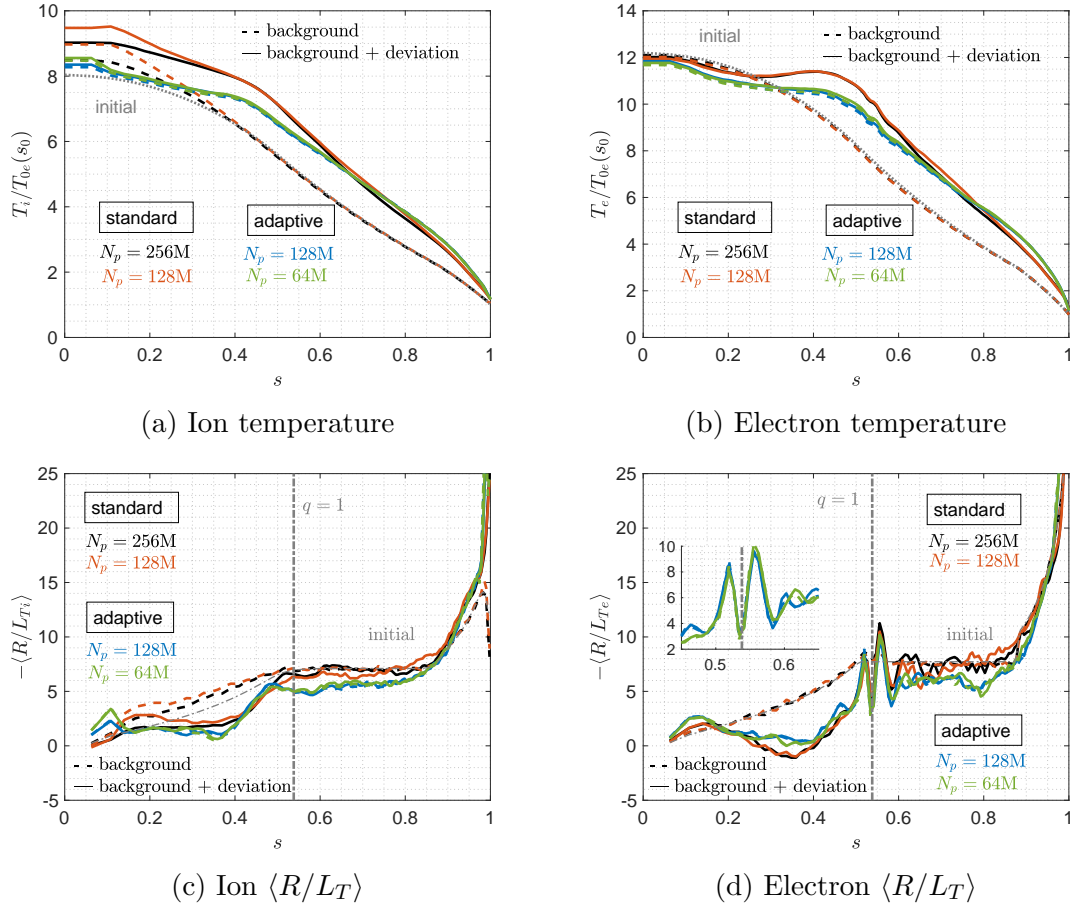


Figure 6.25: Time-averaged $c_s t/a \in [592, 613]$ f.s.a. gyrocentre temperature profile and its logarithmic gradient, for various marker numbers N_p under the standard and adaptive schemes. ‘background’ and ‘background + deviation’ represent contributions from f_0 (dashed curves) and $f_0 + \delta f$ (solid curves) to the profile, respectively. All profiles are the result of binning markers with the appropriate weights, $f_0 \Omega$ and w for f_0 and δf contributions respectively.

Next, we consider the ion and electron temperature profiles as shown in Figs. 6.25a and 6.25b respectively. The initial profiles are indicated by the dotted curves. We first note that there is an increase in ion temperature at the magnetic axis under the standard scheme, with the $N_p = 128M$ case having a larger increase than that of $N_p = 256M$. This effect is not observed for electrons. Hence, we can attribute this to the same problem of the ion phase space volume. Taking a broader look, we see that the temperature has risen more under the standard scheme as compared to the adaptive scheme. All profiles converged in N_p under the respective schemes. Note that while at this point in time, there is no off-axis peak ion temperature profile, there is one for the electron temperature under the standard scheme, at around $s = 0.45$. This is interesting because the peak of the heat source for the electrons (see Fig. 6.17) is at around $s = 0.55$.

The slight corrugation of the electron temperature in the vicinity of $s = 0.55$ for all cases, which is not observed for the ion temperature, perhaps due to ion

inertia, is magnified by looking at the respective logarithmic temperature gradients in Figs. 6.25c and 6.25d. The corrugation location for the electron temperature coincides with the $q = 1$ flux surface. Unlike that of the temperature-gradient-driven case (see Fig. 6.10a), Fig. 6.25c shows no corrugation at $s = 0.55$ for the ions. The corrugation does however appear for the electrons, and, as can be seen in Fig. 6.25d, in the case of the adaptive scheme, the background electron temperature also exhibits such corrugation, illustrating the ability of the evolving background to capture such fine profile features. The feature common to both ions and electrons is that there is a drop in gradient around $s = 0.35$, and an increase in gradient around the pedestal region $s \in [0.9, 1.0]$. The dip at $s = 0.35$ is expected to translate to the magnetic axis at a later time as the heat is transported from the heat source peak towards the core, thus flattening the temperature profiles in this region (as seen in Figs. 6.25a and 6.25b). All cases under the adaptive scheme show a greater flattening of the temperature gradient in the region $s \in [0.5, 0.8]$ than the standard scheme.

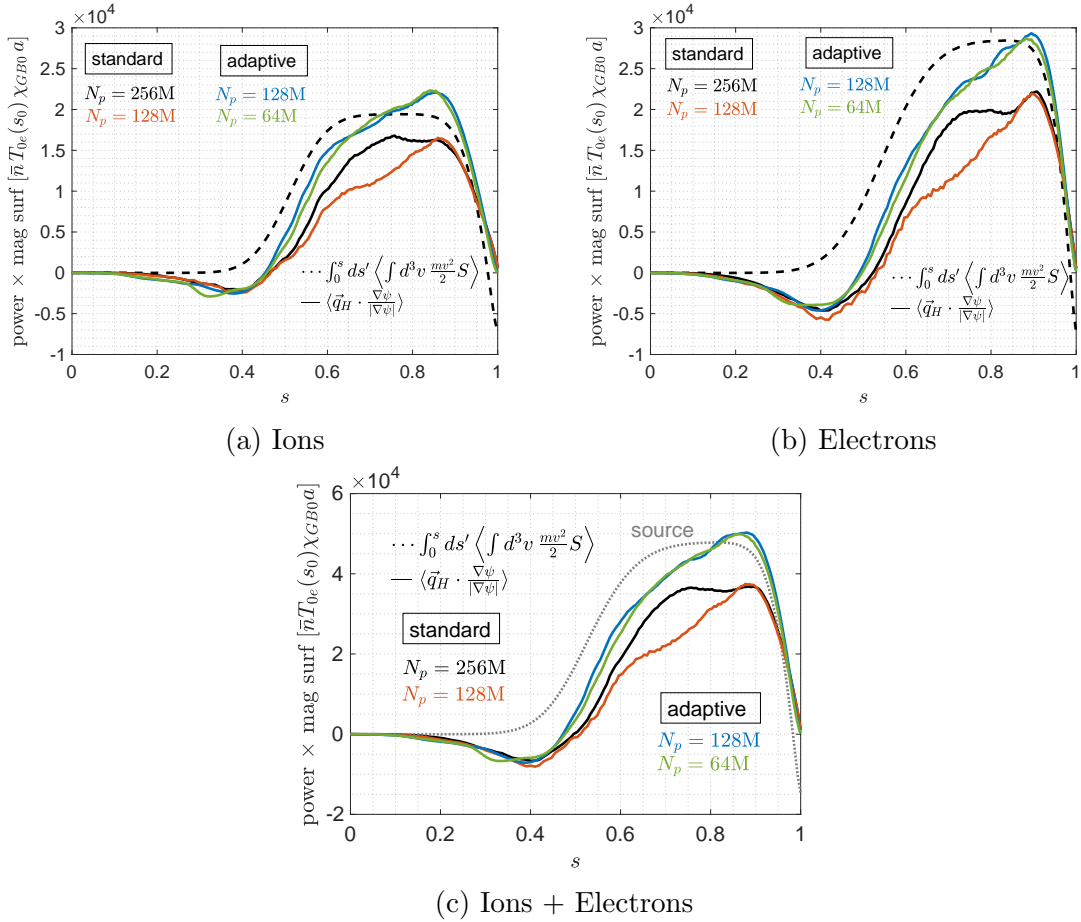


Figure 6.26: Time-averaged volume integrated heat source $\int_0^s ds' \langle \int d^3v \frac{mv^2}{2} S \rangle$ and heat flux through flux surface $\langle \vec{q}_H \cdot \frac{\nabla \psi}{|\nabla \psi|} \rangle$, for various marker numbers N_p under the standard and the adaptive schemes. The electron heat flux includes both passing and trapped contributions. The time averaging window is taken to be $c_s t/a \in [592, 613]$.

To investigate the difference in temperature deviation between the standard and adaptive schemes, we now consider plotting Figs. 6.26a and 6.26b the balance be-

tween the f.s.a. integrated heat source $\int_0^s ds' \left\langle \int d^3v \frac{mv^2}{2} S \right\rangle$ (dashed curves), and the heat flux through magnetic surfaces $\langle \vec{q}_H \cdot \frac{\nabla\psi}{|\nabla\psi|} \rangle$ (solid curves), for the ions and electrons respectively. Since quasi-steady state has not yet been reached at this point, equality between these two quantities is not expected. This is especially true when we consider the sum of both the ion and electron contributions to the heat flux and integrated heat source in Fig. 6.26c. The tapering to negative values of the integrated heat source is due to the buffer placed at the edge, starting from $s = 0.75$ and $s = 0.80$ for the ions and electrons, respectively. In quasi-steady state, which is not the case, one expects the integrated source to go to zero at the LCFS. In this case, the negative heat source near $s = 1.0$ is only the result of the strong cooling of the buffer at the edge region in order to keep the temperature profile stationary there. The trends for both ions and electrons are similar, all cases under the adaptive scheme converging globally to larger heat fluxes than that under the standard scheme. This is reflected in the previously mentioned temperature profile flattening for the adaptive cases. Heat fluxes for all cases peak at the respective buffer entrances, and dip at around $s = 0.4$, indicating an inward flux, right next to the inner side of the peak of the heat source.

One important final point to be noted is that the standard and adaptive cases are not entirely equivalent due to the Krook operator used as noise control. For the standard case, this operator attempts to restore $f(t)$ to its *initial* f.s.a. Maxwellian distribution $f_0(t=0) = f_{\text{init}}$ albeit allowing for f.s.a. density and temperature variations via conservation of lower order moments. On the other hand in the adaptive case, the Krook operator restores $f(t)$ to the *time-evolving* background $f_0(t)$. Nonetheless, with a time-dependent background in this case still being a f.s.a. Maxwellian distribution, under the action of a Krook noise control operator that conserves the f.s.a. density and energy (amongst other low order velocity moments), the difference in the effect of the Krook operator between the standard and adaptive cases lies in the correction term S_n^c (see Eq. (3.80)). Firstly, the conservation is done in each radial bin up to machine precision. However, this does not take in to account the variance of conserved velocity moment contributed by δf in each radial bin, which will lead to inexact conservation once markers migrate across radial bins after each time-step. Secondly, due to the difference in δf under the standard and adaptive schemes, S_n^c may introduce distortion effects in the higher order moments. Studies on higher order moments of δf have not be performed.

6.3.4.2 Phase-space diagnostic and marker distribution

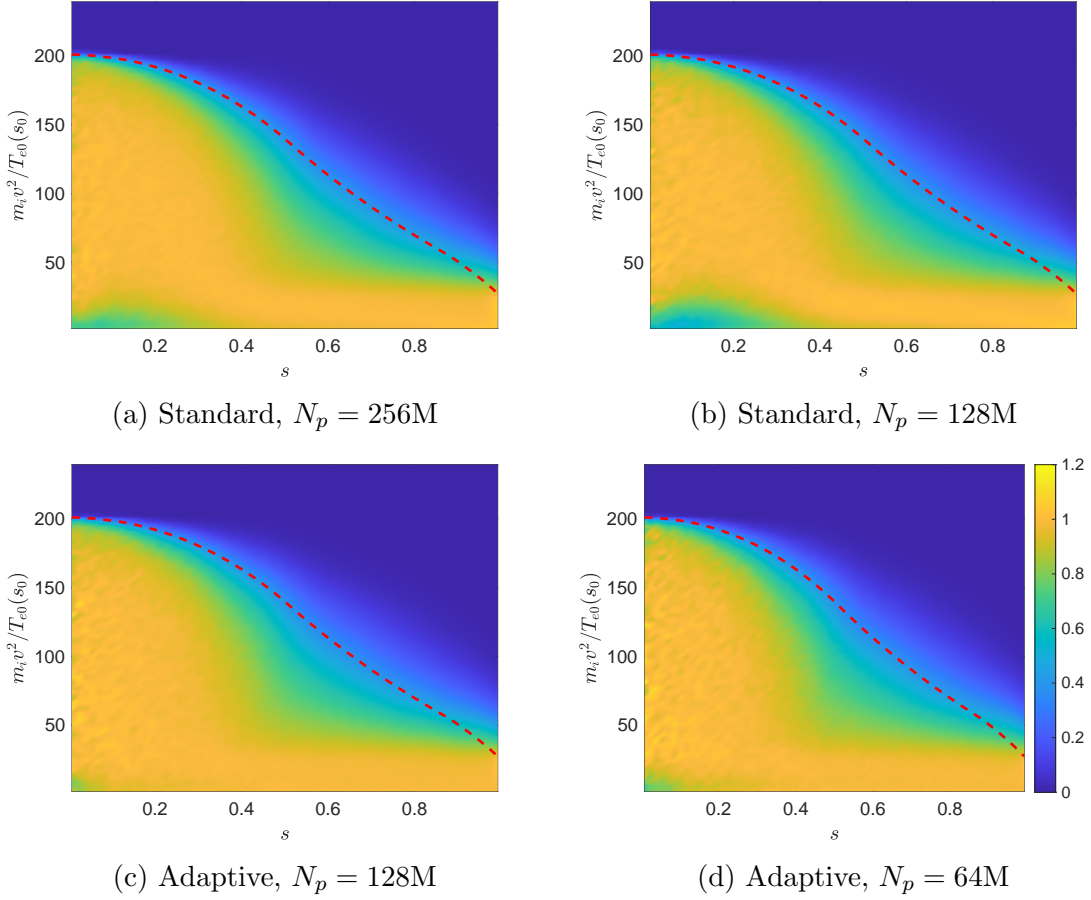


Figure 6.27: Ion phase-space volume diagnostic applied to Cartesian bins in (s, v^2) -space for the standard and adaptive cases for various marker numbers N_p at $c_s t/a = 612$. Shown is the ratio $\Omega(t_{\text{end}})/\Omega^{(a)}$, of which values near 1 reflect good sampling, while ratios deviating significantly from 1 reflect poor/deficient sampling. The red dashed line on the contour plots indicate the energy upper-bound during initial marker loading, given by $m \kappa_v^2 v_{\text{th}}^2(s)$, i.e. $v^2 = \kappa_v^2 v_{\text{th}}^2(s, t = 0)$. As $\Omega^{(a)}$ appears in the denominator, it is taken without the v^2 -cut-off to avoid singularities (see Eq. (3.17)). All plots share the same colour scale.

To see how the adaptive scheme deals with phase space volume representation, and in view of the discrepancies we identified in Sec. 6.3.4.1, we now consider the ion phase-space volume diagnostic at $c_s t/a = 612$ for all cases discussed. Fig. 6.27 shows the result of this diagnostic for ion when applied to bins in (s, v^2) -space, same as in Figs. 6.13 and 6.15. A feature common to all cases is that there is a diffusion of Ω around the velocity cut-off, as expected, with greatest diffusion around $s \in [0.5, 0.6]$. Focusing now on the standard cases, Figs. 6.27a and 6.27b, we see an under-sampling in Ω around $s \in [0, 0.3]$ at low energies. We also see that the situation is improved with higher N_p , indicating that this problem is of numerical origin. This Ω hole could explain the background ion density-drop in Fig. 6.24a and temperature overshoot near the magnetic axis in Fig. 6.25a under the standard cases. Turning to the adaptive cases of Figs. 6.27c and 6.27d, we see that the aforementioned hole has a

smaller span and depth, which appears to be more pronounced for the case with very low marker number $N_p = 64M$.

To consider the problem of the ion phase-space hole further, Fig. 6.28 shows various radial cuts of each sub-plot of Fig. 6.27. We see clearly the under-sampling problem at low energies for the standard cases Figs. 6.28a and 6.28b, represented by the cuts $s = 0.02$ (black) and $s = 0.10$ (orange). By looking at all the s -cuts of the adaptive cases Figs. 6.28c and 6.28d, we see that the phase-space hole is still present, but of a shallower depth. This depth is reduced by having a larger number of markers. Nonetheless under the adaptive scheme with $N_p = 64M$, the under-sampling problem is much better when compared to the standard case with 4-times N_p , i.e. $N_p = 256M$.

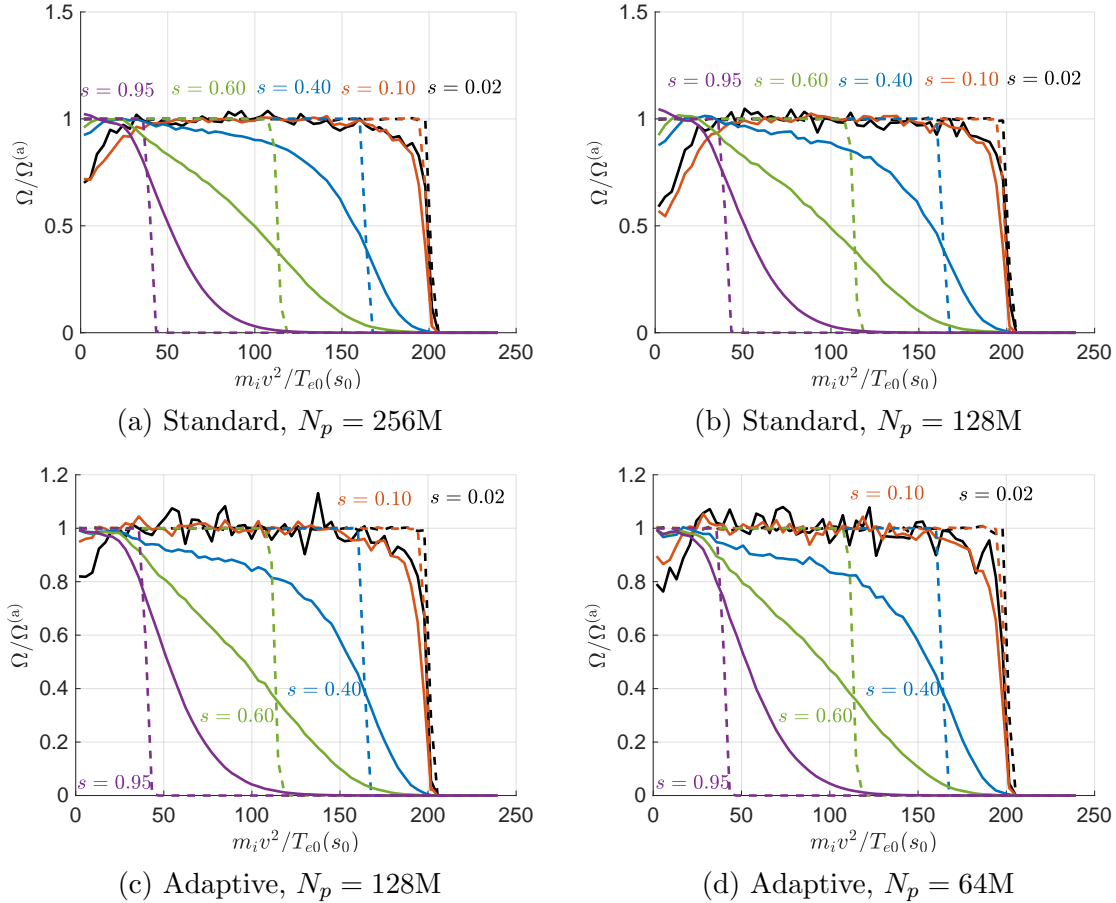


Figure 6.28: Ion phase-space volume diagnostic s -cuts, for various marker numbers N_p under the standard and adaptive schemes at $c_s t/a = 612$. Shown is the ratio $\Omega/\Omega^{(a)}$. Ratio values near 1 reflect good sampling, while ratios deviating significantly from 1 reflect poor/deficient sampling. As $\Omega^{(a)}$ appears in the denominator, it is taken without the v^2 -cut-off to avoid singularities (see Eq. (3.17)). The dashed lines are taken at $t = 0$.

We continue the investigation by looking at the marker distribution at fixed $N_p = 128M$, under the standard and adaptive schemes. Fig. 6.29 shows the difference ΔN in the marker distribution and corresponding radial cuts for the ions. Focusing first on the standard case, we see the diffusion of markers along the velocity cut-off and its accumulation at lower velocities around $s = 0.5$. Given that the phase space

representation Ω for this case (Fig. 6.27b) is roughly uniform around $s = 0.5$, it implies that markers in this phase space region with low velocities on average must have lower associate phase-space volume. This is the same result as discussed in the previous temperature-gradient-driven runs of Sec. 6.2.5. As there are plenty of markers near axis at low energies, taking Fig. 6.28b and 6.29c together, this once again indicates a corruption in Ω , i.e. Eq. (3.12) is not satisfied. Comparing Figs. 6.29c and 6.29d, we see that for the adaptive case, there is more marker accumulation near the magnetic axis at low energies compared to the standard case. This might have reduced the severity of the phase-space hole observed in Fig. 6.27c.

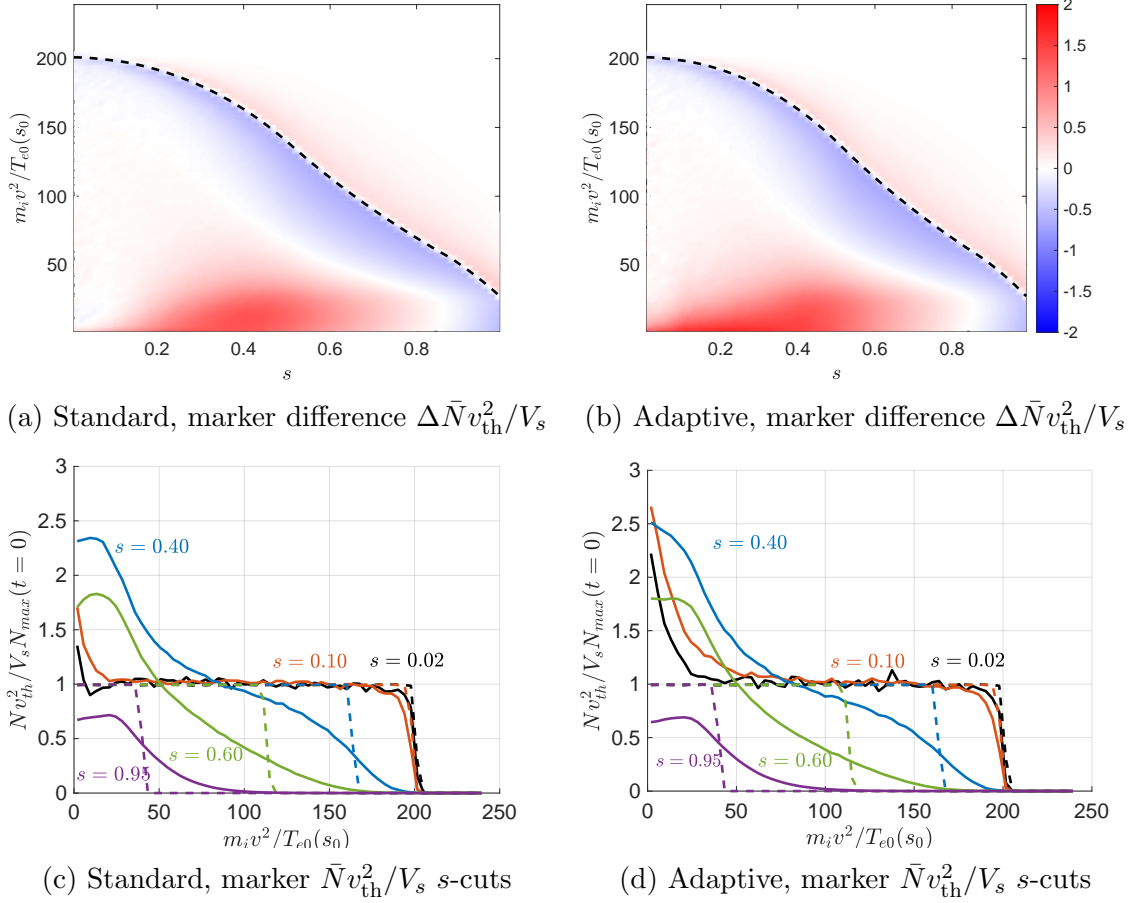


Figure 6.29: Normalised ion marker count $\bar{N} = N(t)/N_{\text{max}}(t=0)$ for the standard and adaptive cases with $N_p = 128\text{M}$ at $c_s t/a = 612$. Here, $N_{\text{max}}(t=0)$ is the global maximum marker count per (s, v^2) -bin at initial time $t=0$. (a) and (b) show marker count differences $\Delta \bar{N} = \bar{N}(t) - \bar{N}(t=0)$. Subplots (c) and (d) show different s -cuts at time $t=0$ (dashed lines) and at t (full lines).

Considering Figs. 6.27, 6.28 and 6.29, we see that the adaptive scheme appears to lead to different ion marker trajectories compared to the standard scheme, namely, markers tend to accumulate more towards lower velocities. The problem of the phase-space hole that appears in the standard cases (see Figs. 6.28a and 6.28b) appears to be ameliorated by the higher accumulation of markers of the adaptive cases (see Figs. 6.29c and 6.29d). In terms of the gyrokinetic equations of motion Eqs. (2.18)-(2.20), the difference between the standard and adaptive schemes lies in the evaluation of the $E \times B$ drift term involving the self-consistent gyroaveraged

6.3. FLUX-DRIVEN SIMULATIONS

electrostatic potential $\tilde{\phi}$. The adaptive scheme allows for a more accurate evaluation of the r.h.s. of the QNE (Eq. (2.38)) using a better control variate f_0 , thus leading to a more accurate solution for the electrostatic potential ϕ . Moreover, under the standard scheme, a better evaluation of ϕ requires a higher N_p . Indeed, based on Fig. 6.27, the case with $N_p = 256\text{M}$ improves the under-sampling situation at $s = 0$ compared to that of $N_p = 128\text{M}$. However, the compressibility of phase space as verified by Eq. (3.12) is verified for any field ϕ , whether it is accurately self-consistent or not. Nonetheless, non-smooth solutions of ϕ as a result of poor integration can lead to spurious $E \times B$ drifts, which leads ultimately to the difference in marker trajectories between the standard and adaptive cases.

The phase-space diagnostic results for the electrons is similar to that of the ions for all cases, however without the under-sampling problem around $s = 0.1$.

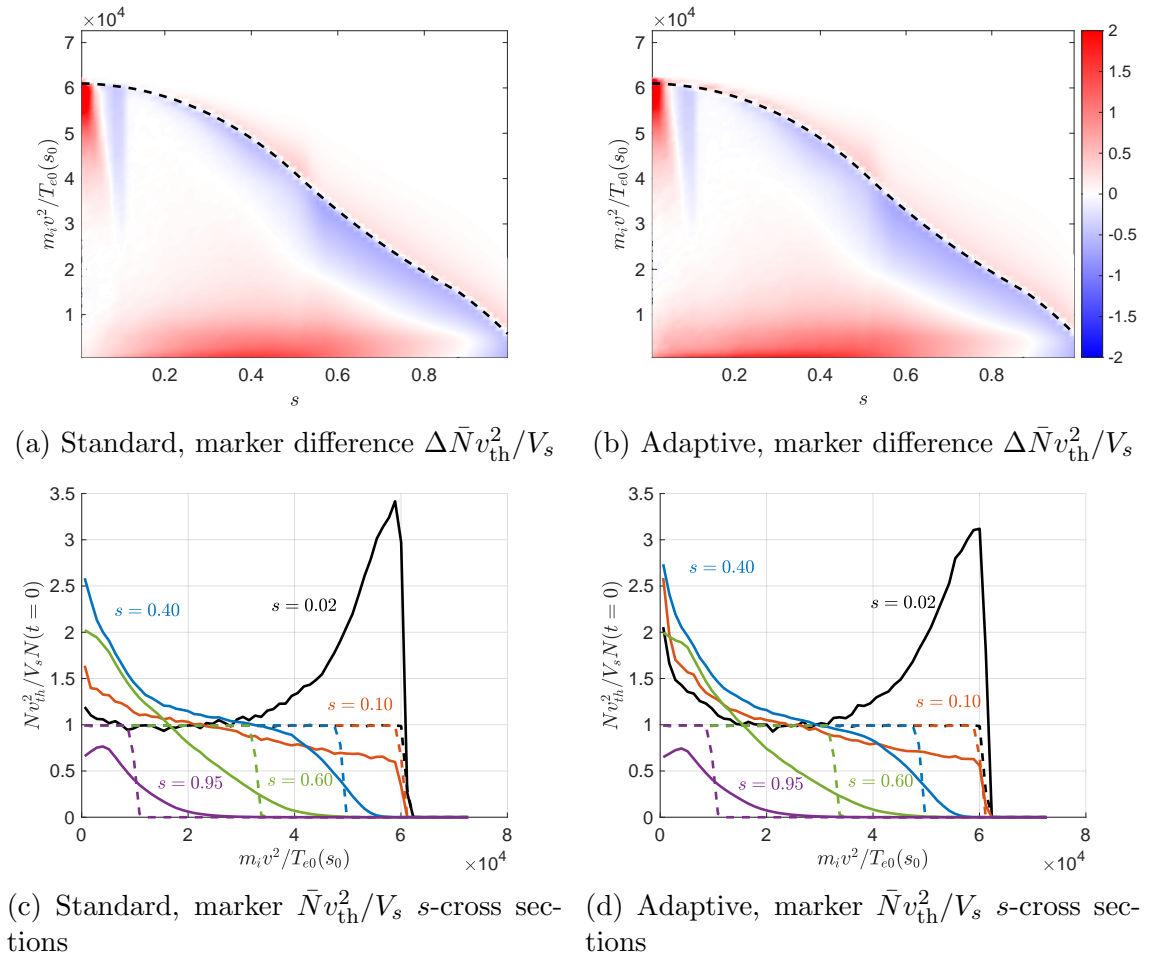


Figure 6.30: Normalised electron marker count $\bar{N} = N(t)/N_{\text{max}}(t = 0)$ distribution using $N_p = 128\text{M}$ markers, normalised to V_s/v_{th}^2 , where N_{max} is the global maximum marker count per bin at marker loading, under the standard and adaptive schemes. The normalisation factor $V_s(s)/v_{\text{th}}^2(s)$ (see Eq. (3.13)) is used to display a uniform distribution at marker loading. Marker difference is given by $\Delta\bar{N} = \bar{N}(t) - \bar{N}(t = 0) \leq -1$. The black dashed curve of (a) and (b) represents the marker loading cut-off in velocity v^2 -space, i.e. $v^2 = \kappa_v^2 v_{\text{th}}^2(s)$. Both (a) and (b) share the same colour scale. The dashed and solid curves of (c) and (d) represent N at $t = 0$ and at $c_s t/a = 612$, respectively.

Finally, we turn to the marker count $N(s, v^2)$ distribution for the electrons at $c_s t/a = 612$ under the standard and adaptive schemes, shown in Fig. 6.30. Unlike for the ions, the electrons share similar $N(s, v^2)$ under both schemes. For the adaptive case, there is no global reduction in marker velocities, but there is a slightly higher accumulation of markers at low velocities in the region $s \lesssim 0.5$, as compared to the standard case. As in the temperature-gradient-driven case (Sec. 6.2.5), there is an accumulation of high velocity electrons near the magnetic axis under both schemes. This is a numerical artifact, as will be explained in Sec. 6.3.5. The observations from the phase-space diagnostic of the ions and electrons require further investigation. In particular, a diagnostic that traces marker trajectories with time should prove useful.

6.3.5 Electron marker count at high energies

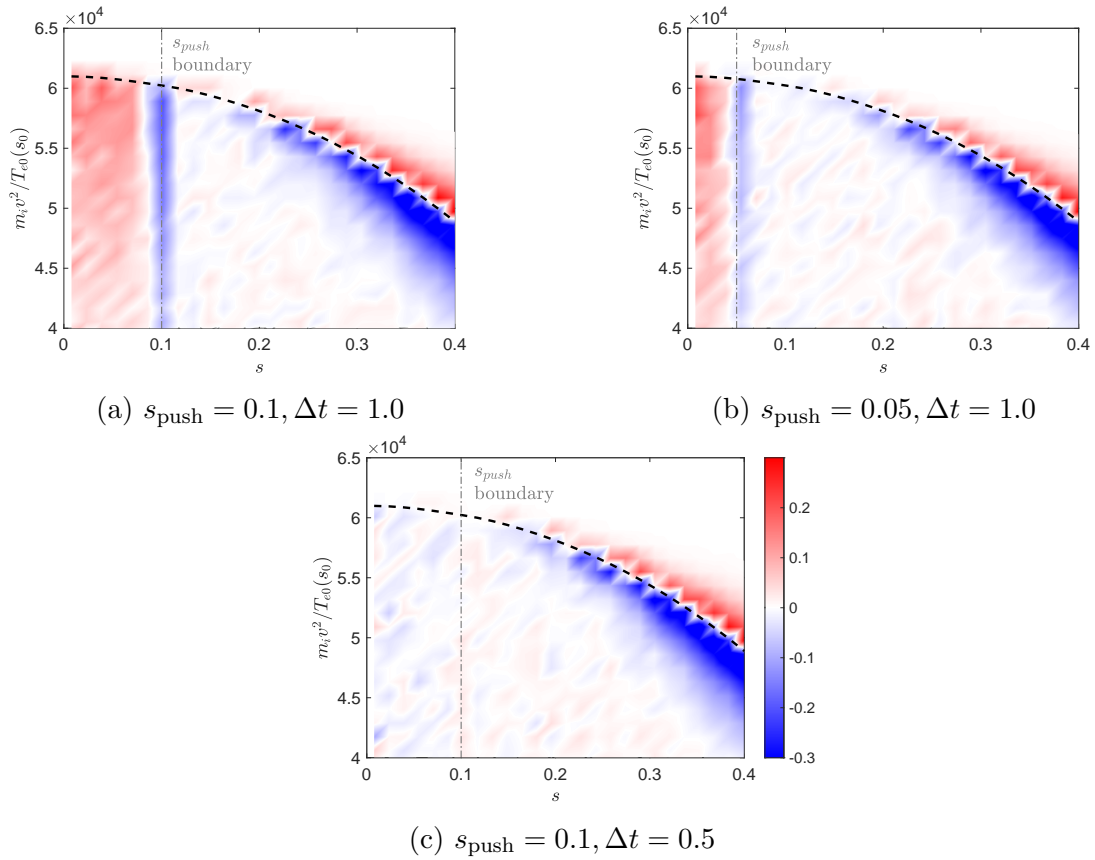


Figure 6.31: Electron marker count fractional difference $\Delta N v_{\text{th}}^2(s)/V_s(s)N_{\text{max}}(t=0)$ at time $c_s t/a = 75$, with $N_p = 64\text{M}$ under the adaptive scheme, for three different sets of marker push boundaries s_{push} and RK4 step-size Δt . $N_{\text{max}}(t=0)$ indicates the global maximum marker number per bin at initial time $t=0$. All figures share the same colour (saturated) scale.

To investigate the accumulation of high energy electrons at the axis, as already observed in Fig. 6.14, 6.16 and 6.30, let us consider the results in Figs. 6.31 and 6.32 which show the marker distribution $N(s, v^2)$ with marker count $N_p = 64\text{M}$ under the adaptive scheme for three different settings at time $c_s t/a = 75$. The two parameters concerned here are s_{push} and the time step-size Δt . In ORB5, markers generally

are ‘pushed’ via the RK4 algorithm along their characteristics in the magnetic coordinates (s, θ^*, φ) . However, to avoid the singularity of $d\theta^*/dt$ at $s = 0$, i.e. at the magnetic axis, one sets a critical magnetic surface $s = s_{\text{push}}$ such that markers within this surface are pushed according to a pseudo-Cartesian coordinate system $[\xi = s \cos \theta^*, \eta = s \sin \theta^*]$. s_{push} is estimated to be the maximum s -distance a marker can cover in a time step in an unperturbed trajectory. The price to pay is that markers are pushed less accurately as radial drifts are not exactly 0, i.e. $ds/dt \approx 0$ when integrated in (ξ, η) . As the RK4 is not a symplectic scheme, for a given step size, error in trajectories are larger for more energetic particles. Therefore, it is no surprise that the markers that are most affected by this are the electrons with high velocities. The situation of electron accumulation towards the magnetic axis, i.e. $s = 0$, is akin to using the RK4 scheme for planetary motion. There, one observes gradual radially-inward drifts of the orbiting planets. For our case, the electrons ‘orbit’ the $s = 0$ axis by variation in θ^* . As Figs. 6.31a and 6.31b illustrate, by shifting s_{push} , the region of accumulation of electrons at high energies, resulting from the error in their trajectory integration, is also shifted. Fig. 6.31c illustrates that, by reducing the time-step, the problem vanishes, as electrons trajectories are integrated more accurately.

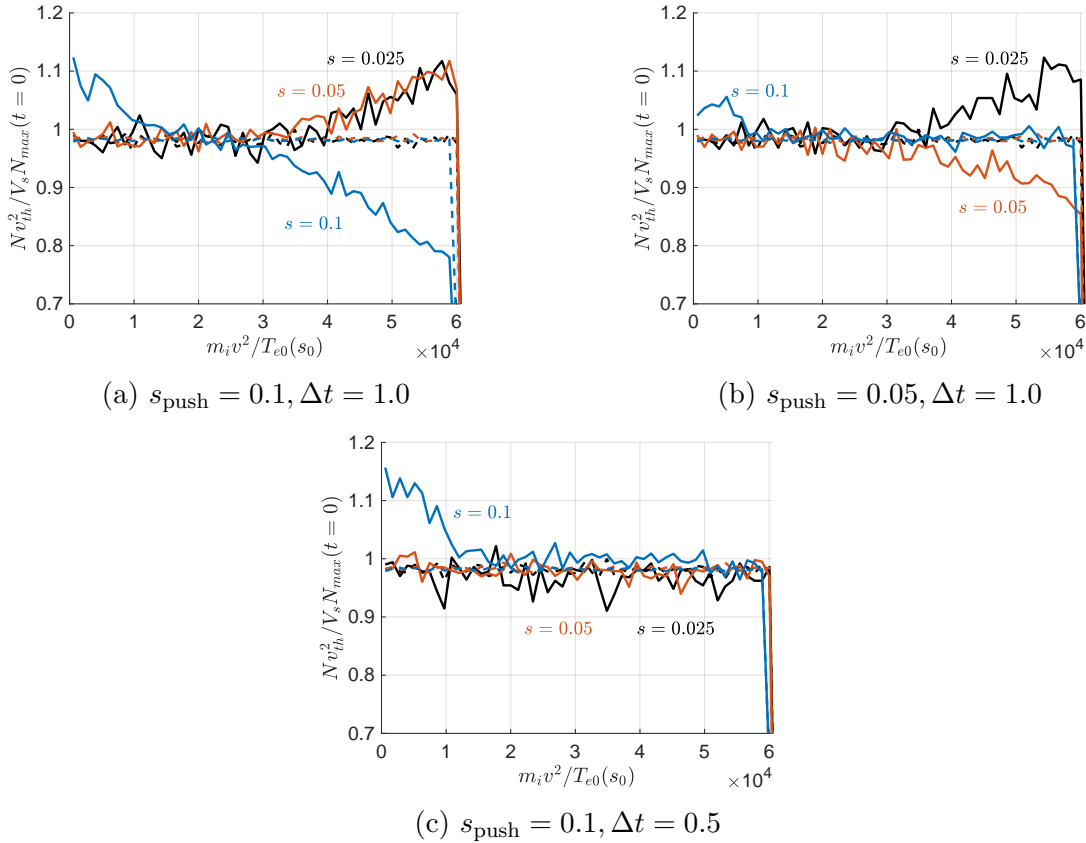


Figure 6.32: s -cuts of the normalised electron marker count $\bar{N} = N(t)/N_{\text{max}}(t=0)$ for adaptive case with $N_p = 64\text{M}$, for different radial positions, corresponding to the 2D plots of Fig. 6.31. Here, $N_{\text{max}}(t=0)$ is the global maximum marker count per (s, v^2) -bin at initial time $t=0$. Dashed and full lines correspond to results for $c_s t/a = 0$ and $c_s t/a = 75$ respectively.

Figure. 6.32, presenting s -cuts of the 2D plots of Fig. 6.31, provides more detailed

representation of the same results. It is interesting to note that reducing Δt only affects the time-integration of electron marker trajectories around $s = s_{\text{push}}$ at high energies, leaving the marker accumulation at lower velocities unchanged. This hints that the latter phenomenon is not of numerical origin.

6.3.6 QNE r.h.s. correction comparison

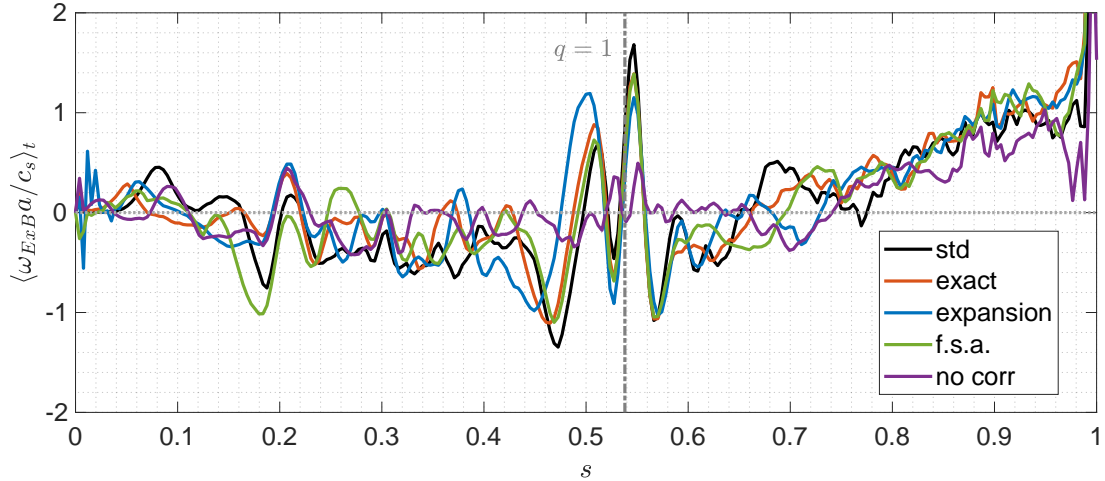


Figure 6.33: Radial profile of the time averaged $c_s t/a \in [102, 123]$ zonal flow $E \times B$ shearing rate $\omega_{E \times B} a / c_s$ with marker number $N_p = 128M$ for various QNE r.h.s. correction models: **exact**: using an exact f_0 (Sec. 3.2.10.1), **expansion**: using an expansion in $(\hat{\psi}_0, \hat{\mathcal{E}})$ for f_0 with $(N_\psi, N_\mathcal{E}, N_{\text{eval}}) = (64, 32, 600)$ (Sec. 3.2.10.2), **f.s.a.**: equates the electron background density to the f.s.a. ion background gyrodensity (Sec. 3.2.10.3), **no corr.**: no r.h.s. correction. These adaptive cases are compared against the standard: **std**.

All cases under the adaptive scheme thus far have the correction term due to the background evolution (see Eq. (3.63)) in the r.h.s. of the QNE evaluated considering an exact expression for f_0 , which is then integrated using grid-based numerical quadrature (see Sec. 3.2.10.1). However, alternative schemes exist (see Secs. 3.2.10.2, 3.2.10.3). The comparison between the different methods for evaluating this correction term is shown in Fig. 6.33, which shows the $\omega_{E \times B}$ radial profile time averaged over $c_s t/a \in [102, 123]$. For comparison the result under the standard scheme is also shown in black. First, by looking at the adaptive case with no correction (purple), we see that it does not capture the corrugation at $s = 0.538$, which corresponds to the location of the $q = 1$ flux surface (see Fig. 5.1). The other curves representing results for various methods of the correction calculation roughly follow the standard case. Amongst these, the case that deviates the most from the standard case is the one which uses a $(\hat{\psi}_0, \hat{\mathcal{E}})$ -expansion for f_0 , with number of basis functions in the $\hat{\psi}_0$ and $\hat{\mathcal{E}}$ dimensions given respectively by $N_\psi = 32$ and $N_\mathcal{E} = 32$. The example (blue) shown here periodically recalculates the basis functions after every $N_{\text{eval}} = 600$ time steps. These numbers are chosen to give a maximum of $\sim 1\%$ relative error against the exact $f_0(\hat{\psi}_0, \mathcal{E}, t)$ at all times for an expected density and temperature profile deviation. Smaller N_{eval} values were shown to not alter the result at the current adaptation rates of $\alpha_n = \alpha_E = 10\% \gamma_{\text{max}}$.

Further considering Fig. 6.33, we see that the case with the f_0 expansion overestimates the left positive peak of the corrugation at $s = 0.538$ compared to the ‘exact’ approach. This can be improved by choosing a smaller N_{eval} at the expense of computation time. Nonetheless, it captures the general trend of $\omega_{E \times B}$. The correction via the exact f_0 and equating the electron background density to the f.s.a. ion background gyrodensity perform equally well. The latter is represented by $n_e(\psi, t) = \langle \tilde{n}_{i0} \rangle$, where \tilde{n}_{i0} is the ion background gyrodensity, which is a function of (s, θ^*) . Despite dropping all poloidal dependence during the assignment of $n_e(\psi, t)$, this method of QNE r.h.s. correction produces essentially the same results as the other methods addressing the background correction term.

Figure 6.34 shows the time evolution up to the time $c_s t/a = 123$ of the zonal flow shearing rate $\omega_{E \times B}$ for the five cases shown in Fig. 6.33. By comparing Fig. 6.34d to the other cases, we can immediately see that the correction term is indeed necessary to obtain the correct $\omega_{E \times B}$ profile after adaptation. Without the correction term, the small transport barrier at $s = 0.5$ is almost vanishing.

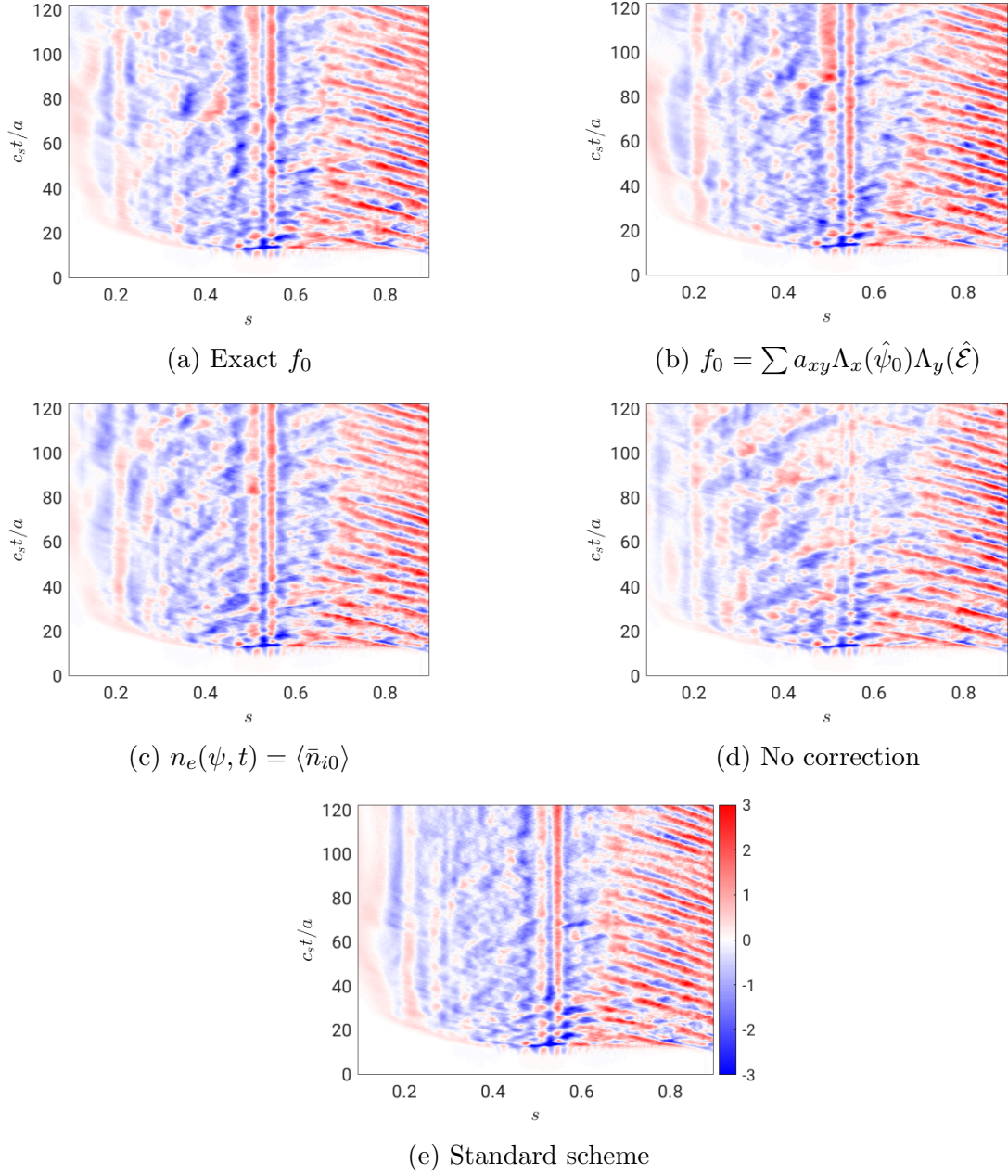


Figure 6.34: Evolution up to time $c_s t/a = 123$ of the radial profile of the zonal flow $E \times B$ shearing rate $\omega_{E \times B}$, with marker number $N_p = 128M$ under various methods of QNE r.h.s. correction calculation under the adaptive scheme (a)-(d). An identical run under the standard scheme is shown in (e) for reference. All results are run with marker number $N_p = 128M$. All plots share the same colour scale.

6.3.7 Quasi-steady state results: second time window

6.3.7.1 Profiles

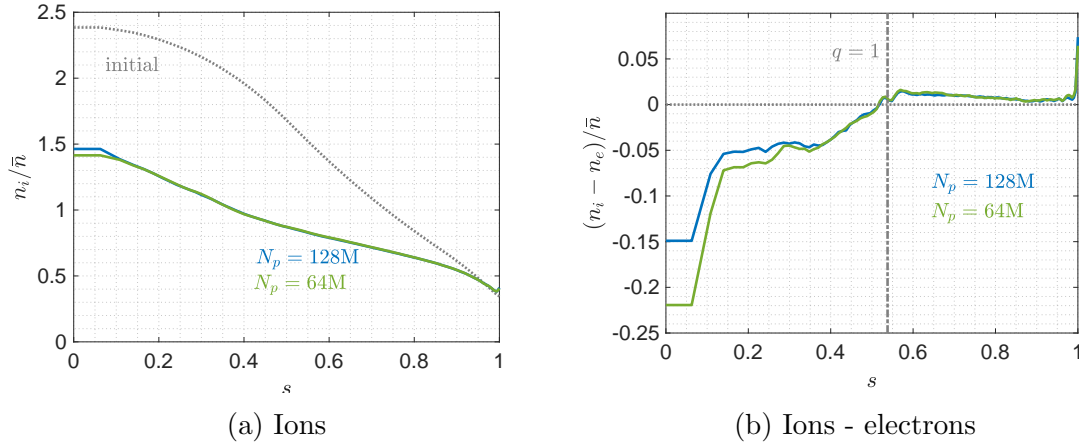


Figure 6.35: Time- and flux-surface- averaged gyrocentre density over the time window $c_s t/a \in [1246, 1266]$, for various marker numbers N_p under the adaptive scheme. Profiles are contributions from both the f_0 and δf . Profiles contributed by f_0 only are indistinguishable to the respective $f_0 + \delta f$ ones. All profiles are the result of binning of markers with $f_0 \Omega + w$ weights.

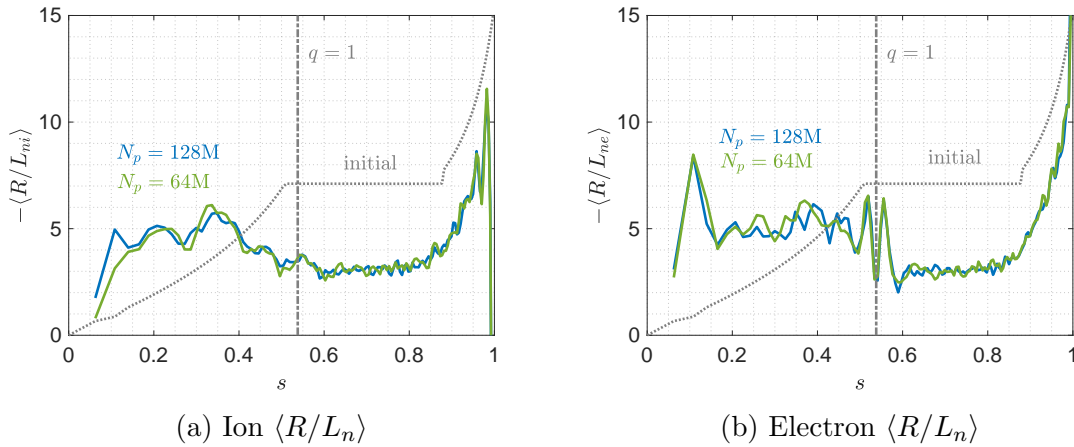


Figure 6.36: Time- and flux-surface averaged logarithmic gradient profiles of gyrocentre density over the time window $c_s t/a \in [1246, 1266]$, for various marker numbers N_p under the adaptive scheme. Profiles are contributions from both the f_0 and δf . Profiles contributed by f_0 only are indistinguishable to the respective $f_0 + \delta f$ ones. All profiles are the result of binning of markers with $f_0 \Omega + w$ weights.

We begin this section by describing profiles that have reached quasi-steady state with just one marker loading at initial time. For the given fluxes, only adaptive cases maintain adequate simulation quality SNR levels to reach this simulation time of $c_s t/a = 1266$ (see Fig. 6.18). Figs. 6.35 shows the density profiles contributed by f_0 (dashed curves) and $f_0 + \delta f$ (solid curves) for both species, with marker numbers $N_p = 128M$ (blue) and $N_p = 64M$ (green) under the adaptive scheme. At quasi-steady state, the density has deviated up to 60% from its initial values. This amount

of deviation would certainly challenge the delta-f PIC constraint of $\|\delta f\|/\|f\| \ll 1$ in the case of the standard method. Next, we see that all adaptive cases converge to the same profile for both $N_p = 128M$ and $N_p = 64M$. This indicates that already with $N_p = 64M$ the simulation is close enough to numerical convergence. Though not shown here, the background profiles are indistinguishable from the profiles contributed by both the f_0 and δf . This indicates that the adaptive rate α_n is large enough, and $\langle \delta f \rangle$ is very small. Considering Fig. 6.35a for ions, we see that there is a difference between cases of $N_p = 128M$ and $N_p = 64M$ near axis. As was shown in Sec. 6.3.7.2, this is due to ion phase-space volume corruption at low velocities (c.f. Fig. 6.27). Fig. 6.35b shows the difference between f.s.a. ion gyrocentre and electron densities, which is 10% for the case with $N_p = 128M$. The reduction of difference by increase in marker number is once again attributed to phase-space volume corruption. Nonetheless, perfect equality between ion gyrocentre and electron densities is not expected one has to account for the ion FLR and polarisation density. To investigate density relaxation further around we consider Fig. 6.36, shows the logarithmic gradient profiles of the ion gyrocentre and electron densities. We see the results of $N_p = 128M$ and $N_p = 64M$ are converged in N_p , and that at the flat logarithmic gradient region $s \in [0.5, 0.9]$, both species have much lower logarithm gradient of density compared to the initial values. However, Fig. 6.36b shows that the electron has density corrugation around the $q = 1$ surface, but not the ions (see Fig. 6.36a). This is related to the assumption of the current hybrid electron model, that passing electrons have an adiabatic response. This assumption breaks down near Mode-Rational-Surfaces (MRS), and such density corrugations have already been observed and studied in reference such as Ref. [19].

We now turn to the temperature profiles at quasi-steady state shown in Fig. 6.37. The background temperature profiles are not shown as they visually coincide with the profiles contributed by both the f_0 and δf . Once again, except near the magnetic axis for the same reason mentioned before when addressing the density profiles, temperature profiles obtained with $N_p = 128M$ and $N_p = 64M$ for each species converge to the same respective profiles. The most notable difference between ions and electrons is that there is an increase in the ion temperature T_i near the magnetic axis, but not for the electron temperature T_e . Avoiding the sampling problems near axis, by considering the region at $s \in [0.1, 0.3]$, we see about a 5% T_i rise. Nonetheless, when compared to the temperature profiles of the previous time window $c_s t/a \in [592, 613]$ shown in Figs. 6.25, we see that the temperature peaks have risen, at $s \simeq 0.3$ and $s \simeq 0.4$ for the ion and electrons. respectively.

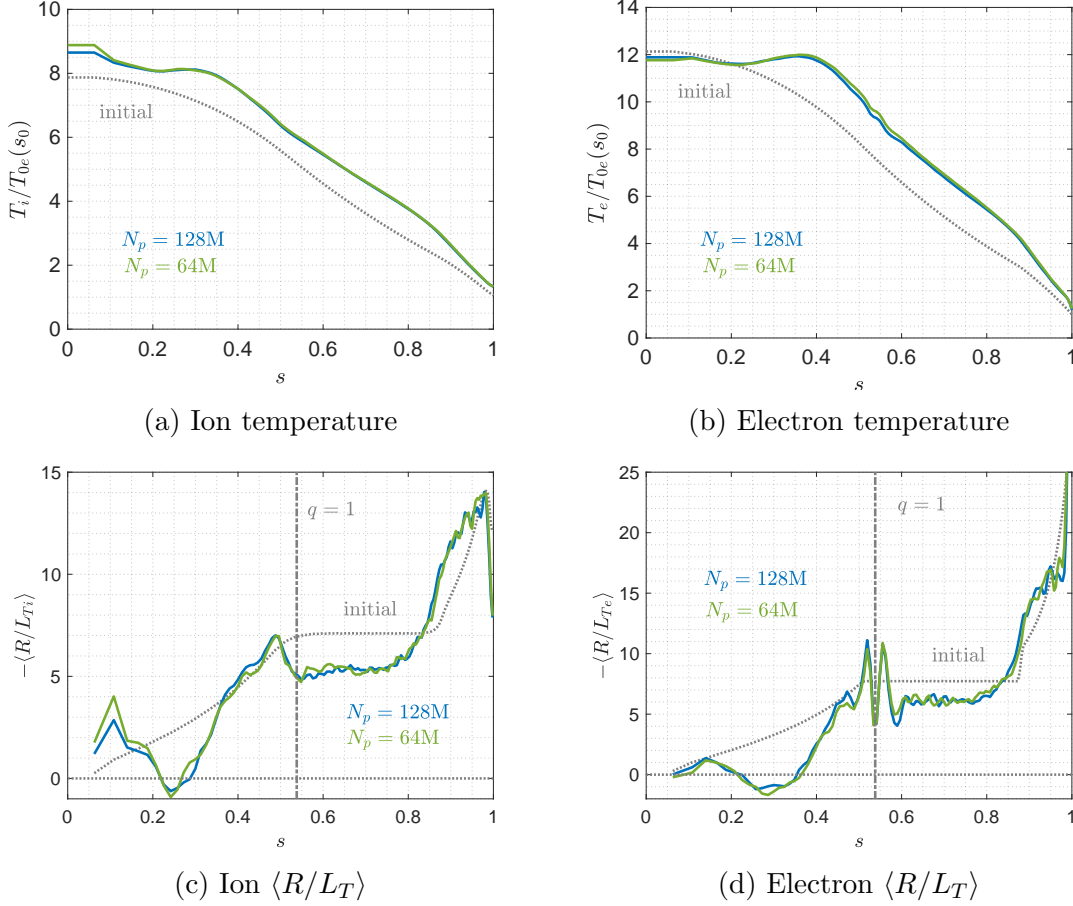


Figure 6.37: Time- and flux-surface- averaged gyrocentre temperature and its logarithmic gradient over the time window $c_s t/a \in [1246, 1266]$, for various marker numbers N_p under the adaptive scheme. Profiles are contributions from both the f_0 and δf . Profiles contributed by f_0 only are indistinguishable to the respective $f_0 + \delta f$ ones. All profiles are the result of binning of markers with $f_0 \Omega + w$ weights.

Next, considering the associated logarithmic gradients of these temperature profiles in Figs. 6.37c and 6.37d, we first note that compared to the initial profiles, both ions and electrons have increased gradients in the ‘pedestal’ region ($s \in [0.8, 1.0]$) and a relaxation to lower gradients in the core ($s \in [0.6, 0.8]$). The increase in gradient at the pedestal is not explained by the effects of local heat sources as this region is well within the buffer (see Fig. 6.17). Moving on to other features, the dip with a negative minimum at $s \in [0.25, 0.3]$ corresponds to the temperature peaks, and the corrugation in T_e gradient is once again located near the $q = 1$ flux surface. The small spike in the T_i gradient around $s = 0.1$ is once again due to the aforementioned sampling problem near axis.

6.3.7.2 The near axis sampling problem

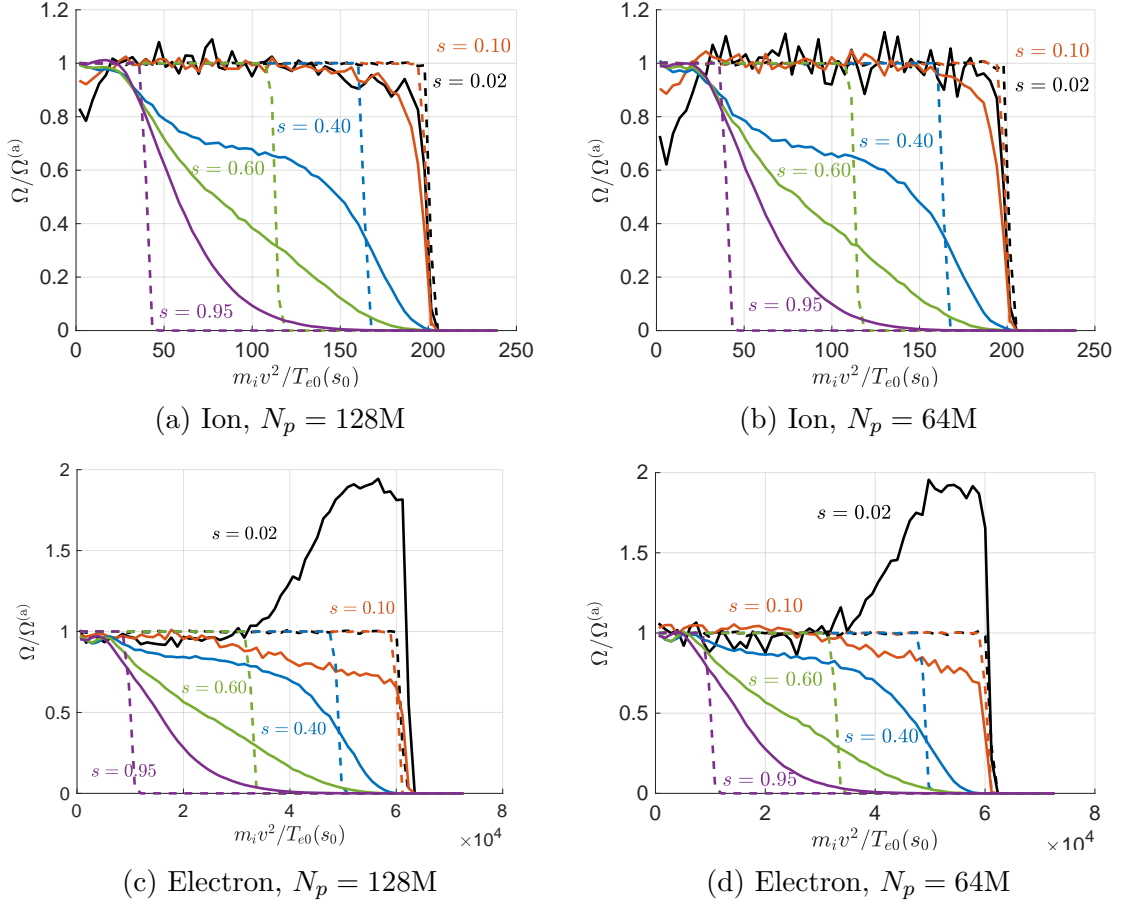


Figure 6.38: Ion and electron phase-space volume diagnostic s -cuts, for marker numbers $N_p = 128M$ and $N_p = 64M$ under the adaptive scheme at $c_s t/a = 1266$. Shown is the ratio $\Omega/\Omega^{(a)}$. Ratio values near 1 reflect good sampling, while ratios deviating significantly from 1 reflect poor/deficient sampling. As $\Omega^{(a)}$ appears in the denominator, it is taken without the v^2 -cut-off to avoid singularities (see Eq. (3.17)). The dashed lines are taken at $t = 0$.

To explain the relative small differences between profiles of $N_p = 128M$ and $N_p = 64M$ for the ions and electrons respectively, we look to the phase-space volume diagnostic at time $c_s t/a = 1266$, as shown in Fig. 6.38. Focusing first on the ions, Figs. 6.38a and 6.38b, we see that the same under-sampling problem of ion phase-space volume near axis (e.g. $s = 0.02$) at low energies becomes more severe for the $N_p = 64M$ compared to the $N_p = 128M$ case. Fig. 6.38b shows that for $s = 0.02$ (black), the sampled ion phase-space volume is already lower than that from the initial marker loading. We therefore see that the adaptive scheme only postpones this problem, which is expected to worsen at even longer simulation times. This is evident when compared to the results at an earlier time window $c_s t/a \in [592, 613]$ as shown by Fig. 6.28c and 6.28d, where we see a $\sim 20\%$ drop in phase-space volume sampled for the adaptive cases of $N_p = 128M$ and $N_p = 64M$ at $s = 0.02$. Also in this comparison, we note significant phase-space volume diffusion at $s = 0.4$ for the adaptive cases

Moving on to the case of the electrons, we again see the accumulation of sampled phase-space volume at $s = 0.02$. As discussed in Sec. 6.3.5, this is due to marker accumulation for $s < s_{\text{push}}$, and can be remedied by reducing the time integration step-size Δt . Next, comparing the cases of $N_p = 128\text{M}$ and $N_p = 64\text{M}$, shown by Figs. 6.38c and 6.38d respectively, we see that for the $N_p = 64\text{M}$ case, we have an under-sampling for $s = 0.02$ at lower energies. This sampling problem is also expected to get worse with simulation time.

Taking the analysis of both ion and electrons together, the problem of low sampling statistics near axis still persists under the adaptive scheme. Its severity can however be postponed as compared to the standard scheme. But after significantly long simulation times, a reloading of marker is needed eventually.

6.4 Results overview

Based on the gradient- and flux-driven simulations of this chapter, initial profiles produce a TEM-dominant turbulent transport. As the density profile evolves, the ion contribution increases, which results in a mixed ITG-TEM regime at quasi-steady state (see Figs.6.3 and 6.18). The latter is characterised by vanishing particle flux[22][60].

The role of lowest order Mode-Rational-Surfaces (MRS) is to create mini-barriers with corrugated zonal flow shearing rate profiles. This effect is partially captured by our trapped electron model that takes into account the f.s.a. passing electron response. An accurate description of this effect would require the fully kinetic electron model. Nonetheless, the simulations show that passing electrons still contribute a significant fraction to radial heat and particle transport, which could in part be due to the large non-physical electron mass used ($m_e/m_i = 1/200$). This enhances the non-adiabatic response of the passing electrons and thus tends to violate the conditions under which it is justified to apply the hybrid model. As a future work, comparison between the hybrid and the fully kinetic models should be done to further quantify the role of passing electrons in transport similar as in Ref. [19].

The flux-driven simulations of this chapter are accompanied with $\mathcal{O}(1)$ profile evolution. The non-adaptive delta-f scheme, i.e. with fixed control variate, is unable to cope with these large profile deviations, resulting in simulations drowned in noise. For the particular profiles and heat sources chosen, the adaptive scheme allows simulations to reach quasi-steady state with only slowly decreasing SNR values (see Fig. 6.23). This is demonstrated to be feasible even with adaptive cases having 1/4 of the numbers markers used by the standard cases (from 256M to 64M markers). Nonetheless, both schemes still suffer from growing regions in phase space due to marker diffusion that are potentially under-sampled as the simulations run over transport time scales. For scenarios with even greater profile deviation, a re-sampling of markers is expected to become necessary, due to marker diffusion and the aforementioned hole in phase space.

Chapter 7

Conclusion and outlook

The aim of this work was to extend the capability of global gyrokinetic turbulence simulations to cases where strong deviations from the initial state occur. Such is typically the case in regions of strong gradients or for long flux-driven simulations. When a particle-based numerical approach is used, this requires to address the issue of accumulation of sampling noise, which was done in this work by introducing an adaptive f.s.a. background as control variate. Specifically, the background that describes the gyrocentre distribution function assumes a Maxwellian form, with time-dependent density and temperature profiles.

To that end, a simple model of an adaptive background temperature scheme was first introduced. The background temperature was evolved through an ad-hoc relaxation equation with associated relaxation rate. Along the simulation, the f.s.a. second order velocity moment, the kinetic energy, that tends to accumulate in the perturbed distribution function was kept low thanks to continuous transfer to the background Maxwellian. This simple model was first tested with the global gyrokinetic PIC code GKengine [65], which assumes fully adiabatic electrons and sheared-slab geometry. Profiles characterised by steep gradients emulating conditions near the plasma edge were used. In order to prevent edge losses, radial profiles were modified to be periodic, and sources/sinks were introduced to prevent profile relaxation beyond critical gradients. When simulating ITG-driven turbulence under such conditions, temperature profiles exhibited relative deviations from initial values as high as 25%. Despite these challenging conditions, the computation with the adaptive background temperature managed to keep the Signal-to-Noise-Ratio (SNR) at quasi-steady values for as long as one could afford the simulations to run, whereas the SNR was found to drop soon after the initial burst for the non-adapted cases. Under this adaptive scheme, noise accumulation in the zonal component was kept to a minimum, thereby preventing an artificial increase in the zonal flow shearing rate which leads to unphysical suppression of turbulence. Convergence studies showed that, under the adaptive scheme, marker numbers as low as 1/4 of the corresponding standard case was sufficient to give even better results, in terms of sustained fluxes and SNR values.

The adaptive scheme was subsequently generalised to be implemented in toroidal geometry. The global gyrokinetic code ORB5 [54] was then used to test the adaptive temperature scheme when simulating toroidal-ITG driven turbulence with adiabatic electrons. These flux-driven simulations have strong heat sources to induce large temperature deviations from initial values. A local control variate with time-

dependent temperature was used, under an adaptive scheme that accounted for possible finite density and parallel flow in δ -f when calculating the perturbed kinetic energy. Associated corrections were found to be necessary in order to keep the adaptive scheme stable when working with adiabatic electrons. For the cases with adaptive background temperature, quasi-steady SNR values and weight variance levels as low as 1/4 those of the corresponding non-adaptive cases were achieved. Similar to the study with the GKengine, the adaptive case with 64M markers was shown to give better results than the corresponding non-adaptive case with 256M markers, in terms of both stationary zonal structures and sustained ion heat diffusivity.

The adaptive scheme was further generalised to adapt both temperature and density of each species. Temperature-gradient- and flux-driven- simulations of turbulence in the mixed ITG-TEM regime were conducted with electrons having an up-graded hybrid response [53], i.e. when solving the quasi-neutrality-equation (QNE) for the self-consistent electrostatic field the model takes into account the drift-kinetic response of all electrons to the zonal perturbations, while for non-zonal perturbations trapped electrons still respond drift-kinetically, the passing electrons however adiabatically. For these runs, the TCV-like profiles [70] exhibited up to 50% deviations from initial values. The adaptive scheme used a canonical Maxwellian control variate, and adapted both density and temperature profiles of ions and electrons independently via an interleaving approach. A comparison of the various methods of calculating the right-hand-side (r.h.s.) correction to the QNE was conducted, and it was shown that the correction term is necessary to keep correct zonal flow structures. Phase-space volume diagnostics developed in Ref. [52] were used to detect phase-space volume depletion at low energies near the axis for ions. Though this problem occurred for both non-adaptive and adaptive cases, the latter seemed to nonetheless be less affected. When compared to the non-adaptive cases, results of the adaptive cases showed higher heat fluxes and lower zonal flow shearing rate amplitudes. The adaptive cases kept the SNR at quasi-steady values, with greatly reduced standard deviation of marker weights. Under the settings of the flux-driven-simulations conducted, though regions of ion phase-space got increasingly under-sampled with simulation time. It was only the adaptive case that managed to reach quasi-steady state.

As future work, a straightforward extension of the current adaptive f.s.a. Maxwellian background to include parallel flow adaptation could be implemented. So as to also extend the evolving background approach to electromagnetic simulations, a similar correction term would need to be added to Ampère's law as the one implemented in the QNE. This would then allow efficient flux-driven simulations of kinetic ballooning, tearing, and internal kink modes. In the presence of fast ions, a time-dependent background could also be useful when simulating Alfvén or energetic particle modes.

Further sophistication to the control variate could be envisaged. One of the methods used to evaluate the correction term of the r.h.s. on the QNE involved expanding the background distribution in terms of basis functions in the canonical toroidal angular momentum and energy. A control variate expanded in a set of basis functions could be pursued. Though only used as an offline diagnostic, Ref. [10] has expressed in ORB5 the background distribution as an expansion in the space of invariants of the unperturbed trajectories. Representing the background velocity distribution velocity space in terms of Hermite and Laguerre polynomial basis func-

tions could be used in tandem with collision operators expressed in such a basis [24]. A mixed representation akin to the XGC code [49, 50], where the control variate consists of an analytic function plus a correction term represented on a phase-space grid could be an alternative. Nonetheless, complexity added to the background translates to complexity added to the code as a whole. A highly complex control variate carries the risk to inherit the disadvantages of both the particle- and grid-based approaches. It may be best to fall-back to the full-f PIC approach for simulations exhibiting high relative fluctuation amplitudes, i.e. in particular for simulating edge/SOL conditions.

Appendix A

Alternative simultaneous adaptive scheme

Using the notation of Eqs. (3.45)-(3.47), and casting them into a linear system of equations leads to

$$\frac{\partial}{\partial t} \begin{bmatrix} n_0 \\ n_0 u_0 \\ \frac{3}{2} n_0 \frac{T_0}{m} + \frac{1}{2} n_0 u_0^2 \end{bmatrix} (\psi, t) = \begin{bmatrix} \alpha_n \langle \int d^3 v \delta f(\vec{Z}, t) \rangle \\ \alpha_u \langle \int d^3 v v_{\parallel} \delta f(\vec{Z}, t) \rangle \\ \alpha_E \langle \int d^3 v \frac{v^2}{2} \delta f(\vec{Z}, t) \rangle \end{bmatrix}$$

$$\begin{bmatrix} 1 & 0 & 0 \\ u_0 & n_0 & 0 \\ \frac{3T_0}{2m} + \frac{u_0^2}{2} & n_0 u_0 & \frac{3n_0}{2} \end{bmatrix} \frac{\partial}{\partial t} \begin{bmatrix} n_0 \\ u_0 \\ \frac{T_0}{m} \end{bmatrix} = \begin{bmatrix} \alpha_n Q_n \\ \alpha_u Q_u \\ \alpha_E Q_E \end{bmatrix}. \quad (\text{A.1})$$

If we now let

$$\mathbb{D}(n_0, u_0, T_0/m) = \begin{bmatrix} 1 & 0 & 0 \\ u_0 & n_0 & 0 \\ \frac{3T_0}{2m} + \frac{u_0^2}{2} & n_0 u_0 & \frac{3n_0}{2} \end{bmatrix},$$

and apply an explicit forward Euler scheme for the partial time derivatives with time step $N_t \Delta t$ (see end of Sec. 3.2.2), the system Eq. (A.1) becomes

$$\Delta \begin{bmatrix} n_0 \\ u_0 \\ \frac{T_0}{m} \end{bmatrix} = N_t \Delta t \mathbb{D}^{-1} \begin{bmatrix} \alpha_n Q_n \\ \alpha_u Q_u \\ \alpha_E Q_E \end{bmatrix}. \quad (\text{A.2})$$

Here, Δ on the l.h.s. of Eq. (A.2) represents the change in background quantities and the matrix \mathbb{D} on the r.h.s. is evaluated using pre-adapted background profiles.

The algorithm for implementation is straightforward. The following is one cycle for the adaptation of all three moments, which spans time $N_t \Delta t$:

1. $Q_n, Q_u, Q_E \leftarrow 0$, do N_t time steps:
 - Advance markers according to Eqs. (2.18)-(2.20)
 - Estimate Q_n, Q_u, Q_E and accumulate individually
2. Calculate time averages: $Q_n \leftarrow Q_n/N_t$, $Q_u \leftarrow Q_u/N_t$, $Q_E \leftarrow Q_E/N_t$

3. Back-solve Eq. (A.2)

4. Solve for

$$\begin{aligned}n_0^{(\text{new})} &\leftarrow n_0 + \Delta n_0 \\u_0^{(\text{new})} &\leftarrow u_0 + \Delta u_0 \\T_0^{(\text{new})} &\leftarrow T_0 + \Delta T_0.\end{aligned}$$

Appendix B

Quadrature point convergence for r.h.s. of QNE

The aim of this section is to determine the number of quadrature points sufficient to integrate the r.h.s. of Eq. (4.5), formally written as

$$\delta\tilde{n} = \frac{1}{2\pi} \int d^3R d^3v d\alpha \delta[\vec{R} + \vec{\rho}_L - \vec{r}] \delta f(\vec{R}, v_{\parallel}, \mu, t). \quad (\text{B.1})$$

To proceed, we introduce a simple but non-trivial form of δf , so that Eq. (B.1) can be solved analytically, namely,

$$\begin{aligned} \delta f &= \frac{\cos(\xi x)}{(2\pi T_i/m_i)^{3/2}} \exp\left[-\frac{v_{\parallel}^2/2 + \mu B}{T_i/m_i}\right] \\ &= \frac{\cos(\xi x)}{(2\pi)^{3/2} v_{th}^3} \exp\left[-\frac{v_{\parallel}^2 + v_{\perp}^2}{2v_{th}^2}\right], \end{aligned} \quad (\text{B.2})$$

with $v_{th} = \sqrt{T_i/m_i}$ the local thermal velocity, $\mu = v_{\perp}^2/2B$ the magnetic moment, and ξ a constant. To simplify further, we shall assume constant T_i and B . Furthermore, given that $B_{\parallel}^* = B[1 + m_i B'_y(x) B_z v_{\parallel} / (eB^3)]$ and all velocity variables v_{\parallel} and v_{\perp} are contained in δf and that δf is an even function of v_{\parallel} , the velocity integration effectively becomes

$$\begin{aligned} \delta f d^3v &= \delta f 2\pi B_{\parallel}^* dv_{\parallel} d\mu \\ &= \delta f 2\pi B dv_{\parallel} d\mu \\ &= \delta f 2\pi v_{\perp} dv_{\perp} dv_{\parallel}. \end{aligned} \quad (\text{B.3})$$

Inserting Eq. (B.2) into Eq. (B.1) gives

$$\delta\tilde{n}(\vec{r}) = \text{Re}\{I(x)\},$$

with

$$\begin{aligned}
I(x) &= \int d\alpha \int_{-\infty}^{\infty} \frac{dv_{\parallel} e^{-\frac{v_{\parallel}^2}{2v_{th}^2}}}{\sqrt{2\pi v_{th}^2}} \times \int_0^{\infty} \frac{dv_{\perp} v_{\perp} e^{-\frac{v_{\perp}^2}{2v_{th}^2}}}{2\pi v_{th}^2} \exp[i\xi(x + \rho_L \sin \alpha)] \\
&= e^{i\xi x} \int d\alpha \frac{1}{2\pi} \int_0^{\infty} \frac{dv_{\perp}}{v_{th}} \frac{v_{\perp}}{v_{th}} e^{-\frac{v_{\perp}^2}{2v_{th}^2}} \exp\left(i\xi \rho_{th} \frac{v_{\perp}}{v_{th}} \sin \alpha\right) \\
&= e^{i\xi x} \int_0^{\infty} \frac{dv_{\perp}}{v_{th}} J_0\left(\xi \rho_{th} \frac{v_{\perp}}{v_{th}}\right) \frac{v_{\perp}}{v_{th}} e^{-\frac{v_{\perp}^2}{2v_{th}^2}} \\
&= \exp\left[i\xi x - \frac{(\xi \rho_{th})^2}{2}\right],
\end{aligned}$$

where $\rho_{th} = v_{th}/\Omega$ is the thermal Larmor radius and J_0 is the zero-th order Bessel function of the first kind.

The evaluation of the field ϕ , which is represented by a B-spline expansion, involves the contraction of the r.h.s. of Eq. (4.5) with a B-spline element of order p , $\Lambda^p(\vec{r} - \vec{r}_{ijk}) = \Lambda^p(x - x_i)\Lambda^p(y - y_j)\Lambda^p(z - z_k)$. Here, the zero-th order B-spline is defined as

$$\Lambda^0(x) = \begin{cases} 1 & |x| < \Delta x/2 \\ 0 & \text{else} \end{cases}$$

so that $\int dx \Lambda^0(x) = \Delta x$, and the higher order elements by the recurrence relation

$$\Lambda^p(x) = \frac{1}{\Delta x} \Lambda^{p-1}(x) * \Lambda^0(x) \quad p \geq 1,$$

where Δx is the grid size of equidistant points along dimension x , and $*$ stands for convolution. Therefore, we conduct a convergence analysis on the real part of the expression:

$$\begin{aligned}
&\int d^3r \Lambda^p(\vec{r} - \vec{r}_{ijk}) \delta \tilde{n}(x) \\
&= \Delta y \Delta z \exp\left[i\xi x_i - \frac{(\xi \rho_{th})^2}{2}\right] \times \int dx \Lambda^p(x - x_i) e^{i\xi(x - x_i)} \\
&= \Delta x \Delta y \Delta z \exp\left[i\xi x_i - \frac{(\xi \rho_{th})^2}{2}\right] \left[\frac{2}{\xi \Delta x} \sin\left(\frac{\xi \Delta x}{2}\right)\right]^p. \tag{B.4}
\end{aligned}$$

In practice, the $f_0(\vec{R}, v_{\parallel}, \mu, t) - f_0(\vec{R}, v_{\parallel}, \mu, 0)$ term of the r.h.s. of Eq. (4.5) is calculated using Gaussian quadratures. Specifically, due to the limits of integration for each of the variables, N_q Legendre points for the x integral, N_c Chebyshev points for the α integral, and N_l Laguerre points for the μ integral have been used. The convergence study for $\xi L_x = 32\pi$, which exceeds the typical wavelength of the integrand for this work, is show in Fig. B.1.

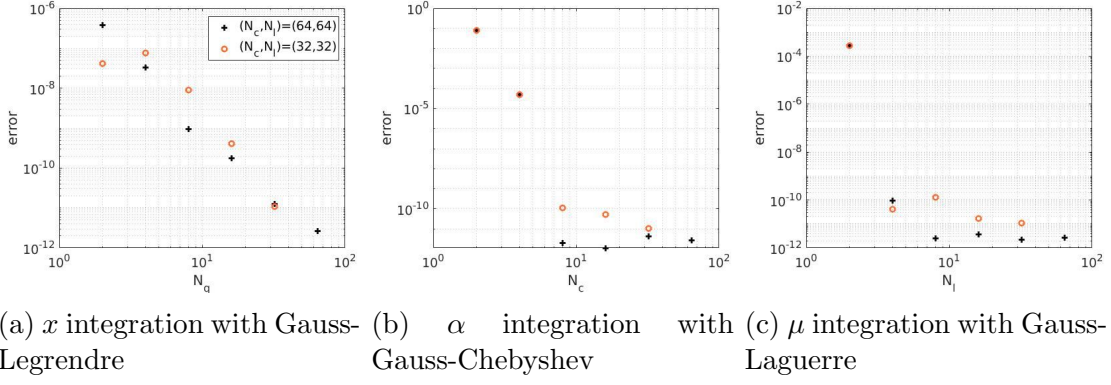


Figure B.1: Convergence analysis with quadrature points of the $f_0(\vec{R}, v_{\parallel}, \mu, t) - f_0(\vec{R}, v_{\parallel}, \mu, 0)$ term of the r.h.s. of Eq. (4.5). (N_q, N_c, N_l) quadrature points are used for the integration of the dimensions x , α and μ respectively. For each of the above cases, the quadrature point number for a dimension is set to vary, while the other two are fixed at either 32 or 64.

Appendix C

Canonical control variate with adiabatic electrons

C.1 Canonical control variate

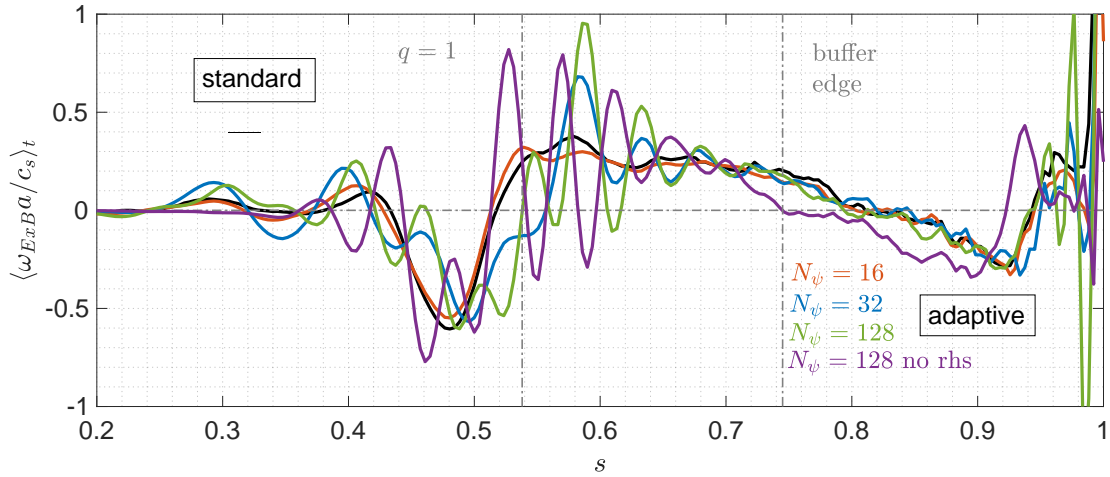


Figure C.1: Radial profile of the time-averaged $c_s t/a \in [531, 612]$ zonal flow shearing rate $\omega_{E \times B}$, for marker number $N_p = 128M$ under the standard (black) and adaptive schemes. The adaptive scheme uses a canonical control variate (see Eq. (3.53)), adapting only the temperature (see Eq. (3.54)). N_ψ refers to the adaptive background profile radial grid resolution (see Eq. (3.48)).

In simulations with fully adiabatic electrons and a canonical control variate, an apparent numerical instability occurs when one attempts to only adapt the f.s.a. ion gyrocentre background temperature profile. The instability was first observed in a form of a radially sinusoidal zonal flow shearing rate $\omega_{E \times B}$ profile with growing amplitudes. Fig. C.1 shows an example of such an instability on the time-averaged $\omega_{E \times B}$ radial profile. Plotted in black is the $\omega_{E \times B}$ profile of the standard case. This sinusoidal pattern does not oscillate with time and appears to be around the $q = 1$ flux surface indicated by the vertical line. Nonetheless, this instability can be suppressed if one chooses a coarse radial grid for the adaptive background temperature profile (see Eq. (3.48)), i.e. $N_\psi \leq 16$ for the simulation parameters of Ch. 5. Above this radial resolution, the $\omega_{E \times B}$ amplitudes grow. It is important to note that this

is not a CFL-like instability as there are several grid points per sinusoidal period. Furthermore, the instability seem to exhibit a fixed wave pattern for all cases above $N_\psi = 16$. This is with the exception of the adaptive case without the r.h.s. correction to the QNE, where it appears to be almost perfectly anti-phase. Fig. C.2 further shows more clearly the growth of the stationary sinusoidal pattern of $\omega_{E \times B}$ for a selection of cases from Fig. C.1.

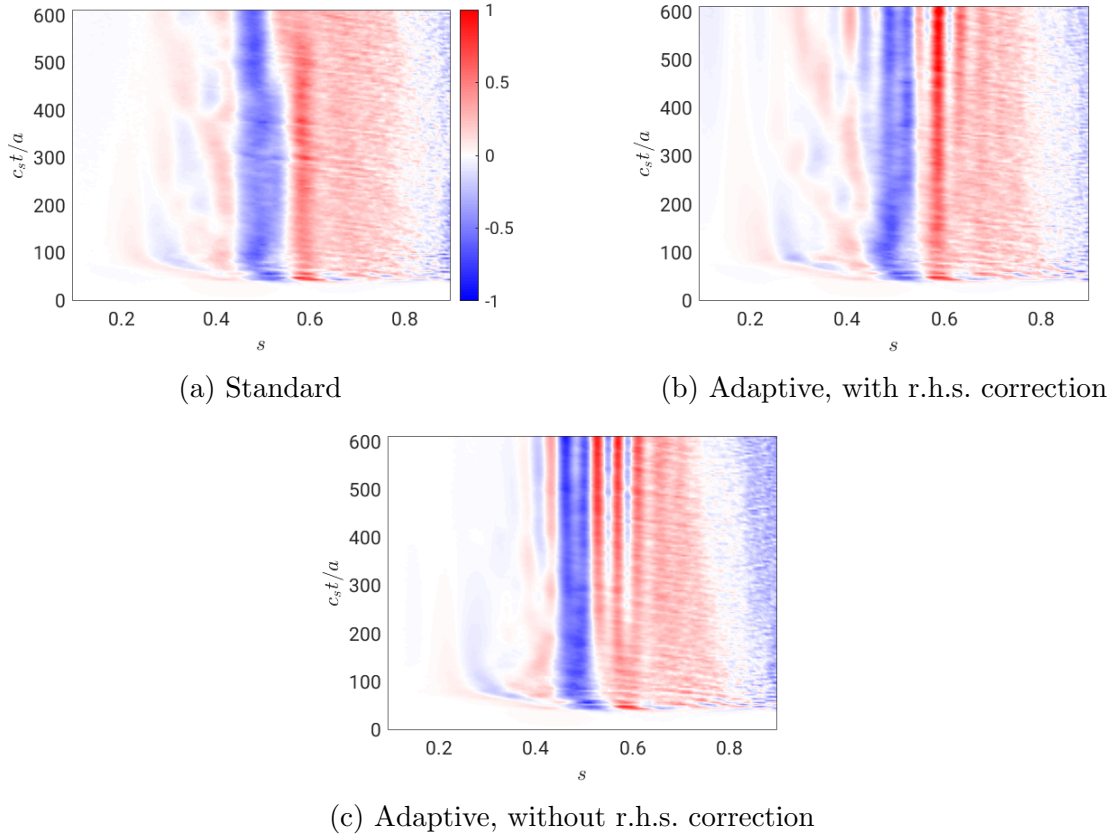


Figure C.2: Time evolution up to $c_s t/a = 612$ of the radial profile of the zonal flow shearing rate, $\omega_{E \times B}(s, t)$, for marker numbers $N_p = 128M$ under the standard and adaptive schemes, with and without r.h.s correction to the QNE (see Eq. (3.63)). The adaptive scheme uses a canonical control variate (see Eq. (3.53)) with $N_\psi = 128$ (see Eq. (3.48)), and for case (b), has correction to the r.h.s. of the QNE calculated exactly (see Sec. 3.2.10.1). All plots share the same colour scale.

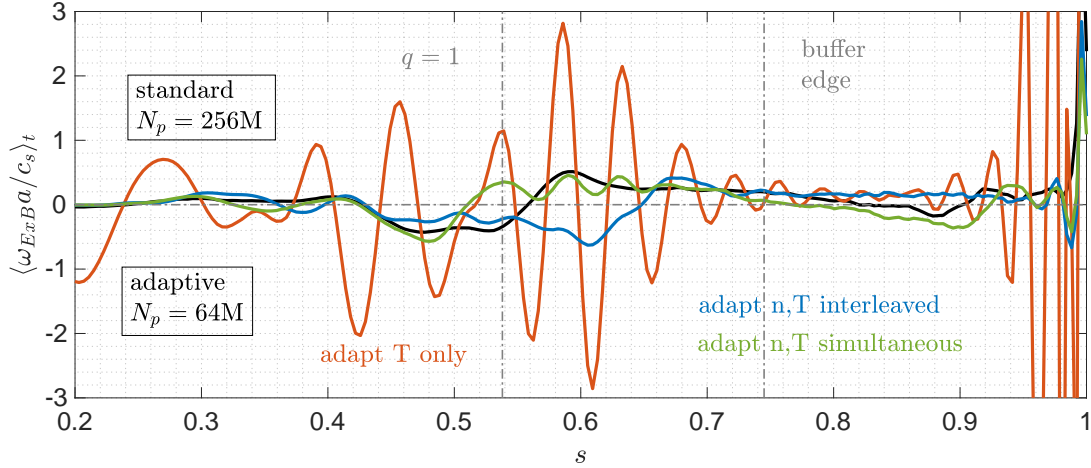


Figure C.3: Radial profile of the time-averaged $c_s t/a \in [1103, 1225]$ zonal flow shearing rate $\omega_{E \times B}$, for marker number $N_p = 128M$ under the standard (black) and adaptive schemes. The adaptive scheme uses a canonical control variate (see Eq. (3.53)) with $N_\psi = 128$ (see Eq. (3.48)), and three different adaptive algorithms: adapt T only (red), adapt both n and T with interleave (blue) and the simultaneous (green) methods, see Sec. 3.2.4.

This problem motivated the development of the ‘simultaneous’ adaptation algorithm (see Sec. 3.2.4). The idea is that the ion δf may contribute to a perturbed gyrocentre density δn , which may produce a perturbed kinetic energy δE_{kin} interpreted by the interleaving algorithm at the temperature-only adaptive stage as variation in the temperature (see Eq. (3.54)). This problem is avoided when changes to δn and δE_{kin} are simultaneously computed. A change in the perturbed parallel flow δv_{\parallel} could also be wrongly interpreted as a temperature change. Note that for the ‘simultaneous’ adaptive results of Fig. C.3, the contribution to δv_{\parallel} was also simultaneously computed.

To correct for the perturbed density, along with any parallel momentum component, all three velocity moments needed to calculate simultaneously in order to determine correction terms to the temperature variation. Fig. C.3 shows the radial profile of $\omega_{E \times B}$, time-averaged after twice the simulation time of Fig. C.1. It shows the results from the different ways of adaptation, using the standard case (black) as reference. $N_\psi = 128$ is set here to induce the instability. We see that adapting the density and temperature in an interleaved fashion (blue) does not give the correct $\omega_{E \times B}$ radial profile. While the method via simultaneous adaptation (green) does come closer to the expected $\omega_{E \times B}$. Fig. C.4 further shows the improvement of the simultaneous algorithm. Comparing Figs. C.4a and C.4d, we note that it is only at a later time $c_s t/a > 1000$ onwards that the instability begins to be noticeable.

Further analysis is required in order to better understand the cause of the instability of the adaptive scheme for a canonical control variate.

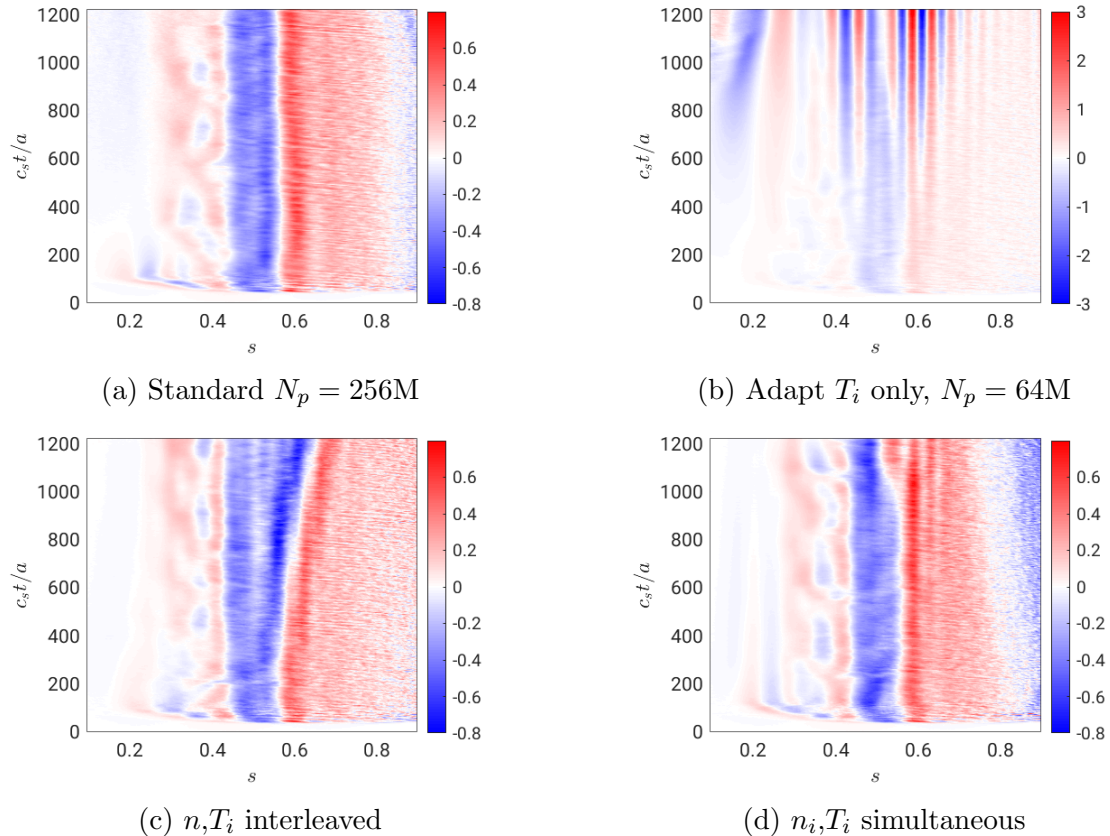


Figure C.4: Time evolution up to $c_s t/a = 1225$ of the radial profile of the zonal flow shearing rate, $\omega_{E \times B}(s, t)$, for various marker numbers N_p under the standard and adaptive schemes. The adaptive scheme uses a canonical control variate (see Eq. (3.53)) with $N_\psi = 128$ (see Eq. (3.48)). The adaptive scheme of: (b) adapts the background temperature only; (c) adapts the density and temperature via the interleaved algorithm (see Sec. 3.2.3); and (d) adapts the density and temperature via the simultaneous algorithm.

C.2 Local control variate

The instability for an adaptive scheme using a local control variate with fully adiabatic electrons is less severe than the option with canonical control variate. Though not shown here, under an adaptive scheme which only adapts the f.s.a. background ion gyrocentre temperature, the instability persists. However, with the simultaneous algorithm adapting both the density and temperature, the instability seems to vanish for all values of N_ψ . Fig. C.6 shows the radial profile of $\omega_{E \times B}$, time averaged over the same time window as Fig. C.3. We see that the adaptive cases (green and purple) almost matches the result of the standard case (black). What remains in the results of the adaptive scheme is a small non-growing interval-sized corrugation. The two adaptive cases plotted differ by N_ψ and the order of the basis functions $\{\Lambda(s)\}$ used (see Eq. (3.48)). This difference seem to have little effect on these fine structures, which are related to the radial grid used for the quasi-neutrality-equation (QNE) ($N_s = 256$, equidistant in s) and not the radial grid used for the adaptive scheme ($N_\psi = 64$ or $N_\psi = 128$, equidistant in s^2). Fig. C.7 shows the time evolution of one of each of the standard and adaptive (green) cases of Fig. C.6. We see that

at least for early times $c_s t/a < 500$, we have a good match with the standard case. The slow radially outward drift of the corrugation structure of the standard case may occur due to sampling noise, but this would require further studies.

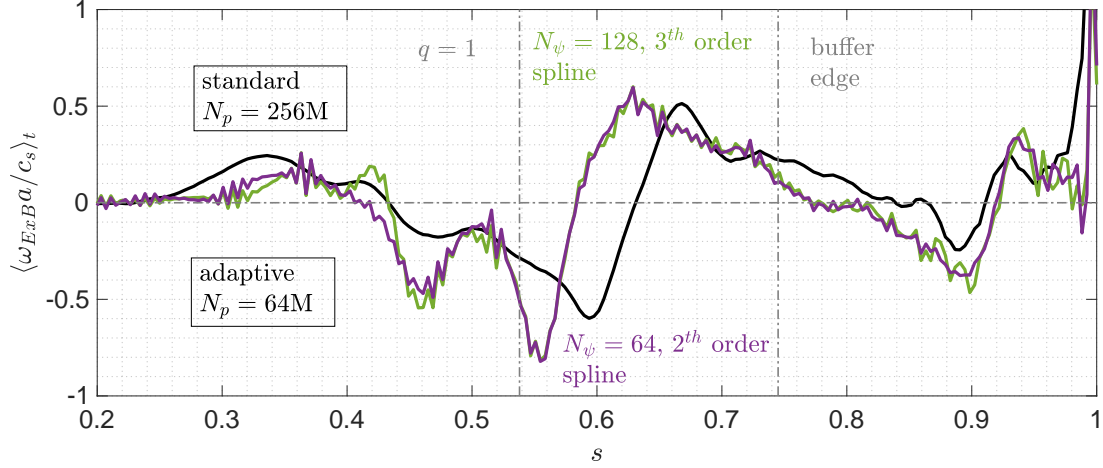
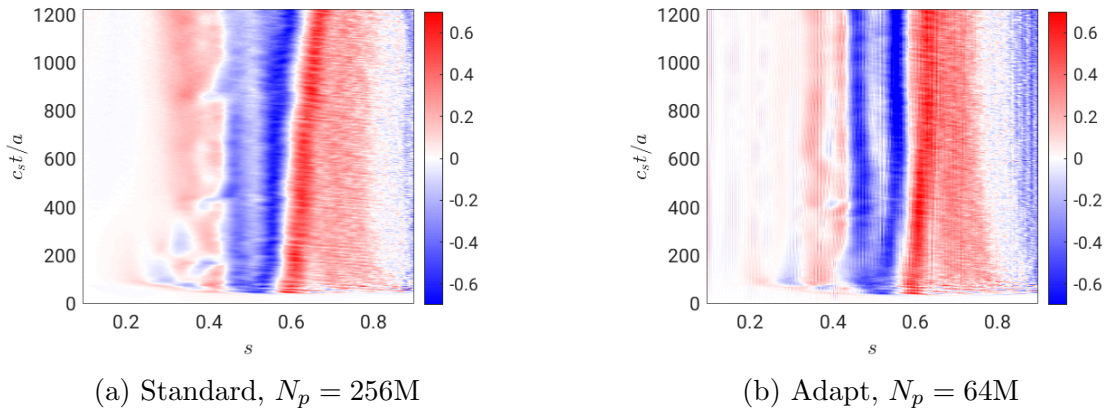


Figure C.5: Shearing rate $\omega_{E \times B}$

Figure C.6: Radial profile of the time-averaged $c_s t/a \in [1103, 1225]$ zonal flow shearing rate $\omega_{E \times B}$, for various marker numbers N_p under the standard (black) and adaptive (green and purple) schemes. The adaptive scheme uses a local control variate (see Eq. (3.53)) and adapts via the simultaneous algorithm (see Sec. 3.2.4). N_ψ is the adaptive background radial grid resolution (see Eq. (3.48)). The 2nd (purple) and 3rd (green) order spline refers to the order of B-spline of the basis functions $\{\Lambda(s)\}$ of Eq. (3.48).



(a) Standard, $N_p = 256M$

(b) Adapt, $N_p = 64M$

Figure C.7: Time evolution up to $c_s t/a = 1225$ of the radial profile of the zonal flow shearing rate, $\omega_{E \times B}(s, t)$, for various marker numbers N_p under the standard (a) and adaptive (b) schemes. The adaptive scheme uses a local control variate (see Eq. (3.42)) with $N_\psi = 128$ with 3rd-order spline basis functions $\{\Lambda(s)\}$ (see Eq. (3.48)).

C.3 Further notes

Three important comments are in order. The first is that the physics of the simulations for the use of the canonical and local control variate shown here are not identical. The former uses the direct- δf approach (see Sec. 3.1.3.4), while the latter uses the standard- δf approach neglecting the neoclassical term. The second is that studies were not conducted to determine the extent to which the approximation Eq. (3.52) affects the instability with canonical control variates. The third is that for simulations with electrons having a hybrid response done in Ch. 6, both simultaneous and interleaved algorithms for the density and temperature adaptation seem to give indistinguishable results.

Bibliography

- [1] C. J. Ajay. “Studying the effect of non-adiabatic passing electron dynamics on microturbulence self-interaction in fusion plasmas using gyrokinetic simulations”. In: *EPFL PhD thesis* 8206 (2020).
- [2] S. J. Allfrey and R. Hatzky. “A revised δf algorithm for nonlinear PIC simulation”. In: *Comput. Phys. Comm.* 154 (2003), p. 98. DOI: 10.1016/S0010-4655(03)00288-1.
- [3] P. Angelino et al. “On the definition of a kinetic equilibrium in global gyrokinetic simulations”. In: *Phys. Plasmas* 13 (2006), p. 052304. DOI: 10.1063/1.2193947.
- [4] P. Angelino et al. “Role of plasma elongation on turbulent transport in magnetically confined plasmas”. In: *Phys. Rev. Lett.* 102 (2009), p. 195002. DOI: 10.1103/PhysRevLett.102.195002.
- [5] C. Angioni et al. “Particle transport in tokamak plasmas, theory and experiment”. In: *Plasma Phys. Control. Fusion* 51 (2009), p. 124017. DOI: 10.1088/0741-3335/51/12/124017.
- [6] A. Y. Aydemir. “A unified Monte Carlo interpretation of particle simulations and applications to non-neutral plasmas”. In: *Phys. Plasmas* 1 (1994), p. 822. DOI: 10.1063/1.870740.
- [7] C. K. Birdsall and A. B. Langdon. *Plasma physics via computer simulations*. 1st ed. CRC Press, Boca Raton, 1991. DOI: 10.1201/9781315275048.
- [8] A. Bottino. “Modelling of global electrostatic microinstabilities in tokamaks: effects of $E \times B$ flow and magnetic shear”. In: *EPFL PhD thesis* 2938 (2004).
- [9] A. Bottino et al. “Nonlinear low noise particle-in-cell simulations of electron temperature gradient driven turbulence”. In: *Phys. Plasmas* 14 (2007), p. 010701. DOI: 10.1063/1.2428280.
- [10] A. Bottino et al. “Time evolution and finite element representation of phase space zonal structures in ORB5”. In: *J. Phys.: Conf. Ser.* 2397 (2022), p. 012019. DOI: 10.1088/1742-6596/2397/1/012019.
- [11] A. J. Brizard. “On the dynamical reduction of the Vlasov equation”. In: *Commun. Nonlinear. Sim.* 13 (2008), p. 24. DOI: 10.1016/j.cnsns.2007.05.006.
- [12] S. Brunner. “Global approach to the spectral problem of microinstabilities in tokamak plasmas using a gyrokinetic model”. In: *EPFL PhD thesis* 1701 (1997).
- [13] S. Brunner, E. Valeo, and J. A. Krommes. “Collisional delta-f scheme with evolving background for transport time scale simulations”. In: *Phys. Plasmas* 6 (1999), p. 4504. DOI: 10.1063/1.873738.

-
- [14] J. Candy and R. E. Walz. “An Eulerian gyrokinetic-Maxwell solver”. In: *J. Comput. Phys.* 186 (2003), p. 545. DOI: 10.1016/S0021-9991(03)00079-2.
- [15] Y. Chen and S. E. Parker. “Particle-in-cell simulation with Vlasov ions and drift kinetic electrons”. In: *Phys. Plasmas* 16 (2009), p. 052305. DOI: doi.org/10.1063/1.3138743.
- [16] Y. Chen and R. B. White. “Collisional δf method”. In: *Phys. Plasmas* 4 (1997), p. 3591. DOI: 10.1063/1.872254.
- [17] W. D. Dhaeseleer et al. *Flux coordinates and magnetic field structure*. 1st ed. Springer Berlin, Heidelberg, 1991. DOI: 10.101007/978-3-642-75595-8.
- [18] P. H. Diamond et al. “Zonal flows in plasma - A review”. In: *Plasma Phys. Control. Fusion* 47 (2005), R35. DOI: 10.1088/0741-3335/47/5/R01.
- [19] J. Dominski. “Development and application of Eulerian and Particle-in-Cell gyrokinetic codes for studying the effect of non-adiabatic passing electron dynamics on microturbulence”. In: *EPFL PhD thesis* 7286 (2016).
- [20] J. Dominski et al. “An arbitrary wavelength solver for global gyrokinetic simulations. Application to the study of fine radial structures on microturbulence due to non-adiabatic passing electron dynamics”. In: *Phys. Plasmas* 24 (2017), p. 022308. DOI: 10.1063/1.4976120.
- [21] W. Dorland et al. “Electron temperature gradient turbulence”. In: *Phys. Rev. Lett.* 85 (2000), p. 5579. DOI: 10.1103/PhysRevLett.85.5579.
- [22] E. Fable. “Experimental and theoretical study of particle transport in the TCV tokamak”. In: *EPFL PhD thesis* 4334 (2009).
- [23] T. K. Fowler. *The fusion quest*. 1st ed. John Hopkins University Press, Baltimore MD, 1997. DOI: 10.1063/1.882155.
- [24] B. J. Frei, S. Ernst, and P. Ricci. “Numerical implementation of the improved Sugama collision operator using a moment approach”. In: *Phys. Plasmas* 29 (2022), p. 093902. DOI: 10.1063/5.0091244.
- [25] J. P. Friedberg. *Computational methods in plasma physics*. Revised. Cambridge University Press, NY, 2014. DOI: 10.1017/CB09780511795046.
- [26] Z. Gao. “Plasma shaping effects on the geodesic acoustic mode in the large orbit drift width limit”. In: *Phys. Plasmas* 17 (2010), p. 092503. DOI: 10.1063/1.3481464.
- [27] X. Garbet and M. Lesur. “Gyrokinetics”. In: *Doctoral* (2023). DOI: hal-03974985v2.
- [28] X. Garbet et al. “Gyrokinetic simulations of turbulent transport”. In: *Nucl. Fusion* 50 (2010), p. 043002. DOI: 10.1088/0029-5515/50/4/043002.
- [29] H. P. Goedbloed. *Principles of magnetohydrodynamics*. 1st ed. Cambridge Printing Press, NY, 2004. DOI: 10.1017/CB09780511616945.
- [30] T. Görler et al. “The global version of the gyrokinetic turbulence code GENE”. In: *J. Comput. Phys.* 230 (2011), p. 7053. DOI: 10.1016/j.jcp.2011.05.034.
- [31] V. Grandgirard et al. “A 5D gyrokinetic full-f global semi-Lagrangian code for flux-driven ion turbulence simulations”. In: *Comput. Phys. Commun.* 207 (2016), p. 35. DOI: 10.1016/j.cpc.2016.05.007.

- [32] T. S. Hahm. “Nonlinear gyrokinetic equations for tokamak microturbulence”. In: *Phys. Fluids* 31 (1988), p. 2670. DOI: 10.1063/1.866544.
- [33] D. R. Hatch et al. “Phase space scales of free energy dissipation in gradient-driven gyrokinetic turbulence”. In: *J. Plasma Phys.* 80 (2014), p. 531. DOI: 10.1017/S0022377814000154.
- [34] R. Hatzky et al. “Energy conservation in a nonlinear gyrokinetic particle-in-cell code for ion-temperature-gradient-driven modes in θ -pinch geometry”. In: *Phys. Plasmas* 9 (2002), p. 898. DOI: 10.1063/1.1449889.
- [35] R. W. Hockeny and J. W. Eastwood. *Computer simulation using particles*. 1st ed. CRC Press, Boca Raton, 1988. DOI: 10.1201/9780367806934.
- [36] W. Horton. “Drift waves and transport”. In: *Rev. Mod. Phys.* 71 (1999), p. 735. DOI: 10.1103/RevModPhys.71.735.
- [37] W. Horton, D. I. Choi, and W. M. Tang. “Toroidal drift modes driven by ion pressure gradients”. In: *Phys. Fluids* 24 (1981), p. 1077. DOI: 10.1063/1.863486.
- [38] I. Idomura, S. Tokuda, and Y. Kishimoto. “Global gyrokinetic simulation of ion temperature gradient driven turbulence in plasmas using a canonical Maxwellian distribution”. In: *Nucl. Fusion* 43 (2003), p. 234. DOI: 10.1088/0029-5515/43/4/303.
- [39] Y. Idomura. “A new hybrid kinetic electron model for full-f gyrokinetic simulations”. In: *J. Comput. Phys.* 313 (2016), p. 511. DOI: 10.1016/j.jcp.2016.02.057.
- [40] Y. Idomura et al. “Study of ion turbulent transport and profile formations using global gyrokinetic full-f vlasov simulation”. In: *Nucl. Fusion* 49 (2009), p. 065029. DOI: 10.1088/0029-5515/49/6/065029.
- [41] S. C. Jardin. *Computational methods in plasma physics*. 1st ed. CRC Press, Boca Raton, 2010. DOI: 10.1201/EBK1439810958.
- [42] F. Jenko et al. “Electron temperature gradient driven turbulence”. In: *Phys. Plasmas* 7 (2000), p. 1904. DOI: 10.1103/PhysRevLett.85.5579.
- [43] S. Jolliet. “Gyrokinetic Particle-In-Cell global simulations of Ion-Temperature-Gradient and collisionless-Trapped-Electron-Mode turbulence in tokamaks”. In: *EPFL PhD thesis* 4326 (2009).
- [44] S. Jolliet et al. “Influence of the parallel nonlinearity on zonal flows and heat transport in global gyrokinetic particle-in-cell simulations”. In: *Phys. Plasmas* 16 (2009), p. 072309. DOI: 10.1063/1.3174433.
- [45] S. Jolliet et al. “Parallel filtering in global gyrokinetic simulations”. In: *J. Comput. Phys.* 231 (2012), p. 745. DOI: 10.1016/j.jcp.2011.01.029.
- [46] R. Kleiber et al. “EUTERPE: A global gyrokinetic code for stellarator geometry”. In: *Comput. Phys. Commun.* 295 (2024), p. 109013. DOI: 10.1016/j.cpc.2023.109013.
- [47] M. Kotschenreuther, G. Rewoldt, and W. M. Tang. “Comparison of initial value and eigenvalue codes for kinetic toroidal plasma instabilities”. In: *Comput. Phys. Commun.* 88 (1995), p. 128. DOI: 10.1016/0010-4655(95)00035-E.

- [48] J. A. Krommes. “Thermostatted δf ”. In: *Phys. Plasmas* 6 (1999), p. 1477. DOI: 10.1063/1.873400.
- [49] S. Ku, C. S. Chang, and P. H. Diamond. “Full-f gyrokinetic particle simulation of centrally heated global ITG turbulence from magnetic axis to edge pedestal top in a realistic tokamak geometry”. In: *Nucl. Fusion* 49 (2009), p. 115021. DOI: 10.1088/0029-5515/49/11/115021.
- [50] S. Ku et al. “A new hybrid-Lagrangian numerical scheme for gyrokinetic simulation of tokamak edge plasma”. In: *J. Comput. Phys.* 315 (2016), p. 467. DOI: 10.1016/j.jcp.2016.03.062.
- [51] J. Lang, Y. Chen, and S. E. Parker. “Gyrokinetic δf particle simulation of trapped electron mode driven turbulence”. In: *Phys. Plasmas* 14 (8 2007), p. 467. DOI: 10.1063/1.2771141.
- [52] E. Lanti. “Global Flux-Driven Simulations of Ion Temperature-Gradient and Trapped-Electron Modes Driven Turbulence With an Improved Multithreaded Gyrokinetic PIC Code”. In: *EPFL PhD thesis* 9575 (2019).
- [53] E. Lanti et al. “Gradient- and flux-driven global gyrokinetic simulations of ITG and TEM turbulence with an improved hybrid kinetic electron model”. In: *J. Phys.: Conf. Ser.* 1125 (2018), p. 012014. DOI: 10.1088/1742-6596/1125/1/012014.
- [54] E. Lanti et al. “ORB5: A global electromagnetic gyrokinetic code using the PIC approach in toroidal geometry ”. In: *Comput. Phys. Comm.* 251 (2020), p. 107072. DOI: 10.1016/j.cpc.2019.107072.
- [55] J. D. Lawson. “Some criteria for a power producing thermonuclear reactor”. In: *Proc. Phys. Soc.* B70 (1957), p. 6. DOI: 10.1088/0370-1301/70/1/303.
- [56] W. W. Lee. “Gyrokinetic particle simulation model”. In: *J. Comput. Phys.* 72.1 (1987), p. 243. DOI: 10.1063/1.864140.
- [57] J. Li and Y. Kishimoto. “Role of collisionless trapped electron mode in tokamak plasmas with electron internal transport barrier”. In: *Plasma Phys. Control. Fusion* 44 (2002), A479. DOI: 10.1088/0741-3335/44/5A/353.
- [58] Z. Lin et al. “Global gyrokinetic particle simulations with kinetic electrons”. In: *Plasma Phys. Control. Fusion* 49 (2007), B163. DOI: 10.1088/0741-3335/49/12B/S15.
- [59] H. Lütjens, A. Bondeson, and Sauter O. “The CHEASE code for toroidal MHD equilibria”. In: *Comput. Phys. Commun.* 97 (2006), p. 219. DOI: 10.1016/0010-4655(96)00046-X.
- [60] A. Mariani et al. “Identifying microturbulence regimes in a TCV discharge making use of physical constraints on particle and heat fluxes”. In: *Phys. Plasmas* 25 (2018), p. 012313. DOI: 10.1063/1.5006408.
- [61] B. F. McMillan et al. “Avalanchelike bursts in global gyrokinetic simulations”. In: *Phys. Plasmas* 16 (2009), p. 022310. DOI: 10.1063/1.2921792.
- [62] B. F. McMillan et al. “Long global gyrokinetic simulations: Source terms and particle noise control”. In: *Phys. Plasmas* 15 (2008), p. 052308. DOI: 10.1063/1.2921792.

- [63] M. Murugappan et al. “Gyrokinetic simulations of turbulence and zonal flows driven by steep profile gradients using a delta-f approach with an evolving background Maxwellian”. In: *Phys. Plasmas* 29 (2022), p. 103904. DOI: 10.1063/5.0106661.
- [64] N. Ohana. “Using an antenna as a tool for studying microturbulence and zonal structures in tokamaks with a global gyrokinetic GPU-enabled particle-in-cell code”. In: *EPFL PhD thesis* 10127 (2020).
- [65] N. Ohana et al. “Towards the optimization of a gyrokinetic Particle-In-Cell (PIC) code on large-scale hybrid architectures”. In: *J. Phys.: Conf. Ser.* 775 (2016), p. 012010. DOI: 10.1088/1742-6596/775/1/012010.
- [66] A. Piel. *Plasma physics*. 2nd ed. Springer Cham, 2017. DOI: 10.1007/978-3-319-63427-2.
- [67] G. Rewoldt and W. M. Tang. “Toroidal microinstability studies of high-temperature tokamaks”. In: *Phys. Fluids B* 2 (1990), p. 318. DOI: 10.1063/1.859320.
- [68] C. P. Robert and G. Casella. *Monte Carlo statistical methods*. 2nd ed. Springer New York, NY, 2004. DOI: 10.1007/978-1-4757-4145-2.
- [69] M. N. Rosenbluth and F. L. Hinton. “Poloidal flow driven by ion-temperature-gradient turbulence in tokamaks”. In: *Phys. Rev. Lett.* 80 (1998), p. 724. DOI: 10.1103/PhysRevLett.80.724.
- [70] O. Sauter et al. “On the non-stiffness of edge transport in L-mode tokamak plasmas”. In: *Phys. Plasmas* 21 (2014), p. 055906. DOI: 10.1063/1.4876612.
- [71] E. Sonnendrücker et al. “The semi-Lagrangian method for the numerical resolution of the vlasov equation”. In: *J. Comput. Phys.* 149 (2014), p. 201. DOI: 10.1006/jcph.1998.6148.
- [72] N. Tronko, A. Bottino, and E. Sonnendrücker. “Second order gyrokinetic theory for particle-in-cell codes”. In: *Phys. Plasmas* 23 (2016), p. 082505. DOI: 10.1063/1.4960039.
- [73] N. Tronko and C. Chandre. “Second-order nonlinear gyrokinetic theory: from the particle to the gyrocentre”. In: *J. Plasma Phys.* 84 (2018), p. 925840301. DOI: 10.1017/S0022377818000430.
- [74] T. Vernay. “Collisions in global gyrokinetic simulations of tokamak plasmas using the delta-f particle-in-cell approach: neoclassical physics and turbulent transport”. In: *EPFL PhD thesis* 5638 (2013).
- [75] L. Villard et al. “Global gyrokinetic ion temperature gradient turbulence simulations of ITER”. In: *Plasma Phys. Control. Fusion* 55 (2013), p. 074017. DOI: 10.1088/0741-3335/55/7/074017.
- [76] L. Villard et al. “Global turbulence features across marginality and non-local pedestal-core interactions”. In: *Plasma Phys. Control. Fusion* 61 (2019), p. 034003. DOI: 10.1088/1361-6587/aaf7e7.
- [77] L. Villard et al. “Radial electric fields and global electrostatic microinstabilities in tokamaks and stellarators”. In: *Phys. Plasmas* 9 (2002), p. 2684. DOI: 10.1063/1.1477921.

- [78] R. E. Waltz, R. L. Dewar, and X. Garbet. “Theory and simulation of rotational shear stabilization of turbulence”. In: *Phys. Plasmas* 5 (1998), p. 1784. DOI: 10.1063/1.872847.
- [79] T. H. Watanabe and H. Sugama. “Kinetic simulation of a quasisteady state in collisionless ion temperature gradient driven turbulence”. In: *Phys. Plasmas* 9 (2002), p. 3659. DOI: 10.1063/1.1501823.
- [80] N. Winsor, J. L. Johnson, and J. M. Dawson. “Geodesic acoustic waves in hydromagnetic systems”. In: *Phys. Fluids* 11 (1968), p. 2448. DOI: 10.1063/1.1691835.

Acknowledgments

I would like to thank my two supervisors, Laurent and Stephan, without whom this thesis will not be possible. Thank you for your unfathomable patience, kindness and wisdom. I only wish to emulate these qualities going forward. Working with you has been the greatest pleasure of my professional career.

Special thanks also to Noé Ohana, Emmanuel Lanti, Peter Donnel, Mohsen Sadr and Giovanni DiGiannatale, for your valuable assistance with, discussions and insights of, the code of GKengine and ORB5. Without you my progress with the enormous code would have been $10\times$ slower.

Next, I would like to thank my office mates Antoine Hoffmann and Arnas Volcõkas. Bouncing ideas off of each other has been one of my favorite moments at SPC. Your random ideas, distractions and memes do also played a big part in my mental processes.

Thank you António Coelho and Claudia Colandrea, for your love and support outside professional life during my time here in the lab and in Lausanne at large. You have played a very significant role in the past 4 years of my Swiss experience.

Chasing my ambitions would have been a lot harder without the support of dear loved ones, near and far: Marina Baumgartner, Liliya Imasheva, Elisabeth Griessbauer, Emmanuel Charles, Ruth Tan, Mei Yee Chew, En Ning Hwa, and Alitara Puangricharern. You have always been there through my good and hard times, calming me down, reminding me that which are important, and encouraging me to achieve greater goals and be better versions of myself.

And finally, I would like to thank my family, to whom this thesis is dedicated. I am entirely grateful for their constant love and support at every step along this journey leading up to this point. Thank you Appa, for instilling in me since my youth a questioning nature. Thank you Mummy, for your demonstration of how one should love, be compassionate and patient. Thank you my sisters, Abii and Narviinya, for the good childhood we had together, and the meaningful conversions that we had.

Moahan Murugappan

Avenue d'Echallens 63 – 1004 Lausanne – Switzerland

☎ +41 798 456 399 • ✉ moahan29@gmail.com

Current Position

Ph.D. Candidate - Doctoral Assistant

Swiss Plasma Center EPFL

Development of a gyrokinetic code for tokamak turbulence

9.2019 - present

- Developer of the global gyrokinetic ORB5 code
- Assistantship in Numerical Physics courses: exercise sessions, exam grading.
- Experience in Tokamak diagnostics data acquisition from TCV discharges.

Education

Ph.D. in Physics

EPFL

Swiss Plasma Center, Supervisor: Prof. Laurent Villard

2019–April 2024 (expected)

Masters in Applied and Engineering Physics

Technische Universität München

Institut für Plasmaphysik, Garching

2016–2018

- Master thesis (supervised by: Dr. Katharina Kormann):
Uncertainty quantification of the Vlasov-Poisson equations
using the hierarchical Tucker format

Bachelor of Science (Hons) 2nd Upper

National University of Singapore

Faculty of Physics

2008–2012

- Bachelor thesis (supervised by: Prof. Lim Hock):
A computational study of electromagnetic waves on corrugated surfaces

A-levels

Methodist College Kuala Lumpur

Physics, Chemistry, Biology, Mathematics

2006–2008

Experiences

Working student

Max Planck Institut für Physik München

Project

11.2018 - 03.2019

Investigation of algorithm for precision placement of dielectric discs for MADMAX

Associate Scientist

CRISP Singapore

Various projects

09.2012 - 02.2016

Super-resolution processing; Focusing of TELIOS-1 satellite camera via MTF measurements, forest fire detection

Language skills

- **English:** Native
- **Malay:** National language
- **Mandarin:** Fluent (spoken)
- **German:** Intermediate (B2)
- **French:** Beginner (A2)

Techincal skills

- **Academic:** Plasma physics, Numerical methods, Partial differential equations
- **Programming:** Fortran, Python, C, C++, Bash, MATLAB, LaTeX, Git

==

Publications and Conferences

Peer reviewed.....

- Murugappan, M, Villard, L, Brunner, S, McMillan, B. F. & Bottino, A. 2022 *Gyrokinetic simulations of turbulence and zonal flows driven by steep profile gradients using a delta-f approach with an evolving background Maxwellian*. Journal of Plasma Physics 29, [103904](#).

Conferences.....

- Murugappan et al. *Gyrokinetic simulations using a delta-f approach with an evolving background Maxwellian*. Poster at the 49th [European Conference on Plasma Physics 2022](#), Bordeaux
- Murugappan et al. *Simulations of microturbulence in magnetised plasmas using a delta-f gyrokinetic approach with an evolving background Maxwellian*. Poster at the [Theory of Fusion Plasmas](#) joint Varenna-Lausanne International Workshop 2022, Varenna IT.
- Di Giannatale, G. and Donnel, P. and Villard, L. and Bottino, A. and Brunner, S. and Lanti, E. and McMillan, B. F. and Mischenko, A. and Murugappan, M. and Hayward-Schneider, T. 2022 *Triangularity effects on global flux-driven gyrokinetic simulations*. Journal of Physics: Conference Series 2397, [012002](#)

Interests and extra-curricular activity

Chief Editor
German Language society

NUS
2010–2011